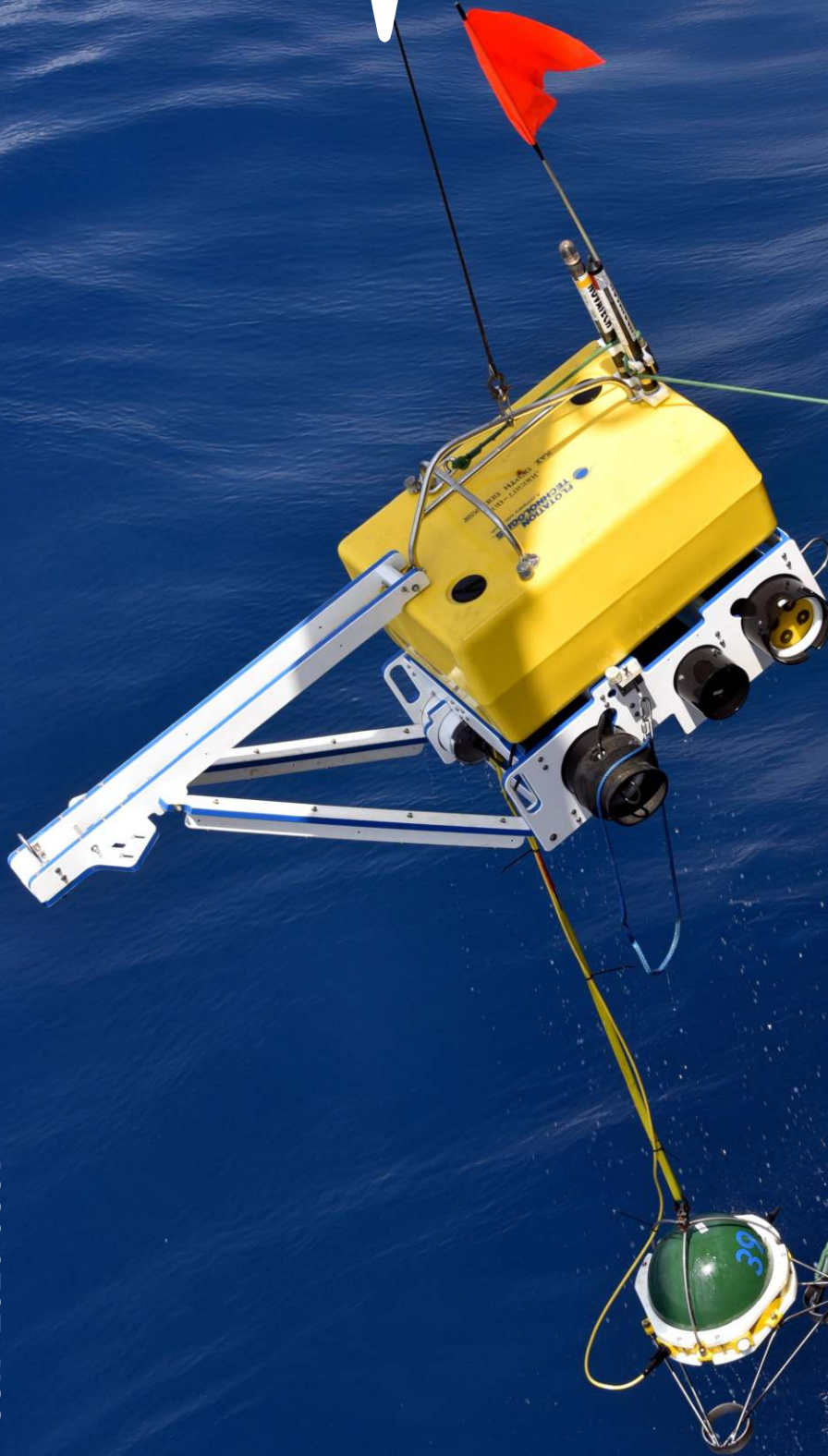


SEISMICA

DECEMBER 2022 | VOL 1 | NO 1



ISSN 2816-9387



McGill

Library
Bibliothèque

Issue 1, Volume 1, 2022

Aims and Scope

Seismica publishes original, novel, peer-reviewed research in the fields of seismology, earthquake science, and related disciplines. Seismica is a community-driven, diamond open-access journal. Articles are free to publish and free to read without a subscription, and authors retain full copyright.

Seismica strives to be **accessible, transparent, respectful, credible, and progressive.**

Seismica's scope includes a wide range of topics in seismological and earthquake sciences. A non-exhaustive list of topics that fall within the scope of Seismica includes: Fault-slip and earthquake source phenomena, Earthquake records, Imaging the Earth, Theoretical and computational seismology, Beyond Earth-tectonic applications, Techniques and instrumentation, Earthquake engineering and engineering seismology, Community engagement, communication and outreach.

For submission instructions, subscription and all other information visit: <https://seismica.library.mcgill.ca/>.

For editorial questions or issues, please contact info@seismica.org.

For technical assistance, please contact info@seismica.org.

For appeals, please contact appeals@seismica.org.

About the cover

Cover Caption Ocean bottom seismometer (OBS) recovery. OBS recovery occurred in March 2017 as part of the PI-LAB (Passive Imaging of the lithosphere-asthenosphere boundary) experiment and EURO-LAB (Experiment to Unearth the Rheological lithosphere-asthenosphere boundary). The experiments included 39 ocean bottom seismometers deployed for 1 year around the Chain Fracture Zone and the equatorial Mid-Atlantic Ridge. The OBS were co-located with 39 ocean bottom magnetotelluric instruments deployed as part of the CA-LAB (Central Atlantic Imaging of the lithosphere-asthenosphere boundary) experiment. There were also several co-located active source experiments. The goal of the experiments was to determine what makes a plate, 'plate-like' by studying young ocean lithosphere with a range of sensitivities and resolutions at a slow spreading end member, the Mid-Atlantic Ridge. Credit: Catherine Rychert and Michael Kendall.

Editorial Board

We warmly thank the following volunteers of the Editorial Board that have been involved in the issue.

Production Editors Gareth Funning , Kiran Kumar Thingbaijam 

Handling Editors Danielle Sumy , Christie Rowe , Alice-Agnes Gabriel , Tiegan Hobbs , Ryo Okuwaki , Mathilde Radiguet , Paula Koelemeijer , Lauren Waszek , Lise Retailleau 

Copy/layout Editors Abhineet Gupta , Hannah Mark , Théa Ragon , Cláudia Reis , Kirsty Bayliss 

Media & Branding Jaime Convers , Ezgi Karasozen , Tran Huynh 

Volunteers

We warmly thank the following volunteers that have been involved in the issue.

Signed Reviewers Laura Ermert , Manuele Faccenda 

Issue 1, Volume 1, 2022

Table of Contents

Articles

A Bayesian approach to the tomographic problem with constraints from geodynamic modeling: Application to a synthetic subduction zone

Magali et al.

The root to the Galápagos mantle plume on the core-mantle boundary

Cottaar et al.

Tilt Corrections for Normal Mode Observations on Ocean Bottom Seismic Data, an example from the PI-LAB experiment

Harmon et al.

Seismic interferometry in the presence of an isolated noise source

Schippkus et al.

Fast Reports

Locating the Nordstream explosions using polarization analysis

Stähler et al.

Source Model and Characteristics of the 27 July 2022 MW 7.0 Northwestern Luzon Earthquake, Philippines

Rimando et al.

Editorials

The launch of Seismica: a seismic shift in publishing

Rowe et al.

A Bayesian Approach to the Tomographic Problem with Constraints from Geodynamic Modeling: Application to a Synthetic Subduction Zone

John Keith Magali  * 1,2, Thomas Bodin  2

¹Université de Lille, CNRS, INRA, ENSCL, UMR 8207 - UMET - Unité Matériaux et Transformations, 59000 Lille, France, ²Univ Lyon, Univ Lyon 1, ENSL, UJM-Saint-Etienne, CNRS, LGL-TPE, F-69622, Villeurbanne, France

Author contributions: *Conceptualization:* JKM, TB. *Methodology:* JKM, TB. *Software:* JKM. *Validation:* JKM. *Formal Analysis:* JKM. *Investigation:* JKM. *Resources:* TB. *Writing - original draft:* JKM. *Writing - Review & Editing:* TB. *Visualization:* JKM. *Supervision:* TB. *Funding acquisition:* TB.

Abstract Geodynamic tomography, an imaging technique that incorporates constraints from geodynamics and mineral physics to restrict the potential number of candidate seismic models down to a subset consistent with geodynamic predictions, is applied to a thermal subduction model. The goal is to test its ability to recover structures harboring complex deformation patterns. The subduction zone is parameterized in terms of four unknown parameters that define its thermal structure: slab length L , thickness R , temperature T_c , and dip angle θ . A temperature-dependent viscosity is prescribed with an activation coefficient E controlling the sensitivity. Using the full forward approach to geodynamic tomography, we generate anisotropic surface wave dispersion measurements as synthetic data. We retrieve the five unknown parameters by inverting the synthetics corrupted with random uncorrelated noise. The final output is an ensemble of models of L , R , θ , T_c , and E cast in a posterior probability distribution with their uncertainty limits. Results show that the parameters are tightly constrained with the apparent existence of a single misfit minima in each of them, implying the implicit retrieval of the complete patterns of upper mantle deformation, and the 21-independent coefficients defining elastic anisotropy. Each model realization, however, fails to swarm around its true value. Such results are attributed to the inability of the surrogate model to accurately replicate the correct forward model for computing anisotropy due to the complexity of the deformation patterns considered. Nevertheless, this proof of concept shows a self-consistent method that incorporates mantle flow modeling in a seismic inversion scheme.

Non-technical summary Seismic tomography is an active area of research in seismology that primarily deals with the imaging of the Earth interior. Here, seismic data are used to recover the heterogeneous structure of the Earth at a given resolution in a process known as inversion. However, seismic inversion methods have to be constantly improved to accurately map these heterogeneities in order to correctly interpret them in terms of recent deformation mechanisms within the Earth. We introduce geodynamic tomography; a new imaging technique that infers the present-day temperature and mantle flow patterns from the inversion of surface wave measurements. We demonstrate this method in a subduction zone setting (an earthquake prone area where materials making up a tectonic plate are recycled into the mantle) by recovering some properties that define its thermal structure: length, thickness, angle of subduction, and slab core temperature.

Production Editor:
Gareth Funning
Handling Editor:
Paula Koelemeijer
Copy & Layout Editor:
Kirsty Bayliss

Received:
July 12, 2022
Accepted:
November 21, 2022
Published:
December 12, 2022

1 Introduction

Backed by numerous seismic tomography studies at the global (e.g. [Montagner and Tanimoto, 1991](#); [Panning and Romanowicz, 2006](#)) and regional scale (e.g. [Montagner and Jobert, 1988](#); [Debayle and Kennett, 2000](#)), the Earth's upper mantle exhibits large scale anisotropy which have been mainly attributed to the development of the crystallographic preferred orientation (CPO) of olivine aggregates as they get advected by mantle flow (see [Long and Becker, 2010](#), for a comprehensive review).

In practice, observations of seismic anisotropy rely on the simplification of the full elastic tensor (*i.e.* a

fourth rank tensor of elasticity with 21 independent coefficients) because seismic waves are only sensitive to a limited number of coefficients. Tilted transverse isotropy (TTI) is one of the most convenient ways to simplify the elastic tensor, if not the most. In such a symmetry, the elastic constants can be defined by the five Love parameters A_0 , C_0 , F_0 , L_0 , and N_0 , and two angles that define the dip and the azimuth, respectively, of the symmetry axis ([Love, 1927](#)). Particularly for S -wave anisotropy, further simplifications can be defined to reduce the model dimensionality. On one end, we have horizontal transverse isotropy (HTI) where the axis of symmetry is horizontal. Also called azimuthal anisotropy, here S -wave speeds vary with propagation direction. On the other, we have vertical transverse isotropy (VTI) where the axis of symme-

*Corresponding author: jkvmagali@gmail.com

try is vertical as a consequence of azimuthal averaging. Also called S -wave radial anisotropy, this property causes shear wave speeds to vary with polarization orientation instead. In theory, constraining the tilt of anisotropy is possible (Montagner and Nataf, 1988), and in practice has already been implemented in the regional scale (Xie et al., 2015, 2017). However due to sparse azimuthal sampling, non-uniqueness of the solutions, and finite frequency effects brought by tilted layers, this may make its implementation discouraging.

Surface waves provide unique constraints to large scale anisotropy in the upper mantle. S -wave radial anisotropy, for instance, can be recovered through joint inversions of Love and Rayleigh wave velocities (Babuska and Cara, 1991). Likewise, azimuthal anisotropy can be effectively constrained by adding the azimuthal terms of surface wave velocities in the data vector (Smith and Dahlen, 1973). Similar to what was previously mentioned, surface waves are effectively sensitive to 9 depth functions of the elastic constants when poor azimuthal coverage is taken into account: 5 for radial anisotropy given by the previously mentioned Love parameters; and 4 for azimuthal anisotropy given by G_c , G_s , and B_c , B_s , whose kernels are identical to that of S - and P -waves, respectively (Montagner and Nataf, 1986). By itself however, 9 unknown parameters are still an excessive amount to be inverted for, and still can be difficult to resolve. Because of this, velocity and anisotropy ratios are imposed ad-hoc for regularization (Obrebski et al., 2010, 2011) which may potentially bias the results. Moreover due to its limited sensitivity to the elastic tensor, we are left with a rudimentary understanding of mantle deformation processes when relying on tomographic images alone. Thus, complete knowledge of the full elastic tensor is imperative to capture the complete patterns of upper mantle deformation.

2 Background: Geodynamic tomography

Geodynamic tomography, as reported in Magali et al. (2021b), is a novel approach to the tomographic problem whose two key features are the reduction of the number of unknowns and the removal of symmetry relations to the elastic tensor through the incorporation of geodynamic and petrological constraints. Due to its high non-linearity, the solutions to the tomographic problem are appraised based on a Bayesian probability framework (i.e. the posterior).

Under Bayesian inference, geodynamic tomography may not be a conventional inverse problem per se because it proposes a set of unknown parameters, computes the forward model, and compares the estimated to the observed data thousands of times. The efficient search for plausible solutions is carried out through a Markov chain Monte Carlo (MCMC) algorithm. Here, MCMC ultimately tends to sample a restricted area of high probability density and operates according to a random-walk behavior. At this point, the chain is said to be converged; meaning that the target posterior has been successfully approximated.

As of its current implementation, the method only inverts local surface wave phase velocity dispersion curves and their azimuthal variations for the retrieval of the thermal structure. In practice, dispersion curves can be obtained by stacking 2-D surface wave velocity maps with period, and then recovering a plot of phase velocities versus period at a given geographical location (e.g. Nakanishi and Anderson, 1983; Romanowicz, 2002). As such, it is under the assumption of geodynamic tomography that dispersion curves (which are also a product of inversion) are readily available. Although there have been a growing number of studies that implement probabilistic approaches to invert for the thermal (and chemical) structure from multiple data types, which include surface wave dispersion measurements such as in Afonso et al. (2013b,a), and Bissig et al. (2021), geodynamic tomography incorporates mantle flow modeling followed by texture evolution computations to constrain strain-induced seismic anisotropy, and potentially the medium rheology.

Given a temperature field and assuming a strictly temperature-dependent viscosity, mantle flow models are obtained using an instantaneous approach. In this approach, it is not necessary to include the conservation of energy in solving the equations of viscous fluid flow. As a result, a steady-state assumption in the flow is implied when tracing flow streamlines backwards in time. Instantaneous models with a steady-state assumption may be valid if we interpret the temperature field as its present-day structure, and assume that the time-scale for the development of strain-induced anisotropy in mantle minerals is much faster than the variations of mantle flow velocities with time. Because of this, geodynamic tomography is not suitable to invert for the evolution history of the temperature field.

For each flow line traced, undeformed aggregates composed of a discrete number of crystals are placed at a position in the streamline corresponding to the first time step. Texture evolution modeling is then implemented to track the strain evolution of the aggregates along the streamline. The texture evolution model currently implemented in our forward problem uses an ‘average field’ formalism (Kaminski et al., 2004). Here, unlike finite-element approaches where the aggregate is explicitly deemed as a spatially extended body, it is not necessary to keep track of the interaction among crystals. Instead, the crystals within the aggregate are finite and are treated as a collective entity in a homogeneously isotropic medium whose properties are the weighted mean of the properties of each crystal. The output of the texture evolution model is the full elastic tensor. This tensor can be decomposed into much simpler forms for easier interpretation. For instance, it can be decomposed into a VTI medium using the method of Montagner and Nataf (1986) to obtain radial anisotropies in P - and S -waves.

Magali et al. (2021b) highlights the success of geodynamic tomography in the recovery of the complete patterns of upper mantle deformation from anisotropic surface wave measurements in the most simple cases (i.e. instantaneous flow induced by spherical tempera-

ture anomalies). This paper explores the ability of the method to capture more complex deformation patterns in the guise of a 3-D instantaneous flow across the upper mantle induced by subduction, and so directly serves as an extension to Magali et al. (2021b). To do so, we model thermal subduction by applying a continuous parameterization of the subducting slab in terms of hyperbolic tangent basis functions on top of a background temperature field. The basis function depends on four parameters which would be treated as unknowns: (1) slab length L , (2) slab thickness R , (3) dip angle θ , and (4) slab temperature T_c . For the medium rheology, we employ a temperature-dependent viscosity controlled by a scalar parameter called the activation coefficient, E ; although it is acknowledged that a realistic parameterization involves the implementation of non-linear rheologies relevant to upper mantle conditions (Karato and Wu, 1993). We implement geodynamic tomography to retrieve these five unknown parameters that define the thermal and rheological structure of a synthetic subduction zone. The method is tested to synthetic data prescribed with very low noise levels to mimic periodically-correlated surface wave dispersion measurements. We demonstrate how the incorporation of geodynamic and petrological constraints tightly recover these five unknowns, which will then imply the implicit retrieval of the complete patterns of upper mantle deformation, and correspondingly, the full elastic tensor.

3 Methodology

Since this work serves as a continuation to Magali et al. (2021b), this section only describes the appropriate changes made to the method to adapt geodynamic tomography to a subduction setting with known geometry.

3.1 Model parameterization

3.1.1 Thermal structure of a subducting slab

We begin by defining a 2.5-D temperature field $T(\mathbf{r})$ that is constructed in a regular grid of size $N_x \times N_y \times N_z$ that extends symmetrically along the y -axis. The temperature field is expressed as the sum of a background temperature $T_{\text{background}}$ derived from a half-space cooling model, and a thermal anomaly δT which translates to:

$$T(\mathbf{r}) = T_{\text{background}}(\mathbf{r}) + \delta T(\mathbf{r}), \quad (1)$$

where $T_{\text{background}}$ is given by:

$$T_{\text{background}}(\mathbf{r}) = (1900\text{K} - 500\text{K}) \operatorname{erf}\left(\frac{z}{2\sqrt{\kappa t}}\right) + 500\text{K}, \quad (2)$$

where \mathbf{r} is any arbitrary position in 3-D space defined by the coordinates $\mathbf{r} = [x, y, z]$, κ is the thermal diffusivity, z is depth, and t is the plate age in million years.

The anomaly δT is a subducting slab defined by three geometrical parameters: (1) dip angle θ , (2) length of the slab L , (3) thickness R , and one scalar parameter T_c that determines the magnitude of the temperature along the axis of symmetry of the slab. We model it

in terms of a hyperbolic tangent function, \tanh where it forces the temperature to be the coldest at the slab's symmetry axis, and that the spread of \tanh relates to the thickness of the slab itself (*i.e.* the parameter R). The temperature anomaly is mathematically defined as:

$$\delta T(\mathbf{r}) = -\frac{T_c}{2} \left[1 - \tanh\left(\frac{\beta}{L_{\text{scale}}}\left(d - \frac{R}{2}\right)\right) \right] \quad (3)$$

where d is the distance from the slab's center axis to any point perpendicular to it, β controls the sharpness of the temperature gradient which is held at a fixed value, and L_{scale} is the length of the vertical domain which we set to 400 km. Fig. 1 shows the thermal structure of the subduction model viewed in 2-D (left panel) and in 3-D (right panel) using the aforementioned parameterization. The model parameters possess the following values: $L = 150$ km, $\theta = 35^\circ$, $R = 120$ km, $T_c = 800$ K.

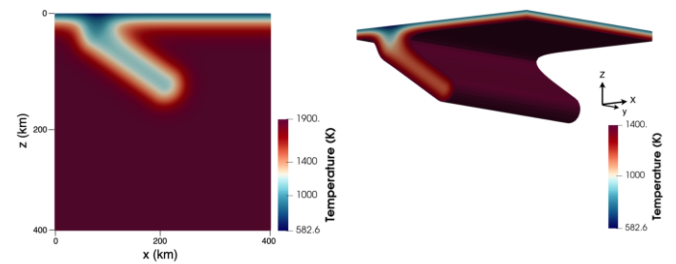


Figure 1 Thermal structure of a subduction zone parameterized in terms of geometrical points. The structure is rendered using the following input parameters: $L = 150$ km, $\theta = 35^\circ$, $R = 120$ km, $T_c = 800$ K. The left panel represents the vertical cross-section of the model whereas the right panel corresponds to the isovolumetric contour plot of the temperature field.

3.1.2 Medium rheology

The medium rheology is modeled following the Frank-Kamenetskii approximation to Arrhenius-type viscosity. This means that the influence of temperature onto viscosity is supervised by the activation coefficient E . The viscosity field η is given by:

$$\eta(\mathbf{r}) = \eta_0 \exp\left[-E \frac{T(\mathbf{r}) - T_0}{T_0}\right], \quad (4)$$

where η_0 and T_0 are reference values for viscosity and temperature, respectively. In the inversions, the total number of parameters to be inverted for are five: four of which L , θ , T_c , and R characterize the temperature field of the subduction model, and the latter E controls the sensitivity of the viscosity to temperature. We choose E as an unknown in order to demonstrate the ability of geodynamic tomography to constrain some properties of the medium rheology. This is essential because we expect that larger values of E make the cold slab more rigid, and thereby lessen the amount of strain-induced anisotropy across it. Since seismic data contain the surface manifestation of strain-induced anisotropy, they then provide potential clues about the rheological structure of the Earth's interior. The variables β , T_0 , and

η_0 are held at fixed values throughout the inversion process. The model vector \mathbf{m} is thus:

$$\mathbf{m} = [L, \theta, T_c, R, E]. \quad (5)$$

3.2 The forward problem

The complete forward problem proceeds as follows: (1) Given the temperature and viscosity fields described by Equations (1) and (4), respectively, we first numerically solve an instantaneous 3-D convection problem with temperature-dependent viscosity that is benchmarked against Samuel (2012, 2018). (2) Using the velocity field obtained from (1), we compute velocity gradients using finite differences. (3) Under a steady-state assumption, we then trace the flow backwards in time using fourth-order Runge-Kutta, and at each time step along the flow line, a local velocity gradient tensor is estimated. (4) We then track CPO evolution of olivine aggregates using D-Rex (Kaminski et al., 2004). This computes the anisotropic part of the elastic tensor. Later in the inverse approach, we replace step (2) with an artificial neural network (Bishop et al., 1995) whose architecture follows that of LeCun et al. (2015). The training data are comprised of a pair of flow lines with local velocity gradients at discrete time steps along the path (training input) and the deviatoric part of the elastic tensor predicted with D-Rex (training output). This speeds up the computation of anisotropy by several orders of magnitude (Magali et al., 2021b), and hence is befitting within a sampling-based inversion scheme (Hansen and Cordua, 2017; Köpke et al., 2018; Conway et al., 2019; Moghadas et al., 2020). (3) From the temperature field and the hydrostatic pressure, we derive the pressure and temperature dependence of the isotropic part of the elastic tensor using a thermodynamic model for a given bulk composition using Perple_X (Connolly, 2005, 2009; Stixrude and Lithgow-Bertelloni, 2011). The result from (2) and (3) is a complete elastic tensor at each point in space. (3) The last step involves computing synthetic surface wave dispersion curves using normal mode summation in a spherical earth (Smith and Dahlen, 1973) using DISPER80 (Saito, 1988) and their azimuthal variations (Montagner and Nataf, 1986) from the elastic tensor. We refer the reader to Magali et al. (2021b), and Chapter 3 of Magali (2021) for a comprehensive description of the full forward problem.

3.3 Synthetic data

The synthetic data to be inverted consists of local surface wave dispersion measurements and their azimuthal variations at the surface. The form of the Rayleigh wave dispersion curve is the sum of an isotropic component $c_{R,0}$ and its azimuthal variations c_1 and c_2 :

$$c_R(P, \psi) = c_{R,0}(P) + c_1(P) \cos(2\psi) + c_2(P) \sin(2\psi), \quad (6)$$

and for Love waves we simply have:

$$c_L(P) = c_{L,0}(P), \quad (7)$$

where P is the period, and ψ is the azimuth of propagation. Notice that we have neglected the azimuthal terms

for Love waves. Such simplifications are reasonable due to sparse azimuthal coverage and higher noise levels on Love waves relative to Rayleigh waves in real-Earth data (Maupin and Park, 2015).

3.4 Inversion method

Bayesian inversion is implemented where the solution is an ensemble of models (*i.e.* model parameters found in Equation (5)) distributed according to the posterior probability density function $p(\mathbf{m}|\mathbf{d}_{\text{obs}})$, accompanied by their uncertainty bounds. In this framework, Bayes' theorem is written as:

$$p(\mathbf{m}|\mathbf{d}_{\text{obs}}) \propto p(\mathbf{m})p(\mathbf{d}_{\text{obs}}|\mathbf{m}). \quad (8)$$

The parameter space is searched using a Markov chain Monte Carlo (MCMC) algorithm. To produce reasonable acceptance rates, we employed an adaptive perturbation scheme.

3.4.1 Likelihood function

The likelihood function $p(\mathbf{m}|\mathbf{d}_{\text{obs}})$ quantifies how well the model parameters fit the observed data. Here we assume that the errors are uncorrelated and follow a univariate Gaussian distribution with zero mean, and variance σ_c^2 , the likelihood function corresponding to a single dispersion measurement can be written as:

$$p(c_{\text{obs}}|\mathbf{m}) = \frac{1}{(2\pi\sigma_c^2)^{N/2}} \exp\left[-\frac{\|\mathbf{c}_{\text{obs}} - \mathbf{c}_{\text{est}}\|^2}{2\sigma_c^2}\right], \quad (9)$$

where \mathbf{m} is the model vector, N is the number of discrete periods, σ_c^2 is the estimated variance of the data noise, \mathbf{c}_{obs} is the observed synthetic data to be inverted, and \mathbf{c}_{est} is the synthetic data estimated during the inversion process. The likelihood functions of the 2θ terms can be cast in the same manner.

3.4.2 Prior distribution

We assume the model parameters to be independent. In this way, the prior distributions for each model parameter are separable and can be expressed as a product of each distribution:

$$p(\mathbf{m}) = \prod p(L)p(\theta)p(R)p(T_c)p(E). \quad (10)$$

Each prior on the model parameters follows a uniform distribution with wide bounds to avoid imposing hard constraints from the prior. Such a setup mimics a scenario where prior knowledge about the regional setting is scant and thus the solution to our inverse problem is more likely driven by the information provided by the data. The prior bounds are as follows: (1) 100 km - 200 km for L , (2) 80 km - 150 km for R , (3) $20^\circ - 45^\circ$ for θ , (4) 500 K to 1000 K for T_c , and (5) 5 to 12 for E .

3.4.3 Generation of new models along the Markov chain

We use a Markov chain Monte Carlo (MCMC) algorithm to search the parameter space that could explain the data. The sampler initiates by randomly drawing a set

of L , R , θ , T_c , and E values within the prior bounds followed by the evaluation of the likelihood function. Then at each iteration in the Markov chain, a new model m' is proposed by randomly selecting one of the possible set of moves:

1. Vary the length of the slab L . The slab length is perturbed according to a univariate Gaussian distribution centered at the current value of L .
2. Vary the dip angle θ . The dip angle is perturbed according to a univariate Gaussian distribution centered at the current value of θ .
3. Vary the thickness of the slab R . The slab thickness is perturbed according to a univariate Gaussian distribution centered at the current value of R .
4. Vary the temperature of the slab T_c . The slab temperature is perturbed according to a univariate Gaussian distribution centered at the current value of T_c .

After choosing one of the four possibilities, the proposal is always accompanied by the perturbation of E . The activation energy is perturbed using a univariate Gaussian distribution centered at the current value of E .

4 Full forward procedure to predict surface wave measurements from the subduction model

Tab. 1 summarizes the true model parameters used to describe the thermal and rheological structure of the synthetic subduction zone. Note that the other scalar variables uninvolved in the inversion procedure, such as the dimensionless parameters defining the Rayleigh number, are preserved as in Magali et al. (2021b). When computing CPO anisotropy with D-Rex, we use the active slip systems of olivine corresponding to dry upper mantle conditions, and estimate the evolution of the texture onto ~ 2000 olivine crystals for 10 My. Other parameters such as the grain boundary mobility and the threshold volume fraction for grain boundary sliding are taken from the reference D-Rex model (Kaminski et al., 2004).

Model parameter	Assigned value
L	150 km
R	120 km
θ	35°
T_c	800 K
E	11.0

Table 1 True model parameters defining the thermal structure of the subduction model.

The instantaneous flow is computed in a $400 \text{ km} \times 400 \text{ km} \times 400 \text{ km}$ box with a $6.25 \text{ km} \times 6.25 \text{ km}$ resolution. Tangential velocities are prescribed at the top to replicate real Earth subduction dynamics. The bottom and lateral boundary conditions are free-slip.

Fig. 2a shows the vertical cross-section of the 3-D instantaneous flow field induced by subduction. We observe one of the conspicuous features of subduction-induced flow, that is the existence of a local convection cell beneath the slab tip attributed to retrograde slab motion. This is accommodated by the existence of back-arc motion towards the trench made responsible mainly by trench suction and in part by the induced leftward motion due to the imposed plate velocity across the overriding plate. This also ensures flow ascension in front of the slab. The vigorous mixing observed across the sub-slab mantle resembling roll-back motion is mainly influenced by horizontal boundary effects. Such effects can be reduced by increasing the size of the model domain. Nevertheless, most features observed across the vertical cross-section are mainly predisposed by poloidal flow (*i.e.*, buoyancy-related motion). In essence as with any divergence-free vector field, our velocity field can be decomposed into a poloidal component, and a toroidal component which relates to horizontal flow due to the presence of lateral viscosity contrasts (Gable et al., 1991; Bercovici, 1995). Since we imposed temperature-dependent viscosity, we are compelled to deal with toroidal motion due to lateral variations in viscosity as shown in Fig. 2b (*i.e.* the horizontal projection of the flow whose plane is normal to the z -axis) where we observe some local vorticities around the slab edges.

Fig. 3 shows the vertical cross-section of the finite strain representation of the subduction model. Solid black lines pertaining to the orientation of the long axis of the finite strain ellipsoid (fse) are superimposed on top of the natural strains (*i.e.*, amplitude of finite deformation in terms of the natural logarithm of the ratio between the long and short axes of the fse). Finite strain orientations to first-order tend to be parallel to the direction of flow, however, may lag behind in some instances where deformation rapidly varies along the flow trajectory (Kaminski and Ribe, 2002). The absence of deformation correlates well with the presence of the fortified and highly-viscous slab.

From the velocity field, we gain access to the macroscopic velocity gradients by finite differencing. The 3-D map of the local velocity gradient in conjunction with the temperature field are utilized to construct an elastic model of the synthetic subduction zone using a micro-mechanical model for CPO evolution for the anisotropic part, and a thermodynamic model for the isotropic part, respectively. At any arbitrary location in 3-D space, the elastic model contains the full elastic tensor. Since it is arduous to interpret a fourth-rank tensor, it is often convenient to decompose \mathbf{S} into a specific symmetry class to better analyse its properties. Fig. 4 illustrates the vertical cross-section of the elastic constants A_0 related to PV -waves and L_0 related to SV -waves associated with the subduction model. The elastic constants are computed from the elastic projection of \mathbf{S} to an azimuthally-averaged VTI medium (Montagner and Nataf, 1986). Both panels robustly map the cold subducting slab with L_0 exhibiting sensitivity to temperature variations more fervently than A_0 . Since the con-

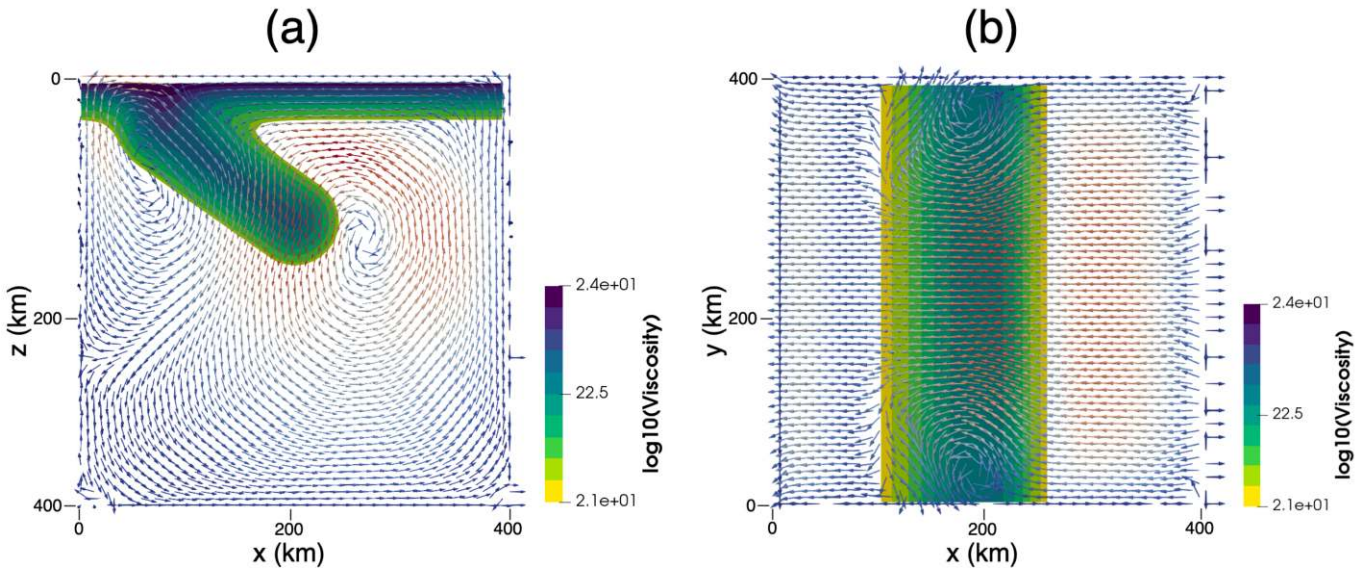


Figure 2 Instantaneous velocity field induced by subduction. The effective viscosity in log units is superimposed. Model domain is of the size $64 \times 64 \times 64$ elements, free-slip boundary conditions are imposed at the lateral and bottom sides. Opposing plate velocities are prescribed at the top to drive horizontal motion. (a) Vertical cross-section of the velocity field. (b) Overhead view of the velocity field at a depth of ~ 100 km. Figure (b) illustrates the significance of lateral viscosity variations to produce toroidal fluid flow.

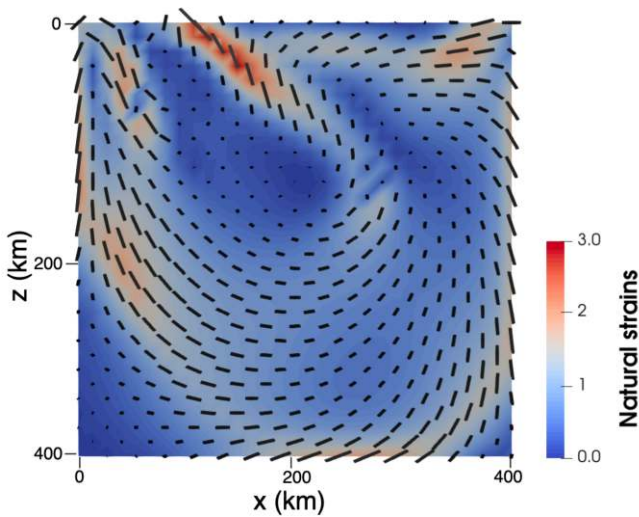


Figure 3 Cross-sectional view in the xz -plane of the natural strains (*i.e.*, amplitude of the fse in terms of the natural logarithm of the ratio between the long and short axes). Solid black lines are attributed to the orientation of the long axis of the fse. Finite strain framework is usually used as a proxy to infer convective flow in the mantle.

stants A_0 and L_0 are not the isotropic averages of the fast and slow velocities but a linear combination of the elastic tensor, they possess small anisotropic perturbations thus explaining the presence of smearing in some areas of the maps.

On the other hand, Fig. 5 represents the vertical cross-section of S -wave radial anisotropy ξ (left panel) and of the amplitude of total anisotropy in terms of the anisotropy index (*i.e.*, norm fraction of the elastic tensor with respect to the isotropic component) (right panel). As observed, regions of positive radial anisotropy $\xi > 1$ correlate well with horizontal flow and of negative ra-

dial anisotropy $\xi < 1$ with vertical flow. In terms of the anisotropy index, the entrained mantle wedge adjacent to the plunging slab, and beneath the back-arc produced the most CPO due to shear deformation initiated by slab pull and reinforced by trench suction. Strong anisotropy produced across the shallower depths of the sub-slab can be attributed to roll-back motion augmented by boundary effects. Across the slab itself, we expect $\xi \approx 1$ since the material is designed to mimic rigid plates that withstand deformation. This is also observed at the right panel where the anisotropy index across the slab appears to be close to zero. Thus in this case, the subducting slab can be regarded as isotropic since no CPO is generated due to its resilient rheological integrity. The presence of small-scale artifacts in the anisotropic structures may be attributed to numerical errors associated with the forward calculations.

From an elastic medium built from the spatial distribution of S , it is now possible to compute 2-D phase velocity maps and their azimuthal variations. For instance, Fig. 6 shows a map of the computed phase velocity and azimuthal anisotropy for Rayleigh waves at 100 s. The increase in velocity on the left portion of the map shown in Fig. 6a indicates the influence of the cold subducting slab. In Fig. 6b, the characteristic blue margin in between the yellow regions corresponds to the slab itself. This is also delineated by the shortening of the fast axis of azimuthal anisotropy within its vicinity (solid black lines). Although the orientation of the fast axis is a sufficient proxy to infer the horizontal projection of flow, it may still fail to render some important characteristics such as the presence of a toroidal component in the flow. This is because azimuthal anisotropy in surface waves is an integrated effect of the elastic anisotropy with depth. Furthermore, the latter depends on the deformation trajectory. Hence, absolute flow

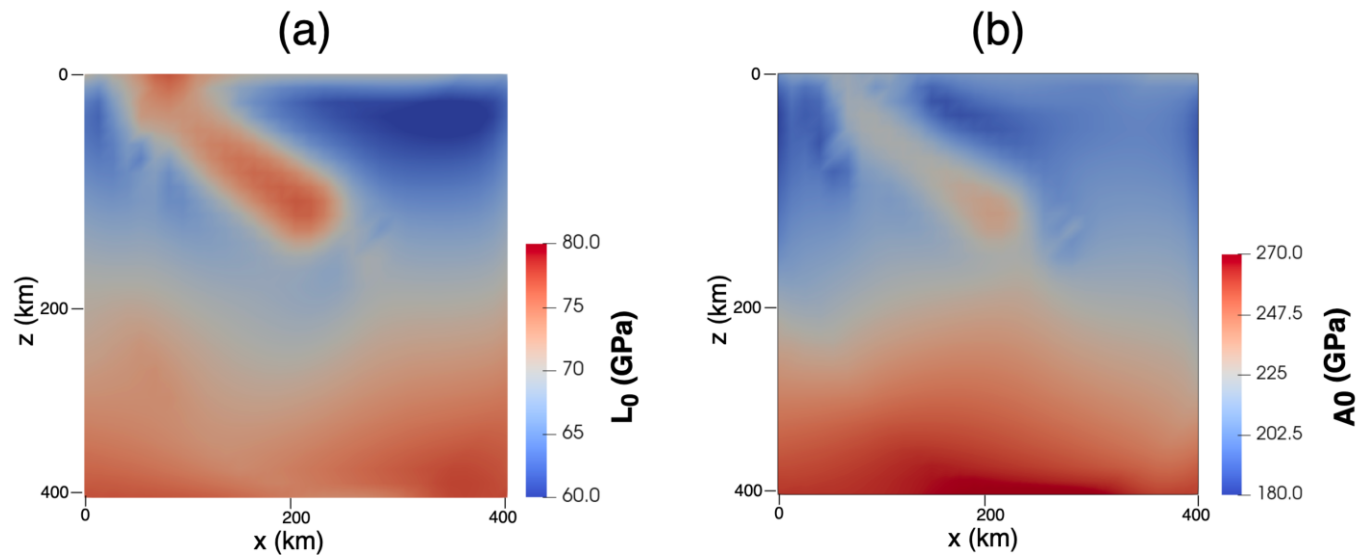


Figure 4 Cross-sectional view in the xz - plane of the elastic constants L_0 (left panel) and A_0 (right panel). Since elasticity strongly depends on temperature, we can easily map the cold subducting slab in the seismic models. The cross sections are taken at the center of the y - axis.

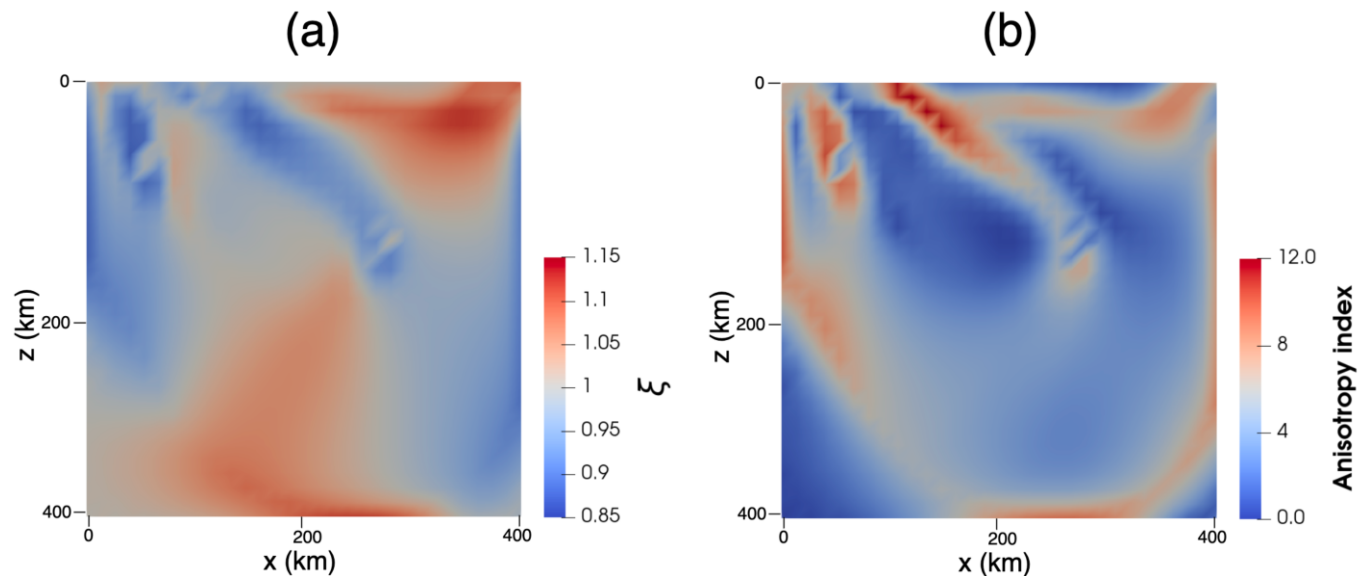


Figure 5 Cross-sectional view in the xz - plane of the S -wave radial anisotropy ξ (left panel) and the anisotropy index expressed in terms of the tensor norm fraction of S with respect to its isotropic component (right panel). The cross sections are taken at the center of the y - axis.

velocities may be well away from the orientation of its fast propagation. Finally, the deformation induced by subduction seemingly produces about 2% azimuthal anisotropy in surface waves which spreads out almost evenly throughout the map and is only restricted by the existence of the slab.

5 Inversion results

Using the values of the model parameters summarized in Tab. 1, we generate synthetic surface wave dispersion curves and their azimuthal variations at periods between 10 and 200 s with 10 s intervals. The complete data consist of a regular array of 8×8 locations containing c_R , c_L , c_1 , and c_2 spanning the entire surface. The synthetic data are computed based on the full elas-

tic tensors (*i.e.* with 21 independent coefficients) calculated with D-Rex.

We add Gaussian uncorrelated noise onto $c_{R,0}$, $c_{L,0}$, c_1 , and c_2 . We assign very low noise levels for $c_{R,0}$ and $c_{L,0}$ with $\sigma_{R,L} = 0.001 \text{ km s}^{-1}$ to mimic periodically-correlated surface wave dispersion measurements. Conversely, the azimuthal variations are assigned with $\sigma_{1,2} = 0.005 \text{ km s}^{-1}$. Fig. 7 shows a synthetic surface wave dispersion curve with and without added noise at one specific geographical location.

The inversion consists of 20 independent Markov chains containing 40 000 samples each initiated at a random model (*i.e.*, values for L , θ , R , T_c , and E are randomized for all chains) to ensure loose compliance to the initial model. Job array processing has been imple-

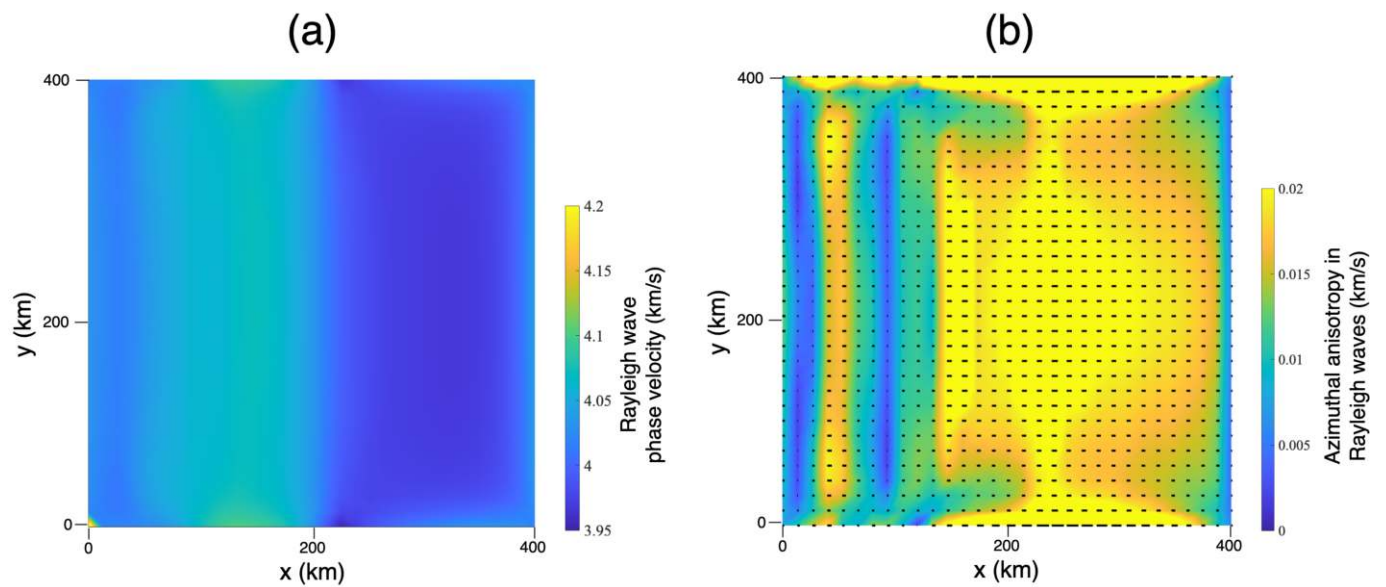


Figure 6 Phase velocity maps derived from a 3-D deforming upper mantle beneath a subduction zone at 100s period. (a) Rayleigh wave phase velocity (km/s). (b) Azimuthal anisotropy in Rayleigh waves (km/s). The solid black lines correspond to the direction of the fast propagation axis. Surface wave maps always lie along the xy – lateral plane.

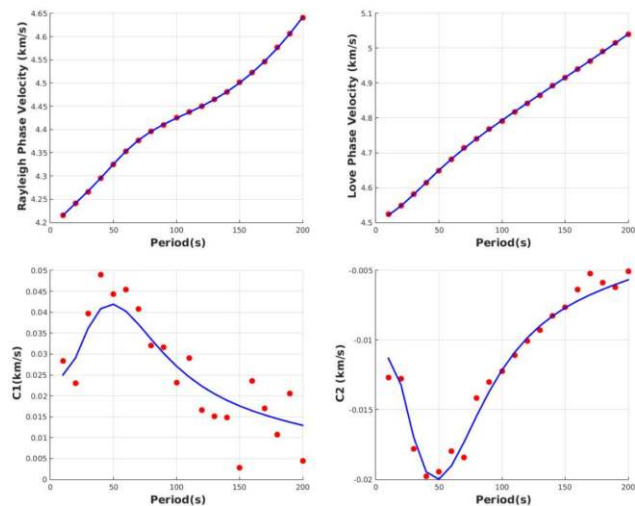


Figure 7 Synthetic surface wave dispersion curves from 10 to 200 s at a given geographical location (blue lines). The data used in the inversions have been added with Gaussian uncorrelated noise (red circles).

mented where each Markov chain is assigned with one element of the job array. Each job array then contains one task per node. Meanwhile for each task (and hence each node), 12 CPUs are assigned for multi-threading flow computations with OpenMP (OpenMP Architecture Review Board, 2008). As for the rest of the computations involved in the full forward procedure, we use a serial implementation for each task. On average it takes approximately 10 seconds to complete one MCMC cycle (*i.e.* model proposition + forward computation + likelihood function computation).

We demonstrate two cases: (1) an isotropic inversion and an (2) anisotropic inversion (*i.e.*, geodynamic tomography). Both cases are imposed with wide uni-

form priors allowing for more mobility when searching the parameter space. For efficient sampling, we commence geodynamic tomography by first employing an isotropic inversion. Once the independent chains have converged in this phase, we then proceed with the actual anisotropic inversion procedure. It is important to emphasize that we implement an artificial neural network (ANN) algorithm to approximate D–Rex. Since the current architecture of the network is problem-specific, it is designed based on training data generated by flow models produced by a family of thermal subduction models described by Equations (1), (2), and (3).

5.1 Marginal posterior probability distributions of the recovered model parameters

Figs 8 and 9 show the 1-D marginal posterior probability distribution on each model parameter (diagonal panels) and the joint marginal posterior probability distribution between a pair of model parameters (off-diagonal panels) to explore possible trade-offs for isotropic inversion and anisotropic inversion, respectively. The red lines and the black circles indicate their correct values. Both cases have exhibited a single misfit minima for the model parameters that define the thermal structure of the subduction model. However by incorporating geodynamic and petrological constraints, we observe that the entirety (this includes E) are much more tightly constrained than the isotropic case, as evidenced by the considerable decrease in the spread of the distributions. The narrow widths of the posterior distributions are also a manifestation of the low noise levels accounted for in the inversions. Between these two effects, it can be implied that the imposition of geodynamic constraints contributes far more toward the robustness of the solutions than the usage of low-noise data. Finally, the existence of a linear trade-off between

a pair of parameters appears to be widespread. Such behavior is most apparent between the temperature of the slab T_c and the slab geometry, particularly L and R . This is likely due to the accommodation of the increase in the slab temperature by an increase in its size.

It is expected that isotropic inversion hardly constrains E since isotropic velocities do not depend on deformation history but are directly derived from temperature and pressure for a given chemical and mineralogical composition. Contrastingly, anisotropic inversion effectively constrains E although the result is clearly biased as it is observed to differ from its true value. In actuality, bias exists in all the parameters at least except for the length of the slab L . Thus the existence of misfit minima that are not in agreement with the true model parameters can either be explained by the use of an incorrect surrogate model in the inversion or the incapability of surface wave data to recover the synthetic subduction zone.

To demonstrate that surface waves can recover simple models of subduction, we include another test where the observed surface wave data is generated by an elastic medium predicted with ANN (*i.e.* the surrogate model). Fig 10 now shows the 1-D and joint marginal probability distributions as a result of this new numerical experiment. Here, we notice the mitigation of model uncertainties through the narrowing of the distributions. Furthermore, we also observe how these distributions are centered at the true values of the model parameters. Based on these results, it is now clear that the behavior exhibited in Fig 9 is a direct consequence of using D-Rex in the full forward procedure and using a surrogate model based on ANN in the inversion. Indeed, implementing the correct forward model to compute anisotropy decreases model uncertainties and eliminates the bias. Since these forward models tend to be computationally expensive when employed with direct-search algorithms, it is imperative to utilize fast-forward approximations such as neural networks. This however necessitates the inclusion of additional training data and/or possibly the partial or complete overhauling of the network architecture.

5.2 Retrieval of the temperature field and some implicitly computed seismic anisotropy variables

Fig. 11 illustrates the reconstructed mean temperature field coming from the 20 Markov chains from both inversions (top panels) and their corresponding uncertainties in terms of the standard deviation (bottom panels). By visual inspection, we notice that the mean temperature field from the isotropic inversion (Fig. 11a) is not much different from the anisotropic case (Fig. 11b). Due to the low levels of noise in the data, anisotropy does not bring much in the recovery of the temperature field. However in the case of larger noise levels, the inclusion of anisotropy in the inversions would be more beneficial. The standard deviation conveys a different story however, as observed by its smaller amplitude in the case of geodynamic tomography (Fig. 11d). In both

cases, the uncertainties are seemingly clustered across subducting slab with two discernible plunging stripes. This indicates a state of relaxation, or more preferably, convergence of the Markov chains towards a stable solution. The plunging stripes therefore are a result of a random-walk behavior of the subducting slab about its center. The center of the slab is delineated by the area of low uncertainty partitioning the two plunging stripes of high uncertainties.

Fig. 12 shows the 1-D depth marginal posterior probability profiles at a given location for temperature, S -wave radial anisotropy ξ , peak-to-peak azimuthal anisotropy in terms of $2G/L_0$ where G is the horizontal azimuthal dependence of L_0 , and the azimuth of the fast direction of azimuthal anisotropy inferred from geodynamic tomography. We successfully jointly recovered azimuthal and radial anisotropy without having to explicitly invert for the elastic tensor. One of the key advantages of geodynamic tomography is its capacity to capture intricate and highly complex features, as exemplified by the recovered amplitude of azimuthal anisotropy and its fast azimuth. Furthermore, one of the long standing problems of conventional surface wave tomography is the depletion of its resolving power with depth since its energy is mostly concentrated across the surface. Here we have demonstrated the ability of geodynamic tomography in the apparent eradication of this effect as evidenced by the preservation of the width of the posteriors in depth.

Lastly, geodynamic tomography offers the capability to resolve 3-D structures of any implicitly computed variable. As a demonstration, Fig. 13a illustrates the S -wave radial anisotropy ξ and Fig. 13b, the anisotropy index obtained from the mean temperature model. A recurring issue is the underestimation of seismic anisotropy in comparison with the true model (Fig. 5) due to the use of an approximate forward operator to model CPO evolution. This is compensated by the weakening of the slab rheology through the reduction of the activation coefficient (Fig. 9 bottom right panel), in order to produce larger levels of anisotropy.

6 Discussion

Most of the limitations of the method have already been laid out in (Magali et al., 2021b). There we discussed several areas for improvement which include but are not limited to: (1) the inclusion of other types of data such as gravity anomalies for better model constraints, (2) the usage of a generalized surrogate model for computing anisotropy, and (3) the underlying assumptions in mantle composition. Here, we discuss the limitations and the resulting implications of using thermally-driven instantaneous models of subduction. Finally, we discuss what the future holds for the method, that is, its potential application to a real Earth problem.

Isotropic inversion

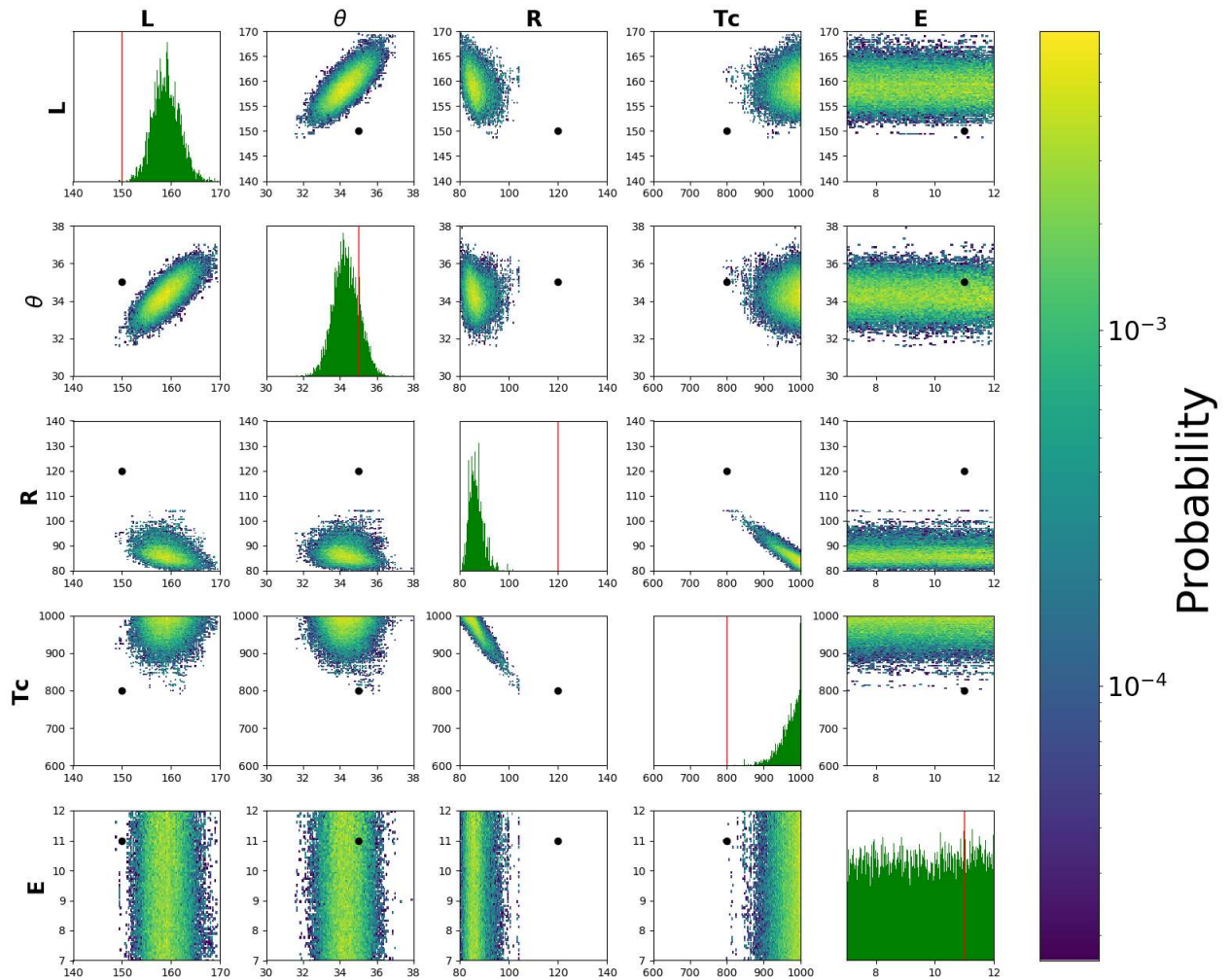


Figure 8 Posterior probability distribution in the five-dimensional parameter space inferred from the isotropic inversion $p(\mathbf{m}|c_R, c_L)$. Diagonal panels show 1-D marginal distributions for each model parameter. Off-diagonal panels show 2-D marginal distributions and depict possible trade-offs between pairs of model parameters. The red vertical lines and the black markers indicate the true model values for the diagonal and the off-diagonal panels, respectively. The intensity pertains to the level of posterior probability (*i.e.*, high intensity means high probability, and thus low misfit).

6.1 Comments on the use of instantaneous subduction model

Our numerical experiments assume that the subduction geometry is already known to a certain degree given the ever-growing geophysical data available. This is similar to the geodynamic inversions demonstrated by [Baumann and Kaus \(2015\)](#). Because of this, the prior bounds we have selected for the model parameters such as the slab length being 100 km – 200 km or the angle of subduction being $20^\circ - 45^\circ$ are reasonable. However, we acknowledge the existence of some end-member slab geometries such as those whose dip angle is nearly vertical (*e.g.* Kermadec and Marianas) and those whose dip angle is constant but whose slab length is > 200 km and some even penetrating the transition zone (*e.g.* Central

and South Kurile) as evidenced by ([Fukao et al., 2009](#)). It is expected that increasing the range of the prior would not have a substantial effect on the shape of the posterior due to the relatively small noise levels prescribed in the observed data (*i.e.*, the narrow shape of the likelihood compared to the prior). Nevertheless, we can ascribe the subduction geometries coming from our prior distribution to short and young, or even detached slabs.

It has already been shown that upper mantle minerals deform by dislocation creep to facilitate the development of CPO ([Karato and Wu, 1993](#); [Hirth and Kohlstedt, 2003](#)). Thus, it would make sense to implement stress-dependent rheologies (*i.e.* non-Newtonian flows) in our geodynamic models. Geodynamic tomography is still at the ‘proof-of-concept’ stage, and so incorpo-

Anisotropic inversion with data computed from D-Rex

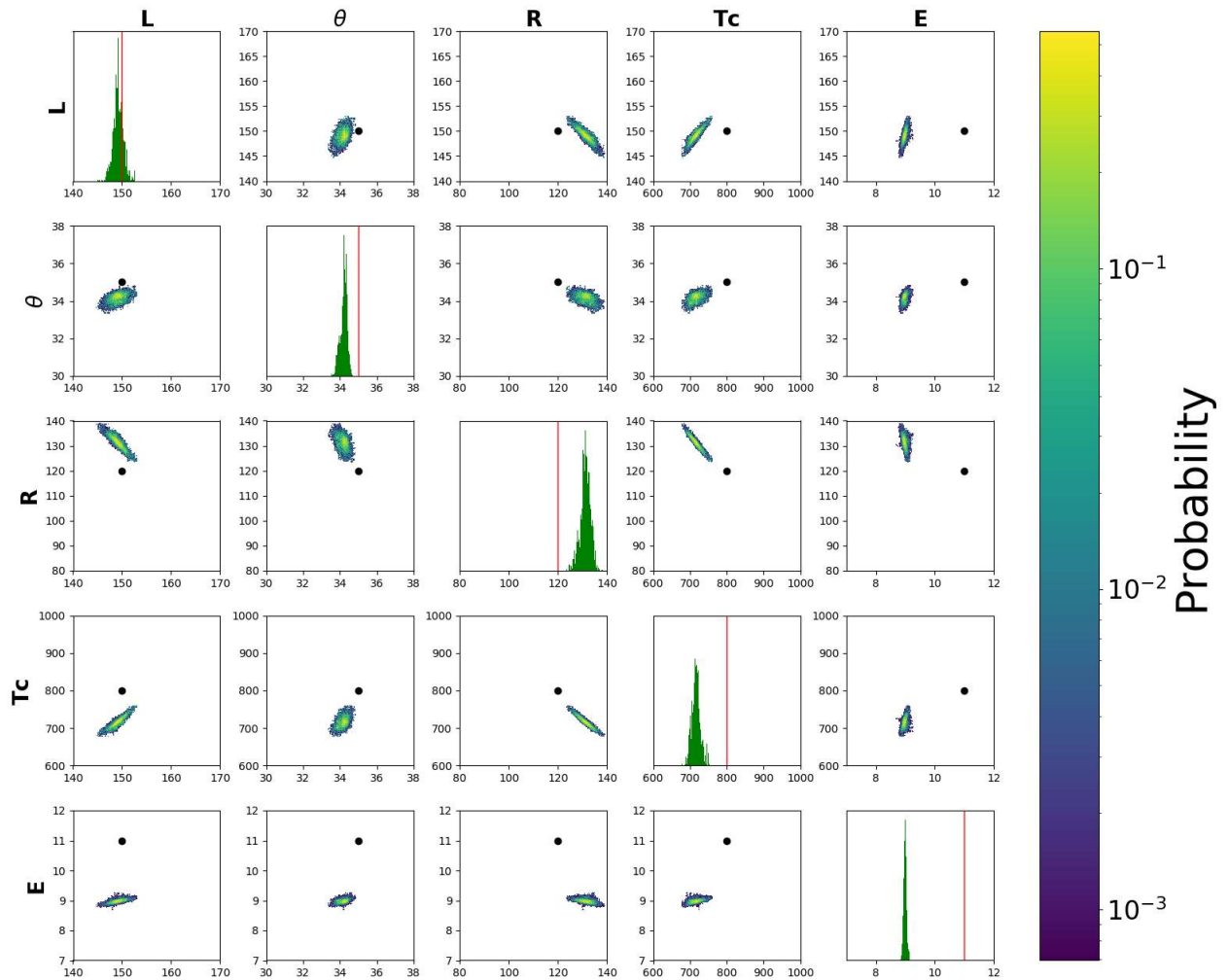


Figure 9 Posterior probability distribution in the five-dimensional parameter space inferred from the anisotropic inversion $p(\mathbf{m}|c_R, c_L, c_1, c_2)$. With D-Rex used to generate the observed data, the marginal distributions are not centered at the true values. The narrowness of the distributions is an imprint of the low noise levels prescribed in the observed data.

rating stress-dependent rheologies onto our instantaneous flow model would require additional effort for optimization (*i.e.* speeding-up flow computations while minimising sharp lateral viscosity contrasts) especially when considering a sampling-based inversion scheme where the flow has to be calculated numerous times. However, it has been reported that Newtonian flows could replicate some aspects of non-Newtonian flows by varying the activation energy (Christensen, 1983; Billen and Hirth, 2005). Still, a Newtonian rheology remains valid when considering the large scale features of subduction-induced mantle flow (Becker et al., 2003; Piromallo et al., 2006), and especially when we expect small-scales to be tomographic-filtered by long-period seismic data (Magali et al., 2021a).

Finally, a steady-state assumption when back-tracing flow streamlines may not be applicable in regions

where transient flow is predominant. As pointed out by Faccenda and Capitanio (2012, 2013), steady-state assumptions imposed onto convergent margins produce anisotropic patterns in that region that are largely biased. A more consistent way of computing anisotropy is to track the evolution with time of the path traversed by several tracer particles, incorporate texture evolution models at each time step, and compute how much strain is accrued by the process as they get forward advected (Faccenda, 2014; Chang et al., 2016). Indeed this can be one of the futures avenues to be delved upon to improve geodynamic tomography. With the steady-state assumption, we anticipate that the anisotropy recovered away from the slab edges, and across the sub-slab mantle or the mantle wedge to remain robust (MacDougall et al., 2017), and close to the convergent margin and slab edges to be interpreted with caution.

Anisotropic inversion with data computed from ANN

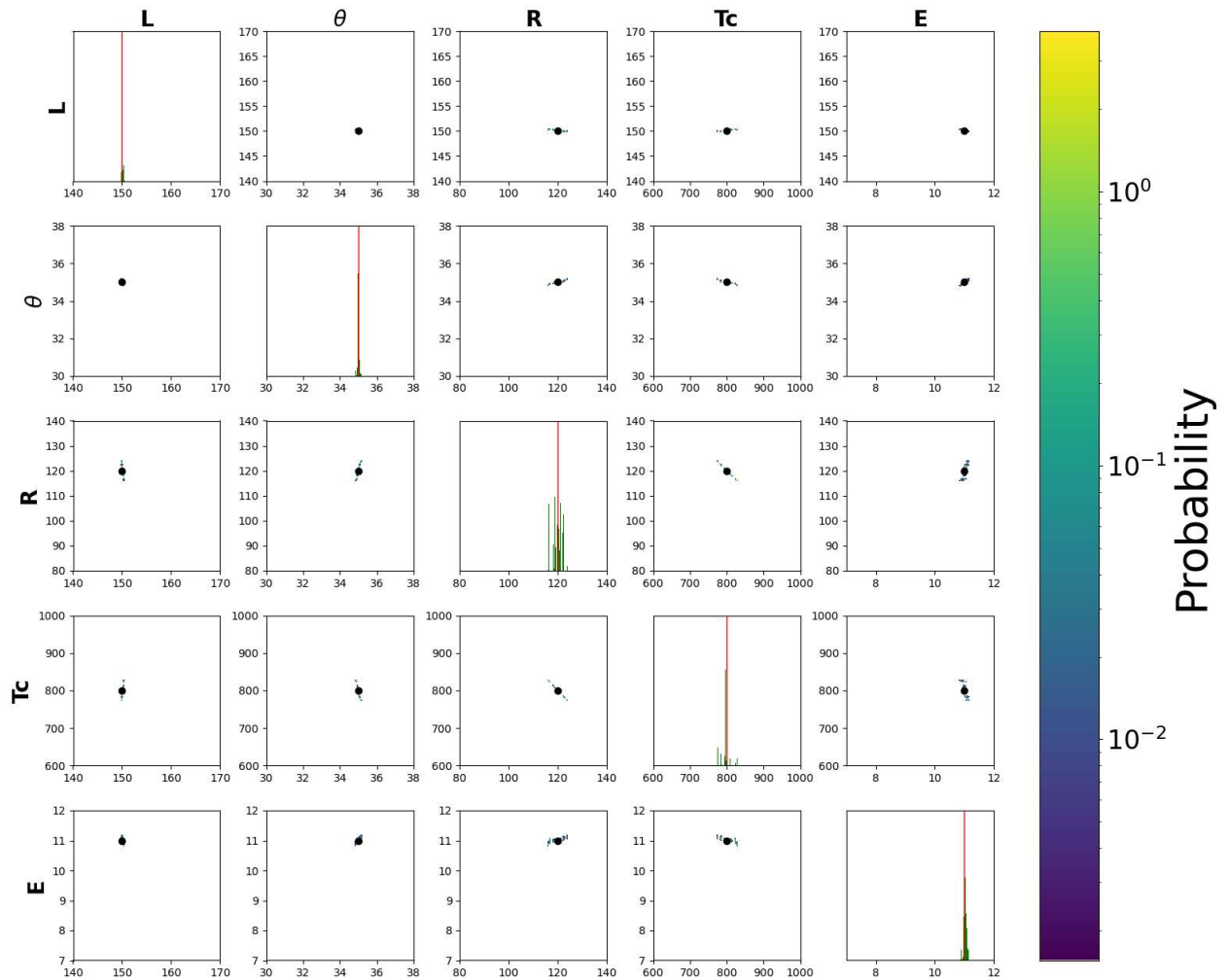


Figure 10 Posterior probability distribution in the five-dimensional parameter space inferred from the anisotropic inversion $p(\mathbf{m} | \mathbf{c}_R, \mathbf{c}_L, c_1, c_2)$. Here, the observed surface wave data is generated coming from an elastic medium predicted with neural networks. By using the correct surrogate model to match the one implemented in the inverse procedure, we observe how the marginal distributions are centered on their respective true values. This numerical experiment confirms that the bias and the model uncertainties observed in Fig. 9 results from the use of an ANN-based surrogate model to compute anisotropy.

6.2 Potential application to real surface wave dispersion measurements

Now that we have shown the capability of geodynamic tomography to recover synthetic structures close to real geodynamic settings, it is obvious that the next step is to apply the method to real Earth data. As such, this section briefly explains some forthcoming strategies to fully implement the method.

To recover the present-day thermal structure of the upper mantle from the inversion of real surface wave data, the inversion strategy should consist of three major stages: (1) In the first stage, we assume that surface wave dispersion maps within the desired period range are readily available. This is arguably the case in most

places where surface wave dispersion measurements are widely available thanks to an ever growing amount of seismic records. From these maps spanning the entire geographical surface, we then invert local isotropic Rayleigh wave phase velocity dispersion curves for 1-D depth isotropic V_S models. (2) From the 1-D structures, the second stage involves the estimation of 1-D depth profiles of temperature T using first-order scaling relations between V_S and T . A more elaborate yet more computationally demanding approach is the inverse implementation of self-consistent thermodynamic modeling to infer T from V_S for any given bulk composition. The 1-D depth profiles of temperature can then be juxtaposed followed by smoothing through various interpolation schemes to build a smooth 3-D temperature field.

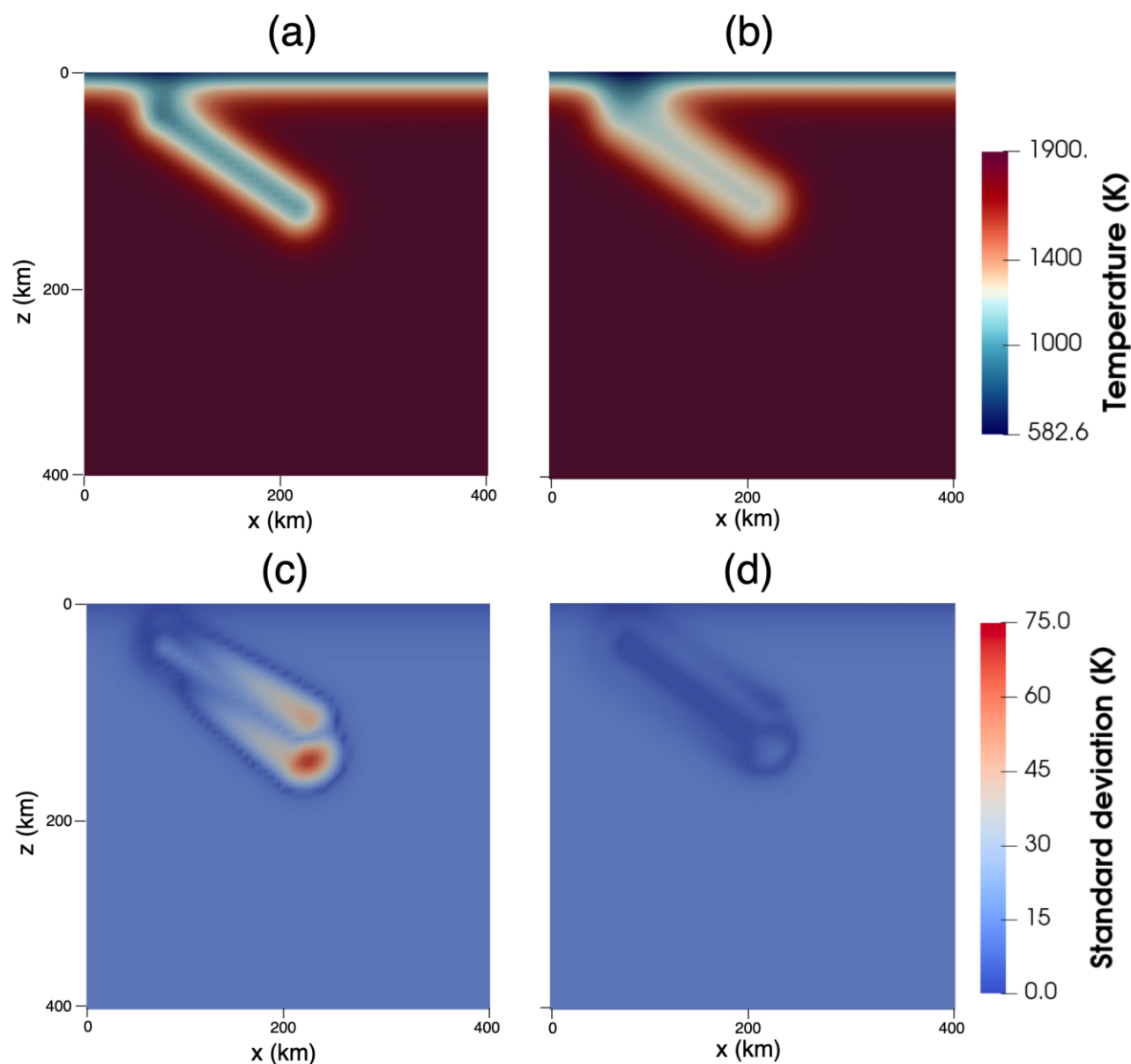


Figure 11 Upper panel: Cross-sectional view in the xz -plane of the mean temperature field recovered from (a) isotropic inversion, and (b) anisotropic inversion. Lower panel: Standard deviations around the mean temperature fields from (c) isotropic inversion, and (d) anisotropic inversion. These cross-sections are taken at the center of the y -axis.

(3) The last stage is geodynamic tomography itself, that is, using the 3-D temperature field inferred from the previous stage as the initial model to iteratively update its structure by inverting anisotropic surface wave dispersion curves. Fig. 14 is a schematic representation of this three-step inversion strategy.

7 Conclusion

We have tested the applicability of geodynamic tomography to a 3-D deforming upper mantle induced by subduction. Isotropic Love and Rayleigh wave phase velocity measurements and their azimuthal variations at a given location were jointly inverted to recover the 3-D thermal structure of a synthetic subduction zone. The method is cast in a Bayesian inversion procedure where the solution is an ensemble of unknown model parameters defining the thermal and rheological structure of

the subduction zone, distributed according to a posterior probability density function.

In the process, not only do we successfully recover the desired thermal structure, we have also constrained the complete pattern of upper mantle deformation induced by subduction, and provided a quantitative interpretation on how these deformation patterns translate to seismic anisotropy that could potentially be imaged by seismic tomography. We have shown that the Bayesian framework propounds the capability to render marginal posterior probability distributions not only of the unknown parameters, but also of any implicitly computed variable such as deformation and anisotropy through geodynamic and texture evolution modeling, and quantify their associated uncertainty limits.

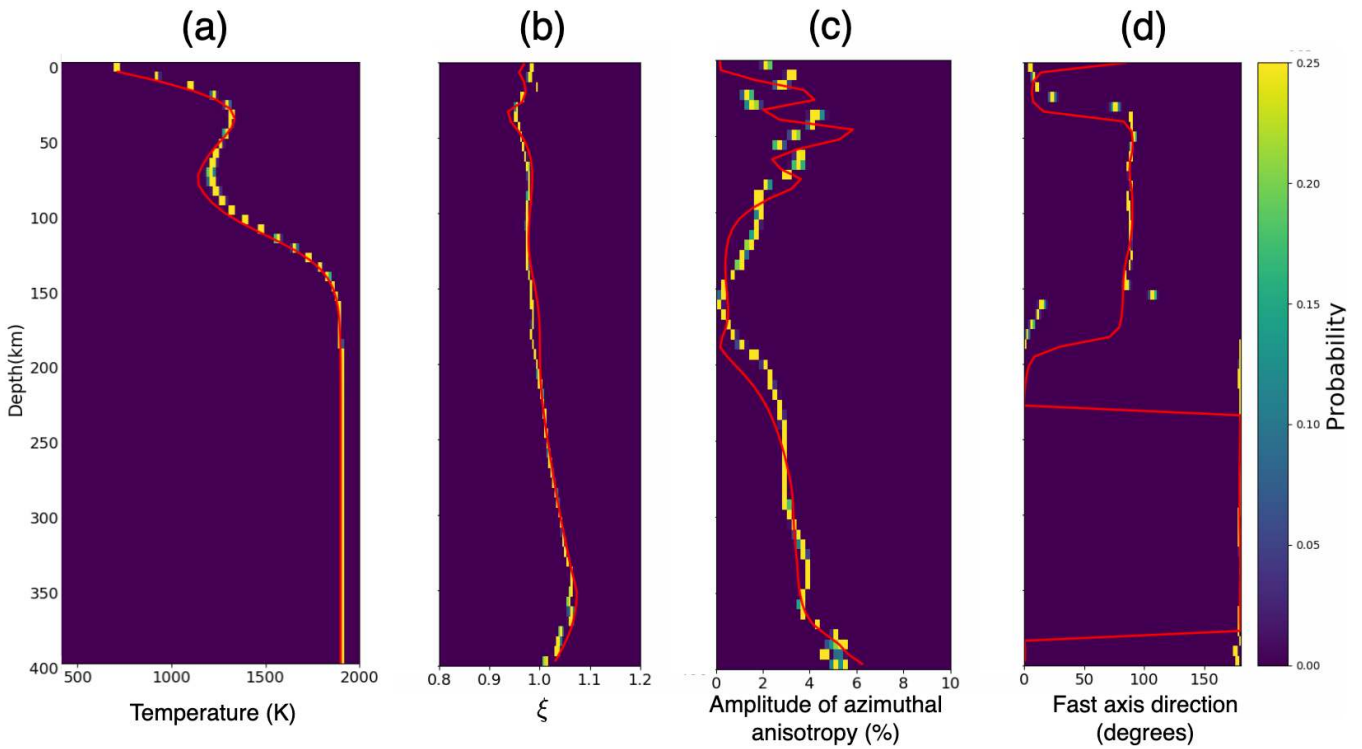


Figure 12 1-D marginal posterior probability profiles with depth of several variables inferred from geodynamic tomography. (a) Temperature. (b) S -wave radial anisotropy ξ . (c) Amplitude of azimuthal anisotropy in terms of $2G/L_0$ where G is an elastic constant corresponding to the horizontal azimuthal dependence of L_0 . (d) Azimuth of the fast direction of azimuthal anisotropy. The depth profiles of temperature and ξ are taken at $(x = 125 \text{ km}, y = 225 \text{ km})$. To show that azimuthal anisotropy is also well-constrained, we took the depth profile at $(x = 175 \text{ km}, y = 225 \text{ km})$, where the patterns of azimuthal anisotropy are highly complex. Geodynamic tomography offers the capability to constrain seismic anisotropy. The solid red lines indicate the true structures.

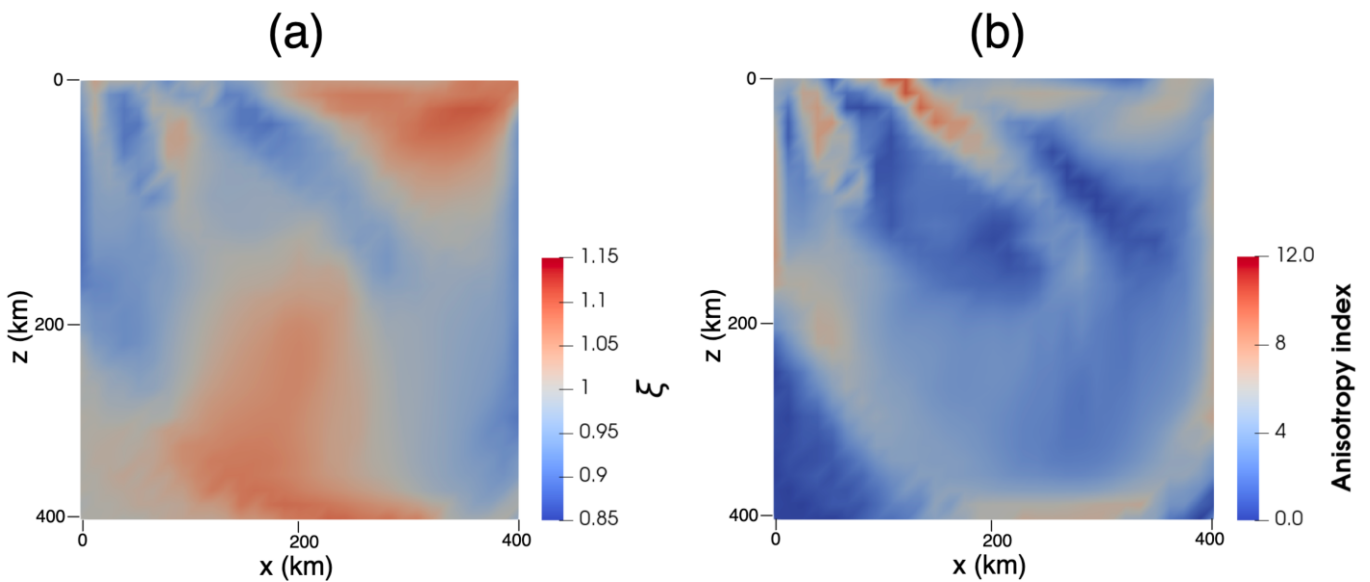


Figure 13 Cross-sectional view in the xz - plane of the S -wave radial anisotropy ξ (a) and the anisotropy index (b) obtained from the mean temperature model. The cross sections are taken at the center of the y - axis.

Acknowledgements

The provision of the computational resources are made possible through the ERC grant TRANSCALE: Reconciling Scales in Global Seismology project. All computations were carried out through the in-house Trans-scale cluster situated at the University of Lyon, France.

We are extremely grateful to editor Paula Koelemeijer, reviewer Manuele Faccenda, and one anonymous reviewer for their constructive feedback.

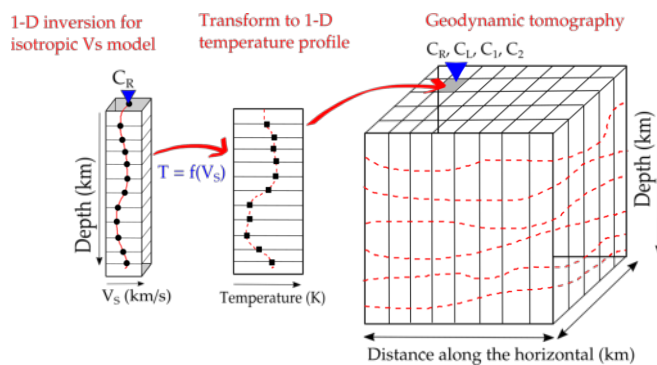


Figure 14 Three-step approach to geodynamic tomography. The first step involves 1-D isotropic surface wave tomography to infer the V_S structure (solid red lines) from a geographical array of isotropic Rayleigh wave dispersion measurements (blue triangle on top of the 1-D column). From the 1-D V_S structures, the second step is the estimation of 1-D temperature profiles (dashed red lines across the 1-D column). From the set of 1-D temperature profiles, one may then build a smooth 3-D model of temperature through interpolation. The 3-D model can thus be viewed as a collection of 1-D columns containing depth profiles of temperature. Geodynamic tomography commences by using the 3-D temperature field (dashed red lines in the 3-D model) as a starting model followed by its iterative update through the inversion of anisotropic surface wave dispersion measurements (blue triangles on top of the 3-D model).

Code and data availability statements

The codes used to generate the synthetic data and to demonstrate geodynamic tomography can be accessed freely at <https://doi.org/10.5281/zenodo.6857279>. This study purely worked on synthetics. No data have been used or produced in this work.

Competing interests

The authors declare no competing interests.

References

- Afonso, J., Fullea, J., Yang, Y., Connolly, J., and Jones, A. 3-D multi-observable probabilistic inversion for the compositional and thermal structure of the lithosphere and upper mantle. II: General methodology and resolution analysis. *Journal of Geophysical Research: Solid Earth*, 118(4):1650–1676, 2013a. doi: <https://doi.org/10.1002/jgrb.50123>.
- Afonso, J. C., Fullea, J., Griffin, W. L., Yang, Y., Jones, A. G., D. Connolly, J. A., and O'Reilly, S. Y. 3-D multiobservable probabilistic inversion for the compositional and thermal structure of the lithosphere and upper mantle. I: a priori petrological information and geophysical observables. *Journal of Geophysical Research: Solid Earth*, 118(5):2586–2617, 2013b. doi: <https://doi.org/10.1002/jgrb.50124>.
- Babuska, V. and Cara, M. *Seismic anisotropy in the Earth*, volume 10. Springer Science & Business Media, 1991. doi: <https://doi.org/10.1007/978-94-011-3600-6>.
- Baumann, T. and Kaus, B. J. Geodynamic inversion to constrain the non-linear rheology of the lithosphere. *Geophys-*

- ical Journal International*, 202(2):1289–1316, 07 2015. doi: [10.1093/gji/ggv201](https://doi.org/10.1093/gji/ggv201).
- Becker, T. W., Kellogg, J. B., Ekström, G., and O'Connell, R. J. Comparison of azimuthal seismic anisotropy from surface waves and finite strain from global mantle-circulation models. *Geophysical Journal International*, 155(2):696–714, 11 2003. doi: [10.1046/j.1365-246X.2003.02085.x](https://doi.org/10.1046/j.1365-246X.2003.02085.x).
- Bercovici, D. On the purpose of toroidal motion in a convecting mantle. *Geophysical Research Letters*, 22(23):3107–3110, 1995. doi: <https://doi.org/10.1029/95GL03082>.
- Billen, M. I. and Hirth, G. Newtonian versus non-Newtonian upper mantle viscosity: Implications for subduction initiation. *Geophysical Research Letters*, 32(19), 2005. doi: <https://doi.org/10.1029/2005GL023457>.
- Bishop, C. M. et al. *Neural networks for pattern recognition*. Oxford university press, 1995.
- Bissig, F., Khan, A., Tauzin, B., Sossi, P. A., Munch, F. D., and Giardini, D. Multifrequency Inversion of Ps and Sp Receiver Functions: Methodology and Application to USArray Data. *Journal of Geophysical Research: Solid Earth*, 126(2):e2020JB020350, 2021. doi: <https://doi.org/10.1029/2020JB020350>.
- Chang, S.-J., Ferreira, A. M., and Faccenda, M. Upper- and mid-mantle interaction between the Samoan plume and the Tonga-Kermadec slabs. *Nature communications*, 7(1):1–9, 2016. doi: <https://doi.org/10.1038/ncomms10799>.
- Christensen, U. Convection in a variable-viscosity fluid: Newtonian versus power-law rheology. *Earth and Planetary Science Letters*, 64(1):153–162, 1983. doi: [https://doi.org/10.1016/0012-821X\(83\)90060-2](https://doi.org/10.1016/0012-821X(83)90060-2).
- Connolly, J. The geodynamic equation of state: what and how. *Geochemistry, Geophysics, Geosystems*, 10(10), 2009. doi: <https://doi.org/10.1029/2009GC002540>.
- Connolly, J. A. Computation of phase equilibria by linear programming: a tool for geodynamic modeling and its application to subduction zone decarbonation. *Earth and Planetary Science Letters*, 236(1-2):524–541, 2005. doi: <https://doi.org/10.1016/j.epsl.2005.04.033>.
- Conway, D., Alexander, B., King, M., Heinson, G., and Kee, Y. Inverting magnetotelluric responses in a three-dimensional earth using fast forward approximations based on artificial neural networks. *Computers & Geosciences*, 127:44–52, 2019. doi: <https://doi.org/10.1016/j.cageo.2019.03.002>.
- Debayle, E. and Kennett, B. Anisotropy in the Australasian upper mantle from Love and Rayleigh waveform inversion. *Earth and Planetary Science Letters*, 184(1):339–351, 2000. doi: [https://doi.org/10.1016/S0012-821X\(00\)00314-9](https://doi.org/10.1016/S0012-821X(00)00314-9).
- Faccenda, M. Mid mantle seismic anisotropy around subduction zones. *Physics of the Earth and Planetary Interiors*, 227:1–19, 2014. doi: <https://doi.org/10.1016/j.pepi.2013.11.015>.
- Faccenda, M. and Capitanio, F. A. Development of mantle seismic anisotropy during subduction-induced 3-D flow. *Geophysical Research Letters*, 39(11), 2012. doi: <https://doi.org/10.1029/2012GL051988>.
- Faccenda, M. and Capitanio, F. A. Seismic anisotropy around subduction zones: Insights from three-dimensional modeling of upper mantle deformation and SKS splitting calculations. *Geochemistry, Geophysics, Geosystems*, 14(1):243–262, 2013. doi: <https://doi.org/10.1002/ggge.20055>.
- Fukao, Y., Obayashi, M., and Nakakuki, T. a. Stagnant Slab: A Review. *Annual Review of Earth and Planetary Sciences*, 37(1):19–46, 2009. doi: [10.1146/annurev.earth.36.031207.124224](https://doi.org/10.1146/annurev.earth.36.031207.124224).
- Gable, C. W., O'Connell, R. J., and Travis, B. J. Convection in three dimensions with surface plates: Generation of toroidal flow.

- Journal of Geophysical Research: Solid Earth*, 96(B5):8391–8405, 1991. doi: <https://doi.org/10.1029/90JB02743>.
- Hansen, T. M. and Cordua, K. S. Efficient Monte Carlo sampling of inverse problems using a neural network-based forward—applied to GPR crosshole traveltime inversion. *Geophysical Journal International*, 211(3):1524–1533, 2017. doi: <https://doi.org/10.1093/gji/ggx380>.
- Hirth, G. and Kohlstedt, D. Rheology of the upper mantle and the mantle wedge: A view from the experimentalists. *Geophysical monograph-american geophysical union*, 138:83–106, 2003. doi: <https://doi.org/10.1029/138GM06>.
- Kaminski, E. and Ribe, N. M. Timescales for the evolution of seismic anisotropy in mantle flow. *Geochemistry, Geophysics, Geosystems*, 3(8):1–17, 2002. doi: <https://doi.org/10.1029/2001GC000222>.
- Kaminski, E., Ribe, N. M., and Browaeys, J. T. D-Rex, a program for calculation of seismic anisotropy due to crystal lattice preferred orientation in the convective upper mantle. *Geophysical Journal International*, 158(2):744–752, 2004. doi: <https://doi.org/10.1111/j.1365-246X.2004.02308.x>.
- Karato, S. and Wu, P. Rheology of the upper mantle: A synthesis. *Science*, 260(5109):771–778, 1993. doi: <https://doi.org/10.1126/science.260.5109.771>.
- Köpke, C., Irving, J., and Elsheikh, A. H. Accounting for model error in Bayesian solutions to hydrogeophysical inverse problems using a local basis approach. *Advances in water resources*, 116:195–207, 2018. doi: <https://doi.org/10.1016/j.advwatres.2017.11.013>.
- LeCun, Y., Bengio, Y., and Hinton, G. Deep learning. *nature*, 521(7553):436, 2015. doi: <https://doi.org/10.1038/nature14539>.
- Long, M. D. and Becker, T. W. Mantle dynamics and seismic anisotropy. *Earth and Planetary Science Letters*, 297(3-4):341–354, 2010. doi: <https://doi.org/10.1016/j.epsl.2010.06.036>.
- Love, A. A Treatise on the Mathematical Theory of Elasticity. *A treatise on the Mathematical Theory of Elasticity*, 643, 1927.
- MacDougall, J. G., Jadamec, M. A., and Fischer, K. M. The zone of influence of the subducting slab in the asthenospheric mantle. *Journal of Geophysical Research: Solid Earth*, 122(8):6599–6624, 2017. doi: <https://doi.org/10.1002/2017JB014445>.
- Magali, J., Bodin, T., Hedjazian, N., Ricard, Y., Capdeville, Y., and Debayle, E. Quantifying intrinsic and extrinsic contributions to radial anisotropy in tomographic models. *Journal of Geophysical Research: Solid Earth*, 126(10):e2021JB022322, 2021a. doi: <https://doi.org/10.1029/2021JB022322>.
- Magali, J. K. *Geodynamic Tomography*. PhD thesis, Université de Lyon, 2021.
- Magali, J. K., Bodin, T., Hedjazian, N., Samuel, H., and Atkins, S. Geodynamic tomography: constraining upper-mantle deformation patterns from Bayesian inversion of surface waves. *Geophysical Journal International*, 224(3):2077–2099, 2021b. doi: <https://doi.org/10.1093/gji/ggaa577>.
- Maupin, V. and Park, J. 1.09—Theory and observations—Seismic anisotropy. *Treatise on Geophysics*, pages 277–305, 2015. doi: <https://doi.org/10.1016/B978-0-444-53802-4.00007-5>.
- Moghadas, D., Behroozmand, A. A., and Christiansen, A. V. Soil electrical conductivity imaging using a neural network-based forward solver: Applied to large-scale Bayesian electromagnetic inversion. *Journal of Applied Geophysics*, page 104012, 2020. doi: <https://doi.org/10.1016/j.jappgeo.2020.104012>.
- Montagner, J.-P. and Jobert, N. Vectorial tomography—ii. Application to the Indian Ocean. *Geophysical Journal International*, 94(2):309–344, 1988. doi: <https://doi.org/10.1111/j.1365-246X.1988.tb05904.x>.
- Montagner, J.-P. and Nataf, H.-C. A simple method for inverting the azimuthal anisotropy of surface waves. *Journal of Geophysical Research: Solid Earth*, 91(B1):511–520, 1986. doi: <https://doi.org/10.1029/JB091iB01p00511>.
- Montagner, J.-P. and Nataf, H.-C. Vectorial tomography—I. Theory. *Geophysical Journal International*, 94(2):295–307, 1988. doi: <https://doi.org/10.1111/j.1365-246X.1988.tb05903.x>.
- Montagner, J.-P. and Tanimoto, T. Global upper mantle tomography of seismic velocities and anisotropies. *Journal of Geophysical Research: Solid Earth*, 96(B12):20337–20351, 1991. doi: <https://doi.org/10.1029/91JB01890>.
- Nakanishi, I. and Anderson, D. L. Measurement of mantle wave velocities and inversion for lateral heterogeneity and anisotropy: 1. Analysis of great circle phase velocities. *Journal of Geophysical Research: Solid Earth*, 88(B12):10267–10283, 1983. doi: <https://doi.org/10.1111/j.1365-246X.1984.tb01964.x>.
- Obrebski, M., Kiselev, S., Vinnik, L., and Montagner, J.-P. Anisotropic stratification beneath Africa from joint inversion of SKS and P receiver functions. *Journal of Geophysical Research: Solid Earth*, 115(B9), 2010. doi: <https://doi.org/10.1029/2009JB006923>.
- Obrebski, M., Allen, R. M., Pollitz, F., and Hung, S.-H. Lithosphere–asthenosphere interaction beneath the western United States from the joint inversion of body-wave traveltimes and surface-wave phase velocities. *Geophysical Journal International*, 185(2):1003–1021, 2011. doi: <https://doi.org/10.1111/j.1365-246X.2011.04990.x>.
- OpenMP Architecture Review Board. OpenMP Application Program Interface Version 3.0, May 2008.
- Panning, M. and Romanowicz, B. A three-dimensional radially anisotropic model of shear velocity in the whole mantle. *Geophysical Journal International*, 167(1):361–379, 2006. doi: <https://doi.org/10.1111/j.1365-246X.2006.03100.x>.
- Piromallo, C., Becker, T., Funicello, F., and Faccenna, C. Three-dimensional instantaneous mantle flow induced by subduction. *Geophysical Research Letters*, 33(8), 2006. doi: <https://doi.org/10.1029/2005GL025390>.
- Romanowicz, B. Inversion of surface waves: a review. *International Geophysics Series*, 81(A):149–174, 2002.
- Saito, M. DISPER80: A subroutine package for the calculation of seismic normal-mode solutions. *Seismological algorithms*, pages 293–319, 1988.
- Samuel, H. Time domain parallelization for computational geodynamics. *Geochemistry, Geophysics, Geosystems*, 13(1), 2012. doi: <https://doi.org/10.1029/2011GC003905>.
- Samuel, H. A Deformable Particle-In-Cell Method for Advective Transport in Geodynamic Modelling. *gji*, 214:1744–1773, 2018. doi: <https://doi.org/10.1093/gji/ggy231>. doi:10.1093/gji/ggy231.
- Smith, M. L. and Dahlen, F. The azimuthal dependence of Love and Rayleigh wave propagation in a slightly anisotropic medium. *Journal of Geophysical Research*, 78(17):3321–3333, 1973. doi: <https://doi.org/10.1029/JB078i017p03321>.
- Stixrude, L. and Lithgow-Bertelloni, C. Thermodynamics of mantle minerals-II. Phase equilibria. *Geophysical Journal International*, 184(3):1180–1213, 2011. doi: <https://doi.org/10.1111/j.1365-246X.2010.04890.x>.
- Xie, J., Ritzwoller, M. H., Brownlee, S., and Hacker, B. Inferring the oriented elastic tensor from surface wave observations: preliminary application across the western United States. *Geophysical Journal International*, 201(2):996–1021, 2015. doi: <https://doi.org/10.1093/gji/ggv054>.
- Xie, J., Ritzwoller, M. H., Shen, W., and Wang, W. Crustal anisotropy

across eastern Tibet and surroundings modeled as a depth-dependent tilted hexagonally symmetric medium. *Geophysical Journal International*, 209(1):466–491, 2017. doi: <https://doi.org/10.1093/gji/ggx004>.

The Root to the Galápagos Mantle Plume on the Core-Mantle Boundary

Sanne Cottaar *¹, Carl Martin ¹, Zhi Li ¹, Rita Parai ²

¹Department of Earth Sciences, University of Cambridge, Cambridge, UK, ²Department of Earth and Planetary Sciences, Washington University in St Louis, St Louis, MO, USA

Author contributions: *Conceptualization:* SC. *Methodology:* SC, CM, ZL. *Investigation:* SC, CM, RP. *Visualization:* SC, CM. *Writing – original draft:* SC, RP. *Writing – review & editing:* SC, CM, ZL, RP.

Abstract Ultra-low velocity zones (ULVZs) are thin anomalous patches on the boundary between the Earth's core and mantle, revealed by their effects on the seismic waves that propagate through them. Here we map a broad ULVZ near the Galápagos hotspot using shear-diffracted waves. Forward modeling assuming a cylindrical shape shows the patch is ~600 km wide, ~20 km high, and its shear velocities are ~25% reduced. The ULVZ is comparable to other broad ULVZs mapped on the core-mantle boundary near Hawaii, Iceland, and Samoa. Strikingly, all four hotspots where the mantle plume appears rooted by these 'mega-ULVZs', show similar anomalous isotopic signatures in He, Ne, and W in their ocean island basalts. This correlation suggests mega-ULVZs might be primordial or caused by interaction with the core, and some material from ULVZs is entrained within the plume. For the Galápagos, the connection implies the plume is offset to the west towards the base of the mantle.

Non-technical summary Observations of deep-diving earthquake waves reveal heterogeneity and dynamics within the Earth. Here we use waves that diffract along the boundary between the core and the mantle to map a patch of anomalous material on top of the boundary. The waves propagating within the patch are slowed down by 25% compared to those propagating in surrounding material, and the waves are refracted when entering and exiting the patch. These waves arrive at seismic stations delayed by tens of seconds. By modeling the waveforms, and mapping the directionality of this delayed energy, we constrain the location of the patch beneath the eastern Pacific and to the west of the Galápagos archipelago. The patch can be approximated as a cylinder with a width of 600 km and height of 20 km. Such patches are named ultra-low velocity zones or ULVZs. Similar large ULVZs are found near other intraplate volcanic hotspots, i.e. Hawaii, Iceland and Samoa. Volcanic basalts on these islands and the Galápagos show anomalous isotopic signatures, which could be dragged up in a mantle plume from the ULVZ at the core-mantle boundary and indicate that the material within the ULVZs was either created early in Earth's history or contains material leaking from the core.

Production Editor:
Gareth Funning
Handling Editor:
Lauren Waszek
Copy & Layout Editor:
Théa Ragon

Received:
July 1, 2022
Accepted:
September 20, 2022
Published:
October 28, 2022

1 Introduction

The lowermost hundreds of kilometers of the mantle are the lower thermal boundary layer in mantle dynamics, which is partially driven by heat flow across the core-mantle boundary. The layer plays a major role in Earth's thermal and dynamical history. Seismic waves have revealed it is characterized by strong lateral variations in seismic wave speed, which are linked to variations in temperature and composition. On the global scale, there are two widespread regions with relatively slow seismic velocities, dubbed Large Low Velocity Provinces (LLVPs, e.g. Cottaar and Lekić, 2016; Garnero et al., 2016), which are surrounded by regions of relatively fast seismic velocities that can be interpreted as the accumulation of subducted tectonic plates or slabs (e.g. Domeier et al., 2016; Hilst et al., 1997). Much thinner in nature, on the order of 10s of km, but more extreme in their velocity anomaly, are the

ultra-low velocity zones (ULVZs). ULVZs appear patchy in nature and are directly on the core-mantle boundary. While only a fraction of the core-mantle boundary has been targeted for these anomalies, there is a weak trend that these patches appear within or near the LLVPs (Yu and Garnero, 2018). In studies that produce ULVZ probability maps using a single data type over a large swath of the core-mantle boundary, this trend is disputed (Thorne et al., 2020, 2021). However, the appearance of ULVZs within LLVPs is certainly true for the broadest of ULVZs that have been mapped in 3D (Cottaar and Romanowicz, 2012; Thorne et al., 2013; Yuan and Romanowicz, 2017; Jenkins et al., 2021; Krier et al., 2021; Lai et al., 2022; Li et al., 2022), and can be dubbed 'mega-ULVZs' after Thorne et al. (2013). The three mega-ULVZs currently mapped lie in the vicinity of the Hawaiian, Icelandic and Samoan hotspots, and such large structures appear otherwise rare, at least across a large swath of the Pacific (Kim et al., 2020). Suggestions of the presence of other mega-ULVZs have been made be-

*Corresponding author: sc845@cam.ac.uk

low Marquesas and Caroline hotspots (Kim et al., 2020; Thorne et al., 2021), but these have not been mapped to the same detail.

The nature and origin of ULVZs are uncertain. Their velocity reductions are so extreme that their composition must be anomalous, and enrichment of magnesiowüstites is a prime candidate (Wicks et al., 2017; Dobrosavljevic et al., 2019). The presence of partial melt is also proposed, but is unlikely to form stable ULVZs as the melt is dense due to enriched in Fe and drains to the core-mantle boundary (Hernlund and Jellinek, 2010; Dannberg et al., 2021). Solid-state ULVZs could be remnants of an early molten mantle, becoming enriched in magnesiowüstite due to fractional crystallization, and therefore have a primordial origin (Labrosse et al., 2007). The potential of Fe-enrichment by the core has also been proposed, through mechanisms of diffusion (Hayden and Watson, 2007; Lesher et al., 2020) or mechanisms driven by morphological instabilities (Kanda and Stevenson, 2006; Otsuka and Karato, 2012; Lim et al., 2021). If ULVZs are dense in composition, questions remain as to whether they are passive markers of surrounding convection (Li et al., 2017, 2022), play an active role by rooting mantle plumes (Jellinek and Manga, 2004), and if their material can be entrained in plumes (Jones et al., 2019).

Here we present evidence for the presence of a mega-ULVZ on the core-mantle boundary to the west of the Galápagos hotspot using shear diffracted waves. Shear diffracted energy incident upon a mega-ULVZ, causes guided waves within. This energy is refracted due to the velocity contrast at the entry to and exit from the ULVZ. At a seismic station, the refracted energy arrives off-angle and delayed by 10s of seconds. We refer to this as the ‘Sdiff postcursor’. The frequency content of the postcursors is sensitive to the height of the ULVZ. Their delay times are sensitive to the size, shape, and velocity reduction of the ULVZ. We focus on four earthquakes with Sdiff postcursors sampling the core-mantle boundary near the Galápagos Islands. Our preferred ULVZ model is found by synthetic waveform modeling for 3D ULVZ models, and by imaging the directionality of the postcursor energy.

2 Data and Methods

2.1 Data Catalogue

Recognizing consistent arrivals of Sdiff postcursors caused by a mega-ULVZ requires dense data coverage. The Transportable Array (TA) is a large-scale deployment of 400 seismic stations that has gradually moved from west to east across the conterminous United States between 2004 and 2015 with a rough station spacing of 70 km. The presence of the TA here played a major role in the discovery and mapping of the Hawaiian, Samoan and Icelandic mega-ULVZs (Cottaar and Romanowicz, 2012; Thorne et al., 2013; Yuan and Romanowicz, 2017). Over several years since 2014, the TA was transferred to Alaska, monitoring the most seismically active state of the US with unprecedented coverage, while also providing new geometries to study the core-mantle boundary.

Observations of Sdiff waves from Chilean earthquakes to the Alaska TA provided us with the first evidence of the presence of Sdiff postcursors caused by a ULVZ beneath the eastern Pacific. Subsequently, we built a catalogue of postcursor observations.

We visually assess earthquake data for the presence of Sdiff postcursors caused by a ULVZ near the Galápagos Islands from a globally compiled data set of Sdiff phases for all earthquakes over a magnitude of 5.7 and for all depth ranges. Data are filtered between 10 and 30 s. To assess, Sdiff phases are aligned on their predicted arrival time and organized as a function of azimuth. A postcursor is recognized by strong later arrival that has a move-out in time as a function of azimuth with respect to the main Sdiff arrival. They can only be observed if there is sufficient data coverage, a good signal-to-noise ratio (judged by eye), and no strong interfering depth phases. A catalogue of promising observations of postcursors caused by the Galápagos ULVZ is given in Table S1. We focus on four high quality events that sample the Galápagos ULVZ from a variety of angles. For these events, we quality check the data by eye, and remove traces with low signal-to-noise ratio. Several further examples of postcursor observations are presented in the supplementary materials.

2.2 Forward modeling

We compute full waveform synthetics for 3D ULVZ models using the ‘sandwiched’ version of the Coupled Spectral Element Method (sandwiched-CSEM, Capdeville et al., 2002, 2003), similar to Cottaar and Romanowicz (2012) and Yuan and Romanowicz (2017). The ‘sandwiched’-CSEM computes the spectral element solution for a full 3D model in the lowermost 370 km of the mantle, and couples this to a normal mode summation for a 1D model in the rest of the mantle and the core. This method allows for relative computational efficiency to compute synthetics down to periods of 10 seconds for a finely meshed model in the lowermost mantle, at the cost of not having a fully 3D model in the rest of the planet. The internal SEM mesh is defined to have a boundary at the top of the ULVZ.

To reduce the parameter space to search, we assume a cylindrical anomaly for which we determine the radius, height, shear wave velocity reduction, and location in latitude and longitude. Computing full-waveform synthetics is too computationally expensive to allow for a full grid search of all five parameters. Instead, we evaluate the delays, move-outs and amplitudes of resulting postcursors by eye, and adjust the model to approach a better fit.

In the background, we use the radially anisotropic shear velocities of SEMUCB-WM1 (French and Romanowicz, 2014), and a scaled P-wave model. Both models are tapered to the background 1D model in the top 70 km of the SEM mesh. Inside the ULVZ, the isotropic shear wave velocities are reduced. The V_p reduction is scaled by a factor of 1, but this choice has negligible effect on the Sdiff waveforms. The density deviation is scaled by a factor of -0.5, and is thus increased within the ULVZ, but again has little effect on the Sdiff

	Date	Depth [km]	Lat. [°N]	Long.[°W]	M_w	Location
A	2016/12/25	21.5	-43.41	-73.94	7.6	Southern Chile
B	2019/09/29	16.7	-35.56	-73.10	6.7	Off Coast of Central Chile
C	2015/05/19	14.9	-54.53	-132.39	6.6	Pacific-Antarctic Ridge
D	2017/02/24	417.9	-23.44	-178.77	7.0	South of Fiji Islands

Table 1 Parameters for the earthquakes. All earthquake parameters are from the Global Centroid-Moment Tensor project (Ekström et al., 2012) except for event A, for which the W-phase solution published by the USGS National Earthquake Information Centre provided a better waveform fit. See Table S1 for full catalogue.

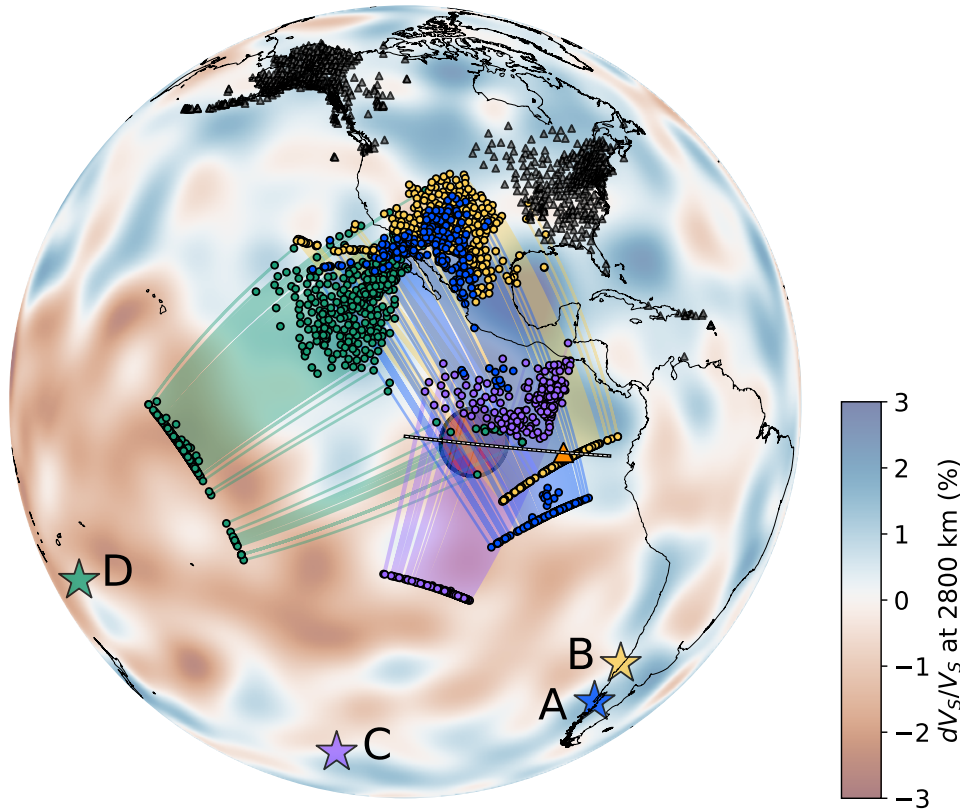


Figure 1 Map shows the geometry of the shear diffracted waves. Data geometries are shown by earthquake location (star), station locations (grey triangles), and ray path sensitivity to the core-mantle boundary (shaded regions between piercing points at 2800 km depth). Earthquake locations and ray paths are colored per event: A-blue, B-yellow, C-purple, and D-green. For earthquake parameters, see Table 1. The Galápagos hotspot is indicated by an orange triangle. The location of the Galápagos ULVZ, as constrained in this study, is shown as the red-filled circle. Background model is showing the shear wave velocity deviations at 2800 km depth from the tomographic SEMUCB-WM1 (French and Romanowicz, 2014). Black line with white dash shows the geometry of the cross-sections in Fig. 8.

waveforms.

2.3 Beamforming

Using arrays of seismic stations, we can determine the directionality of incoming energy. Searching over the incoming backazimuth is called beamforming, while searching over the slowness or incident angle is called slant-stacking (or vespa processing, e.g. Rost and Thomas, 2002). Shear diffracted waves have a predicted slowness of 8.32 s/dg for PREM (Dziewonski and Anderson, 1981), but this could vary due to the velocities in the lowermost mantle at the location where the energy propagates upwards to the seismic array. The slowness, or incident angle, could vary slightly between the main wave and the postcursor when they come from different directions. For these reasons, we do not fix the slowness when beamforming, but search over coherent en-

ergy by stacking the signals, $s_j(t)$, as a function of time t , slowness, u_{hor} , and backazimuth, θ , for a given subarray,

$$S(t, u_{hor}, \theta) = \sum_{j=1}^N s_j(t - u_{hor}(\theta) \cdot x_j) \quad (1)$$

where $u_{hor}(\theta) = u_{hor} \begin{pmatrix} \sin \theta \\ \cos \theta \end{pmatrix} = \begin{pmatrix} u_{EW} \\ u_{NS} \end{pmatrix}$ is the horizontal slowness vector, and $x_j = \begin{pmatrix} x_{EW} \\ x_{NS} \end{pmatrix}_j$ is the distance vector to the centre of the subarray.

A seismic signal can be expressed in amplitude and instantaneous phase:

$$s_j(t) = A_j(t) \exp[i\Phi_j(t)] \quad (2)$$

We create two separate stacks, one stack for the amplitude envelope, S_A , setting $s_j(t) = A_j(t)$, and one

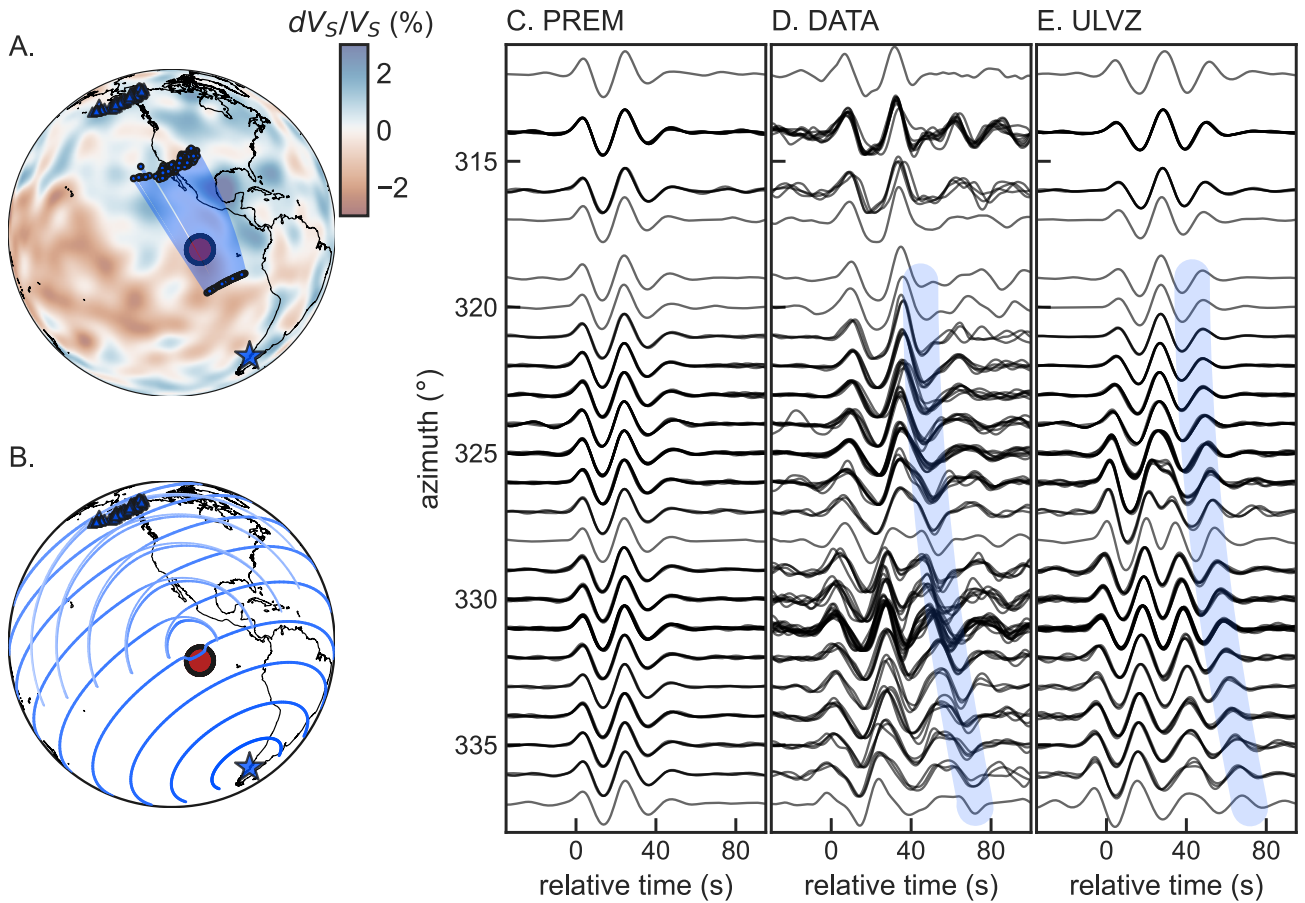


Figure 2 Geometry, data, and synthetics for event A. (A) Geometry of data coverage, event (star), stations (triangles), and sensitivity to the core-mantle boundary (shaded region) and ULVZ model (red circle). Background shows the shear wave velocity deviations at 2800 km depth from the tomographic SEMUCB-WM1 (French and Romanowicz, 2014). (B) Wavefront predictions for modeled ULVZ illustrating the cause of the postcursors. For an animation, see Movie S1. (C) Synthetic waveforms for 1D Earth model PREM (Dziewonski and Anderson, 1981). (D) Observed data. (E) Synthetics including background tomographic model and the preferred cylindrical ULVZ model. Data panels show SHdiff on the transverse component filtered between 10 and 30 s, binned by azimuth and centered on the predicted arrival times. Postcursor energy is highlighted by shaded region.

stack over the phase, S_Φ , setting $s_j(t) = \exp[i\Phi_j(t)]$. Finally, we interpret a phase weighted envelope stack (Schimmel and Paulssen, 1997), where the phase is weighted by a factor of 4,

$$PWES = S_A S_\Phi^4 \quad (3)$$

where all stacks are 3D arrays as a function of (t, u_{hor}, θ) .

A light Gaussian filter is applied to the stack to reduce irregularities and allow automated picking of peaks. The main peak and other peaks above 10% of the maximum peak are picked. Uncertainty is established by taking the minimum and maximum values for the contour at 95% of the peak amplitude. An example of a high-quality stack is shown in Fig. S13.

To build subarrays for an event, we create a sliding window in distance-azimuth space. The window is both 5° in distance and in azimuth, and we shift the window every 2° in azimuth and distance. For each window that has at least 12 stations, a stack is considered. The stacks are manually quality controlled for having one or two clear peaks that are well constrained in time-slowness-backazimuth space.

3 Results

3.1 Sdiff postcursor data set

Our analyses are based on waveform data from four different earthquakes (Fig. 1, Table 1). We use shear-diffracted waves recorded at the Alaska TA from two major earthquakes in Chile that sample the core-mantle boundary beneath the Eastern Pacific (Events A and B). Events A and B are shallow thrust events along the Chilean subduction zone of magnitude 7.6 on 25 December 2016 and magnitude 6.7 on 29 September 2019, respectively.

With Sdiff observations from only one azimuthal direction, the location of the ULVZ in the direction of their propagation remains non-unique. To fully constrain the location of ULVZs, we need rays crossing at a different angle. This is provided by Event C, which is a magnitude 7.2 on the Pacific-Antarctic ridge, recorded in the north-eastern US and south-eastern Canada. Additional evidence from a third angle comes from recordings across the Caribbean for an event in Fiji, although coverage in this direction is poor (Event D).

Figs. 2-5 show the expected and observed data for

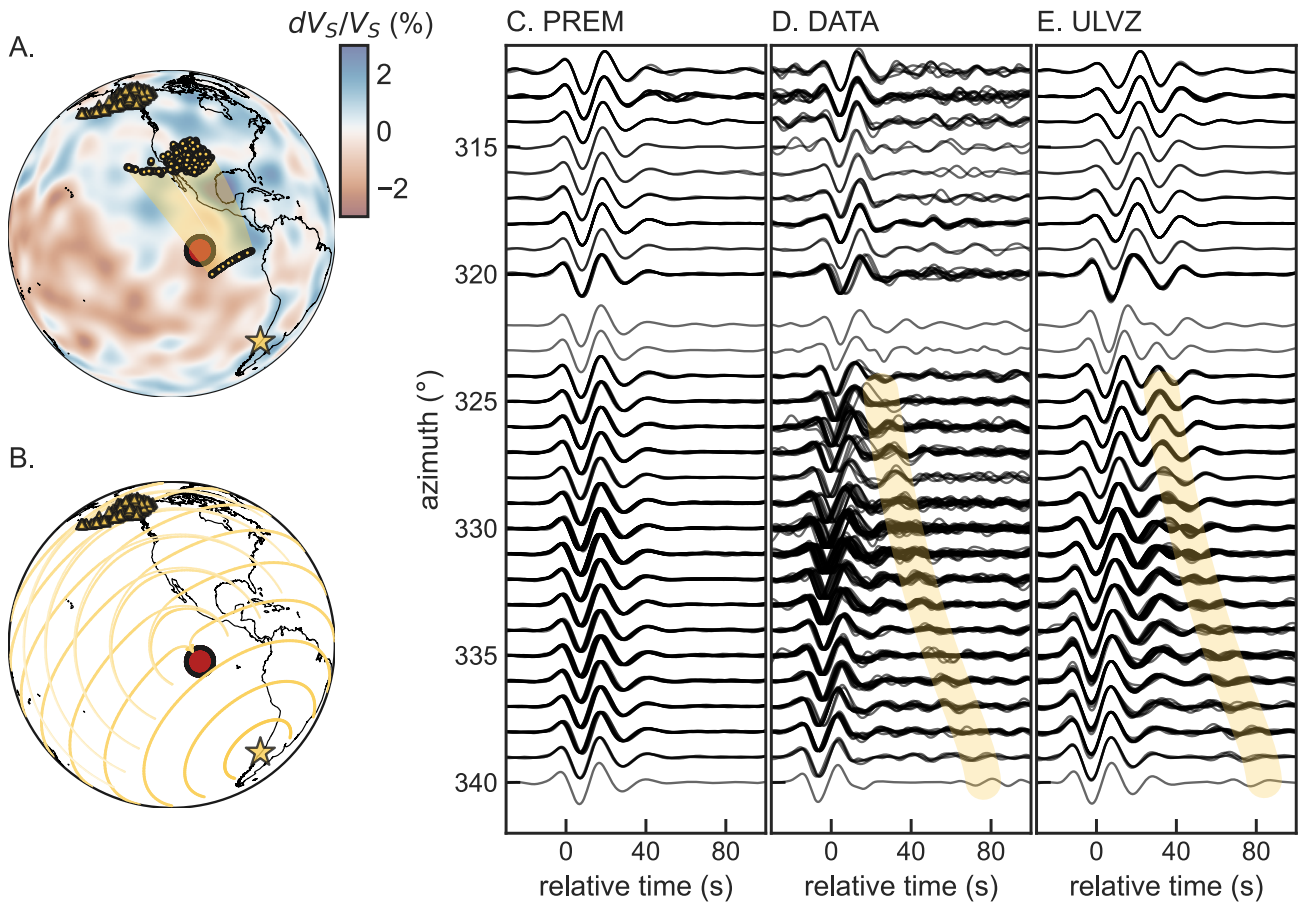


Figure 3 Geometry, data, and synthetics for event B. Same as Figure 2, but for Event B. For an animation, see Movie S2.

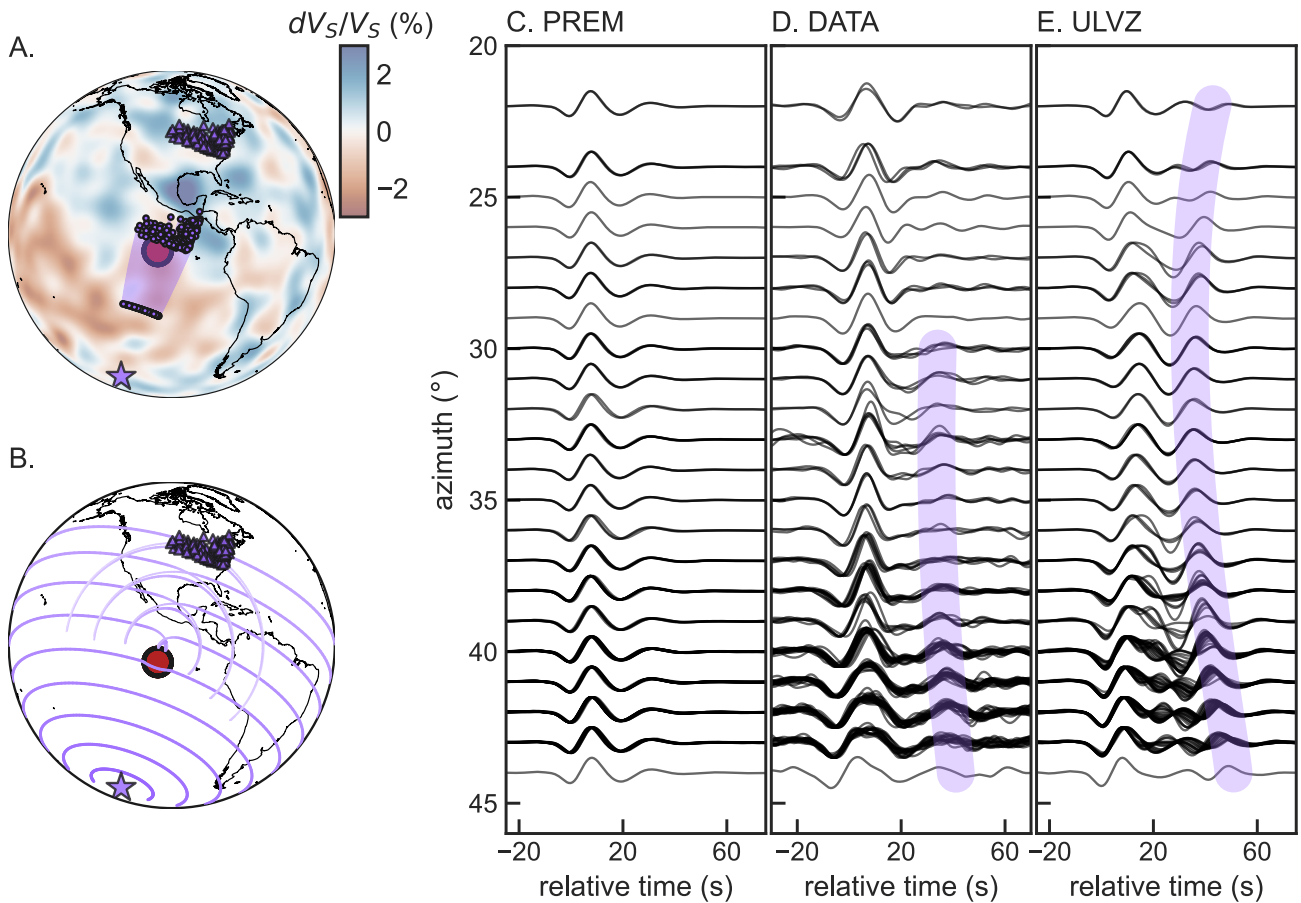


Figure 4 Geometry, data, and synthetics for event C. Same as Figure 2, but for Event C. For an animation, see Movie S3.

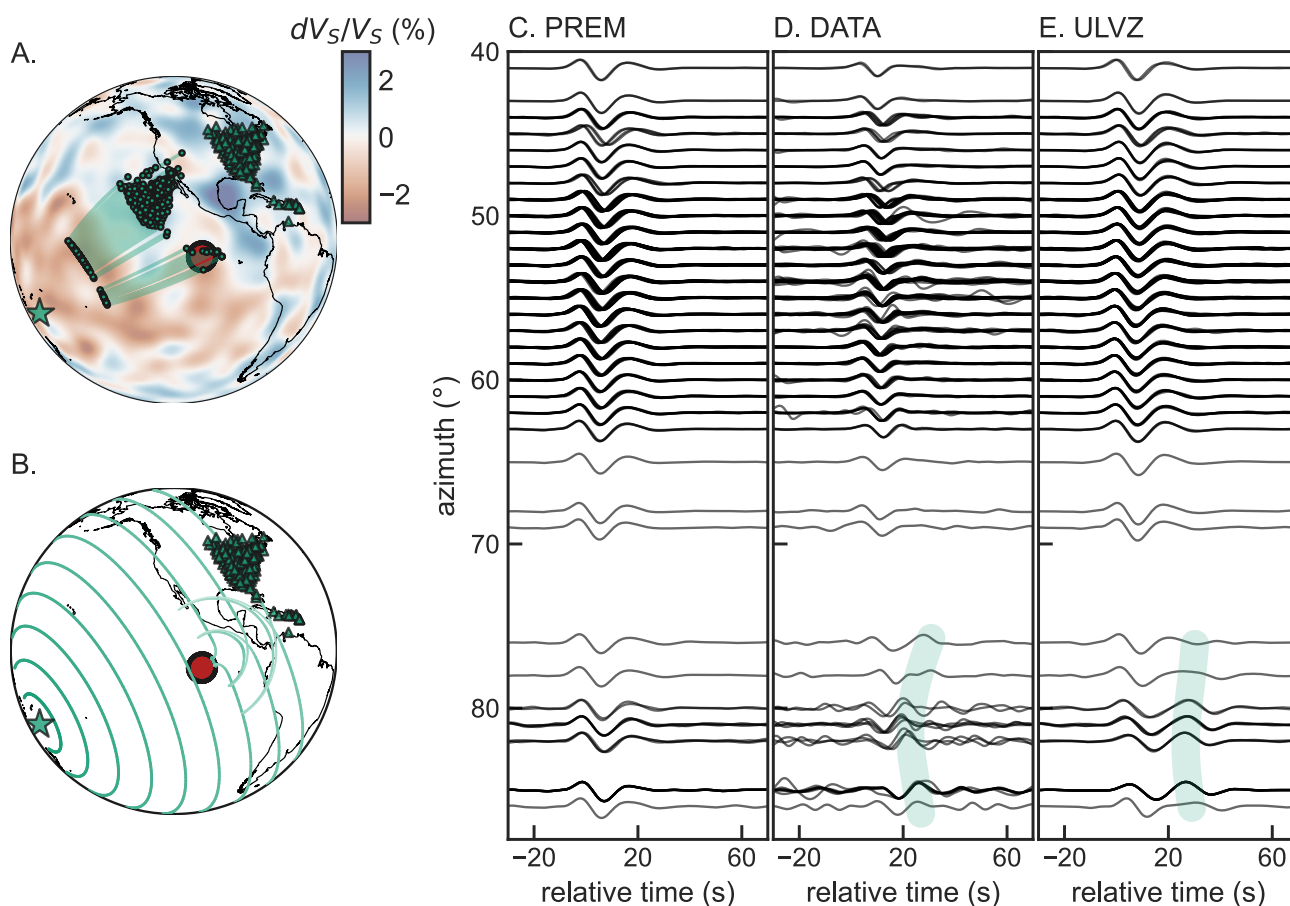


Figure 5 Geometry, data, and synthetics for event D. Same as Figure 2, but for Event D. For an animation, see Movie S4.

events A-D. The SH component of the shear diffracted wave and its postcursor attenuates less along the core-mantle boundary and therefore these phases are best observed on the transverse component. Transverse components shown are bandpass filtered between periods of 10 and 30s. Data are organized as a function of azimuthal angle from the earthquake and windowed around the predicted arrivals times of Sdiff for 1D radial Earth model (PREM, Dziewonski and Anderson, 1981). Expected waveforms are computed synthetics for this 1D radial Earth model showing waveform variations predicted due to source effects, but little waveform complexities, due to the absence of any mantle heterogeneity in the model.

Event A (Fig. 2) is a shallow event, causing the depth phases (pSdiff and sSdiff) to arrive shortly after the main phase. The observed compared to the expected waveforms show evidence for deep 3D heterogeneity in two ways. Firstly, the initial Sdiff phases arrive later at smaller azimuths and earlier at larger azimuths. This variation in travel time is caused by the dichotomy in the lowermost mantle where the waves at smaller azimuths propagate through the LLVP beneath the Pacific, and the waves at larger azimuths propagate through broad areas of likely subducted slab material (Fig. 1). Secondly, and this is the focus of this study, delayed and significant postcursors are present. The postcursors interfere with the main arrivals at azimuths of 321-327° and move out in time towards larger azimuths. The nature of these postcursors is comparable to those observed for

the Hawaiian and Icelandic mega-ULVZs (Cottaar and Romanowicz, 2012; Yuan and Romanowicz, 2017).

Event B (Fig. 3) shows comparable observations to event A. Again, the main Sdiff arrival shows a trend in arrival time with azimuth related to the LLVP boundary, and there is the presence of a postcursor that moves out towards larger azimuth with respect to the main Sdiff phases. However, the postcursor for this event is much weaker in amplitude relative to the main phase.

Event C (Fig. 4) shows postcursors with a very different propagation path through the same area at the core-mantle boundary. Its postcursors are stronger in amplitude towards larger azimuths and display a weaker move-out with time.

Event D (Fig. 5) shows hints of postcursor energy after the main phase at azimuths above 75°. Due to the poor station coverage in this area though, it is hard to observe any trends in the postcursor behavior. Potentially this data is also affected by a mega-ULVZ beneath the Marquesas as suggested by (Kim et al., 2020), implying there could be two postcursors. The data imaged by stations in the US at smaller azimuths show diffracted waves with no discernible postcursors, suggesting there are no mega-ULVZs located in a broad region of the core-mantle boundary between Hawaii and Marquesas.

3.2 Preferred model

Our best fitting ULVZ is centered at 105° W and 2° N. It has a height of 20 km and a width of 600 km, which is equal to nearly 10° on the core-mantle boundary. The

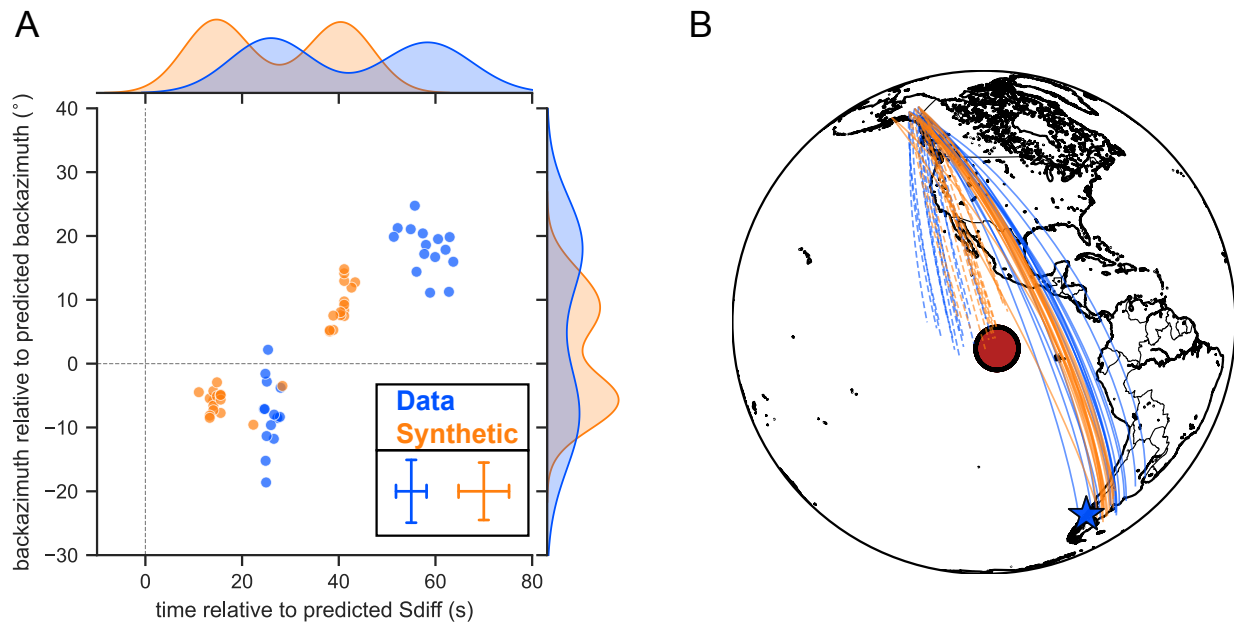


Figure 6 Beamforming results for event A. (A) Relative time versus relative backazimuth for picked peaks in beamform stack for real data (blue) and synthetic data for the ULVZ model (orange). Error bars in lower right shows median uncertainty for the observations. Note the bimodal distribution in both time and backazimuth related to the main and postcursor arrival. (B) Back-projection of determined backazimuths for energy peaks. Solid lines represent the main Sdiff arrival (defined as arrivals before 35 s), while the dashed lines represent the Sdiff postcursors (arrivals after 35s).

shear wave velocity within is reduced by 25% compared to surroundings. In Figs. 2-5, subplot B shows the wavefront predictions for this ULVZ model computed using a modified version of the wavefront tracker by (Hauser et al., 2008). Subplots E show the synthetic waveforms for the preferred ULVZ model. This reproduces the general move-out of the postcursors for Events A-C. It shows the relatively small amplitude postcursor for event B in comparison to event A, which is caused by the earthquake source of event B emitting relatively less shear energy in the direction of the ULVZ. For event C, the weaker move-out of the postcursor with time is predicted. For this event, the synthetics show clear and strong postcursors at smaller azimuths, which is not observed in the data. This could either mean that the assumed source mechanism is poor or that one side of the ULVZ has an irregular boundary or decreases in thickness.

Trade-offs and uncertainties do remain (see Supplementary Materials). Waveform results for shifted and resized ULVZ models are shown in the Figs. S6-S12 to illustrate the sensitivity of the data to various parameters. Based on these tests, estimated uncertainties on the preferred cylindrical model are at least 2° on location, 100 km in width, 5 km in height and 5% in velocity reduction.

3.3 Directionality of postcursors

Our preferred ULVZ model is confirmed by analyzing the directionality of the postcursor waveform by beamforming the energy for subarrays of stations where the main and postcursor are well separated. Fig. 6 shows the results for the significant postcursors present in event A, comparing the results for observations and synthetics. Both data and synthetics show a bimodal

distribution of energy peaks, with the later cluster offset by $20\text{-}30^\circ$ in backazimuth. Within error, the offset arrivals originate from the western boundary of the modeled ULVZ. There is an absolute time shift between the data and synthetics, which indicates unmodeled velocity variations along the Sdiff paths, but which are beyond the scope of this study. Beamforming results for other events are discussed in Supplementary Materials and for event C are shown in Fig. S14.

4 Discussion

The Galápagos ULVZ falls into the category of broad-scale mega-ULVZs, which are so far uncovered by diffracted phases. Other occurrences are mapped in 3D near Hawaii (Cottaar and Romanowicz, 2012; Jenkins et al., 2021; Lai et al., 2022; Li et al., 2022), Samoa (Thorne et al., 2013; Krier et al., 2021), and Iceland (Yuan and Romanowicz, 2017); these are shown in Fig. 7 combined with the global database of ULVZs by (Yu and Garnero, 2018). In general, a large variation of geometries of ULVZs has been suggested, and it is unclear if these all have comparable compositions and origins, and are shaped due to surrounding flows, or if these are distinctive features formed in different ways. To the south of the Galápagos Islands, for example, ULVZs have been mapped using PKP precursor phases that appear pile- or ridge-like with a width of 30 km and a height of 30 km (Ma et al., 2019), showing a very different aspect ratio from the mega-ULVZ observed here.

The edge of our preferred ULVZ location lies $\sim 10^\circ$ to the west of the Galápagos hotspot. A connection would require the Galápagos mantle plume to be offset in this direction. Seismic tomographic models identify low velocity anomalies beneath the Galápagos Islands, which

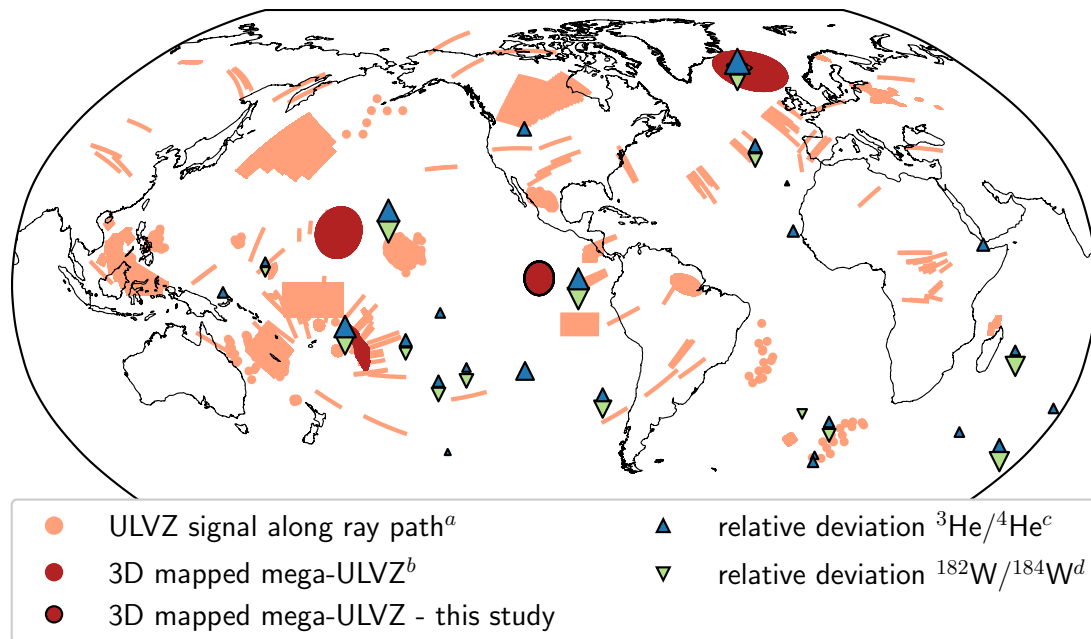


Figure 7 Mapped ULVZs and ocean island basalt isotopic signatures. Previous suggested locations of ULVZs (light orange) and recently 3D mapped mega-ULVZs (red) combined with helium and tungsten isotope ratio deviations observed in ocean island basalts compared to mid-ocean ridge basalts (scaled blue and green triangles, respectively). *a.* Compilation of ULVZ studies (Yu and Garnero, 2018) and a box is added for the region where small-scale ridges are found to the south of Galápagos Islands (Ma et al., 2019), *b.* Icelandic mega-ULVZ (Yuan and Romanowicz, 2017), Samoan mega-ULVZ from Thorne et al. (2013) and with 0.5 probability contour from Thorne et al. (2021), Hawaiian mega-ULVZ (Li et al., 2022). Note that other modeling studies for the mega-ULVZs near Hawaii (Jenkins et al., 2021; Lai et al., 2022; Li et al., 2022) and Samoa (Krier et al., 2021) not represented here. *c.* Scaled maximum observed positive $^3\text{He}/^4\text{He}$ isotopic ratio deviations from 9 Ra, the upper end of the MORB range, based on data compiled by Williams et al. (2019); Jackson et al. (2017); see references therein, and with additions from Jackson et al. (2020); Peters et al. (2021). *d.* Largest observed negative deviations in $\mu^{182}\text{W}$ compiled from Mundl et al. (2017); Rizo et al. (2019); Mundl-Petermeier et al. (2020). Note that the largest deviations for He and W do not always occur in the same samples for a given hotspot, and hotspots might be affected to different degrees by overprinting by recycled crust (Parai et al., 2019; Jackson et al., 2020; Péron et al., 2021; Day et al., 2022). Additionally, both the compilations of the ULVZs and the isotopic anomalies have a degree of geographical bias to where (more) studies have been conducted.

could be interpreted as plumes, but do not all agree on its direction of tilt or continuity across the mantle (Fig. 8). The resolution of the models beneath the Galápagos will be biased due to the seismic stations being largely located on land to the east and north. Some of the latest global mantle shear wave velocity models suggest the plume is offset to the southwest (French and Romanowicz, 2015; Lei et al., 2020) and this offset also results when combining shear velocity models with a geodynamical model (Williams et al., 2019). A recent innovative use of increasing coverage around the hotspot by using passively floating seismometers resulted in a P wave velocity model with a vertical plume down to 1900 km, beneath which resolution might be lost (Nolet et al., 2019). A different recent P wave velocity model focused on adding coverage in the lower mantle, observes a vertical plume down to 1000 km depth with fast velocities underneath (Hosseini et al., 2020). In both of these P wave models, the suggested plume is vertical. It is however easy to speculate that if there is a whole-mantle plume, that it originates within or at the edge of the LLVP (Steinberger and Torsvik, 2012; Li and Zhong, 2017) and its base is therefore offset to the west or southwest of the hotspot at the surface.

The geochemistry of basalts from the Galápagos

archipelago indicate a plume with at least three distinct components, each manifesting in geographically-restricted portions of the archipelago along with a depleted upper mantle component (Harpp and White, 2001; Gleeson et al., 2021; Geist et al., 1988; White et al., 1993). Harpp and Weis (2020) observed that the plume component mixture evident in the southwestern part of the archipelago is distinct from that in the northeast and argued for a bilaterally asymmetric Galápagos plume. Notably, subaerial and submarine samples from the westernmost island of Fernandina exhibit the highest $^3\text{He}/^4\text{He}$ ratios in the archipelago (Graham et al., 1993; Kurz and Geist, 1999; Kurz et al., 2009), and the most solar-like Ne isotopic compositions of ocean islands globally (Kurz et al., 2009; Péron et al., 2021). Solar nebular helium and neon are thought to have dissolved into a terrestrial magma ocean during Earth's accretion (Harper and Jacobsen, 1996). High $^3\text{He}/^4\text{He}$ ratios in ocean island basalts (compared to those measured in mid-ocean ridge basalts) reflect greater retention of the primordial helium budget, which mutes the impact of radiogenic ^4He ingrowth by decay of U and Th over Earth history (Mukhopadhyay and Parai, 2019; Parai et al., 2019). The Fernandina helium and neon isotopic signatures indicate that the southwestern side of

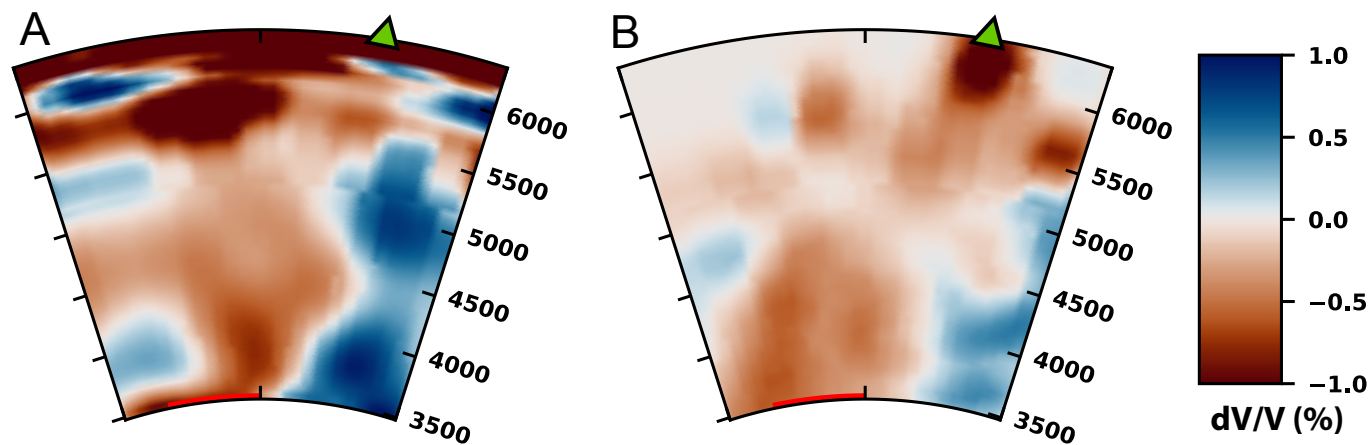


Figure 8 Cross-sections through the Galapagos ULVZ and hotspot. (A) Shear wave velocity deviations in SEMUCB-wm1 (French and Romanowicz, 2014). (B) P wave velocity deviations in DETOX-P2 (Hosseini et al., 2020). Red line on the core-mantle boundary shows location of ULVZ. Green triangle at the surface shows the location of hotspot. See Fig. 1 for location of the cross-section.

the Galápagos plume samples a reservoir that has experienced relatively little degassing and thus retained a high proportion of primordial solar He and Ne from Earth's accretion.

Four hotspot locations (Hawaii, Iceland, Samoa and Galápagos) that have a mega-ULVZ situated near their projection down onto the core-mantle boundary share a collective set of geochemical features. Samples from these locations exhibit high $^3\text{He}/^4\text{He}$ ratios, relatively solar-like Ne isotopes, and anomalous ^{182}W isotopic signatures (Fig. 7). ^{182}W was produced by decay of the extinct radionuclide ^{182}Hf in the first ~ 60 Myr of Earth history. Core segregation within the lifetime of ^{182}Hf fractionated Hf/W ratios and generated a radiogenic ^{182}W isotopic signature ($\mu^{182}\text{W}=0$, where $\mu^{182}\text{W}$ signifies the part per million deviation in $^{182}\text{W}/^{184}\text{W}$ from a laboratory standard) in the bulk silicate Earth compared to chondrites (Kleine et al., 2002; Yin et al., 2002). The core locked in an unradiogenic ^{182}W signature (negative $\mu^{182}\text{W}$), as would any other siderophile-enriched reservoir in the interior that formed during the lifetime of ^{182}Hf . Among hotspots, Hawaii, Iceland, Samoa, and Galápagos have the highest measured $^3\text{He}/^4\text{He}$ ratios (Kurz et al., 1983, 2009; Hilton et al., 1999; Jackson et al., 2007) and the most solar-like Ne isotopes (Valbracht et al., 1997; Trierloff et al., 2000; Kurz et al., 2009; Mukhopadhyay, 2012; Jackson et al., 2020; Péron et al., 2021; Peto et al., 2013). Some of the strongest negative $\mu^{182}\text{W}$ anomalies occur in samples with high $^3\text{He}/^4\text{He}$ ratios from these same hotspots (Mundl et al., 2017; Mundl-Petermeier et al., 2020, see Fig. 7).

The helium and neon isotopic signatures of the mega-ULVZ affiliated hotspots suggest a relatively undegassed source, which is commonly suggested to come from a deep mantle reservoir (Allègre et al., 1983; Parai et al., 2019), but has also been suggested to originate from the outer core (Bouhifd et al., 2020). Xe isotopes measured in samples with high $^3\text{He}/^4\text{He}$ and solar-like Ne from Iceland and Samoa require that the reservoir that hosts this signature separated from the upper mantle within the first ~ 100 Myr of Earth history (Mukhopadhyay, 2012; Peto et al., 2013). The anomalous tung-

sten isotope signature (negative $\mu^{182}\text{W}$) suggests the involvement of a siderophile-enriched reservoir that likewise formed early in Earth's history. An obvious candidate for this reservoir is the core, and many potential processes to transfer material or isotopic signatures across the core-mantle boundary have been proposed (Kanda and Stevenson, 2006; Hayden and Watson, 2007; Otsuka and Karato, 2012; Leshner et al., 2020; Buffett et al., 2000; Lim et al., 2021). However, direct material transfer from the core would impart strongly fractionated noble gas elemental ratios to a plume, and these are not observed (Wang et al., 2022). An alternative is an early-formed, iron-rich deep mantle reservoir. Mundl-Petermeier et al. (2020) suggests that to explain the full space of helium-tungsten isotope observations, two high $^3\text{He}/^4\text{He}$ components are needed: one with negative $\mu^{182}\text{W}$ and one with tungsten isotopes similar to the bulk silicate Earth. These distinct components could potentially reflect material entrainment from an LLVP and a ULVZ, with the ULVZ providing the negative tungsten isotope signature. Geodynamical modeling shows mantle plumes can sample LLVP material, and to a degree the much denser ULVZ material (Jones et al., 2019). The correlation between these mega-ULVZs and the isotopic signatures is striking and should be tested in further localities.

5 Conclusion

We present seismic evidence of a mega-ULVZ on the core-mantle boundary to the west of the Galápagos Islands in the form of postcursors to the Sdiff phase. Modeling the delay times and move-out of the postcursors allows us to constrain a simplified cylindrical shape with a width of ~ 600 km, a height of 20 km, a shear wave velocity reduction of 25%, and centered at 105° W and 2° N. This model also largely reproduces the observed incoming directionality of the postcursors. Similar mega-ULVZs have been mapped beneath or near the Hawaiian, Samoan and Icelandic hotspots. Ocean island basalts in all four locations show anomalous signatures in He, Ne, and W, which could be clues to

the mega-ULVZs representing a primordial reservoir or containing a component of outer core material.

Acknowledgements

The authors thank Curtis Williams, Helen Williams, and Vedran Lekić for discussion of this work. SC, CM, and ZL were funded by the European Research Council (ERC) under the European Union's Horizon 2020 research and innovation programme (grant agreement No. 804071 -ZoomDeep). RP was funded by National Science Foundation grant EAR 2145663. This work was performed using resources provided by the Cambridge Service for Data Driven Discovery (CSD3) operated by the University of Cambridge Research Computing Service (www.csd3.cam.ac.uk).

Data and code availability

Processed and quality controlled observed data, synthetic data, and codes for data processing and plotting are available at <https://doi.org/10.5281/zenodo.7229683>. Processing scripts make use of ObsPy (www.obspy.org). We use sandwiched-CSEM (Capdeville et al., 2003) to compute the synthetics; contact the authors of that study for access. Cross-sections for Figure 7 are taken from Submachine (<http://www.earth.ox.ac.uk/~smachine/>). The facilities of IRIS Data Services (www.iris.edu), and specifically the IRIS Data Management Center, were used for access to waveforms and related metadata. IRIS Data Services are funded through the Seismological Facilities for the Advancement of Geoscience (SAGE) Award of the National Science Foundation under Cooperative Support Agreement EAR-1851048. Data from the TA network were made freely available as part of the EarthScope USArray facility, operated by Incorporated Research Institutions for Seismology (IRIS) and supported by the National Science Foundation, under Cooperative Agreements EAR-1261681. Earthquake parameters were used from the Global CMT Project (www.globalcmt.org) and USGS National Earthquake Information Centre (earthquake.usgs.gov).

References

- Allègre, C., Staudacher, T., Sarda, P., and Kurz, M. Constraints on evolution of Earth's mantle from rare gas systematics. *Nature*, 303(5920):762–766, 1983. doi: 10.1038/303762a0.
- Bouhifd, M., Jephcoat, A., Porcelli, D., Kelley, S., and Marty, B. Potential of Earth's core as a reservoir for noble gases: Case for helium and neon. *Geochemical Perspectives Letters*, 15:15–18, 2020. doi: 10.7185/geochemlet.2028.
- Buffett, B., Garnero, E., and Jeanloz, R. Sediments at the Top of Earth's Core. *Science*, 290(5495):1338–1342, 2000. doi: 10.1126/science.290.5495.1338.
- Capdeville, Y., Larmat, C., Vilotte, J.-P., and Montagner, J.-P. A new coupled spectral element and modal solution method for global seismology: A first application to the scattering induced by a plume-like anomaly. *Geophysical Research Letters*, 29(9): 32–1–32–4, 2002. doi: 10.1029/2001GL013747.
- Capdeville, Y., To, A., and Romanowicz, B. Coupling spectral elements and modes in a spherical Earth: an extension to the “sandwich” case. *Geophysical Journal International*, 154(1): 44–57, 2003. doi: 10.1046/j.1365-246X.2003.01959.x.
- Cottaar, S. and Lekić, V. Morphology of seismically slow lower-mantle structures. *Geophys. J. Int.*, 207(2):1122–1136, 2016. doi: 10.1093/gji/ggw324.
- Cottaar, S. and Romanowicz, B. An unusually large ULVZ at the base of the mantle near Hawaii. *Earth and Planetary Science Letters*, 355–356:213–222, 2012. doi: 10.1016/j.epsl.2012.09.005.
- Dannberg, J., Myhill, R., Gassmüller, R., and Cottaar, S. The morphology, evolution and seismic visibility of partial melt at the core-mantle boundary: Implications for ULVZs. *Geophysical Journal International*, 227(2):1028–1059, 2021. doi: 10.1093/gji/ggab242.
- Day, J., Jones, T., and Nicklas, R. Mantle sources of ocean islands basalts revealed from noble gas isotope systematics. *Chemical Geology*, 587:120626, 2022. doi: 10.1016/j.chemgeo.2021.120626.
- Dobrosavljevic, V., Sturhahn, W., and Jackson, J. Evaluating the role of iron-rich (Mg,Fe)O in ultralow velocity zones. *Minerals*, 9 (12):762, 2019. doi: 10.3390/min9120762.
- Domeier, M., Doubrovine, P., Torsvik, T., Spakman, W., and Bull, A. Global correlation of lower mantle structure and past subduction. *Geophysical Research Letters*, 43(10):4945–4953, 2016. doi: 10.1002/2016GL068827.
- Dziewonski, A. and Anderson, D. Preliminary reference Earth model. *Physics of the Earth and Planetary Interiors*, 25(4): 297–356, 1981. doi: 10.1016/0031-9201(81)90046-7.
- Ekström, G., Nettles, M., and Dziewoński, A. The global CMT project 2004-2010: Centroid-moment tensors for 13,017 Earthquakes. *Physics of the Earth and Planetary Interiors*, 200–201:1–9, 2012. doi: 10.1016/j.pepi.2012.04.002.
- French, S. and Romanowicz, B. Whole-mantle radially anisotropic shear velocity structure from spectral-element waveform tomography. *Geophysical Journal International*, 199(3): 1303–1327, 2014. doi: 10.1093/gji/ggu334.
- French, S. and Romanowicz, B. Broad plumes rooted at the base of the Earth's mantle beneath major hotspots. *Nature*, 525(7567): 95–9, 2015. doi: 10.1038/nature14876.
- Garnero, E., McNamara, A., and Shim, S.-H. Continent-sized anomalous zones with low seismic velocity at the base of Earth's mantle. *Nature Geosci*, 9(7):481–489, 2016. doi: 10.1038/ngeo2733.
- Geist, D., White, W., and McBirney, A. Plume-asthenosphere mixing beneath the Galapagos archipelago. *Nature*, 333(6174): 657–660, 1988. doi: 10.1038/333657a0.
- Gleeson, M., Soderman, C., Matthews, S., Cottaar, S., and Gibson, S. Geochemical Constraints on the Structure of the Earth's Deep Mantle and the Origin of the LLSVPs. *Geochemistry, Geophysics, Geosystems*, 22(9), 2021. doi: 10.1029/2021GC009932.
- Graham, D., Christie, D., Harpp, K., and Lupton, J. Mantle plume helium in submarine basalts from the Galápagos platform. *Science*, 262(5142):2023–2026, 1993. doi: 10.1126/science.262.5142.2023.
- Harper, C. and Jacobsen, S. Noble gases and Earth's accretion. *Science*, 273(5283):1814–1818, 1996. doi: 10.1126/science.273.5283.1814.
- Harpp, K. and Weis, D. Insights Into the Origins and Compositions of Mantle Plumes: A Comparison of Galápagos and Hawai'i. *Geochemistry, Geophysics, Geosystems*, 21(9), 2020. doi: 10.1029/2019GC008887.
- Harpp, K. and White, W. Tracing a mantle plume: Iso-

- topic and trace element variations of Galápagos seamounts. *Geochemistry, Geophysics, Geosystems*, 2(6), 2001. doi: 10.1029/2000gc000137.
- Hauser, J., Sambridge, M., and Rawlinson, N. Multiarrival wavefront tracking and its applications. *Geochemistry, Geophysics, Geosystems*, 9(11), 2008. doi: 10.1029/2008GC002069.
- Hayden, L. and Watson, E. A diffusion mechanism for core–mantle interaction. *Nature*, 450(7170):709–711, 2007. doi: 10.1038/nature06380.
- Hernlund, J. and Jellinek, A. Dynamics and structure of a stirred partially molten ultralow-velocity zone. *Earth and Planetary Science Letters*, 296(1–2):1–8, 2010. doi: 10.1016/j.epsl.2010.04.027.
- Hilst, R., Widiyantoro, S., and Engdahl, E. Evidence for deep mantle circulation from global tomography. *Nature*, 386(6625):578–584, 1997. doi: 10.1038/386578a0.
- Hilton, D., Grönvold, K., Macpherson, C., and Castillo, P. Extreme $3\text{He}/4\text{He}$ ratios in northwest Iceland: Constraining the common component in mantle plumes. *Earth and Planetary Science Letters*, 173(1–2):53–60, 1999. doi: 10.1016/S0012-821X(99)00215-0.
- Hosseini, K., Sigloch, K., Tsekhmistrenko, M., Zaheri, A., Nissen-Meyer, T., and Igel, H. Global mantle structure from multifrequency tomography using P, PP and P-diffracted waves. *Geophysical Journal International*, 220(1):96–141, 2020. doi: 10.1093/gji/ggz394.
- Jackson, M., Kurz, M., Hart, S., and Workman, R. New Samoan lavas from Ofu Island reveal a hemispherically heterogeneous high $3\text{He}/4\text{He}$ mantle. *Earth and Planetary Science Letters*, 264(3–4):360–374, 2007. doi: 10.1016/j.epsl.2007.09.023.
- Jackson, M., Konter, J., and Becker, T. Primordial helium entrained by the hottest mantle plumes. *Nature*, 542(7641):340–343, 2017. doi: 10.1038/nature21023.
- Jackson, M., Blichert-Toft, J., Halldórsson, S., Mundl-Petermeier, A., Bizimis, M., Kurz, M., Price, A., Haroardóttir, S., Willhite, L., Breddam, K., Becker, T., and Fischer, R. Ancient helium and tungsten isotopic signatures preserved in mantle domains least modified by crustal recycling. *Proceedings of the National Academy of Sciences of the United States of America*, 117(49):30993–31001, 2020. doi: 10.1073/pnas.2009663117.
- Jellinek, A. and Manga, M. Links between long-lived hot spots, mantle plumes, D”, and plate tectonics. *Reviews of Geophysics*, 42(3):3002, 2004. doi: 10.1029/2003RG000144.
- Jenkins, J., Mousavi, S., Li, Z., and Cottaar, S. A high-resolution map of Hawaiian ULVZ morphology from ScS phases. *Earth and Planetary Science Letters*, 563:116885, 2021. doi: 10.1016/j.epsl.2021.116885.
- Jones, T., Davies, D., and Sossi, P. Tungsten isotopes in mantle plumes: Heads it’s positive, tails it’s negative. *Earth and Planetary Science Letters*, 506:255–267, 2019. doi: 10.1016/J.EPSL.2018.11.008.
- Kanda, R. and Stevenson, D. Suction mechanism for iron entrainment into the lower mantle. *Geophys. Res. Lett.*, 33(2):02310, 2006. doi: 10.1029/2005GL025009.
- Kim, D., Lekić, V., Ménard, B., Baron, D., and Taghizadeh-Popp, M. Sequencing seismograms: A panoptic view of scattering in the core-mantle boundary region. *Science*, 368(6496):1223–1228, 2020. doi: 10.1126/science.aba8972.
- Kleine, T., Münker, C., Mezger, K., and Palme, H. Rapid accretion and early core formation on asteroids and the terrestrial planets from Hf-W chronometry. *Nature*, 418(6901):952–955, 2002. doi: 10.1038/nature00982.
- Krier, J., Thorne, M., Leng, K., and Nissen-Meyer, T. A Compositional Component to the Samoa Ultralow-Velocity Zone Revealed Through 2- and 3-D Waveform Modeling of SKS and SKKS Differential Travel-Times and Amplitudes. *Journal of Geophysical Research: Solid Earth*, 126(7):2021 021897, 2021. doi: 10.1029/2021JB021897.
- Kurz, M. and Geist, D. Dynamics of the Galapagos hotspot from helium isotope geochemistry. *Geochimica et Cosmochimica Acta*, 63(23–24):4139–4156, 1999. doi: 10.1016/s0016-7037(99)00314-2.
- Kurz, M., Jenkins, W., Hart, S., and Clague, D. Helium isotopic variations in volcanic rocks from Loihi Seamount and the Island of Hawaii. *Earth and Planetary Science Letters*, 66(C):388–406, 1983. doi: 10.1016/0012-821X(83)90154-1.
- Kurz, M., Curtice, J., Fornari, D., Geist, D., and Moreira, M. Primitive neon from the center of the Galápagos hotspot. *Earth and Planetary Science Letters*, 286(1–2):23–34, 2009. doi: 10.1016/j.epsl.2009.06.008.
- Labrosse, S., Hernlund, J., and Coltice, N. A crystallizing dense magma ocean at the base of the Earth’s mantle. *Nature*, 450(7171):866–9, 2007. doi: 10.1038/nature06355.
- Lai, V., Helmberger, D., Dobrosavljevic, V., Wu, W., Sun, D., Jackson, J., and Gurnis, M. Strong ULVZ and Slab Interaction at the Northeastern Edge of the Pacific LLSVP Favors Plume Generation. *Geochemistry, Geophysics, Geosystems*, 23(2), 2022. doi: 10.1029/2021gc010020.
- Lei, W., Ruan, Y., Bozdağ, E., Peter, D., Lefebvre, M., Komatitsch, D., Tromp, J., Hill, J., Podhorszki, N., and Pugmire, D. Global adjoint tomography - Model GLAD-M25. *Geophysical Journal International*, 223(1):1–21, 2020. doi: 10.1093/gji/ggaa253.
- Leshner, C., Dannberg, J., Barfod, G., Bennett, N., Glessner, J., Lacks, D., and Brennan, J. Iron isotope fractionation at the core–mantle boundary by thermodiffusion. *Nature Geoscience*, 13(5):382–386, 2020. doi: 10.1038/s41561-020-0560-y.
- Li, J., Sun, D., and Bower, D. Slab control on the mega-sized North Pacific ultra-low velocity zone. *Nature Communications*, 13(1):1042, 2022. doi: 10.1038/s41467-022-28708-8.
- Li, M. and Zhong, S. The source location of mantle plumes from 3D spherical models of mantle convection. *Earth and Planetary Science Letters*, 478:47–57, 2017. doi: 10.1016/J.EPSL.2017.08.033.
- Li, M., McNamara, A., Garnero, E., and Yu, S. Compositionally-distinct ultra-low velocity zones on Earth’s core-mantle boundary. *Nature comm*, 8(1):177, 2017. doi: 10.1038/s41467-017-00219-x.
- Lim, K., Bonati, I., and Hernlund, J. A Hybrid Mechanism for Enhanced Core-Mantle Boundary Chemical Interaction. *Geophysical Research Letters*, 48(23), 2021. doi: 10.1029/2021GL094456.
- Ma, X., Sun, X., and Thomas, C. Localized ultra-low velocity zones at the eastern boundary of Pacific LLSVP. *Earth and Planetary Science Letters*, 507:40–49, 2019. doi: 10.1016/J.EPSL.2018.11.037.
- Mukhopadhyay, S. Early differentiation and volatile accretion recorded in deep-mantle neon and xenon. *Nature*, 486(7401):101–104, 2012. doi: 10.1038/nature11141.
- Mukhopadhyay, S. and Parai, R. Noble gases: A record of Earth’s evolution and mantle dynamics. *Annual Review of Earth and Planetary Sciences. Annual Reviews*, page 389–419, 2019. doi: 10.1146/annurev-Earth-053018-060238.
- Mundl, A., Touboul, M., Jackson, M., Day, J., Kurz, M., Lekic, V., Helz, R., and Walker, R. Tungsten-182 heterogeneity in modern ocean island basalts. *Science*, 356(6333):66–69, 2017. doi: 10.1126/science.aal4179.
- Mundl-Petermeier, A., Walker, R., Fischer, R., Lekic, V., Jackson, M., and Kurz, M. Anomalous 182W in high $3\text{He}/4\text{He}$ ocean

- island basalts: Fingerprints of Earth's core? *Geochimica et Cosmochimica Acta*, 271:194–211, 2020. doi: 10.1016/j.gca.2019.12.020.
- Nolet, G., Hello, Y., Lee, S. d., Bonnieux, S., Ruiz, M., Pazmino, N., Deschamps, A., Regnier, M., Font, Y., Chen, Y., and Simons, F. Imaging the Galápagos mantle plume with an unconventional application of floating seismometers. *Scientific Reports*, 9(1): 1326, 2019. doi: 10.1038/s41598-018-36835-w.
- Otsuka, K. and Karato, S. Deep penetration of molten iron into the mantle caused by a morphological instability. *Nature*, 492 (7428):243–246, 2012. doi: 10.1038/nature11663.
- Parai, R., Mukhopadhyay, S., Tucker, J., and Pető, M. The emerging portrait of an ancient, heterogeneous and continuously evolving mantle plume source. *Lithos. Elsevier*, page 105153, 2019. doi: 10.1016/j.lithos.2019.105153.
- Peters, B., Mundl-Petermeier, A., Carlson, R., Walker, R., and Day, J. Combined Lithophile-Siderophile Isotopic Constraints on Hadean Processes Preserved in Ocean Island Basalt Sources. *Geochemistry, Geophysics, Geosystems*, 22(3), 2021. doi: 10.1029/2020GC009479.
- Peto, M., Mukhopadhyay, S., and Kelley, K. Heterogeneities from the first 100 million years recorded in deep mantle noble gases from the Northern Lau Back-arc Basin. *Earth and Planetary Science Letters*, 369–370:13–23, 2013. doi: 10.1016/j.epsl.2013.02.012.
- Péron, S., Mukhopadhyay, S., Kurz, M., and Graham, D. Deep-mantle krypton reveals Earth's early accretion of carbonaceous matter. *Nature*, 600(7889):462–467, 2021. doi: 10.1038/s41586-021-04092-z.
- Rizo, H., Andrault, D., Bennett, N., Humayun, M., Brandon, A., Vlastelic, I., Moine, B., Poirier, A., Bouhifd, M., and Murphy, D. 182W evidence for core-mantle interaction in the source of mantle plumes. *Geochemical Perspectives Letters*, 11:6–11, 2019. doi: 10.7185/geochemlet.1917.
- Rost, S. and Thomas, C. Array seismology: Methods and applications. *Reviews of Geophysics*, 40(3):1008, 2002. doi: 10.1029/2000RG000100.
- Schimmel, M. and Paulssen, H. Noise reduction and detection of weak, coherent signals through phase-weighted stacks. *Geophysical Journal International*, 130(2):497–505, 1997. doi: 10.1111/j.1365-246X.1997.tb05664.x.
- Steinberger, B. and Torsvik, T. A geodynamic model of plumes from the margins of Large Low Shear Velocity Provinces. *Geochemistry, Geophysics, Geosystems*, 13(1):–, 2012. doi: 10.1029/2011GC003808.
- Thorne, M., Garnero, E., Jahnke, G., Igel, H., and McNamara, A. Mega ultra low velocity zone and mantle flow. *Earth and Planetary Science Letters*, 364:59–67, 2013. doi: 10.1016/j.epsl.2012.12.034.
- Thorne, M., Pachhai, S., Leng, K., Wicks, J., and Nissen-Meyer, T. New Candidate Ultralow-Velocity Zone Locations from Highly Anomalous SPdKS Waveforms. *Minerals*, 10(3):211, 2020. doi: 10.3390/min10030211.
- Thorne, M., Leng, K., Pachhai, S., Rost, S., Wicks, J., and Nissen-Meyer, T. The Most Parsimonious Ultralow-Velocity Zone Distribution From Highly Anomalous SPdKS Waveforms. *Geochemistry, Geophysics, Geosystems*, 22(1):2020 009467, 2021. doi: 10.1029/2020GC009467.
- Trieloff, M., Kunz, J., Clague, D., Harrison, D., and Allègre, C. The nature of pristine noble gases in mantle plumes. *Science*, 288 (5468):1036–1038, 2000. doi: 10.1126/science.288.5468.1036.
- Valbracht, P., Staudacher, T., Malahoff, A., and Allègre, C. Noble gas systematics of deep rift zone glasses from Loihi Seamount, Hawaii. *Earth and Planetary Science Letters*, 150(3–4):399–411, 1997. doi: 10.1016/s0012-821x(97)00094-0.
- Wang, K., Lu, X., Liu, X., Zhou, M., and Yin, K. Partitioning of noble gases (He, Ne, Ar, Kr, Xe) during Earth's core segregation: A possible core reservoir for primordial noble gases. *Geochimica et Cosmochimica Acta*, 321:329–342, 2022. doi: 10.1016/j.gca.2022.01.009.
- White, W., McBirney, A., and Duncan, R. Petrology and geochemistry of the Galapagos Islands: portrait of a pathological mantle plume. *Journal of Geophysical Research*, 98(B11):19533–19563, 1993. doi: 10.1029/93jb02018.
- Wicks, J., Jackson, J., Sturhahn, W., and Zhang, D. Sound velocity and density of magnesio-wüstites: Implications for ultralow-velocity zone topography. *Geophysical Research Letters*, 44(5): 2148–2158, 2017. doi: 10.1002/2016GL071225.
- Williams, C., Mukhopadhyay, S., Rudolph, M., and Romanowicz, B. Primitive Helium Is Sourced From Seismically Slow Regions in the Lowermost Mantle. *Geochemistry, Geophysics, Geosystems*, 20(8):4130–4145, 2019. doi: 10.1029/2019GC008437.
- Yin, Q., Jacobsen, S., Yamashita, K., Blichert-Toft, J., Télouk, P., and Albarède, F. A short timescale for terrestrial planet formation from Hf-W chronometry of meteorites. *Nature*, 418(6901): 949–952, 2002. doi: 10.1038/nature00995.
- Yu, S. and Garnero, E. Ultralow Velocity Zone Locations: A Global Assessment. *Geochemistry, Geophysics, Geosystems*, 19(2): 396–414, 2018. doi: 10.1002/2017GC007281.
- Yuan, K. and Romanowicz, B. Seismic evidence for partial melting at the root of major hot spot plumes. *Science*, 357:393–397, 2017. doi: 10.1126/science.aan0760.

The article *The Root to the Galápagos Mantle Plume on the Core-Mantle Boundary* © 2022 by Sanne Cottaar is licensed under CC BY 4.0.

Tilt Corrections for Normal Mode Observations on Ocean Bottom Seismic Data, an example from the PI-LAB experiment

Nicholas Harmon  ^{*1,2}, Gabi Laske  ³, Wayne Crawford  ⁴, Catherine A. Rychert  ^{1,2}

¹Ocean and Earth Science, University of Southampton, Southampton, UK, ²Geology and Geophysics, Woods Hole Oceanographic Institution, Woods Hole, MA, USA, ³Institute of Geophysics and Planetary Physics, Scripps Institution of Oceanography, La Jolla, CA, USA, ⁴Institut de Physique Du Globe De Paris, Centre National de la Recherche Scientifique, Paris, France

Author contributions: *Conceptualization:* N. Harmon, G. Laske, W. Crawford, C. A. Rychert. *Funding Acquisition:* N. Harmon, C. A. Rychert. *Formal Analysis:* N. Harmon, G. Laske, W. Crawford, C. A. Rychert. *Software:* N. Harmon, G. Laske, W. Crawford, C. A. Rychert. *Writing – original draft:* N. Harmon, G. Laske, W. Crawford, C. A. Rychert. *Writing – review & editing:* N. Harmon, G. Laske, W. Crawford, C. A. Rychert.

Abstract Earth's normal modes are fundamental observations used in global seismic tomography to understand Earth structure. Land seismic station coverage is sufficient to constrain the broadest scale Earth structures. However, 70% of Earth's surface is covered by the oceans, hampering our ability to observe variations in local mode frequencies that contribute to imaging small-scale structures. Broadband ocean bottom seismometers can record spheroidal modes to fill in gaps in global data coverage. Ocean bottom recordings are contaminated by signals from complex interactions between ocean and solid Earth dynamics at normal mode frequencies. We present a method for correcting tilt on broadband ocean bottom seismometers by rotation. The correction improves the ability of some instruments to observe spheroidal modes down to ${}_0S_4$. We demonstrate this method using 15 broadband ocean bottom seismometers from the PI-LAB array. We measure normal mode peak frequency shifts and compare with 1-D reference mode frequencies and predictions from 3-D global models. Our measurements agree with the 3-D models for modes between ${}_0S_{14}$ – ${}_0S_{37}$ with small but significant differences. These differences likely reflect real Earth structure. This suggests incorporating ocean bottom normal mode measurements into global inversions will improve models of global seismic velocity structure.

Production Editor:
Gareth Funning
Handling Editor:
Danielle Sumy
Copy & Layout Editor:
Hannah F. Mark

Received:
July 1 2022
Accepted:
September 16 2022
Published:
November 2 2022

1 Introduction

Earth's free oscillations or normal modes provide important seismic observational constraints on the Earth's elastic and anelastic structure from the core to the upper mantle (Masters and Widmer, 1995). These oscillations group into radial, spheroidal, and toroidal modes. Spherically averaged measurements of the frequency and width (or amplitude and phase) of mode spectral peaks observed after large earthquakes can be inverted to investigate the 1-D structure of the Earth (e.g., Gilbert and Dziewonski, 1975; Dziewonski and Anderson, 1981), while details of mode splitting reveal long-wavelength three-dimensional variations (Masters et al., 1982; Smith and Masters, 1989; Woodhouse and Dziewonski, 1984). Normal mode data can also be combined with other complementary seismic phases and waveforms to invert for higher resolution 3-D Earth models (e.g., Dziewonski and Anderson, 1981; Moulik and Ekström, 2014; Ritsema et al., 2011). At the lowest frequencies ($f < 1$ mHz) measurements of relatively few earthquakes on relatively few but nevertheless globally well-distributed very-broadband seismic stations suffice to sample the three-dimensional structure of the Earth reasonably well. However, observations of

higher-frequency normal modes, that sample shorter-wavelength Earth structure, require networks of instrumentation on finer spatial scales. Although permanent land stations have been installed on many ocean islands, the ambient-noise conditions are sometimes less than ideal. In addition, ocean island coverage is sparse. The U.S.-operated global seismograph network (GSN) reached its design goal with maximum global coverage in 2004 with plans to expand GSN to more seafloor locations (Kohler et al., 2020), but many regions remain under-sampled (Butler et al., 2004). 70% of the Earth's surface is covered by oceans. Therefore, further progress in station coverage requires the deployment of ocean bottom seismometers (OBS). High-end very-broadband OBSs have been deployed in seafloor boreholes (Stephen et al., 2003) or buried cabled arrays (Duennebie et al., 2002) using ROVs. Alternatively, free-fall OBSs can be deployed on the seafloor from ships. In this case the instruments fall through the water and then record autonomously for about 1 year before returning to the surface for recovery. Typically, OBSs are deployed for targeted regional studies, using instrumentation that is often not sensitive to seismic signals at frequencies below 1 mHz. However, a growing number of deployments with broadband, high-fidelity sensors to periods 120 s or longer means that the

*Corresponding author: Nicholas.harmon@whoi.edu

normal mode coverage gaps in the ocean are becoming filled.

Several studies reported observations of spheroidal normal modes on vertical components of very broadband OBS as the vertical components tend to be quieter than the horizontal components (Bécel et al., 2011; Deen et al., 2017; Laske, 2021). Normal modes were reported in data recorded by free fall instruments in the Lesser Antilles using Scripps-designed OBSs equipped with Nanometrics Trillium T-240 broadband seismometers (Bécel et al., 2011). The instruments recorded the $M_w=8.1$ April 1, 2007 Solomon Islands event, and low-frequency modes were observed down to ${}_0S_6$ ($f = 1.04$ mHz). Another study, using the same type of OBSs in the Rhum-Rhum experiment in the Indian ocean, consistently recorded normal modes in Earth's Hum band between 2.49 – 4.5 mHz throughout the year-long deployment from 2012 to 2013 (Deen et al., 2017). Observation of these modes was possible after applying deglitching of electrical noise, caused by the leveling cycles of the seismometer, as well as tilt and compliance corrections (Bell et al., 2015; Crawford and Webb, 2000). In a recent study, Laske (2021) evaluated spheroidal normal mode signals from several large magnitude earthquakes recorded on OBSs deployed as part of the PLUME experiment near Hawaii (Wolfe et al., 2009), the NoMELT experiment in the central Pacific (Lin et al., 2016), and the ALBACORE (Bowden et al., 2016) and ADDOSS (Berger et al., 2016) arrays offshore of California. The Scripps-designed OBSs equipped with the T-240 seismometers were consistently successful at recording spheroidal modes on vertical components, with perhaps surprisingly high signal-to-noise (SNR) levels, although site effects, ocean currents, infragravity waves and/or isolated technical limitations at individual sites generated some variability in the performance. Where direct comparisons were available, however, land-based seismometers yielded substantially better low-frequency spectra than free-fall OBSs. For example, Laske (2021) documented that the land-based GSN observatory station Kipapa, Hawaii (KIP) recorded normal mode ${}_0S_3$ ($f = 0.47$ mHz) for the 28 March 2005 Sumatra-Andaman earthquake, but the 'best' PLUME OBSs recorded high-SNR modes only down to ${}_0S_8$ (1.41 mHz). Hence, it is appropriate to note that all these publications are a manifest that broadband sensors can record spheroidal normal modes, though with some caveats. First, corrections to the data often need to be applied to account for tilt and compliance noise due to the propagation of ocean infragravity waves. Second, the horizontal components needed for measuring toroidal normal modes are generally not useable, although the PLUME records yielded Love wave phase velocity curves for frequencies $f \geq 10$ mHz (Anarde and Laske, 2010).

In this paper we present observations of spheroidal normal modes from a broadband OBS array in the equatorial Mid-Atlantic deployed as part of the Passive-Imaging of the Lithosphere-Asthenosphere Boundary (PI-LAB) experiment and the Experiment to Unearth the Rheological Lithosphere-Asthenosphere Boundary (EURO-LAB) which consisted of 39 OBSs. The OBSs were co-located with 39 magnetotelluric instru-

ments deployed by the Central Atlantic Lithosphere-Asthenosphere Boundary (CA-LAB) experiment. There were also several active source components including the Trans-Atlantic I-Lab experiment (Mehouachi and Singh, 2018). The combined experiments were designed to use methodologies sensitive to a range of resolutions and sensitivities in a single study area beneath seafloor formed at the nearby slow spreading Mid-Atlantic Ridge to image the lithosphere-asthenosphere system and determine what makes a plate, "plate-like." These studies found that the lithosphere-asthenosphere boundary beneath the Atlantic is defined to first order by temperature, but that it is also dynamic and dictated by variations in melt generation and migration (Fischer et al., 2020; Harmon et al., 2018, 2020, 2021; Rychert et al., 2020, 2021; Wang et al., 2019, 2020; Saikia et al., 2021a,b). A number of other studies were possible with the data including, for instance, locating the source regions of infragravity waves (Bogiatzis et al., 2020), local seismicity work (Hicks et al., 2020; Leptokarpoulos et al., 2021, 2022; Schlaphorst et al., 2022), sediment constraints (Agius et al., 2018; Saikia et al., 2020), mantle transition zone imaging (Agius et al., 2021), and the work presented in this manuscript. In the experiment 24 OBSs were equipped with a Nanometrics T-240 broadband seismometers (Fig. 1), and 15 OBSs were equipped with a Nanometrics Trillium Compact wide-band seismometers. The latter 15 OBS are not considered here. Of the 24 broadband OBSs, 15 provided useable data for the purposes of this paper. We present a new means for correcting tilt through a simple rotation rather than the commonly utilized spectral transfer function method (Deen et al., 2017; Crawford and Webb, 2000). We show that in some cases it substantially improves SNR ratios at low frequencies ($f < 3$ mHz). The rotation also conserves the energy on the seismograms without introducing artefacts to the vertical component that can be caused by band-limited spectral multiplication. We also make measurements of frequency shifts of the spheroidal modes and demonstrate that OBS records can be used to contribute to global data sets for improving global estimates of 3-D structure.

2 Methods

We use three component seismogram recordings and Cox-Webb differential pressure gauge (DPG) records (Cox et al., 1984) from Scripps-designed broadband OBSs that are equipped with Nanometrics T-240 seismometers from two OBS pools, Scripps Institution of Oceanography (SIO) and Institut de Physique du Globe de Paris (IPGP). The IPGP equipment are an older generation of the SIO design and have an electrical glitch approximately every hour caused by the leveling schedule. The SIO equipment have a variable leveling schedule, approximately every week for the majority of the deployment. Station names beginning with "I" are from the IPGP pool and those beginning with "S" are from the Scripps pool.

The time series are from two $M_w=7.9$ earthquakes located in Papua New Guinea on December 17, 2016 at 10:51 GMT at 153.52°E, 4.5049°S and 94.5 km depth and

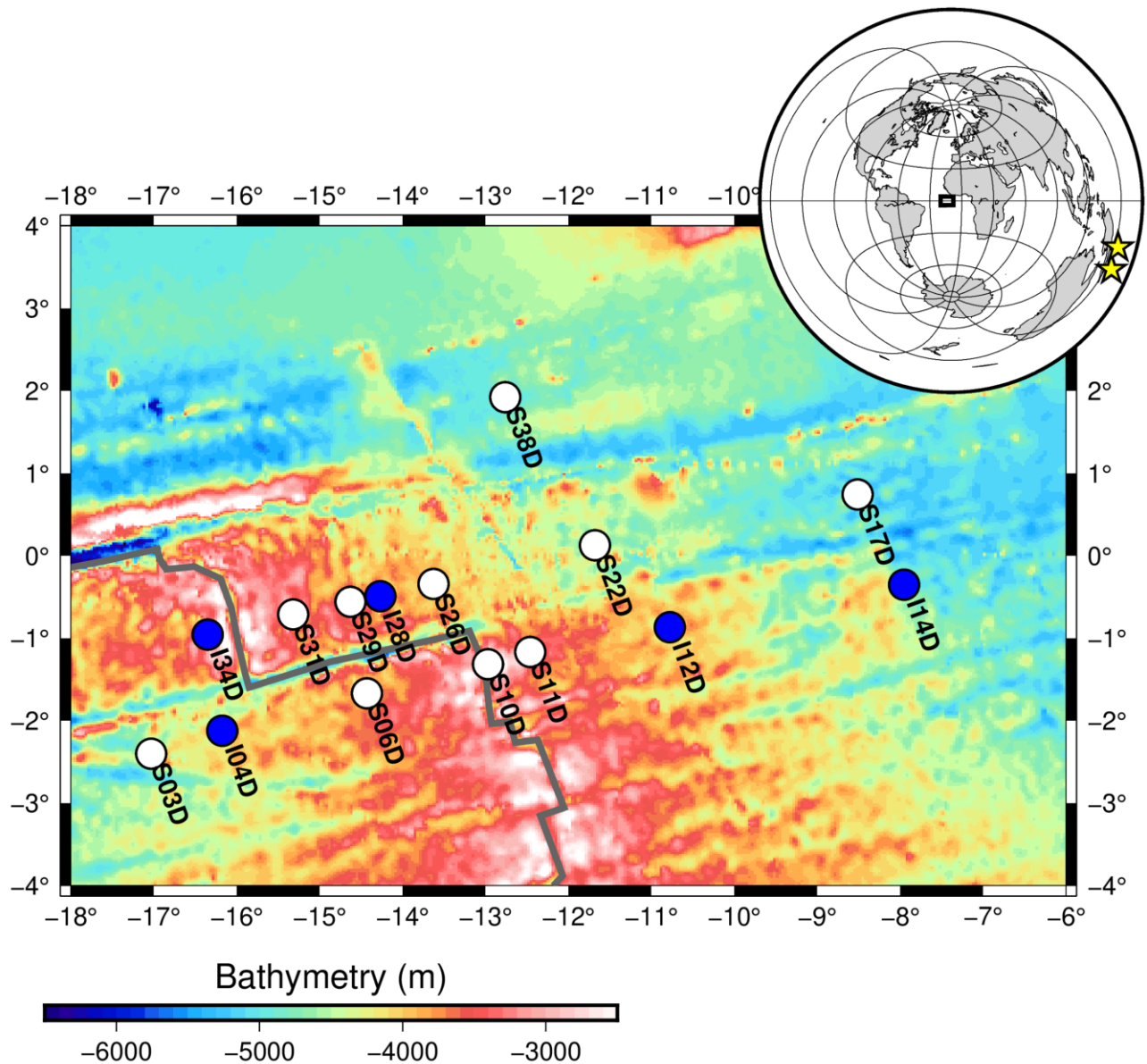


Figure 1 Bathymetry map of the PI-LAB study region. Locations of the T-240 seismometers are shown as circles, white for Scripps Institution of Oceanography instruments, blue for Institut du Physique du Globe instruments. Stations names are as labeled. Grey line shows the location of the Mid-Atlantic Ridge system. Inset map shows the location of the PI-LAB study area (black box) and the location of earthquakes used in this study (yellow stars).

on January 22, 2017 03:07 GMT at 155.1718°E , 6.2463°S and 135 km depth (Fig. 1 inset). We use time series that begin 5000 s before the event origin time and last for two days after the origin time.

We pre-process the IGP data to remove the electrical leveling glitch using a comb filter and following a similar method to Deen et al. (2017). We first identify a target glitch waveform during a quiet period (Figs. 2, 3). This waveform is then correlated with the entire waveform to identify the time range of each glitch in the time series. We search in all time periods where we expect the glitch to occur, i.e., every hour. For each glitch time range we solve for the best fitting amplitude of the target glitch waveform and subtract it from the waveform. A detailed example of the deglitching is showing in Figure 3.

We determine the tilt of the vertical component for all stations. We assume the tilt is static for the duration of the time window of our normal mode analysis. Even though tilt may change through time, especially after a re-leveling cycle of the OBS, our static tilt assumption is likely valid. Our analysis time periods are chosen to roughly fall in between leveling cycles to avoid those time periods. Therefore, the resulting tilt corrections are typically consistent through time for each instrument (Tables 1, 2). We bandpass filter the raw data between 0.1 – 10 mHz for one day of quiescent data approximately two days after the main event. We then search for the best-fitting tilt from vertical and azimuthal rotation angle, i.e., azimuthal direction of tilt, that minimizes the root-mean-square of the rotated vertical com-

ponent. Specifically, we apply an azimuthal rotation for the BH1 and BH2 horizontal components into a radial (in the azimuthal direction of the tilt) and transverse (perpendicular to the azimuthal direction of the tilt) component for a potential tilt direction. No information about the true orientation of the instrument's horizontal components is required. We then apply a vertical – radial component rotation to minimize the energy on the rotated vertical component. Once these angles are determined the rotation is applied to the raw data to determine the tilt corrected data. We then estimate a compliance correction to the vertical component using the spectral transfer function method between the differential pressure gauge record (DPG) and the tilt corrected vertical component. We use the same day-long time series (Crawford and Webb, 2000) used in the tilt estimations. The transfer function is used to estimate a predicted vertical component from the DPG record, which is then subtracted from the tilt corrected vertical component. We apply the compliance correction in the frequency band where the coherence between the pressure and tilt corrected vertical component is > 0.8 . The instrument response is then removed, and the velocity seismograms are differentiated to acceleration. Acceleration records are used as opposed to velocity or displacement for two reasons: 1) the community's normal mode theory is based on acceleration and 2) the amplitudes at ultra-low frequencies are suppressed, i.e., those where we usually see increased noise levels because they are beyond the frequency roll-off of almost all seismometers.

We then estimate the normal mode spectra from the vertical components of the events. First, we apply a 4th order Butterworth filter with a 0.3 mHz high pass corner frequency. We choose a time window that begins 5000 s before the origin time and ends two days after the origin time. This window is optimal because it includes as many stations as possible, while avoiding the variable leveling cycles of the Scripps instruments. We then estimate the spectra using a single Slepian taper (NW=2, with 1 taper used). This is similar to using a single Hanning window, which has been successfully used in previous studies (e.g. Masters and Widmer, 1995). We compare the spectra of the resulting data, i.e., with the instrument response, glitch, tilt, and compliance corrections applied, to the spectra of data that have had just the instrument response removed and a high pass filter applied. We will refer to the first case as “corrected,” and the second case as “uncorrected.”

To assess the effects of the seismogram corrections on normal mode observables, we measure normal mode peak frequencies, at each of the PI-LAB stations, for each weakly coupled mode between ${}_0S_9$ and ${}_0S_{40}$. The procedure is interactive, where we fit a decaying cosine function to the corresponding spectral peak in a least-squares fitting process. To compute the mode spectrum for a specific mode, we use an optimal window length corresponding to Q-cycles of a mode (Dahlen, 1982), the time within which the mode decays to $1/e$ of its initial amplitude. A Hanning taper is applied. A successful fit and removal of the cosine function leads to a residual spectrum with a ‘clean hole’

left in the spectrum that allows the analyst to assess whether or not a fit was successful or if the measurement has to be discarded. In the latter case, the synthetic mode has a realistic frequency but unrealistic attenuation, and the residual spectrum has remaining spectral peaks adjacent to the synthetic mode. Reasons for unsuccessful fits include noisy signals and the presence of other modes. This mode measurement method was used by Smith and Masters (1989) to explore long-wavelength 3-D structure in the mantle. The underlying principle here follows the assumption that a mode frequency shift that is measured at a recording station is caused by structure only along the source-receiver great circle, and is represented by structure at the two poles of that great circle (Backus, 1964). Even though an isolated mode ${}_0S_1$ is sensitive to structure of harmonic degree up to $s=2l$, asymptotic peak shift theory is a valid approximation only as long as $s \ll l$. A second caveat to this theory is that second-order effects introduce a ‘jitter’ in the frequency measurements that depends on epicentral distance (Dahlen and Tromp, 1998). For these reasons, asymptotic peak shift theory and associated work fell out of favor and is currently not typically pursued. However, the interactive measurement technique is suitable for initial quality assessment and to explore the internal consistency of normal mode data measured on PI-LAB OBS records. Therefore, we apply it here.

3 Results

We present time domain vertical component waveforms for the 2016 event for three representative stations, I28D, S11D and S17D to illustrate the data quality and the effects of the deglitching and tilt corrections. We present I28D to illustrate the leveling glitches. S11D is a quiet station with little to no tilt. S17D is a station that has a high tilt, 0.89° . The noise levels are visibly low for the vertical component for all three stations prior to the event in the uncorrected data (Fig. 2, black lines) and in the corrected data (Fig. 2, orange lines). In addition, the Rayleigh wave orbits (Fig. 2, R1 – 9) are visible on S11D, which is a particularly quiet station. The Rayleigh wave orbits are less visible on S17D in the uncorrected data as there are several transient high noise time periods visible, an example of which is indicated by the blue arrow above the record. In the corrected data, these transients are substantially reduced, in particular near the blue arrow. In general, the corrections have a minimal impact on the amplitude of the observed phases, reducing the amplitude within R1 by $< 10\%$ for S17D, and by 3 – 4% for S11D. For I28D, two of the leveling glitches are indicated by cyan arrows above the traces, although several others are visible in the record. The effect of the corrections greatly reduces the amplitude of the glitches in comparison to those of the uncorrected data (orange vs. black lines, respectively), although the tilt noise is relatively low for this station, and there are no noise transients visible away from the glitches as in S17D. Greater deglitching detail is shown in Figure 3. Figure 3 highlights the contamination of the glitches on measurements of the modes. Many of the glitch harmonics (black stars) occur at frequen-

Station	Tilt Azimuth (Relative to North) °	Tilt Angle From Vertical °
S03D	321.87	0.48
S06D	107.25	0.40
S10D	76.91	0.18
S11D	308.40	0.13
S17D	288.97	0.89
S22D	154.27	0.17
S26D	118.11	0.18
S29D	245.43	0.16
S31D	225.19	0.23
S38D	94.07	0.09
I04D	42.93	0.07
I12D	34.08	0.02
I14D	54.32	0.09
I28D	46.52	0.05
I34D	61.07	0.07

Table 1 Tilt Corrections for Mw = 7.9, 2016-12-17T10:51:10, Papua New Guinea

Station	Tilt Azimuth (Relative to North) °	Tilt Angle From Vertical °
S03D	311.90	0.65
S06D	115.30	0.46
S10D	77.46	0.19
S11D	298.18	0.09
S17D	288.80	0.91
S22D	154.90	0.14
S26D	119.80	0.20
S29D	243.89	0.19
S31D	224.71	0.19
S38D	92.87	0.11
I04D	34.05	0.07
I12D	41.94	0.02
I14D	54.26	0.09
I28D	46.01	0.05
I34D	65.93	0.07

Table 2 Tilt Corrections for Mw = 7.9, 2017-01-22T04:30:22, Papua New Guinea

cies near fundamental-mode frequencies (thin vertical black lines). The noise levels after deglitching also increase at frequency < 2 mHz, likely due to imperfect glitch removal. Although a correction for compliance due to infragravity waves using the pressure component (Webb and Crawford, 1999) is applied to all of the data, its magnitude is very small for the time period of the two events.

We show the effect of the tilt corrections on the spectra for station S17D for the 2016 event in Figure 4. The spectra from uncorrected data are shown in black and the tilt corrected waveforms are in orange. Spectral peaks associated with most of the zero order modes, with global average frequencies (Masters and Widmer, 1995), indicated by thin vertical lines, can be seen in the uncorrected and corrected data above 2.75 mHz. For the uncorrected spectra the peaks are clearly visible as low as 1.75 mHz, although the spectra have a high noise background, around 0.5×10^{-13} m/s²/Hz, at frequencies lower than 2.75 mHz. This high noise background obscures many of the smaller peaks associated with modes between ${}_0S_{10}$ to ${}_0S_{19}$. The corrected spectra have a much lower noise background in general, particularly below 2.75 mHz with a noise floor of $\sim 1 \times 10^{-16}$ m/s²/Hz (orange line, Fig. 4). Peaks associated with ${}_0S_6$ to ${}_0S_{19}$ and other

modes are visible, standing clearly out from the background. In the corrected records, the amplitudes of some of the modes above ${}_0S_{19}$ are reduced relative to the uncorrected spectra, by up to 28% in some cases (${}_0S_{19}$). In other words, the correction has minimized the background noise, which is a similar order of magnitude in the 1.5–2.5 mHz band to the modes, in the instrument uncorrected spectra (black lines).

We also compare the results of the rotational tilt correction and spectral compliance correction presented here to the results using the spectral tilt and compliance correction method (Bell et al., 2015; Crawford and Webb, 2000) for station S17D in Figure 4b (cyan line). We use a variation of the method that employs a grid search of tilt azimuth for the highest average coherence in the frequency band of interest between a test radial component for the direction of tilt and the vertical (Bell et al., 2015). It shows a similar improvement to the rotational tilt correction presented here above 1 mHz. However, the spectral method performs worse at reducing noise at < 1 mHz, likely due to lower coherence in the lowest frequencies. The same is true at other stations with less tilt (Figs. S1 and S2).

The corrected normal mode spectra are shown for all useable stations from the array for the 2016 event

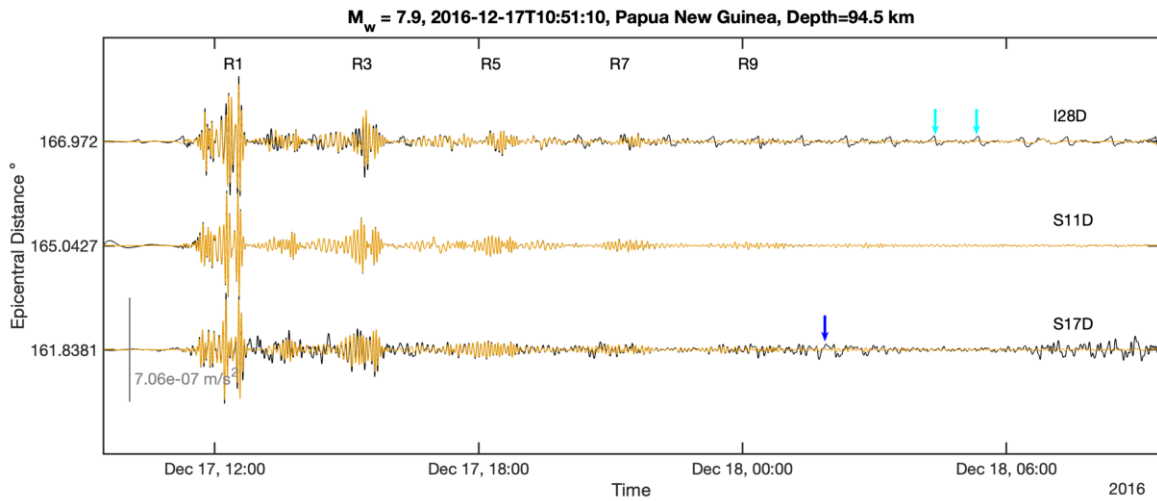


Figure 2 Example acceleration seismograms from the 2016 event used in this study. The seismograms are plotted as a function of epicentral distance in degrees, indicated on the y-axis. Scale bar for the amplitude of the seismograms is given (grey vertical line). Black seismograms show uncorrected seismograms (only instrument response removed and high pass filter applied), while orange lines show corrected seismograms. The seismograms have been filtered between 0.3 – 10.0 mHz. Station names are given above each trace. Theoretically predicted minor arc (odd) R1-R9 arrivals are indicated. Major arc (even) arrivals are not indicated as they arrive shortly before subsequent minor arc arrivals due to the large epicentral distance. Cyan arrows indicate two example leveling glitches on the I28D stations. Blue arrow indicates a region where tilt correction removes a substantial amount of noise.

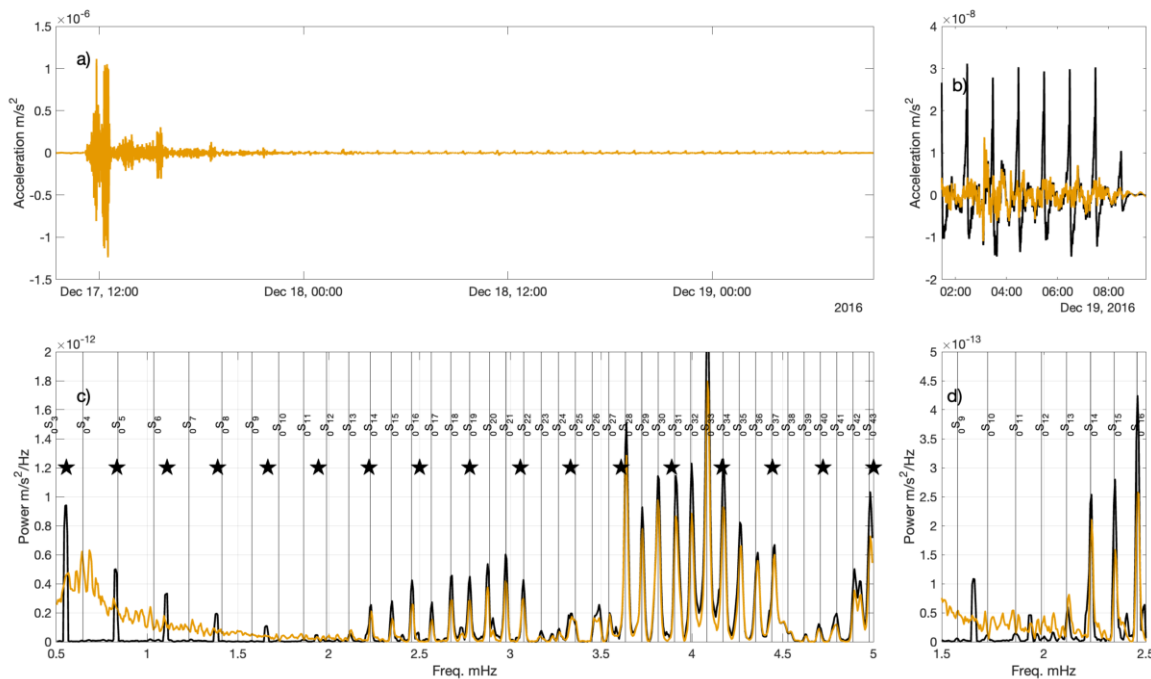


Figure 3 Leveling glitch correction for station I34D. Black lines show the uncorrected data and orange lines show the corrected data. a) The time series over a 48 hour period and b) a zoom of an 8 hour period are shown. c) The spectra from 0.5-5.0 mHz and d) a zoom from 1.5-2.5 mHz are shown. Black stars indicate the location of hourly harmonics from the leveling glitch. Global average fundamental mode frequencies are shown by thin vertical lines, and modes are labeled at amplitude = 1.5 (Masters and Widmer, 1995).

(Fig. 5) and the 2017 event (Fig. 6). The tilt corrections applied to each station for each event are given in Tables 1 and 2, respectively. The records show very consistent peaks for the zero order spheroidal modes, especially above ${}_0S_{11}$ for the 2016 event, while for the 2017 event peaks are consistently observed above ${}_0S_{14}$.

In the 2016 event a strong beating pattern is observed in all the records that becomes broader and shifts toward higher frequencies with increasing epicentral distance. This is the predicted behavior of the amplitudes of the zero order spherical harmonics at a given distance from the source to its pole (Laske and Widmer-

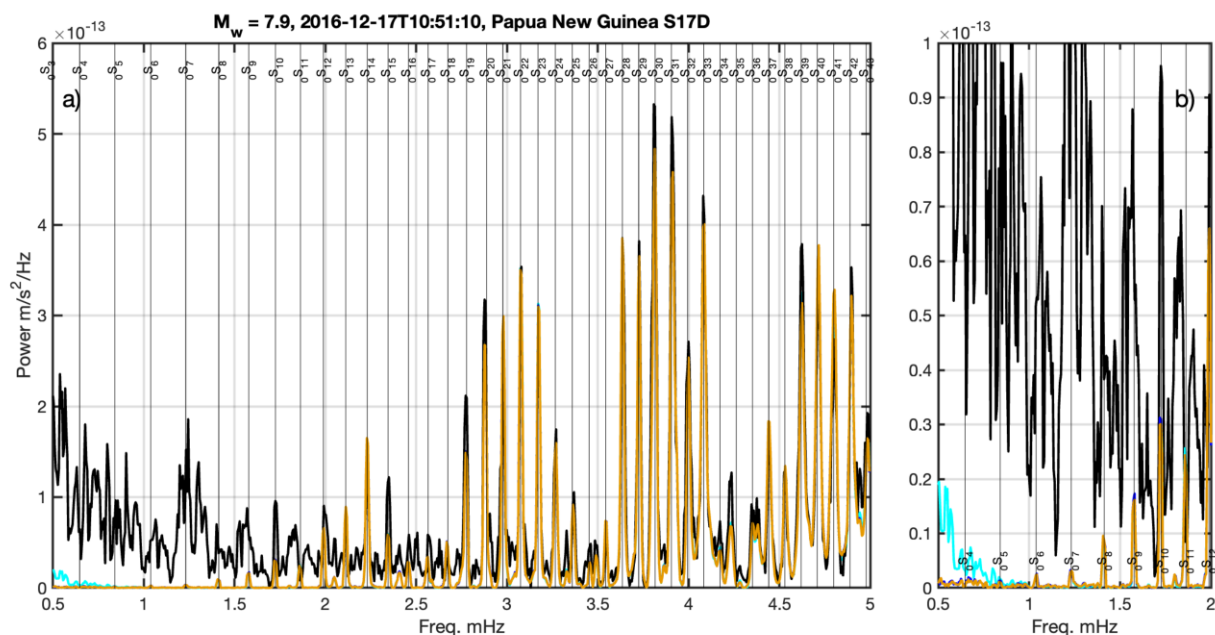


Figure 4 Example spectra after the application of tilt and compliance corrections for the 2016 event to station S17D which had a tilt of 0.89° . a) The spectra from 0.5-5.0 mHz and b) a zoom of 0.5-2.0 mHz are shown. In both panels, the black lines show the spectra of the uncorrected data. The blue line (for instance, visible in b) near ${}_0S_4$ behind the orange line) shows the tilt response corrected data. The orange line shows the tilt and compliance corrected data. The blue and orange lines are nearly identical, with the largest difference (7%) observed at ${}_0S_9$. The cyan line shows the result from the spectral tilt correction (Bell et al., 2015; Crawford and Webb, 2000). Global average fundamental mode frequencies are shown by thin vertical lines, and modes are labeled (Masters and Widmer, 1995)

Schmidrig, 2015). In other words, each station spatially samples the modes slightly differently depending on its epicentral distance to the event because adjacent modes with similar wavelengths come into and out of phase with each other. This beating pattern is less visible in the 2017 event. The lowest zero order mode observable in the data set is ${}_0S_4$, which is observed at S29D for the 2016 event, and ${}_0S_5$, which is observed at several stations for the 2017 event. In detail several other modes are visible in the spectra as smaller peaks adjacent to the zero order modes. In general, the IPGP stations are noisier by an order of magnitude or more, especially at frequencies below 2 mHz. This is mostly due to imperfect removal of the leveling glitches, which have strong harmonics in this frequency range (harmonic locations indicated by black stars, Fig. 3). IPGP records above 2 mHz are comparable to the SIO stations.

All the measurements for the array for modes ${}_0S_{14}$ and ${}_0S_{23}$ are displayed in Figure 7. We observe a surprisingly complex pattern of frequency shifts across the network, and hypothesize based on modelling work that long-wavelength 3-D structure can cause such variations. For this comparison, we compute normal mode structure coefficients, c_s^t for mantle model S20RTS (Ritsema et al., 1999) but include harmonic degrees only up to $s = 12$ to compute predicted peak shifts. Even then, the patterns in the theoretical peak shifts are quite complex, and exhibit similarities with our observed peak shifts. Note that the frequency shifts are plotted at the stations, while using asymptotic peak shift theory implies that associated structural variation would be located at the two

source-receiver great circle poles, which are broadly located in northern Russia (about $65^\circ\text{N}/75^\circ\text{E}$) and in the Southern Ocean east of the Antarctic peninsula (about $65^\circ\text{S}/105^\circ\text{W}$).

Measurements for other modes are not as internally consistent, but we can still assess overall average mode frequency observations across the array. These are shown in Figure 8. We omit measurements for modes that are strongly coupled to toroidal modes, ${}_0S_{11}$, ${}_0S_{18}$ and ${}_0S_{19}$. We take two sets of measurements, one on the raw seismic records, and one on the rotation and compliance corrected seismograms. We find that the correction does not change overall averages to a significant level. In fact, measurements for modes of angular order $l < 20$ may exhibit smaller standard deviations, indicating a more internally consistent set of measurements.

4 Discussion

The deglitching we perform on the IPGP instruments is effective. Without the correction there are strong harmonics in the data that interfere with the normal modes, making clear analysis difficult (black lines, Fig. 3). After the correction the leveling glitch harmonics are greatly reduced in the spectra, and the normal modes stand out better (orange lines, Fig. 3). We observe small artifacts in our time domain waveform due to the leveling glitch removal, which may explain why noise remains relatively high at the lowest frequencies. The IPGP station noise levels are higher than the SIO station noise levels below 2 mHz even after applying the

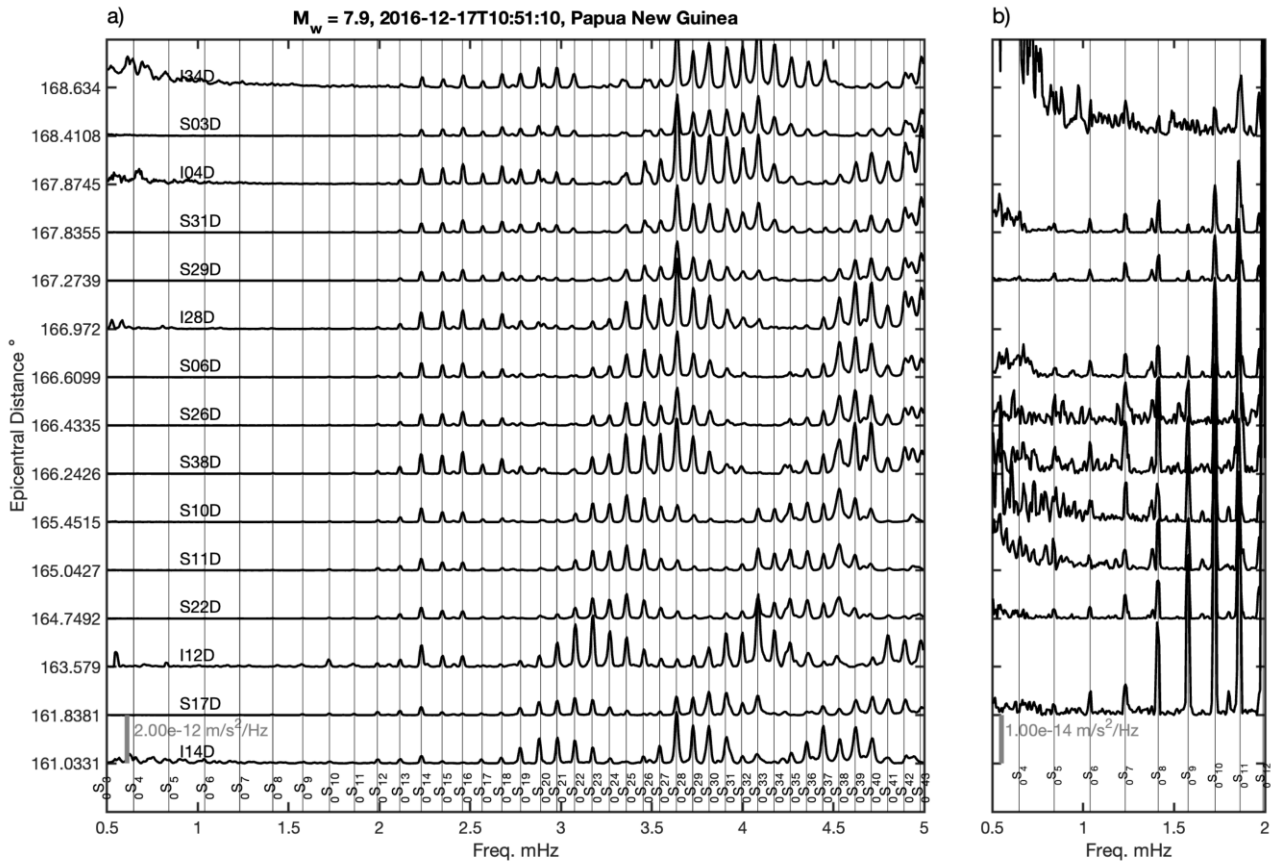


Figure 5 Compiled spectra for all useable stations for the 2016 event. a) The spectra as a function of epicentral distance indicated on the y-axis over the 0.5-5.0 mHz range and b) a zoom into the 0.5-2.0 mHz range are shown. Stations are labeled and a scale bar (grey vertical line) is given in each panel. Global average fundamental mode frequencies are shown by thin vertical lines, and the modes are labeled (Masters and Widmer, 1995). In panel b) stations with high noise are excluded from the plot.

deglitching correction (Fig. 5 and 6). Our findings are similar to previous work (Deen et al., 2017), which found similar success in removing the leveling glitches. Our result suggests that data from earlier deployments with the same leveling glitches might be used for future normal mode studies at least above 2 mHz.

The corrections applied here allow us to observe modes at a similar range observed in previous OBS data, but they also improve the number of stations that observe the lowest modes. We observe spheroidal modes down to ${}_0S_4$ or ${}_0S_5$ depending on the instrument. This is similar to reports from deployments using similar instrumentation, which observe spheroidal modes down to ${}_0S_4$ (Bécel et al., 2011; Laske, 2021). Our quietest station (S29D) yields the widest frequency band of observation and is comparable to the performance of the same type of instrument in numerous other ocean bottom deployments. Given the large number of usable stations and the routine observations of spheroidal modes to ${}_0S_9$ at 9 out of 15 stations for the 2016 event and 10 out of 15 stations for the 2017, we are able to make estimates of frequency shifts relative to 1-D reference mode frequencies (Masters and Widmer, 1995) over ${}_0S_9 - {}_0S_{40}$. Although the lowest modes observed are similar to pre-

vious work, the corrections allow us to observe lower modes at several stations that would otherwise not have been possible, which we describe in the next three paragraphs.

The simple rotation to correct for tilt presented here offers an effective alternative to the commonly used spectral tilt correction (Crawford and Webb, 2000) for reducing long period noise. The advantage of this method is that it conserves energy across all three components and across all frequencies as it rotates the energy between the components. The spectral domain tilt correction is typically only applied in a frequency band where the coherence is high between the vertical and horizontal components, and so may only improve SNR in this band. The rotation tilt correction provides the greatest noise reduction below 3 – 3.5 mHz in the example shown in Figure 3, in which the noise floor is reduced by 2 – 3 orders of magnitude. Similar performance below 3 mHz is observed at several other stations. Below 1 mHz, the rotational method outperforms the spectral tilt correction. Tilt angles from the vertical component estimated for the stations used here range from 0.91° to 0.02° for the two events. Unfortunately, the tilt correction is not successful at enhancing SNR on

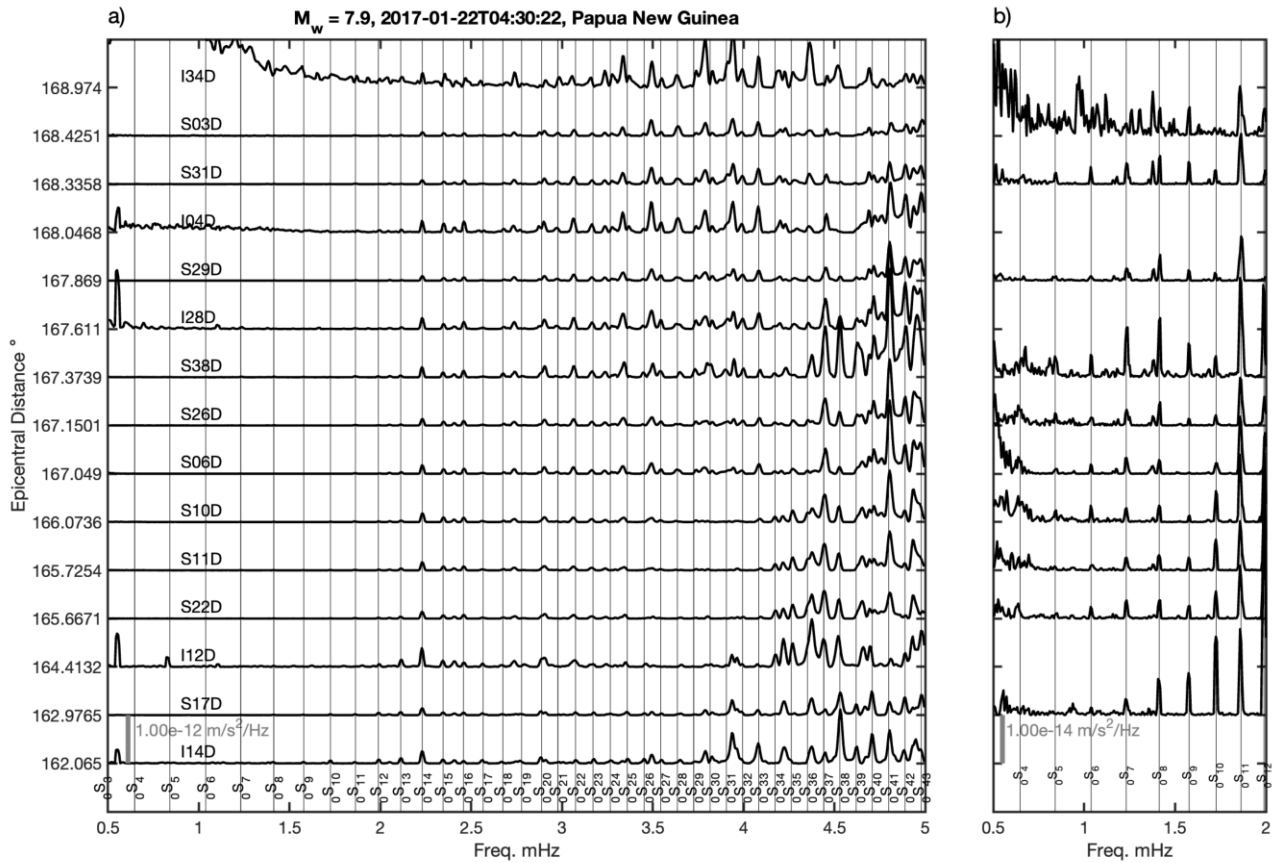


Figure 6 Compiled spectra for all useable stations for the 2017 event. a) The spectra as a function of epicentral distance are indicated on the y-axis over the 0.5-5.0 mHz range and b) a zoom into the 0.5-2.0 mHz range are shown. Stations are labelled and an amplitude scale bar (grey vertical line) is given in each panel. Global average fundamental mode frequencies are shown by thin vertical lines, and modes are labelled (Masters and Widmer, 1995). In panel b) stations with high noise are excluded from the plot.

the horizontal components for these events. However, future deployments may yield toroidal modes in quieter settings. The pressure correction that is required is very small and, in most cases, has little effect on the SNR of the normal mode spectra. The small correction is likely due to the low infragravity wave conditions for most of December 2016 and January 2017 (Bogiatzis et al., 2020).

The leveling glitch correction applied here shows some improvement in comparison to previous work. One-hour harmonics were deleted in the spectra shown in Bécel et al. (2011) from the leveling glitches, effectively eliminating information at the frequency of the glitches. The corrections we use here greatly reduce these harmonics without deleting sections of the data. Using the correction approach of this work the glitch harmonics, i.e., the peaks in between the 1-D reference mode frequencies (Harmon et al., 2021) (black lines at < 2 mHz, Fig. 3) are not visible in the orange lines, but our spectra maintain information at these frequencies. The performance of our method is similar to the performance reported in Deen et al. (2017). These corrections are needed to measure normal modes using data with glitch harmonics.

The tilt correction lowers the noise floor at low fre-

quencies, effectively allowing mode observations and measurements. The noise floor at < 2.75 mHz is high in previous work (Bécel et al., 2011; Laske, 2021), likely due to tilt, increasing by up to 20 dB below 1 mHz. This high noise floor below 2.75 mHz is visible in other deployments as well, for example several stations (e.g. PL05, PL35) from the PLUME experiment (Laske, 2021). The tilt correction effectively removes similar noise in our study (black vs. orange lines in Fig. 4), again facilitating observation and measurement of the modes at frequencies below 2.75 mHz. This tilt noise likely exists in data from other previous experiments. Therefore, mode observation and measurement can likely be improved for this previous data.

Comparison of our mode frequency shifts to the 1-D reference mode frequencies (Masters and Widmer, 1995) highlights important deviations that reflect unaccounted for Earth structure. In comparison to the 1-D reference mode frequencies we find deviations that increase with increasing angular order l (Masters and Widmer, 1995). This indicates structural deviation from the underlying 1-D reference model for our sampled source-receiver great circles. These deviations are likely related to structural heterogeneity in the up-

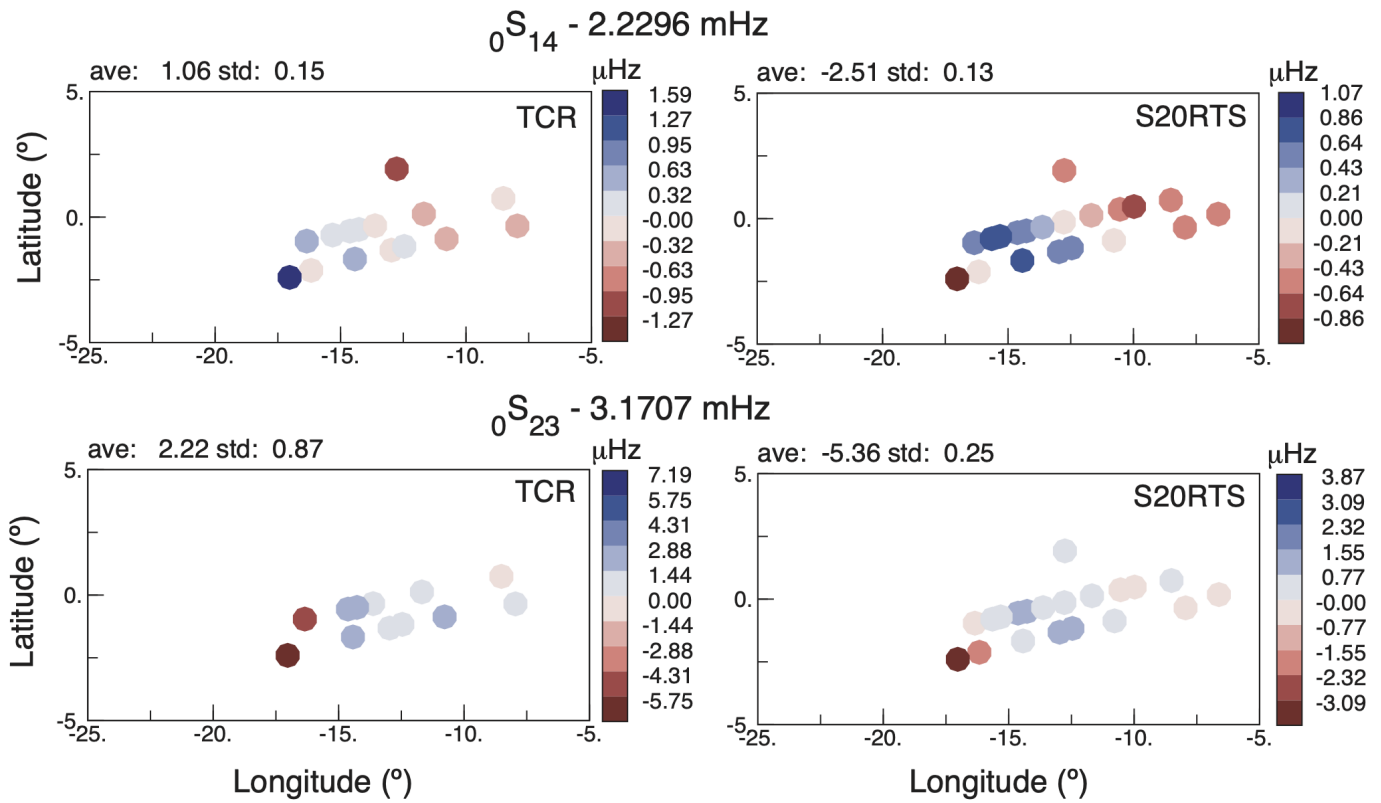


Figure 7 PI-LAB peak shift measurements for modes ${}_0S_{14}$ and ${}_0S_{23}$ (left column, tilt, compliance, and rotation correction) and corresponding predictions for model S20RTS (Ritsema et al., 1999) (right column) relative to the global 1-D reference mode frequencies of Masters and Widmer (1995). Earth’s hydrostatic ellipticity has not been considered in the predictions for model S20RTS. The averages of the measurements were removed before plotting (upper left of panels). Measurements are plotted at the respective PI-LAB station locations. The titles identify the mode names and the average mode frequencies from Masters and Widmer (1995).

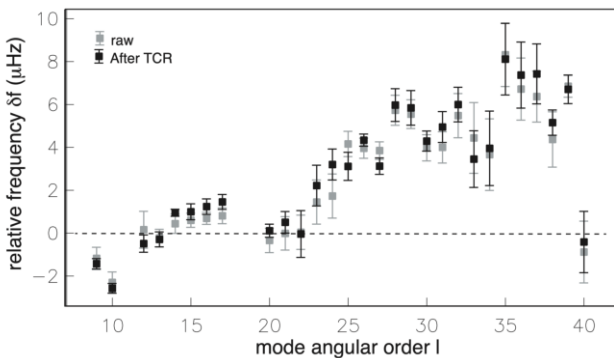


Figure 8 Averages of PI-LAB mode frequencies relative to those of Masters and Widmer (1995). Grey: raw measurements; black: after tilt, compliance and rotation correction (TCR). Error bars denote the standard deviation in the measurements taken across the network.

per mantle rather than in the lower mantle as modes around ${}_0S_{30}$ reach only into the mantle transition zone, but not beyond.

Ultimately, we want to compare our mode frequency shift results with 3-D global velocity model predictions (Masters et al., 2000; Ritsema et al., 1999), for consistency. The predictions for 3-D global velocity model S20RTS are shown in Figure 9 (blue diamonds). Inspection of our results compared to 3-D model predic-

tions indicates a discrepancy of a DC shift of $\sim 5 \mu\text{Hz}$. The discrepancy can be explained by the need to account for hydrostatic ellipticity in the predictions. Ellipticity has a significant effect that increases with angular order l , when compared to the 1-D reference mode frequencies (brown diamonds in comparison to black dashed line, Fig. 9) (Masters and Widmer, 1995). The predicted frequency shifts for S20RTS without ellipticity (blue diamonds) are smaller and mostly negative than those including the ellipticity correction (black squares). However, the two have very similar shapes given the nearly linear shape of the ellipticity correction. We also compare PREM (Dziewonski and Anderson, 1981) to our 1-D reference mode frequencies (Masters and Widmer, 1995) and find relatively small deviations (grey diamonds vs. black dashed line, Fig. 9).

Our results compare favorably with two global models: S20RTS (Ritsema et al., 1999), including the ellipticity correction, and SB4L18 (Masters et al., 2000), including the ellipticity correction in the range $14 \leq l \leq 37$. This suggests that we are recovering information about real Earth structure (Fig. 10). At lower angular orders, $9 \leq l \leq 14$, the agreement between our result and the two 3-D models is poor, suggesting our observations may not be as reliable for determining Earth structure for $l \leq 14$. We find good general agreement between our model, S20RTS, and SB4L18 at $15 \leq l \leq 20$. From $21 \leq l \leq 32$ our result agrees better with predictions from S20RTS, al-

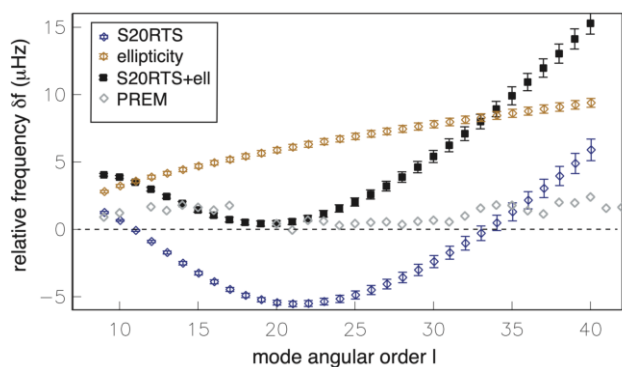


Figure 9 Averages of predicted mode peak shifts relative to those of Masters and Widmer (1995). Predicted mode frequencies are computed at all PI-LAB stations before averaging. We present a 3-D model S20RTS (blue diamonds) (Ritsema et al., 1999), Earth’s hydrostatic ellipticity (orange diamonds), and the sum of the two (S20RTS+ell, black squares). Grey symbols mark frequency differences to Masters and Widmer (1995) computed for PREM (Dziewonski and Anderson, 1981) as published in Masters and Widmer (1995). The sum of PREM and S20RTS+ell is similar in magnitude and shape to the observations in Figure 8 and 10, indicating the need for the ellipticity correction.

though not consistently within error. From $33 \leq l \leq 37$ we find better agreement between our result and the predictions from SB4L18, typically within error. At $l > 37$, the differences between our result and the predictions from the 3-D models are large, suggesting that our result does not represent real Earth structure. The small but significant variations found between our observations and the two global models at $21 \leq l \leq 32$ indicates that incorporating information from OBS arrays such as ours into global normal mode inversions might improve our knowledge of Earth structure.

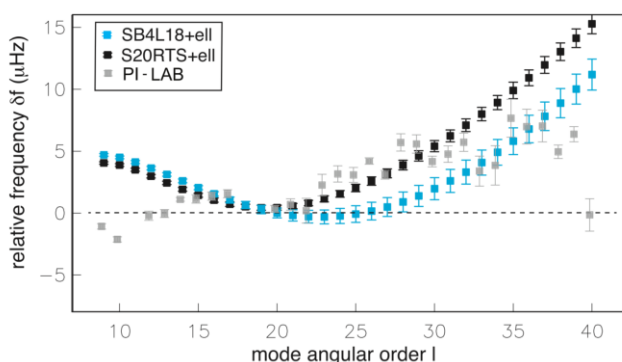


Figure 10 Averages of predicted mode peak shifts relative to those of Masters and Widmer (1995). These are shown for S20RTS (black symbols) (Ritsema et al., 1999) and SB4L18 (blue symbols) (Masters et al., 2000) both with Earth’s hydrostatic ellipticity included (+ell). Grey symbols mark observations from PI-LAB shown in Figure 8 from the corrected data.

5 Conclusion

Broadband OBS can help to deepen our understanding of the interior of the Earth via normal mode observations by filling in the current gaps in global station coverage. We provide a new tilt correction technique using a simple rotation to improve observations at low frequencies that will be useful for recovering lower modes at additional stations as well as for other types of seismic observations. We present some of the first measurements of frequency shifts from a broadband ocean bottom seismic array, that could be combined with other global observations to invert for three-dimensional Earth structure. Very broadband OBS are more expensive than more band limited instruments. However, installing very broadband instruments is preferable given that the data can be corrected to measure normal modes, filling in gaps in global observations, and improving constraints on Earth structures. This is especially true given the expense, time, effort, and logistical challenges involved in any seagoing expedition.

Acknowledgments

We thank the captain and crew of the R/V Marcus Langseth and the RRS Discovery and also the scientific technicians of the Scripps, Lamont Doherty and INSU pools. C.A.R. and N.H. were funded by the Natural Environment Research Council (NE/M003507/1) (PI-LAB) and the European Research Council (GA 638665) (EURO-LAB). G. L. was funded by NSF grant OCE1830959. We used data from the XS network (https://doi.org/10.7914/SN/XS_2016) (Rychert et al., 2016).

Data Availability

Data is archived in the IRIS DMC and will be restricted until funding on EURO-LAB ends. Rotation code is available with this publication in the supplemental material and at <https://doi.org/10.5258/SOTON/D2394>.

References

- Agius, M., Harmon, N., Rychert, C., Tharimena, S., and Kendall, J. Sediment Characterization at the Equatorial Mid-Atlantic Ridge From P-to-S Teleseismic Phase Conversions Recorded on the PI-LAB Experiment. *Geophysical Research Letters*, 45, 2018. doi: 10.1029/2018GL080565.
- Agius, M., Rychert, C., Harmon, N., Tharimena, S., and Kendall, J. A thin mantle transition zone beneath the equatorial Mid-Atlantic Ridge. *Nature*, 589(7843):562–566, 2021. doi: 10.1038/s41586-020-03139-x.
- Anarde, K. and Laske, G. A Joint Rayleigh and Love Wave Analysis for the Hawaiian PLUME. In *Project AGU Fall Meeting*, San Francisco, 2010.
- Backus, G. Geographical interpretation of measurements of average phase velocities of surface waves over great circular and great semi-circular paths. *Bull. Seis. Soc. Am*, 54(2):571–610, 1964. doi: 10.1785/bssa0540020571.
- Bell, S., Forsyth, D., and Ruan, Y. Removing Noise from the Vertical Component Records of Ocean-Bottom Seismometers: Results

- from Year One of the Cascadia Initiative. *Bull. Seis. Soc. Am*, 105(1):300–313, 2015. doi: 10.1785/0120140054.
- Berger, J., Laske, G., Babcock, J., and Orcutt, J. An ocean bottom seismic observatory with near real-time telemetry. *Earth and Space Science*, 3(2):68–77, 2016. doi: 10.1002/2015EA000137.
- Bogiatzis, P., Karamitrou, A., Ward Neale, J., Harmon, N., Rychert, C., and Srokosz, M. Source Regions of Infragravity Waves Recorded at the Bottom of the Equatorial Atlantic Ocean, Using OBS of the PI-LAB Experiment. *Journal of Geophysical Research: Oceans*, 125(6):2019 015430, 2020. doi: 10.1029/2019JC015430.
- Bowden, D., Kohler, M., Tsai, V., and Weeraratne, D. Off-shore Southern California lithospheric velocity structure from noise cross-correlation functions. *Journal of Geophysical Research: Solid Earth*, 121(5):3415–3427, 2016. doi: 10.1002/2016JB012919.
- Butler, R., Lay, T., Creager, K., Earl, P., Fischer, K., Gaherty, J., Laske, G., Leith, B., Park, J., Ritzwolle, M., Tromp, J., and Wen, L. The global seismographic network surpasses its design goal. *Eos, Transactions American Geophysical Union*, 85(23):225–229, 2004. doi: 10.1029/2004EO230001.
- Bécel, A., Laigle, M., Diaz, J., Montagner, J.-P., and Hirn, A. Earth's free oscillations recorded by free-fall OBS ocean-bottom seismometers at the Lesser Antilles subduction zone. *Geophysical Research Letters*, 38(24), 2011. doi: 10.1029/2011GL049533.
- Cox, C., Deaton, T., and Webb, S. A Deep-Sea Differential Pressure Gauge. *Journal of Atmospheric and Oceanic Technology*, 1(3): 237–246, 1984. doi: 10.1175/1520-0426(1984)001.
- Crawford, W. and Webb, S. Identifying and Removing Tilt Noise from Low-Frequency (<0.1 Hz) Seafloor Vertical Seismic Data. *Bull. Seismol. Soc. Am*, 90(4):952–963, 2000.
- Dahlen, F. The effect of data windows on the estimation of free oscillation parameters. *Geophys. J. Int*, 69(2):537–549, 1982. doi: 10.1111/j.1365-246X.1982.tb04964.x.
- Dahlen, F. and Tromp, J. *Theoretical Global Seismology*. Princeton University Press, 1998.
- Deen, M., Wielandt, E., Stutzmann, E., Crawford, W., Barruol, G., and Sigloch, K. First Observation of the Earth's Permanent Free Oscillations on Ocean Bottom Seismometers. *Geophysical Research Letters*, 44(21):10,988–910,996, 2017. doi: 10.1002/2017GL074892.
- Duennebie, F., Harris, D., Jolly, J., Caplan-Auerbach, J., Jordan, R., Copson, D., Stiffel, K., Babinec, J., and Bosel, J. HUGO: the Hawaii Undersea Geo-Observatory. *IEEE Journal of Oceanic Engineering*, 27(2):218–227, 2002. doi: 10.1109/JOE.2002.1002476.
- Dziewonski, A. and Anderson, D. Preliminary Reference Earth Model. *Physics of the Earth and Planetary Interiors*, 25(4): 297–356, 1981.
- Fischer, K., Rychert, C., Dalton, C., Miller, M., Beghein, C., and Schutt, D. A comparison of oceanic and continental mantle lithosphere. *Physics of the Earth and Planetary Interiors*, 309: 106600, 2020. doi: 10.1016/j.pepi.2020.106600.
- Gilbert, F. and Dziewonski, A. An application of normal mode theory to the retrieval of structural parameters and source mechanisms from seismic spectra. *Philosophical Transactions of the Royal Society of London. Series A, Mathematical and Physical Sciences*, 278(1280):187–269, 1975. doi: 10.1098/rsta.1975.0025.
- Harmon, N., Rychert, C., Agius, M., Tharimena, S., Le Bas, T., Kendall, J., and Constable, S. Marine geophysical investigation of the Chain Fracture Zone in the equatorial Atlantic from the PI-LAB Experiment. *J. Geophys. Res*, 123:11,016– 011,030, 2018. doi: 10.1029/2018JB015982.
- Harmon, N., Rychert, C., Kendall, J., Agius, M., Bogiatzis, P., and Tharimena, S. Evolution of the Oceanic Lithosphere in the Equatorial Atlantic From Rayleigh Wave Tomography, Evidence for Small-Scale Convection From the PI-LAB Experiment. *Geochemistry Geophysics Geosystems*, 21(9), 2020. doi: 10.1029/2020GC009174.
- Harmon, N., Wang, S., Rychert, C., Constable, S., and Kendall, J. Shear Velocity Inversion Guided by Resistivity Structure From the PI-LAB Experiment for Integrated Estimates of Partial Melt in the Mantle. *Journal of Geophysical Research: Solid Earth*, 126(8):2021 022202, 2021. doi: 10.1029/2021JB022202.
- Hicks, S., Okuwaki, R., Steinberg, A., Rychert, C., Harmon, N., Abercrombie, R., Bogiatzis, P., Schlaphorst, D., Zahradnik, J., Kendall, J., Yagi, Y., Shimizu, K., and Sudhaus, H. Back-propagating supershear rupture in the 2016 Mw 7.1 Romanche transform fault earthquake. *Nature Geoscience*, 2020. doi: 10.1038/s41561-020-0619-9.
- Kohler, M., Hafner, K., Park, J., Irving, J., Caplan-Auerbach, J., Collins, J., Berger, J., Tréhu, A., Romanowicz, B., and Woodward, R. A Plan for a Long-Term, Automated, Broadband Seismic Monitoring Network on the Global Seafloor. *Seismological Research Letters*, 91(3):1343–1355, 2020. doi: 10.1785/0220190123.
- Laske, G. Observations of Earth's Normal Modes on Broadband Ocean Bottom Seismometers [Original Research. *Frontiers in Earth Science*, 9, 2021. doi: 10.3389/feart.2021.679958.
- Laske, G. and Widmer-Schmidrig, R. 1.04 - Theory and Observations: Normal Mode and Surface Wave Observations. In Schubert, G., editor, *Treatise on Geophysics*, page 117–167. Elsevier, second edition, 2015. doi: 10.1016/B978-0-444-53802-4.00003-8.
- Leptokaropoulos, K., Harmon, N., Hicks, S., Rychert, C., Schlaphorst, D., and Kendall, J. Tidal Triggering of Microseismicity at the Equatorial Mid-Atlantic Ridge, Inferred From the PI-LAB Experiment. *Journal of Geophysical Research: Solid Earth*, 126(9):2021 022251, 2021. doi: 10.1029/2021JB022251.
- Leptokaropoulos, K., Rychert, C., Harmon, N., and Kendall, J.-M. Seismicity properties of the Chain Transform Fault inferred using data from the PI-LAB experiment. *Earth and Space Science Open Archive*, 35, 2022. doi: 10.1002/essoar.10511418.1.
- Lin, P., Gaherty, J., Jin, G., Collins, J., Lizarralde, D., Evans, R., and Hirth, G. High-resolution seismic constraints on flow dynamics in the ocean asthenosphere. *Nature*, 535:538–541, 2016. doi: 10.1038/nature18012.
- Masters, G., Jordan, T., Silver, P., and Gilbert, F. Aspherical Earth structure from fundamental spheroidal-mode data. *Nature*, 298(5875):609–613, 1982. doi: 10.1038/298609a0.
- Masters, G., Laske, G., Bolton, H., and Dziewonski, A. The relative behavior of shear velocity, bulk sound speed, and compressional velocity in the mantle: Implications for chemical and thermal structure. *Washington DC American Geophysical Union Geophysical Monograph Series*, 117:63–87, 2000. doi: 10.1029/GM117p0063.
- Masters, T. and Widmer, R. Free Oscillations: Frequencies and Attenuations, 1995.
- Mehouachi, F. and Singh, S. Water-rich sublithospheric melt channel in the equatorial Atlantic Ocean. *Nat. Geosci*, 11:65–69, 2018. doi: 10.1038/s41561-017-0034-z.
- Moulik, P. and Ekström, G. An anisotropic shear velocity model of the Earth's mantle using normal modes, body waves, surface waves and long-period waveforms. *Geophys. J. Int*, 199(3): 1713–1738, 2014. doi: 10.1093/gji/ggu356.
- Ritsema, J., Heijst, H., and Woodhouse, J. Complex shear wave velocity structure imaged beneath Africa and Iceland. *Science*, 286(5446):1925–1928, 1999.

- Ritsema, J., Deuss, A., Heijst, H., and Woodhouse, J. S40RTS: a degree-40 shear-velocity model for the mantle from new Rayleigh wave dispersion, teleseismic traveltime and normal-mode splitting function measurements. *Geophysical Journal International*, 184(3):1223–1236, 2011. doi: 10.1111/j.1365-246X.2010.04884.x.
- Rychert, C., Kendall, J., and Harmon, N. Passive Imaging of the Lithosphere-Asthenosphere Boundary, 2016.
- Rychert, C., Harmon, N., Constable, S., and Wang, S. The Nature of the Lithosphere-Asthenosphere Boundary. *Journal of Geophysical Research-Solid Earth*, 125(10), 2020.
- Rychert, C., Tharimena, S., Harmon, N., Wang, S., Constable, S., Kendall, J., Bogiatzis, P., Agius, M., and Schlaphorst, D. A dynamic lithosphere-asthenosphere boundary near the equatorial Mid-Atlantic Ridge. *Earth and Planetary Science Letters*, 566: 116949, 2021. doi: 10.1016/j.epsl.2021.116949.
- Saikia, U., Rychert, C., Harmon, N., and Kendall, J. Sediment structure at the equatorial mid-atlantic ridge constrained by seafloor admittance using data from the PI-LAB experiment. *Marine Geophysical Research*, 41(1):10 1007 11001–020–09402–0, 2020.
- Saikia, U., Rychert, C., Harmon, N., and Kendall, J. Upper Mantle Anisotropic Shear Velocity Structure at the Equatorial Mid-Atlantic Ridge Constrained by Rayleigh Wave Group Velocity Analysis From the PI-LAB Experiment. *Geochemistry, Geophysics, Geosystems*, 22(3):2020 009495, 2021a. doi: 10.1029/2020GC009495.
- Saikia, U., Rychert, C., Harmon, N., and Michael Kendall, J. Seismic Attenuation at the Equatorial Mid-Atlantic Ridge Constrained by Local Rayleigh Wave Analysis From the PI-LAB Experiment. *Geochemistry, Geophysics, Geosystems*, 22(12):2021 010085, 2021b. doi: 10.1029/2021GC010085.
- Schlaphorst, D., Rychert, C., Harmon, N., Hicks, S., Bogiatzis, P., Kendall, J., and Abercrombie, R. Local seismicity around the Chain Transform Fault at the Mid-Atlantic Ridge from OBS observations. *Earth and Space Science Open Archive*, 38, 2022. doi: 10.1002/essoar.10511147.1.
- Smith, M. and Masters, G. Aspherical structure constraints from free oscillation frequency and attenuation measurements. *Journal of Geophysical Research: Solid Earth*, 94(B2):1953–1976, 1989. doi: 10.1029/JB094iB02p01953.
- Stephen, R., Spiess, F., Collins, J., Hildebrand, J., Orcutt, J., Peal, K., Vernon, F., and Wooding, F. Ocean Seismic Network Pilot Experiment. *Geochemistry, Geophysics, Geosystems*, 4(10), 2003. doi: 10.1029/2002GC000485.
- Wang, S., Constable, S., Reyes-Ortega, V., and Rychert, C. A newly distinguished marine magnetotelluric coast effect sensitive to the lithosphere-asthenosphere boundary. *Geophys. J. Int*, 218 (2):978–987, 2019. doi: 10.1093/gji/ggz202.
- Wang, S., Constable, S., Rychert, C., and Harmon, N. A Lithosphere-Asthenosphere Boundary and Partial Melt Estimated Using Marine Magnetotelluric Data at the Central Middle Atlantic Ridge. *Geochemistry Geophysics Geosystems*, 21(9), 2020. doi: 10.1029/2020GC009177.
- Webb, S. and Crawford, W. Long-period seafloor seismology and deformation under ocean waves. *Bull. Seis. Soc. Am*, 89(6): 1535–1542, 1999.
- Wolfe, C., Solomon, S., Laske, G., Collins, J., Detrick, R., Orcutt, J., Bercovici, D., and Hauri, E. Mantle shear-wave velocity structure beneath the Hawaiian hotspot. *Science*, 326:1388–1390, 2009.
- Woodhouse, J. and Dziewonski, A. Mapping the upper mantle: Three-dimensional modeling of earth structure by inversion of seismic waveforms. *Journal of Geophysical Research: Solid Earth*, 89(B7):5953–5986, 1984. doi: 10.1029/JB089iB07p05953.

Seismic interferometry in the presence of an isolated noise source

S. Schippkus  *¹, R. Snieder  ², C. Hadziioannou  ¹

¹Institute of Geophysics, Centre for Earth System Research and Sustainability (CEN), Universität Hamburg, Hamburg, Germany, ²Center for Wave Phenomena, Colorado School of Mines, Golden, CO, USA

Author contributions: *Conceptualization:* SS, RS. *Methodology:* SS, RS. *Software:* SS. *Data curation:* SS. *Formal Analysis:* SS, RS. *Writing - original draft:* SS, RS. *Writing - Review & Editing:* SS, RS, CH. *Visualization:* SS. *Supervision:* CH. *Project administration:* SS. *Funding acquisition:* CH, SS.

Abstract Seismic interferometry gives rise to a correlation wavefield that is closely related to the Green's function under the condition of uniformly distributed noise sources. In the presence of an additional isolated noise source, a second contribution to this wavefield is introduced that emerges from the isolated source location at negative lapse time. These two contributions interfere, which may bias surface wave dispersion measurements significantly. To avoid bias, the causal and acausal parts of correlation functions need to be treated separately. We illustrate this by applying seismic interferometry to field data from a large-N array where a wind farm is present within the array.

Production Editor:
Gareth Funning
Handling Editor:
Lise Retailleau
Copy & Layout Editor:
Hannah F. Mark

Received:
1 July 2022
Accepted:
17 October 2022
Published:
4 April 1900

1 Introduction

Seismic interferometry is a well-established technique to estimate wavefields propagating between pairs of stations from recordings of ambient seismic noise (Nakata et al., 2019, and references therein). These wavefields are commonly used to image (e.g., Lin et al., 2008; de Ridder and Biondi, 2015; Schippkus et al., 2018) and monitor (e.g., Wegler and Sens-Schönfelder, 2007; Brenguier et al., 2008; Steinmann et al., 2021) Earth's structure. For a uniform distribution of uncorrelated noise sources, the wavefield that emerges from cross-correlation of seismic records between two stations is closely related to the Green's function between them. This relation may be derived by assuming a diffuse wavefield (Lobkis and Weaver, 2001), equipartition of energy across seismic wave modes (Weaver, 2010), or sources on a boundary surrounding the two stations (Wapenaar et al., 2005).

In this study, we investigate the case where the presence of an additional isolated source violates these assumptions and introduces an additional contribution to cross-correlation functions. We consider vertical component recordings of surface waves. In the following, we demonstrate the isolated-source contribution using data from a large-N deployment in the Vienna basin, Austria, derive the expected behaviour of this contribution, compare our predictions with observations from the large array, and explore what impact the second contribution may have in practice.

2 Cross-correlation of the recorded wavefield

We use data from 4907 seismic stations with $\sim 200\text{m}$ inter-station spacing in the Vienna basin, Austria (Fig. 1). Stations were deployed in March 2019 as part of a seismic exploration survey by OMV E&P GmbH and recorded data continuously over four weeks. This deployment is similar to the one described in Schippkus et al. (2020), with comparable instruments – several co-located 10 Hz geophones (Sercel JF-20DX) per station, stacked and recorded with AutoSeis High Definition Recorders – and in an area that is partly overlapping with the previous deployment towards the Southeast. Therefore, the same sources of seismic noise characterised by Schippkus et al. (2020) are also present in this data: wind farms, railway tracks, roads, and oil pump-jacks, among others.

Schippkus et al. (2020) already hinted at the potential impact of strong isolated sources on correlation functions in this region. To investigate the impact of these sources, we compute cross correlations between all stations and a master station at location r_M in the center of the deployment (Fig. 2a). The seismograms were spectrally whitened and cut into 1 hr-long windows before cross-correlation, stacked linearly after cross-correlation, and bandpass-filtered from 0.5 to 1.0 Hz. There were no significant earthquakes globally or regionally during the recorded timeframe. A movie of correlation function amplitudes over time is provided in the electronic supplementary material.

Figure 2 and the supplemental movie show two dis-

*Corresponding author: sven.schippkus@uni-hamburg.de

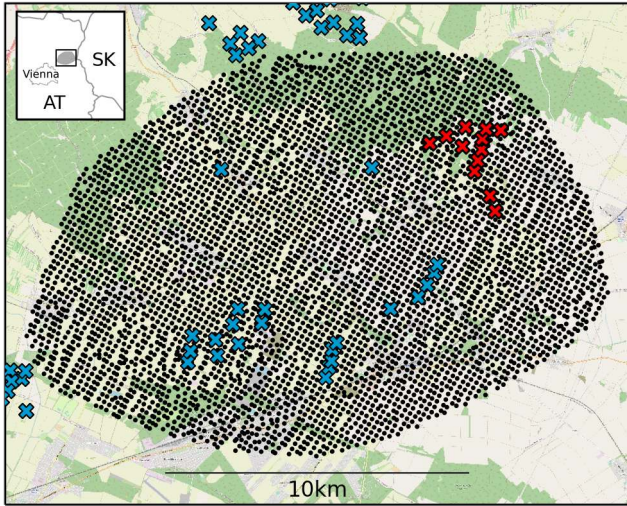


Figure 1 Map of the study area. 4907 seismic stations (black dots) Northeast of Vienna, near the Austrian-Slovakian border. Wind turbines in the wind farm Prottes-Ollersdorf are marked with red crosses; blue crosses mark all other wind turbines.

tinct contributions to the correlation wavefield. First, there is a contribution converging onto the master station \mathbf{r}_M at acausal lapse times $\tau < 0$ and diverging at causal lapse times $\tau > 0$ (Fig. 2a). This is the expected behaviour that commonly arises from seismic interferometry under the assumptions described above (e.g., Lin et al., 2008). In addition, there is a second contribution emerging from a location \mathbf{r}_N in the Northeast of the deployment at $\tau \approx -12$ sec that propagates only outwards from \mathbf{r}_N . The center of this wavefield contribution coincides with the location of the wind farm Prottes-Ollersdorf (red crosses in Fig. 1), the strongest and most consistent source of anthropogenic noise at these frequencies in the region (Schippkus et al., 2020). There are other wind farms in the region (blue crosses in Fig. 1), which do not appear to excite a significant contribution to the correlation wavefield. This is consistent with previous observations that these wind turbines produce much lower seismic energy (Schippkus et al., 2020). Similarly, the other anthropogenic noise sources in the region also appear to be negligible. Wind turbine towers excite seismic energy at frequencies related to the eigenfrequencies of the towers and passing frequency of the rotor blades, including the in the range of 0.5 to 1.0 Hz (Neuffer et al., 2021). In the next section, we derive the behaviour of the contribution by the wind turbines to the cross correlations.

3 Cross-correlation in the presence of an isolated noise source

We consider a wavefield that is generated by a combination of noise sources on a closed boundary S surrounding the array and an isolated noise source within the boundary with noise spectrum $N_I(\omega)$ at location \mathbf{r}_N (Fig. 2). The treatment of this section is formulated in the frequency domain. We assume that the noise

sources on the boundary have equal power spectrum $|N_B|^2$, and that the noise generated at different locations are uncorrelated. This means that

$$\langle N_B(\mathbf{r}')N_B^*(\mathbf{r}'') \rangle = |N_B|^2\delta(\mathbf{r}' - \mathbf{r}'') , \quad (1)$$

where $\langle \dots \rangle$ denotes the expected value. We also assume that the noise on the boundary and the noise from the isolated noise source with spectrum N_I is uncorrelated, hence

$$\begin{aligned} \langle N_B(\mathbf{r}')N_I^* \rangle &= \langle N_I N_B^*(\mathbf{r}') \rangle \\ &= 0 . \end{aligned} \quad (2)$$

The wavefield is excited by the superposition of noise sources at the boundary S and the isolated noise source, hence

$$u(\mathbf{r}) = \oint_S G(\mathbf{r}, \mathbf{r}')N_B(\mathbf{r}')d\mathbf{r}' + G(\mathbf{r}, \mathbf{r}_N)N_I . \quad (3)$$

The cross correlation of the wavefield at location \mathbf{r} with the wavefield at the master station at \mathbf{r}_M is given by

$$\begin{aligned} \langle u(\mathbf{r})u^*(\mathbf{r}_M) \rangle &= \\ &\oint_S \oint_S G(\mathbf{r}, \mathbf{r}')G^*(\mathbf{r}_M, \mathbf{r}'')\langle N_B(\mathbf{r}')N_B^*(\mathbf{r}'') \rangle d\mathbf{r}'d\mathbf{r}'' \\ &+ \oint_S G(\mathbf{r}, \mathbf{r}')G^*(\mathbf{r}_M, \mathbf{r}_N)\langle N_B(\mathbf{r}')N_I^* \rangle d\mathbf{r}' \\ &+ \oint_S G(\mathbf{r}, \mathbf{r}_N)G^*(\mathbf{r}_M, \mathbf{r}')\langle N_I N_B^*(\mathbf{r}') \rangle d\mathbf{r}' \\ &+ G(\mathbf{r}, \mathbf{r}_N)G^*(\mathbf{r}_M, \mathbf{r}_N)|N_I|^2 . \end{aligned} \quad (4)$$

Because of expression (1) the double integral in the first term reduces to a single integral, and because of equation (2) the second and the third term in equation (4) vanish, hence

$$\begin{aligned} \langle u(\mathbf{r})u^*(\mathbf{r}_M) \rangle &= \oint_S G(\mathbf{r}, \mathbf{r}')G^*(\mathbf{r}_M, \mathbf{r}')d^2\mathbf{r}'|N_B|^2 \\ &+ G(\mathbf{r}, \mathbf{r}_N)G^*(\mathbf{r}_M, \mathbf{r}_N)|N_I|^2 . \end{aligned} \quad (5)$$

Note the symmetry between the contribution of the surface sources and the contribution of the isolated source.

The surface integral in the first term can be rewritten using equation (11) of Wapenaar et al. (2005), which in the notation of this paper is given by $G(\mathbf{r}, \mathbf{r}_M) + G^*(\mathbf{r}, \mathbf{r}_M) = (2/\rho c) \oint_S G(\mathbf{r}, \mathbf{r}')G^*(\mathbf{r}_M, \mathbf{r}')d^2\mathbf{r}'$, hence equation (5) can be written as

$$\begin{aligned} \langle u(\mathbf{r})u^*(\mathbf{r}_M) \rangle &= \frac{\rho c |N_B|^2}{2} (G(\mathbf{r}, \mathbf{r}_M) + G^*(\mathbf{r}, \mathbf{r}_M)) \\ &+ |N_I|^2 G(\mathbf{r}, \mathbf{r}_N)G^*(\mathbf{r}_M, \mathbf{r}_N) . \end{aligned} \quad (6)$$

The first term on the right hand denotes the superposition of the Green's function and its time-reversed counterpart. These terms usually arise in seismic interferometry. The second term on the right hand side describes an additional contribution to the cross-correlation of the wavefield that is caused by the isolated noise source. We analyse the kinematics of this term in the next section.

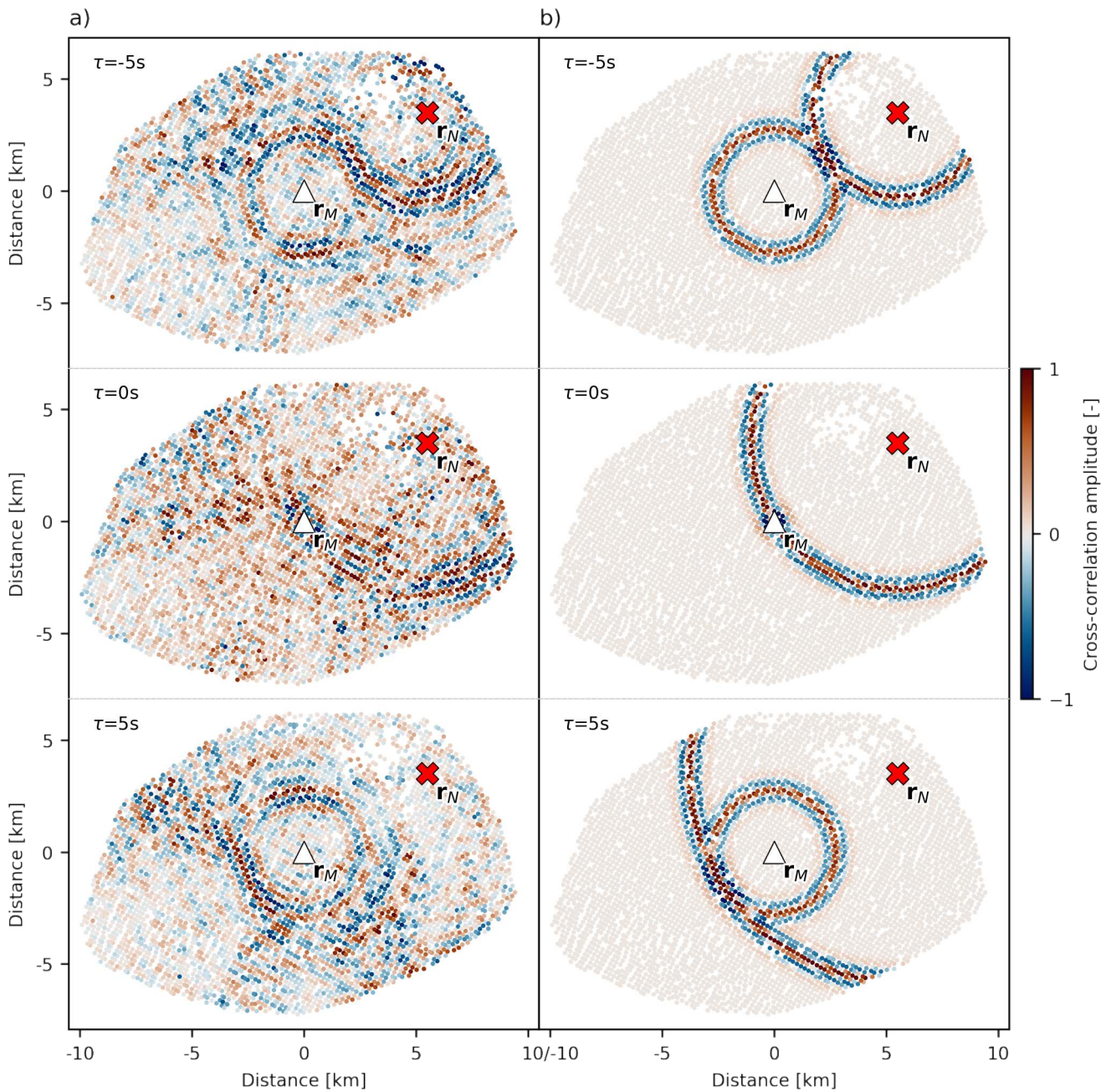


Figure 2 Snapshots of cross-correlation function amplitudes in the presence of an isolated source at different lapse times $\tau = [-5, 0, 5]$ sec. The white triangle marks the master station r_M , the red cross marks the approximate location of the isolated source r_N . a) Correlation functions from four weeks of data, bandpass-filtered from 0.5 to 1.0Hz. The isolated source induces a contribution centered on r_N . b) Modelled correlation functions for the two contributions by sources on a boundary and by the isolated source (eq. 9) predict the observations.

4 Kinematics of the isolated noise source contribution

The surface wave Green's function is, in the far field, proportional to

$$G(\mathbf{r}, \mathbf{r}_N) \propto e^{i(k|\mathbf{r}-\mathbf{r}_N|+\pi/4)}, \quad (7)$$

with wavenumber k (Aki and Richards, 2009). Thus, in the far field the last term in expression (6) satisfies

$$|N_I|^2 G(\mathbf{r}, \mathbf{r}_N) G^*(\mathbf{r}_M, \mathbf{r}_N) \propto |N_I|^2 e^{ik(|\mathbf{r}-\mathbf{r}_N| - |\mathbf{r}_M - \mathbf{r}_N|)}, \quad (8)$$

which gives an arrival at lapse time

$$\tau(\mathbf{r}) = \frac{|\mathbf{r} - \mathbf{r}_N|}{c} - \frac{|\mathbf{r}_M - \mathbf{r}_N|}{c}, \quad (9)$$

for a homogeneous medium with velocity c . Note that for a given master station $|\mathbf{r}_M - \mathbf{r}_N|/c = \text{constant}$. Equation (9) shows that all locations \mathbf{r} with the same distance to \mathbf{r}_N have the same arrival time $\tau(\mathbf{r})$; the travel time of the contribution to the correlation wavefield induced by the isolated source is constant on a circle centered on \mathbf{r}_N . This contribution emerges from \mathbf{r}_N at

$$\tau(\mathbf{r} = \mathbf{r}_N) = -\frac{|\mathbf{r}_M - \mathbf{r}_N|}{c}, \quad (10)$$

and reaches the master station at $\tau(\mathbf{r} = \mathbf{r}_M) = 0$.

To understand the relation between the waveforms described by the first term of equation (6) and the additional term, we analyze the arrival time of these waves on a line from \mathbf{r}_M to \mathbf{r}_N . Take the x -axis to point in the positive direction from \mathbf{r}_M to \mathbf{r}_N and consider points on the line between these locations, hence $x_M < x < x_N$. For a given location x , the acausal wave described by the term $G^*(\mathbf{r}, \mathbf{r}_M)$ gives an arrival at time $t = -|\mathbf{r} - \mathbf{r}_M|/c = -(x - x_M)/c$. This means that for a given time t , the acausal direct wave is located at

$$x_{dir} = x_M - ct. \quad (11)$$

(Note that since $t < 0$, $x > x_M$.) The additional arrival due to the isolated noise source gives for a location x according to expression (9) an arrival at $t = (x_N - x)/c - (x_N - x_M)/c = -(x - x_M)/c$, so that for a given time t the wave is at location

$$x_{add} = x_M - ct. \quad (12)$$

This means that for a time t the wavefronts from the acausal direct wave and the contribution from the isolated noise source are at the same location at the line from \mathbf{r}_M to \mathbf{r}_N . Geometrically speaking, the incoming wave to \mathbf{r}_M and the outgoing wave from \mathbf{r}_N touch at the line from \mathbf{r}_M to \mathbf{r}_N . Similarly, the contribution by the isolated noise source touches the causal wave described by the term $G(\mathbf{r}, \mathbf{r}_M)$ for locations $x < x_M$. This behavior is confirmed by the touching wavefronts in Figure 2 and the supplemental movie. Note that there is no acausal contribution in the second term of expression (6), because the original wavefield induced at \mathbf{r}_N only propagates in one direction (away from \mathbf{r}_N), in contrast

to the wavefield emitted at the boundary, which propagates in all directions. Therefore, the contribution to the correlation wavefield by the isolated source has no energy at $\tau(\mathbf{r}) < -|\mathbf{r}_M - \mathbf{r}_N|/c$.

We model the described kinematics and compare against our observations (Fig. 2). We approximate the wind farm Prottes-Ollersdorf as a single source and assume that both the boundary sources and the isolated source emit the same Ricker wavelets. For demonstration purposes, we assume a constant medium velocity $c \approx 550$ m/s, estimated from the time the isolated-source contribution emerges $\tau(\mathbf{r} = \mathbf{r}_N)$ and the distance $|\mathbf{r}_M - \mathbf{r}_N|$. We do not consider amplitude effects. Our model explains the observed contributions to the correlation wavefield.

5 Velocity measurement errors due to interference

Because the wavefronts from the two contributions touch and have the same wavelengths, they interfere. Along the line connecting \mathbf{r}_N and \mathbf{r}_M they are exactly in phase, and show varying degrees of constructive and destructive interference away from this line (Fig. 2). This behaviour implies that measurements on cross-correlation functions may be adversely affected in the presence of an isolated source for station pairs not on this line. In a standard ambient noise tomography application, travel times of seismic waves are measured between all station pairs from correlation functions and inverted for maps of seismic wave speed.

We demonstrate the impact the isolated source has on such measurements by measuring group travel times from the modelled correlation functions (Fig. 2b). From these measurements we compute relative group-velocity measurement errors (Fig. 3). Two cases are investigated: one where the isolated source induces a contribution in the correlation wavefield with 25% higher amplitudes than the contribution due to sources on the boundary (Fig. 3a), and one where the boundary sources produce the stronger contribution (also 25%, Fig. 3b).

In the first case, the measurement errors vanish only along the line connecting \mathbf{r}_N and \mathbf{r}_M where the two contributions are in phase (Fig. 3a). Away from this line, measurement errors increase to infinity (apparent travel times of 0) for stations \mathbf{r} with $|\mathbf{r} - \mathbf{r}_N| = |\mathbf{r}_M - \mathbf{r}_N|$. In practice, velocity measurements deviating significantly from expected values are commonly classified as outliers or attributed to spurious arrivals and discarded. Our results show that measurement errors of at least 10% occur for the majority of station pairs in the case of a stronger isolated source.

In the case of a weaker isolated source, we find a distinct pattern of measurement errors of several percent (Fig. 3b). Such measurement errors would likely not be identified as clear outliers or spurious arrivals and could bias results. To illustrate why this pattern occurs, we show the group travel time measurements at five stations (Fig. 3e-g, red circles in Fig. 3b). Starting at the line connecting \mathbf{r}_N and \mathbf{r}_M , we find that both contributions are in phase, resulting in no error (Fig. 3c).

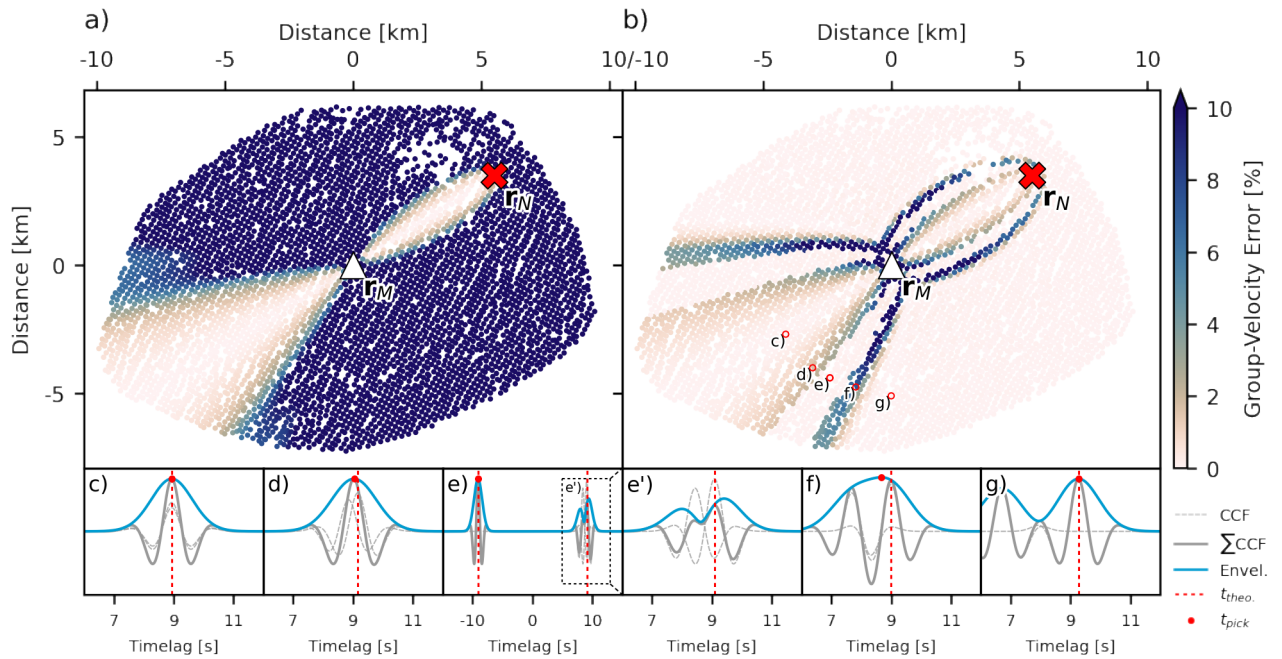


Figure 3 Group-velocity measurement errors due to the interference between the two contributions to the correlation wavefield. We cap the colormap at 10% error for illustration purposes. a) Errors if the correlation wavefield induced by the isolated source r_N has higher amplitudes. Interference of the two contributions results in significant measurement errors away from the line connecting r_N and r_M . b) Errors if the correlation wavefield induced by the sources on the boundary has higher amplitudes. Significant errors due to interference. c-g) Picked group arrivals on correlation functions for b). These show correlation function contributions by the two types of sources (dashed grey lines), sum of the two contributions (thick grey line), the sum's envelope (blue line), theoretical arrival time (red dashed line), and picked arrival time (red dot). Note the wider time window in e) and its zoom-in e').

As we increase distance to this line, a slight shift between the two contributions shifts the envelope's peak towards lower lapse time, resulting in a higher-velocity estimate (Fig. 3d). This error increases until another band with zero error (Fig. 3e). This band exists because destructive interference decreases amplitudes to values lower than the acausal part of the correlation function, which is caused only by the boundary sources at this location. The travel time is then automatically picked on the acausal side where no interference occurs (Fig. 3e). If the travel time was picked in the causal part instead, interference would result in negative velocity errors (zoom-in Fig. 3e'). At a certain distance, the two contributions interfere constructively again (Fig. 3f), resulting in a bias similar to the case in Figure 3d. Finally, as the two wavefields separate, no interference occurs and the envelope of the stronger contribution to the correlation wavefield is picked; in this case the contribution of the boundary sources (Fig. 3g). This also explains the behaviour in the first case, where the isolated source dominates the measurement away from the line simply due to higher amplitudes.

The distribution of errors for both cases depends on relative amplitudes of the two contributions, source terms, frequency range, and the locations of r_M and r_N . With knowledge of these factors, measurement errors can be avoided. One straightforward strategy is to avoid measuring where interference occurs by selecting which side of the correlation functions to measure on – depending on the geometry of r , r_N and r_M – in com-

bination with a windowing function around expected arrival times. In the case of a stronger contribution by the boundary sources (Fig. 3b) selecting the side of the correlation function without interference is sufficient (Suppl. Fig. S1b). In the case of a strong isolated source, an additional windowing function is necessary (Suppl. Figs. S2, S3). See supplementary material for more details.

6 Discussion

We describe the contribution of an isolated noise source to the cross-correlation wavefield in seismic interferometry and how it relates to the contribution by boundary sources. Our derivation predicts the observed correlation wavefield (Fig. 2). In the following, we discuss the implications our results have for studies based on seismic interferometry and how this work may be expanded upon in the future.

The dataset in this study is not the first to record isolated noise sources that are used in the context of seismic interferometry. Zeng and Ni (2010) located an isolated source at primary microseism frequencies near Kyushu Island, Japan. Droznin et al. (2015) used cross-correlation of continuous recordings of volcanic tremor to estimate their location. Retailleau et al. (2017) investigated spurious arrivals in correlation functions to locate noise sources near Iceland at ~ 20 sec. Dales et al. (2017) exploited the correlation wavefield contribution from continuously operating ore crushers for monitor-

ing of an underground mine. Brenguier et al. (2019) proposed to use body waves from train signals excited in the stationary phase of two arrays for structural monitoring of a fault between the two arrays. The crucial feature these sources have in common is that they are fairly localised and excite seismic energy repeatedly, similar to the wind farm in our dataset. In previous studies that use such sources, the correlation wavefield has often been dominated by the isolated source contribution, masking the contribution by boundary sources (Droznin et al., 2015; Dales et al., 2017; Brenguier et al., 2019). In other cases, both contributions have comparable amplitudes and the isolated source contribution arrives earlier than the expected direct wave (Zeng and Ni, 2010; Retailleau et al., 2017).

Signals that arrive before the expected direct wave in correlation functions are often called "spurious" arrivals (Snieder et al., 2006, 2008). The ambient seismic noise community often distinguishes two kinds of spurious arrivals: those that are induced directly by isolated noise sources (this study; Zeng and Ni, 2010; Retailleau et al., 2017), and those that emerge from uncanceled cross terms in correlation functions (Snieder et al., 2006; Colombi et al., 2014; Li et al., 2020). So far, cross terms in correlation functions have been observed between direct and reflected body waves (Li et al., 2020; Colombi et al., 2014). In principle, there may also be uncanceled cross terms between boundary sources (in violation of equation 1) but we are not aware of any field data example of this. In any case, understanding the cause of spurious arrivals (be they from isolated noise sources or direct-wave to reflected-wave cross terms) is necessary to exploit them for information. In this study, we investigate the behaviour of surface wave contributions induced directly by isolated noise sources and see no evidence for contributions due to uncanceled cross terms. Isolated source contributions to the correlation wavefield always emerge at negative lapse time for any chosen master station and propagate only outwards (Eq. 10, Fig. 2). These additional arrivals often manifest in distance-vs-lapse-time plots of correlation functions as nearly parallel (depending on velocity structure and exact geometry) to the causal direct arrivals emitted from the master station (see e.g., Zeng and Ni, 2010). The spurious arrivals exploited by Retailleau et al. (2017) show the same behaviour but reversed in time due to a different convention during processing, i.e., taking the time-reversed signals of the receiver stations instead of the master station for cross-correlation.

In this study, we also recover the two different contributions to the correlation wavefield, by the isolated noise source and by the boundary sources, simultaneously. Expression (6) shows that for both contributions to the correlation wavefield to have comparable amplitudes, the source terms must have the "right" ratio of energy. For our data, both contributions emerge clearly only with spectral whitening applied, i.e., normalisation of energy across frequencies. Without spectral whitening, the correlation wavefield is dominated by the contribution of the wind farm Prottes-Ollersdorf, similar to how the 26s microseism biases correlation functions in Bensen et al. (2007). It is likely that whiten-

ing is successful on our data because wind turbines excite seismic energy most effectively at specific frequencies related to the eigenmodes of the wind turbine towers (Neuffer et al., 2021), whereas other sources of ambient noise in the region excite energy over a wider frequency range at lower energy levels (Schippkus et al., 2020). Normalising the energy levels across frequencies changes their relative strength to be comparable in the wideband correlation functions we investigate here. Early tests have shown that using only time windows with wind speeds below the minimum operation specifications of the wind turbines in the wind farm Prottes-Ollersdorf, cross-correlations show a reduced but not eliminated wind farm contribution. Additional contributions to the correlation wavefield may also occur at lower frequencies where the presence of isolated sources is usually not considered, e.g., near the secondary microseism band (Zeng and Ni, 2010; Retailleau et al., 2017). Our analysis demonstrates the contribution of an isolated noise source can have significant impact on travel-time measurements (Fig. 3), which may be missed if one is unaware of the presence of an isolated source. This applies in a similar manner to measurements of amplitudes or phase velocities, as can be seen from Figure 3c-g.

The basic approach we propose to avoid travel-time measurement errors requires a nearly symmetric contribution to the correlation wavefield by the boundary sources, i.e., an even distribution of boundary sources (Snieder et al., 2008). In real-world applications, strongly asymmetric correlation functions with sufficient signal-to-noise ratio on only one side are common (e.g., Brenguier et al., 2008; Retailleau et al., 2017; Schippkus et al., 2018). If that side also is the side that contains the contribution by the isolated source, our proposed strategy is not applicable. In the context of tomography, one may still achieve sufficient coverage of measurements when applying a windowing function. Related to this, the causal and acausal parts of correlation functions are often stacked ("folded") to increase signal-to-noise ratio (e.g., Lin et al., 2008; de Ridder and Biondi, 2015; Schippkus et al., 2018). In the presence of an isolated noise source, folding correlations effectively forces the asymmetric contribution of the isolated source to become symmetric. In the case of a stronger boundary source contribution, this can result in too slow group velocity measurements for some station pairs (negative errors in Fig. S4b), an effect that was entirely avoided by not folding (Fig. 3). While a windowing function may still be applied, such a function is not sufficient to eliminate all errors (Fig. S2). Folding prevents selection of the appropriate side of the correlation function for measurement and results in irreconcilable errors. A related approach for stabilising velocity measurements is to measure on both sides of the correlation function and compute the mean, often combined with a quality criterion based on consistency (e.g., Stehly et al., 2009; Boué et al., 2014; Zigone et al., 2015). This approach is similarly adversely affected in the presence of an isolated noise source. The considerations above are also instructive for deployments where receiver stations are only available on the side of the master station

away from the isolated noise source, e.g., in a scenario where ocean noise acts as an isolated source with the master station near the coast and all receiver stations further inland. This resembles the geometry in Figure 3 for stations to the Southwest of r_M , i.e., for station pairs where r_N is located within the Fresnel zone (Wapenaar et al., 2010). In such cases, folding of correlations or measuring on both sides of correlation functions may be used to increase signal-to-noise ratio without introducing additional measurement errors but this depends on the exact geometry of r , r_M , and r_N . Without detailed knowledge of r_N , we advise against folding correlations or similar post-processing.

Isolated noise sources may also have significant implications for monitoring applications that exploit the coda of correlation functions. While the direct waves of both contributions to the correlation wavefield only interfere for certain station pair geometries (Fig. 2), coda waves of both contributions can overlap and interfere for a larger range of geometries. Because correlation functions contain the sum of multiple contributions to the correlation wavefield (Eq. 6), changes in the strength of the isolated source over time could induce apparent velocity changes due to interference, similar to how velocity measurement errors on the direct wave depend on relative amplitude (Fig. 3). However, this would likely be accompanied by a drop in correlation coefficient, which can indicate a change in source distribution and is often used as a quality criterion (e.g., Wegler and Sens-Schönfelder, 2007). Additionally, the origin of the coda wavefield dictates its spatial sensitivity (Margerin et al., 2016). If the origin is misattributed, it may lead to misinterpretation of results. Isolated noise sources that move over time can also lead to bias in measurements of velocity variations and their spatial interpretation and should be considered carefully (Hadziioannou et al., 2009). Similar to the strategy for travel-time measurements described above, careful coda window selection, based on the asymmetry of the isolated source contribution, may help avoid these effects also for monitoring applications.

We treat the wind farm Prottes-Ollersdorf as a single source in our derivation and modelling (Fig. 2). When considering multiple isolated noise sources, the derivation straightforwardly gives rise to a single contribution for each of those sources, assuming they are uncorrelated. Indeed, when we consider each wind turbine in the wind farm separately, the fit with observed correlation functions appears to improve (Fig. S5). This suggests that knowledge about the presence and characteristics of isolated sources may be used to remove their contributions and achieve correlation functions that are less impacted by local sources. Multiple isolated noise sources complicate the estimation of velocity measurement errors due to further interference between each individual source contribution. Above, we investigate the edge case of a single source, i.e., the worst-case scenario. The other edge case of isolated noise sources at every possible location approaches the condition of sources on a closed boundary, which would eliminate any isolated source contributions and reduce errors to zero. In practice, the real impact most likely lies some-

where in between.

In our analysis, we have only considered vertical components, because only vertical component recordings are available in our dataset. Because the two contributions to the correlation wavefield propagate in different directions for some station pairs, questions arise about the interaction between differently polarised wave types with different velocities when analysing horizontal component recordings, i.e., potential interference of Love and Rayleigh waves. They may not be well-separated and may interfere to affect measurements, similar to the above. Defining an appropriate windowing function may prove more difficult in that case. The case of horizontal components is a potential target for future works.

We demonstrate that different contributions to the correlation wavefield can carry similar energy and interfere. For certain station geometries this leads to significant travel-time measurement errors, if not properly accounted for. Ideally, studies that rely on seismic interferometry should always consider the possibility of isolated noise sources in their data and how such sources may impact results, especially at frequencies where anthropogenic sources dominate.

Data Availability and Resources

Seismograms used in this study were collected using an array for industrial exploration by OMV E&P GmbH. Due to a non-disclosure agreement with OMV E&P GmbH, the authors cannot make this data publicly available. The supplemental material includes a movie of cross-correlation function amplitudes over time, more details on the proposed strategy to avoid measurement errors, and the case when multiple isolated noise sources are considered. Colormaps used for illustrations are perceptually uniform (Cramer, 2021).

Acknowledgements

The authors thank Laura Ermert and one anonymous reviewer for their insightful comments, which helped improve the manuscript considerably. The authors thank OMV E&P GmbH for granting access to the seismic data. This research was partially funded by the Federal Ministry of Education and Research (BMBF) and the Free and Hanseatic City of Hamburg under the Excellence Strategy of the Federal Government and the Länder. This work was partially funded by the Emmy Noether program (HA7019/1-1) of the German Research Foundation (DFG). This work was partially funded by the European Union's Horizon 2020 research and innovation programme under the Marie Skłodowska-Curie grant agreement No. 955515 (SPIN ITN).

References

- Aki, K. and Richards, P. G. *Quantitative Seismology*. Univ. Science Books, Sausalito, Calif, 2. ed., corr. print edition, 2009.
- Bensen, G. D., Ritzwoller, M. H., Barmin, M. P., Levshin, A. L., Lin, F., Moschetti, M. P., Shapiro, N. M., and Yang, Y. Pro-

- cessing Seismic Ambient Noise Data to Obtain Reliable Broad-Band Surface Wave Dispersion Measurements. *Geophysical Journal International*, 169(3):1239–1260, June 2007. doi: 10.1111/j.1365-246X.2007.03374.x.
- Boué, P., Roux, P., Campillo, M., and Briand, X. Phase Velocity Tomography of Surface Waves Using Ambient Noise Cross Correlation and Array Processing. *Journal of Geophysical Research: Solid Earth*, 119(1):519–529, 2014. doi: 10.1002/2013JB010446.
- Brenguier, F., Campillo, M., Hadziioannou, C., Shapiro, N. M., Nadeau, R. M., and Larose, E. Postseismic Relaxation along the San Andreas Fault at Parkfield from Continuous Seismological Observations. *Science (New York, N.Y.)*, 321(5895):1478–1481, Sept. 2008. doi: 10.1126/science.1160943.
- Brenguier, F., Boué, P., Ben-Zion, Y., Vernon, F. L., Johnson, C. W., Mordret, A., Coutant, O., Share, P. E., Beaucé, E., Hollis, D., and Lecocq, T. Train Traffic as a Powerful Noise Source for Monitoring Active Faults with Seismic Interferometry. *Geophysical Research Letters*, 46(16):9529–9536, Aug. 2019. doi: 10.1029/2019GL083438.
- Colombi, A., Boschi, L., Roux, P., and Campillo, M. Green's Function Retrieval through Cross-Correlations in a Two-Dimensional Complex Reverberating Medium. *The Journal of the Acoustical Society of America*, 135(3):1034–1043, Mar. 2014. doi: 10.1121/1.4864485.
- Crameri, F. Scientific Colour Maps. Sept. 2021. doi: 10.5281/ZENODO.5501399.
- Dales, P., Audet, P., and Olivier, G. Seismic Interferometry Using Persistent Noise Sources for Temporal Subsurface Monitoring. *Geophysical Research Letters*, 44(21):10,863–10,870, 2017. doi: 10.1002/2017GL075342.
- de Ridder, S. A. L. and Biondi, B. L. Ambient Seismic Noise Tomography at Ekofisk. *GEOPHYSICS*, 80(6):B167–B176, Nov. 2015. doi: 10.1190/geo2014-0558.1.
- Droznin, D., Shapiro, N., Droznina, S. Y., Senyukov, S., Chebrov, V., and Gordeev, E. Detecting and Locating Volcanic Tremors on the Klyuchevskoy Group of Volcanoes (Kamchatka) Based on Correlations of Continuous Seismic Records. *Geophysical Journal International*, 203(2):1001–1010, Nov. 2015. doi: 10.1093/gji/ggv342.
- Hadziioannou, C., Larose, E., Coutant, O., Roux, P., and Campillo, M. Stability of Monitoring Weak Changes in Multiply Scattering Media with Ambient Noise Correlation: Laboratory Experiments. *The Journal of the Acoustical Society of America*, 125(6):3688–3695, June 2009. doi: 10.1121/1.3125345.
- Li, L., Boué, P., and Campillo, M. Observation and Explanation of Spurious Seismic Signals Emerging in Teleseismic Noise Correlations. *Solid Earth*, 11(1):173–184, 2020. doi: 10.5194/se-11-173-2020.
- Lin, F.-C., Moschetti, M. P., and Ritzwoller, M. H. Surface Wave Tomography of the Western United States from Ambient Seismic Noise: Rayleigh and Love Wave Phase Velocity Maps. *Geophysical Journal International*, 173(1):281–298, 2008. doi: 10.1111/j.1365-246X.2008.03720.x.
- Lobkis, O. I. and Weaver, R. L. On the Emergence of the Green's Function in the Correlations of a Diffuse Field. *J. Acoust. Soc. Am.*, 110(3011):7, 2001. doi: 10.1121/1.1417528.
- Margerin, L., Planès, T., Mayor, J., and Calvet, M. Sensitivity Kernels for Coda-Wave Interferometry and Scattering Tomography: Theory and Numerical Evaluation in Two-Dimensional Anisotropically Scattering Media. *Geophysical Journal International*, 204(1):650–666, Jan. 2016. doi: 10.1093/gji/ggv470.
- Nakata, N., Gualtieri, L., and Fichtner, A., editors. *Seismic Ambient Noise*. Cambridge University Press, Cambridge, 2019. doi: 10.1017/9781108264808.
- Neuffer, T., Kremers, S., Meckbach, P., and Mistler, M. Characterization of the Seismic Wave Field Radiated by a Wind Turbine. *Journal of Seismology*, 25(3):825–844, June 2021. doi: 10.1007/s10950-021-10003-6.
- Retailleau, L., Boué, P., Stehly, L., and Campillo, M. Locating Microseism Sources Using Spurious Arrivals in Intercontinental Noise Correlations. *Journal of Geophysical Research: Solid Earth*, 122(10):8107–8120, 2017. doi: 10.1002/2017JB014593.
- Schippkus, S., Zigone, D., Bokelmann, G. H. R., and the AlpArray Working Group. Ambient-Noise Tomography of the Wider Vienna Basin Region. *Geophysical Journal International*, 215(1):102–117, June 2018. doi: 10.1093/gji/ggy259.
- Schippkus, S., Garden, M., and Bokelmann, G. Characteristics of the Ambient Seismic Field on a Large-N Seismic Array in the Vienna Basin. *Seismological Research Letters*, 91(5):2803–2816, July 2020. doi: 10.1785/0220200153.
- Snieder, R., Wapenaar, K., and Larner, K. Spurious Multiples in Seismic Interferometry of Primaries. *GEOPHYSICS*, 71(4):SI111–SI124, July 2006. doi: 10.1190/1.2211507.
- Snieder, R., van Wijk, K., Haney, M., and Calvert, R. Cancellation of Spurious Arrivals in Green's Function Extraction and the Generalized Optical Theorem. *Physical Review E*, 78(3):036606, Sept. 2008. doi: 10.1103/PhysRevE.78.036606.
- Stehly, L., Fry, B., Campillo, M., Shapiro, N. M., Guilbert, J., Boschi, L., and Giardini, D. Tomography of the Alpine Region from Observations of Seismic Ambient Noise. *Geophysical Journal International*, 178(1):338–350, July 2009. doi: 10.1111/j.1365-246X.2009.04132.x.
- Steinmann, R., Hadziioannou, C., and Larose, E. Effect of Centimetric Freezing of the near Subsurface on Rayleigh and Love Wave Velocity in Ambient Seismic Noise Correlations. *Geophysical Journal International*, 224(1):626–636, Jan. 2021. doi: 10.1093/gji/ggaa406.
- Wapenaar, K., Fokkema, J., and Snieder, R. Retrieving the Green's Function in an Open System by Cross Correlation: A Comparison of Approaches (L). *The Journal of the Acoustical Society of America*, 118(5):2783–2786, Nov. 2005. doi: 10.1121/1.2046847.
- Wapenaar, K., Draganov, D., Snieder, R., Campman, X., and Verdel, A. Tutorial on Seismic Interferometry: Part 1 — Basic Principles and Applications. *GEOPHYSICS*, 75(5):75A195–75A209, Sept. 2010. doi: 10.1190/1.3457445.
- Weaver, R. L. Equipartition and Retrieval of Green's Function. *Earthquake Science*, 23(5):397–402, Oct. 2010. doi: 10.1007/s11589-010-0738-2.
- Wegler, U. and Sens-Schönfelder, C. Fault Zone Monitoring with Passive Image Interferometry. *Geophysical Journal International*, 168(3):1029–1033, Mar. 2007. doi: 10.1111/j.1365-246X.2006.03284.x.
- Zeng, X. and Ni, S. A Persistent Localized Microseismic Source near the Kyushu Island, Japan. *Geophysical Research Letters*, 37(24), 2010. doi: 10.1029/2010GL045774.
- Zigone, D., Ben-Zion, Y., Campillo, M., and Roux, P. Seismic Tomography of the Southern California Plate Boundary Region from Noise-Based Rayleigh and Love Waves. *Pure and Applied Geophysics*, 172(5):1007–1032, 2015. doi: 10.1007/s00024-014-0872-1.

Supplementary Material

S1 Avoiding erroneous group-velocity measurements

One strategy to avoid erroneous group-velocity measurements (Fig. 3) is to carefully select which parts of the correlation functions to measure velocities on. The goal is to avoid all cases where interference occurs and may bias measurements. We propose to make the selection in two steps: first a rough causal/acausal selection based on geometry (this is already sufficient in the case of a stronger boundary source contribution), and second a windowing function around expected arrival times, which is necessary if the isolated source causes the stronger contribution.

In a first step, we select the line perpendicular to the line connection \mathbf{r}_M and \mathbf{r}_N and going through \mathbf{r}_M (dashed grey line in Fig. S1). West of this line, we measure group travel times on the acausal part of the correlation functions, and East of the line on the causal part. Because the correlation wavefield contribution emerging from \mathbf{r}_N emerges at negative lapse time $\tau(\mathbf{r} = \mathbf{r}_N) = -|\mathbf{r}_M - \mathbf{r}_N|/c$, there can be no interference to the West of the defined line.

To the East of the line, where we measure on the causal part of the correlation function, the resulting errors depend on which contribution has higher amplitude. In the case of a higher contribution by the boundary sources (Fig. S1b), we have avoided all measurement errors except for stations very close to \mathbf{r}_M . These remaining errors occur for stations where $|\mathbf{r} - \mathbf{r}_M| \leq w$, with w the width of the wavelet, due to interference of causal and acausal parts of the correlation functions. Station pairs with distances shorter than a few wavelengths are commonly excluded in studies of seismic interferometry for this exact reason.

For the case of a stronger isolated source contribution (Fig. S1a), a circle of correct velocity measurements emerges to the East of the line, because this contribution propagates through the circle at negative lapse times. Because we pick at positive lapse times on this side, we pick the undisturbed contribution by the boundary sources. Outside of this circle and up to the defined line, measurements are affected by the contribution of the isolated source, because it has higher amplitudes.

A second criterion helps avoid those remaining measurement errors. We define a symmetric windowing function around the master station's location \mathbf{r}_M of expected arrival time windows and pick only within this windowing function (Fig. S2). We choose the half-width of the Ricker wavelet as the window width. In practice, due to unknown velocity structure, a wider windowing function would be needed. We show the the impact of the narrow windowing function to illustrate the best-case scenario one can reach with only a windowing function. The case of a stronger isolated noise source (Fig. S2) approaches the measurement errors one finds for a weaker isolated noise source (Figs. 3b and S2b).

Finally, if we combine the two criteria, we avoid velocity measurement errors for all station pairs except the

stations near \mathbf{r}_M , as described above (Fig. S3).

A different strategy may be to define the windowing function around the isolated noise source instead of the master station. Still, one would need a two-step approach and this would require more precise knowledge of the isolated source location. The strategy proposed above relies on the fact that the isolated source contribution is asymmetric, whereas the boundary source contribution is symmetric. If this is violated, a different strategy is necessary.

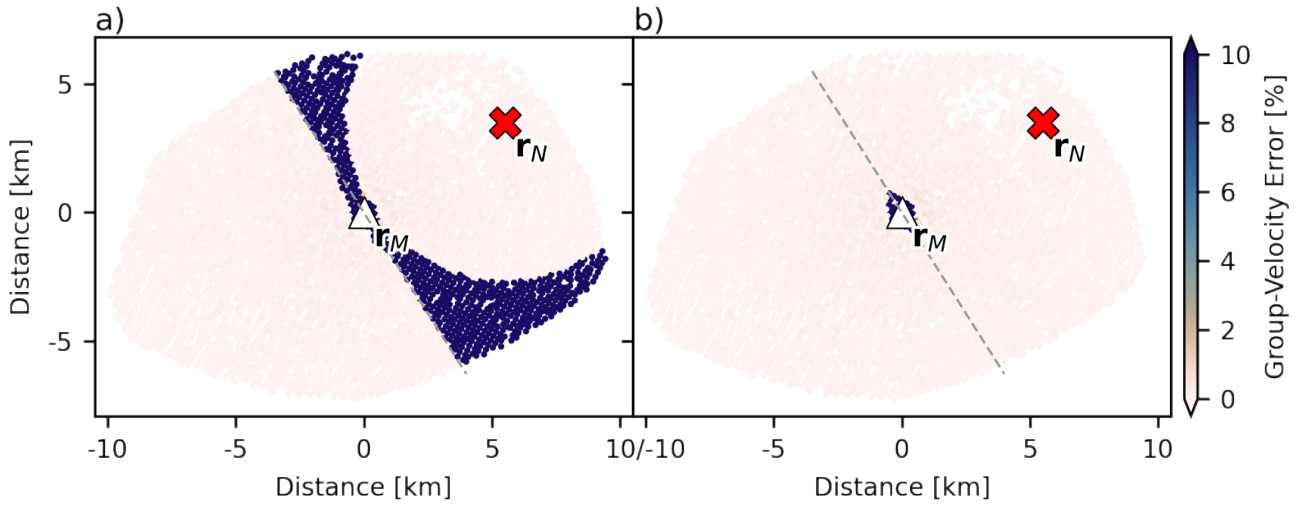


Figure S1 Same as Figure 3 when measuring travel times only on the causal part of correlation functions for stations to the East the dashed line, and only on the acausal part for stations to the West of the dashed line.

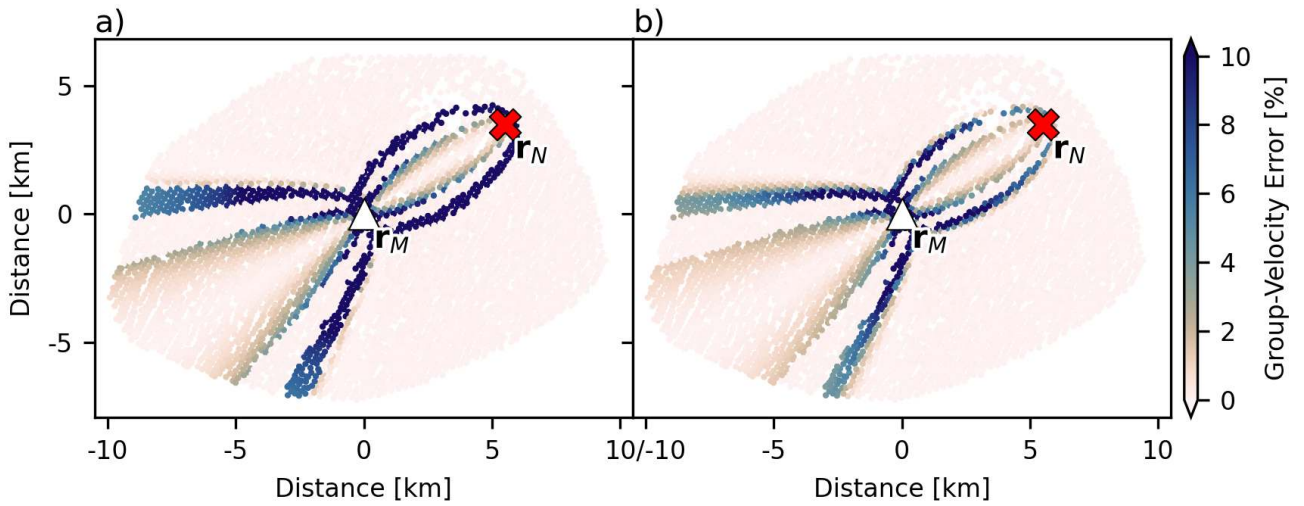


Figure S2 Same as Figure 3 when limiting measurements to an expected arrival window.

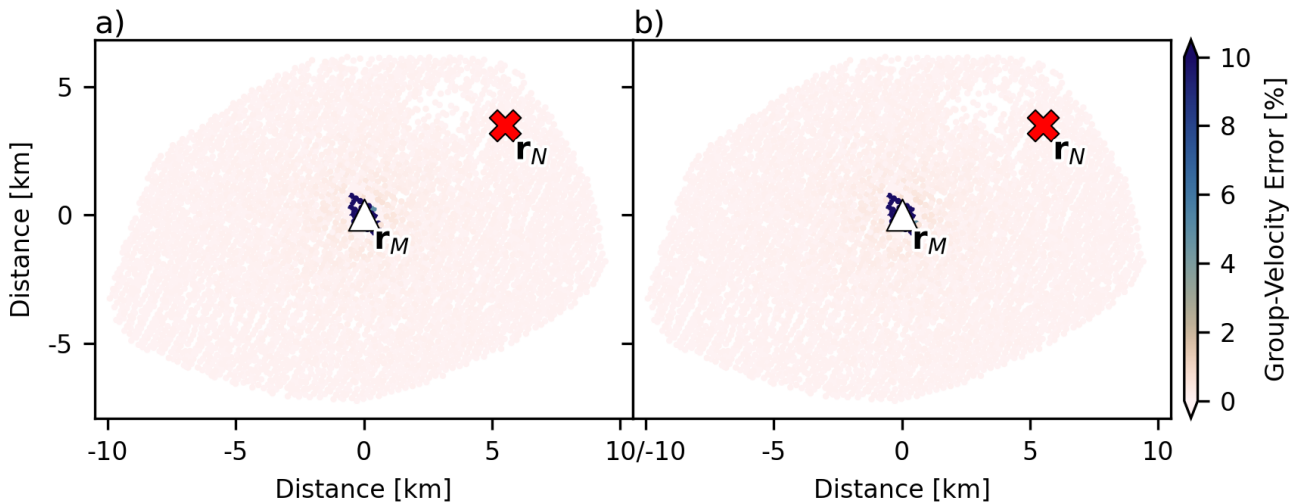


Figure S3 Same as Figure 3 when combining the causal/acausal selection (Fig. S1) and the windowing function (Fig. S2).

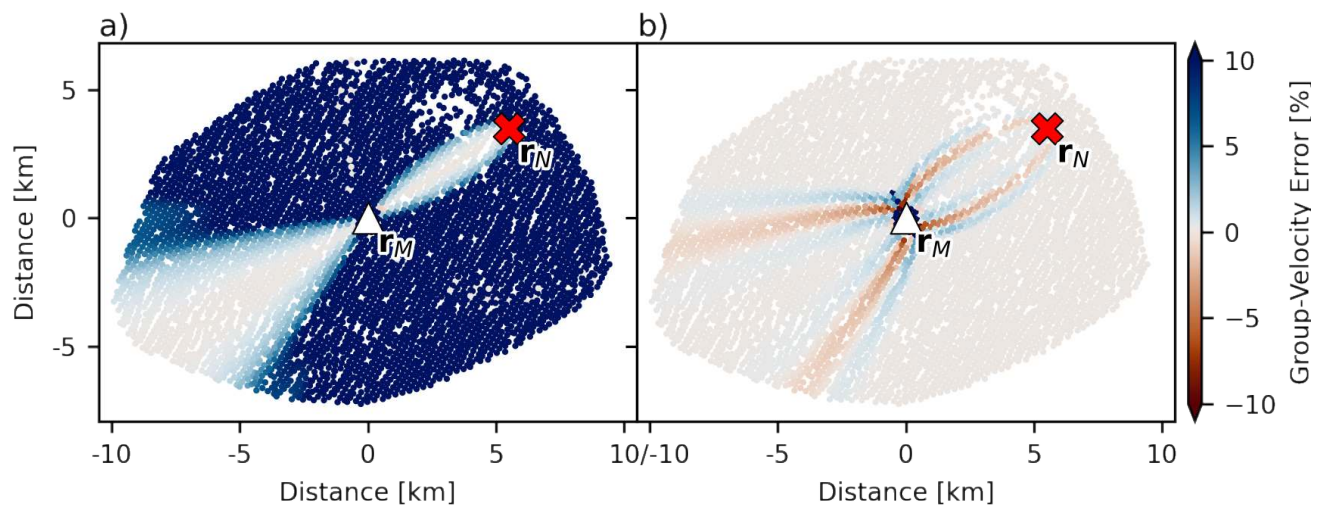


Figure S4 Same as Figure 3 for "folded" correlations, i.e., the causal and acausal parts of the correlation function are stacked.

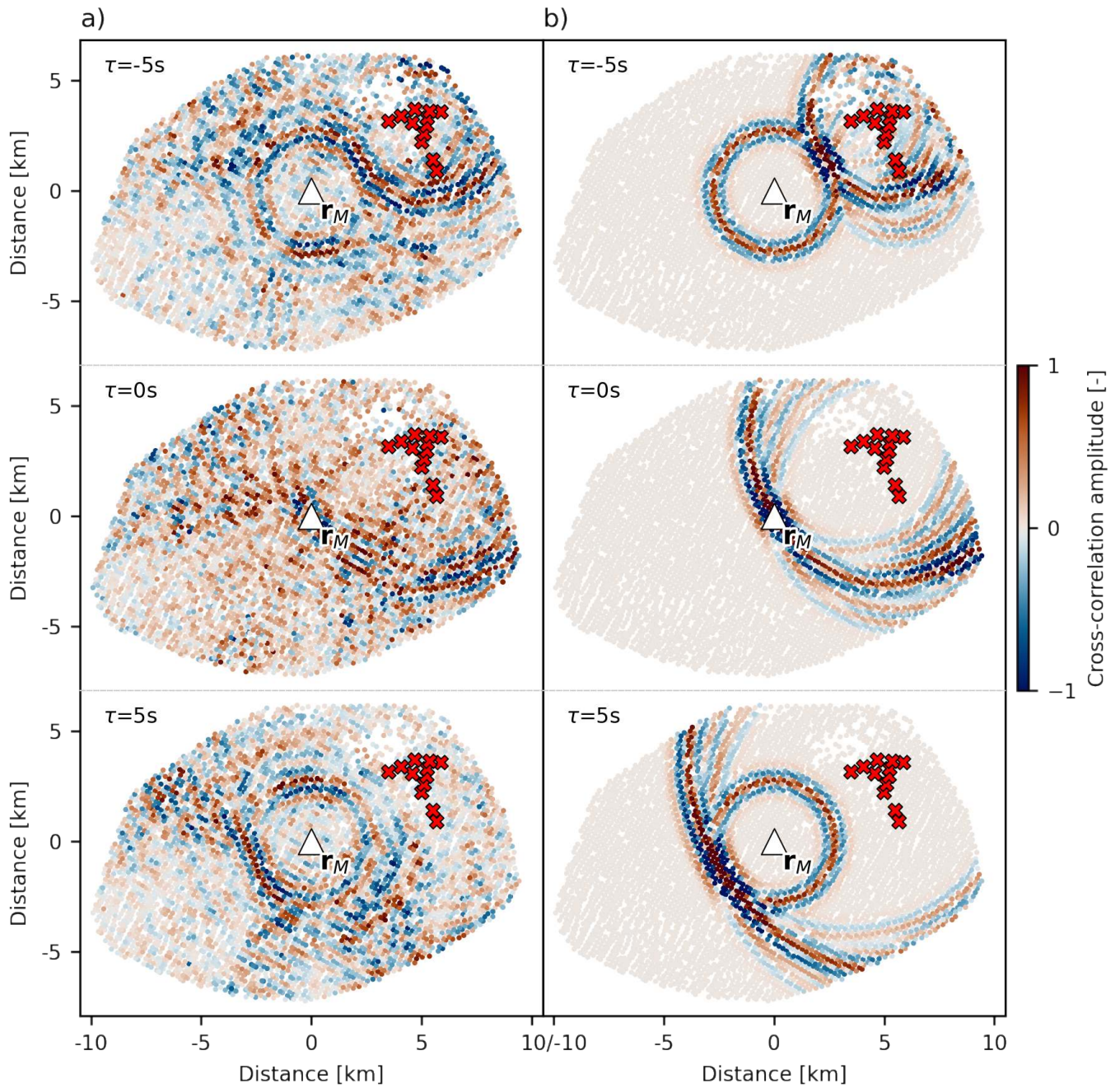


Figure S5 Same as Figure 2 but with all turbines of the wind farm Prottes-Ollersdorf treated as individual sources. Improved fit with the observations compared to Figure 2.

Locating the Nordstream explosions using polarization analysis

S. C. Stähler  * ¹, G. Zenhäusern  ¹, J. Clinton  ², D. Giardini  ¹

¹Institute for Geophysics, ETH Zürich, Switzerland, ²Swiss Seismological Service, ETH Zürich, Switzerland

Author contributions: *Conceptualization:* S. C. Stähler. *Software:* G. Zenhäusern. *Formal Analysis:* S. C. Stähler, G. Zenhäusern. *Writing - original draft:* S. C. Stähler. *Writing - Review & Editing:* S. C. Stähler, G. Zenhäusern, J. Clinton, D. Giardini. *Visualization:* G. Zenhäusern. *Supervision:* D. Giardini.

Abstract The seismic events that preceded the leaks in the Nordstream natural gas pipelines in the Baltic Sea have been interpreted as explosions on the seabed. We use a polarization-based location method initially developed for marsquakes to locate the source region without the need for a subsurface velocity model. We show that the 2 largest seismic events can be unambiguously attributed to the methane plumes observed on the sea surface. The two largest events can be located with this method, using 4 and 5 stations located around the source, with the uncertainties in elliptical bounds of 30×30 km and 10×60 km, respectively. We can further show that both events emitted seismic energy for at least ten minutes after the initial explosion, indicative of resonances in the water column or the depressurizing pipeline.

Zusammenfassung Die Lecks in den Röhren der beiden Nord-Stream-Pipelines wurden von zwei signifikanten Seebeben begleitet. Der Charakter dieser Seebeben spricht gegen einen tektonischen Prozess und für eine Explosion, gefolgt von schneller Dekompression des Gases. Wir verwenden eine Polarisationsanalyse, die die Richtung der Bodenbewegung analysiert, um die Beben zu lokalisieren. Diese Methode wurde ursprünglich entwickelt, um die Epizentren von Beben auf dem Mars mit einem einzelnen Seismometer zu bestimmen. Wir zeigen, dass mithilfe von 5 Stationen in der Nähe der westliche Ostsee die beiden Explosionen sicher den an der Oberfläche beobachteten Methan-Strudeln zugeordnet werden können. Darüber hinaus können wir zeigen, dass auf die Explosionen ein mindestens zehnminütiger energiereicher Dekompressionsprozess folgte. Mehrere Resonanzfrequenzen in den analysierten Signalen deuten auf Reverberationen in der Wassersäule oder den geplatzten Leitungen hin.

Non-technical summary The leaks in the Nordstream pipelines, which transport natural gas from the Siberian gas fields to central and western Europe have been accompanied by seismic events consistent with underwater explosions. Seismic network operators located these explosions using the arrival times of different seismic wave types (P-waves, S-waves), that travel with different velocities. However, these velocities depend on the geological structure of a region and are often not well known, specifically in locations without many earthquakes. We therefore apply a method that uses the polarization, i.e. the direction, in which the ground is moving to determine the direction towards the seismic events. Using 5 stations around the Western Baltic Sea, we show that the two seismic events are located next to the observed gas leaks. We also show that the seismic events consisted of an initial explosion followed by an at least ten minute long process near the source, likely related to the rapid decompression of the pipeline and sound reflections between the sea floor and the surface.

Introduction

The catastrophic leakage events that occurred in the Nordstream 1 and 2 natural gas pipelines in the Baltic Sea on 26 September 2022 generated global interest due to their significance for the European gas supply and the relationship between the Russian Federation and the Western European nations at each end of the pipeline. Shortly after 02:00 local time, a pressure drop was noticed at the German (western) end of the pipeline by the operators. Later, Danish military intelligence reported large methane plumes at the sea surface and restricted the area to marine traffic (Navigational warning NW-230-22 by the Danish Marine Authority). A sec-

ond larger event occurred that evening shortly after 19:00 local time (17:00 UTC) and resulted in a second methane plume at the surface (NW-237-22). Despite the fact that the pipelines were not transporting any gas at the time of the leak, they were fully pressurized and thus several million tons of methane were released after the leak. A few hours after the initial leak, the Swedish national seismic network SNSN at Uppsala University (Lund et al., 2021) reported an earthquake of $M_L = 2.7$ near the now-confirmed location of the leak, based on picking arrival times of seismic waves (SNSN, 1904, event 2022092603_Y4GNpS). The second event was also reported by SNSN as $M_L = 3.1$ (SNSN, 1904, event 20220926135_nj3BWW), close to the location of the second leak, clearly on the Nordstream 2 pipeline. Since

Production Editor:
Kiran Kumar Thingbaijam
Handling Editor:
Ryo Okuwaki
Copy & Layout Editor:
Théa Ragon

Received:
October 7, 2022
Accepted:
October 26, 2022
Published:
October 28, 2022

*Corresponding author: mail@simonstaehler.com

	Event 1		Station	P arrival	S arrival	Back-azimuth [deg]
Origin time	00:03:24		UP.DEL	00:03:55	00:04:25	153 (142-165)
Local time	02:03:24		PL.GKP	00:04:37	00:04:48	-
Latitude	54.768		DK.BSD	00:03:32	-	125 (111-139)
Longitude	15.431		DK.LLD	00:04:00	-	100 (71-125)
Magnitude	2.7		KQ.PEEM	00:03:50	00:04:08	54 (20-81)
	Event 2A	Event 2B	Station	P arrival	S arrival	Back-azimuth [deg]
Origin time	17:03:50	17:03:58	UP.DEL	17:04:15	17:04:37	135 (128-143)
Local time	19:03:50	19:03:58	PL.GKP	17:04:27	-	325 (265-2)
Latitude	55.6	55.617	DK.BSD	17:04:03	17:04:11	55 (37-70)
Longitude	15.71	15.745	DK.LLD	17:04:30	-	85 (46-113)
Magnitude	3.1	3.1	KQ.PEEM	17:04:20	17:04:45	33 (356-79)

Table 1 Summary of key parameters from open accessible nearby stations. P and S-wave arrival times for each station with estimated back-azimuth. Back-azimuth uncertainty ranges are given in parentheses. All times are on 2022-09-26 (UTC), local time is in CEST. Event location, origin time and magnitudes are taken from the SNSN catalog (SNSN, 1904)

the Baltic Sea is a region of very low seismicity (Grünthal et al., 2008), it is plausible to identify these seismic events with the leaks and attribute them to an explosion. The localization was facilitated by the relatively high amplitude of the signal, so that its arrival time could be observed on tens of stations. We here present an approach that uses a minimum number of stations and does not require a prior velocity model.

Seismic detection of man-made explosions is a task that dates back to the mid-20th century, when nuclear explosions were monitored by both super-powers. Coincidentally, the Norwegian Seismic Array (NORSAR), which first reported the Nordstream seismic events considered in this study, was set up precisely for this task (Schweitzer et al., 2021). In the early period for seismology, event detection and location was not done using global networks but rather by single arrays that determined the back-azimuth and incident angle of seismic body waves by measuring the apparent horizontal slowness, i.e. the difference in arrival times, over a network of 10–100 km aperture. The main motivation for using single arrays was that in the 1970s and 1980s, near real-time communication, as well as clock synchronization was not guaranteed in a global seismic network, so local arrays provided a more robust way to observe nuclear test signals from regional to teleseismic distances. Based on differential arrival time of seismic phases, the incident angle and the back-azimuth, an event could be located within the territory of a Nuclear power and attributed to a known test site, and its magnitude estimated to obtain the yield of a nuclear test. Improvement came with the installation of a global seismic network of digital recorders connected via satellite, by using arrival times at different stations and triangulate the source location. This however requires a reasonable model of seismic velocities. In many regions of the world such models do not exist, coincidentally also in the Baltic Sea, a mostly aseismic region. The Baltic sea basin itself is an eroded basin created during the the Pleistocene glaciation (Hall and van Boeckel, 2020), similar to the Great Lakes in Northern America. The sea floor is covered with several 100 m of soft quaternary sediments but does show a surprising complex-

ity. Specifically south of Bornholm, a system of graben faults points SW/NE, and the shallower Arnager block has exposed cretaceous bedrock at the surface. Hence the seismic velocity profile in the uppermost kilometers is complex (Ostrovsky et al., 1994; Vejrbæk et al., 1994). The low slope however makes landslides unlikely.

We therefore apply a method for event localization that does not require a seismic velocity model and which was initially developed to locate seismic events on Mars (Zenhäusern et al., 2022a). On Mars, we separately determine the distance and direction of the marsquake as seen from a single seismic station (Böse et al., 2016). The direction (back-azimuth) is determined based on the polarization of the main body waves: P and S. Since the P-wave is a compressional wave, its particle motion is in the direction of propagation, i.e. on a line pointing away from the epicenter. The S-wave is transversally polarized, i.e. orthogonal to the direction of polarization, which helps to determine the back-azimuth if the P-wave is not sufficiently polarized (e.g. low signal amplitude, scattering effects). The method is described in Zenhäusern et al. (2022a), where successful application to teleseismic events on Earth is demonstrated. It is now routinely applied by the InSight Marsquake Service (MQS, Clinton et al., 2021; Ceylan et al., 2022) to locate seismic events on Mars, where only a single seismometer (Lognonné et al., 2019) operates and thus classical multi-station methods cannot be applied.

Method

We apply a complete polarization analysis of P and S body waves to determine the back-azimuth of seismic events. The three-component seismogram is transformed into time–frequency domain using a continuous wavelet transform (Kristekova et al., 2006) to produce a time–frequency dependent complex spectral matrix. For each time–frequency pixel, the matrix is decomposed into eigenvectors to obtain information on the instantaneous polarization of the seismic signal. This method is based on the work of (Samson, 1983) and was first applied to seismic data by Schimmel and Gallart

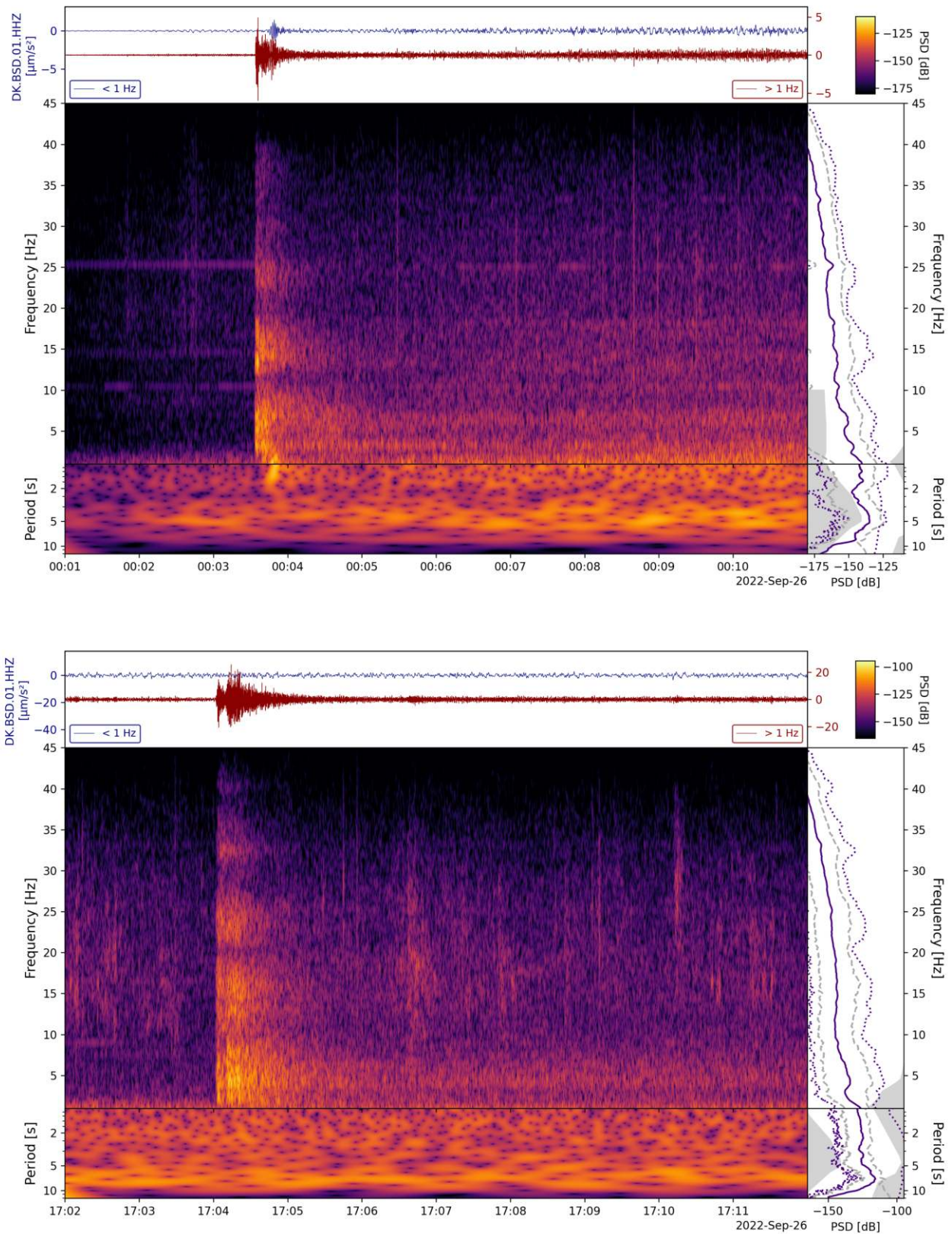


Figure 1 Seismograms and spectrograms of both seismic events from station DK.BSD. The top subplot in each combined figure shows seismograms filtered above (red) and below (blue) 1 Hz. For better visibility of long-period energy, the spectrogram is plot on a logarithmic scale below 1 Hz. In the right subplot, the median (solid purple line) and 5th, and 25th (purple dotted and dashed grey), as well as 75th and 95th percentiles (dashed grey and purple dotted) of acceleration are plot together with the NLNM and NHHM as grey areas (Peterson, 1993). The 95th percentiles of the spectrogram shows the continued excitation of several bands after the event.

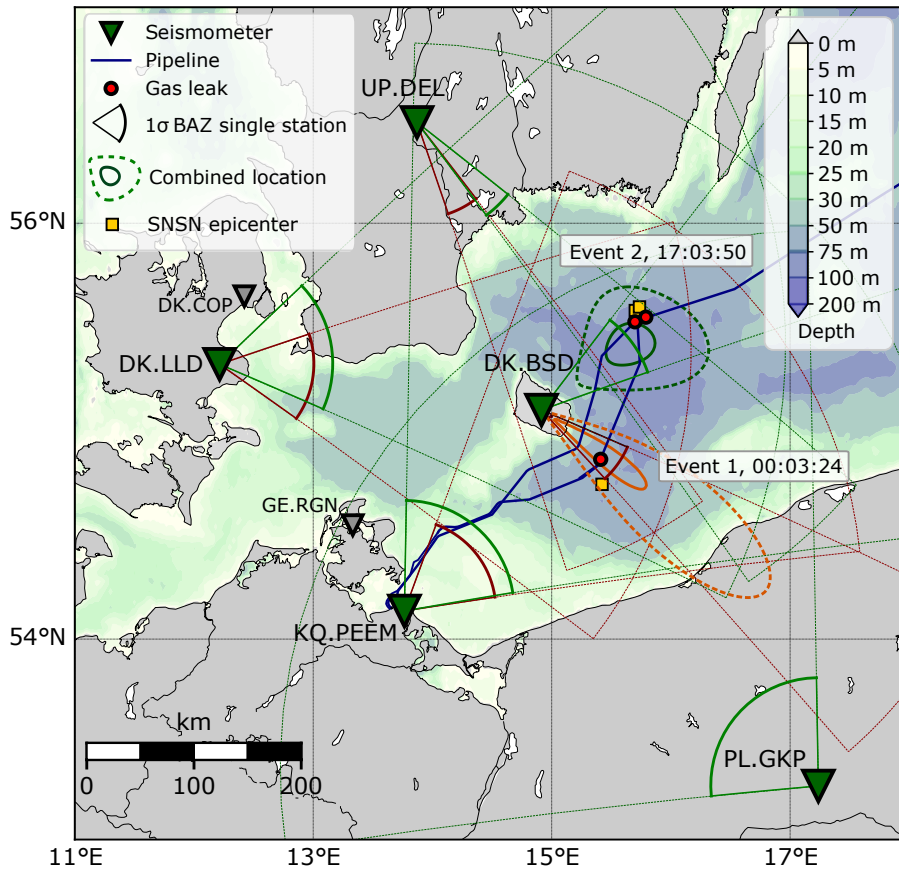


Figure 2 Overview map of the Western Baltic Sea. We could obtain clear back-azimuths from four stations for event 1 (generally marked by red colors) and five for event 2 (marked by green colors). The grey triangles are stations where we detected an arrival, but could not obtain a clear polarization. Solid lines mark the 1 sigma location for each event combined from all usable stations, dashed lines the 2 sigma location. Event 1 is located less well, mainly due to the less favourable geometry of UP.DEL and DK.BSD, the two stations with best azimuth constraints. Squares mark epicenters from the SNSN catalog, leak locations (circles) are based on navigational warnings NW-230-22 and NW-237-22 by the Danish Maritime Authority. The bathymetry map uses the SRTM30_PLUS dataset (Becker et al., 2009), the pipeline can be obtained from OpenStreetMap (relation 2006544).

(2003). We use all open access stations from the European Integrated Data Archives (EIDA, Strollo et al., 2021) within 3° (333 km) great-circle-arc distance around the reported position of the leaks. We download all HHZ, HHN, and HHE channels (high-sensitivity seismometer, typically sampled at 100 Hz) and correct the data to displacement using EVALRESP as implemented in ObsPy (Krischer et al., 2015). We then manually scan the data of days 2022-09-25 and 2022-09-26, i.e. including the day before the leaks were reported, for signals of nearby, seismic events with energy above 10 Hz using daily spectrograms. As reported by SNSN, one event was found on 2022-09-26 00:03:24 UTC and a second event around 2022-09-26 17:03:50 UTC (see figure 1 for seismograms and spectrograms of both events.). Table 1 has an overview over all stations on which the events were clearly detectable. For each of these stations, we identify a P-wave arrival window and apply our back-azimuth analysis to it in a 15 second time window starting 5 seconds before the arrival. See figure 3 for an example of our polarization analysis plot (Zenhäusern et al., 2022a). Polarization plots for all investigated stations can be found in the supplement. To locate the event, we combine the probability $p_i(\alpha)$ of multiple sta-

tions i as a function of backazimuth α by multiplication

$$p_{\text{total}}(\varphi, \theta) = \prod_{i=1}^N p_i(\alpha(\varphi, \theta)), \quad (1)$$

to obtain a probability density function for latitude θ and longitude φ . From this density function, a maximum likelihood value and an error ellipse is obtained and plotted in figure 2.

Results

We find clearly polarized P-waves at 4 (event 1) and 5 (event 2) stations in a distance range from 50 to 250 km. The clearest observation is on station DK.BSD located on Bornholm Island (see figure 3 for the first explosion), with a mostly marine path. For both events, the back-azimuth is constrained to less than 30° (table 1). The energy in the seismograms ranges from 0.2 to 40 Hz, with a clear P-wave but no obvious S-wave. A Rayleigh wave with clear elliptical polarization arrives 10 seconds after the P. The overlap between S and Rayleigh is consistent with other quakes in distances of 50-100 km. The lack of a Love wave or transversally polarized S-waves (SH) supports an isotropic source, such as an explosion. The

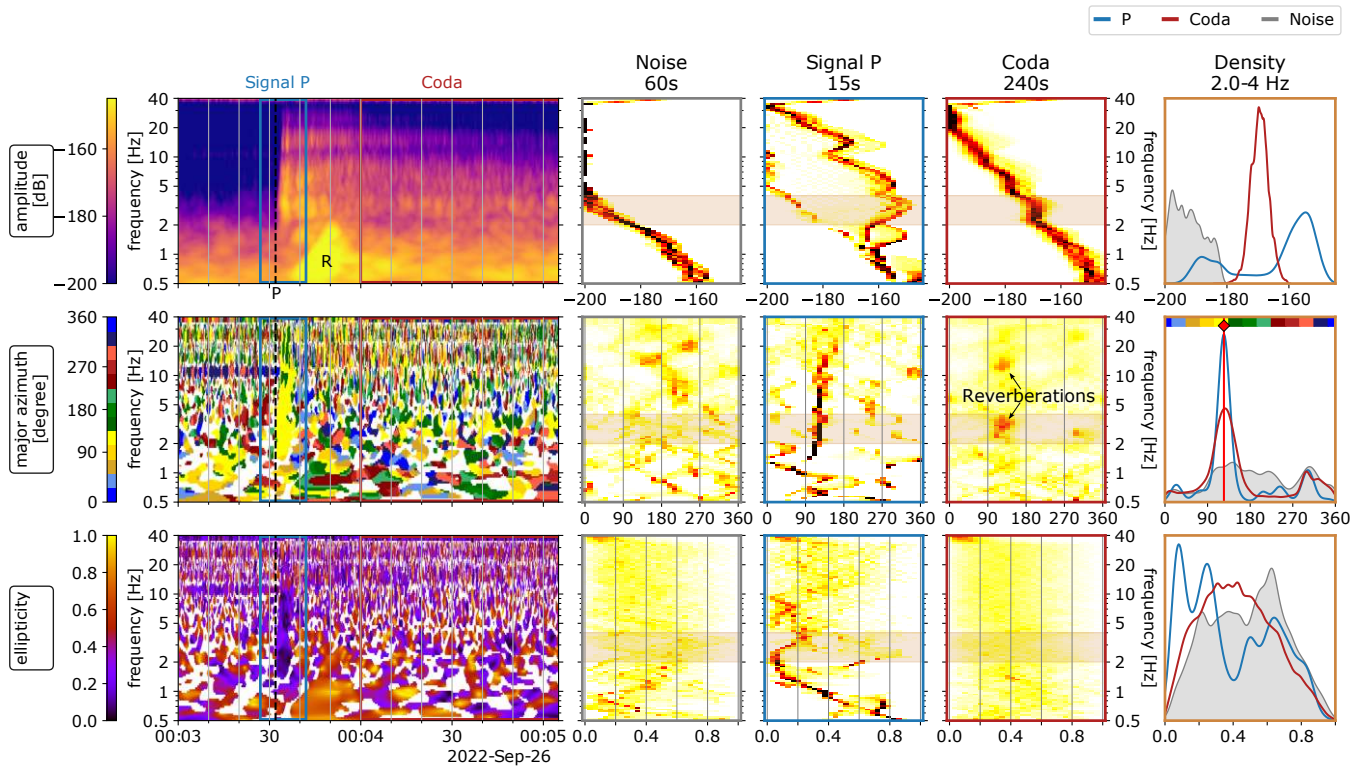


Figure 3 Polarization analysis of event 1 (2022-09-26 00:03:24 UTC) for Station DK.BSD. Shown are the amplitude in $(m/s)^2/Hz$ [dB] (top row), azimuth (middle row), and ellipticity (bottom row). A linear signal corresponds to a low ellipticity. (left) Time-frequency plots for the different parameters, with marked time windows. The noise window is from 2 min to 1 min before the P pick (outside of depicted time range). (columns 2-4) Histogram depiction of the time windows seen on the left. The x-axis corresponds to the scale of the respective colorbar on the left. (right) Kernel density estimate (KDE) calculated from the time window between 2–4 Hz (shaded area in histogram plots). The x-axis again corresponds to the colorbar scale. The KDE peak of the P-wave is marked with a red vertical line and diamond. The signals from this first event shows a clearly polarized P-wave up to 20 Hz, a Rayleigh wave between 0.5 and 2 Hz and sustained polarization after the event. The back-azimuth is estimated to 125 ± 14 degree from the P-wave. After the P-wave, polarization in the same direction is seen at 3.5 and 15 Hz, estimated as a continued pulsation at the source location. This is visible in the coda of the event, where there are distinct clusters (row 2, column 4; marked with 'Reverberations'). Further, the KDE of the coda shows a similar azimuth distribution as the P-window, albeit with lower signal amplitude.

signal has an overall duration of at least 10 minutes before falling to pre-event noise levels. SNSN reported two separate explosions for the second seismic event, separated by 8 seconds, which we find to be consistent with the observation that the second pulse has the same polarization attributes as the first.

The second-closest station KQ.PEEM in Peenemünde, Germany, in 100 (event 1) and 150 km (event 2) distance has clearly visible signals as well. Both P and S-arrivals are visible, but back-azimuths are less constrained (60° uncertainty for event 1, 80° for event 2). The reduced amplitude is possibly due to the extended shallow sea over half of the distance to the events. The third station, UP.DEL in Southern Sweden, is significantly clearer in signal and shows a comparable back-azimuth constraint to DK.BSD. Surprisingly, this works even for the first event, which is located behind the Bornholm island as seen from the station. The fourth station, DK.LLD, shows a similarly bad constraint as KQ.PEEM, which is plausible given a low amplitude and paths that cross the Bornholm island and the lands of Southern Sweden. A signal is visible on several other openly accessible stations in Germany, Denmark, and Sweden (e.g. DK.COP,

DK.LLD, GE.RGN, GR.BSEG, UP.VIKU), but the polarization analysis did not obtain any additional constraints on the source locations. Polarization plots for these stations can be found in the supplement. Multiplication of the probability density functions for all "good" stations results in source regions close to the reported leaks. The first event has a very elongated uncertainty ellipse. For this event, the stations DK.BSD and UP.DEL are almost located in a line. The actual leak, as given by the navigational warning NW-230-22 is located inside the 1σ region. For the second event, the stations are better positioned to constrain the location of the event very closely. The navigational warning NW-237-22 is just outside the 1σ region, mainly due to the broad uncertainty from DK.BSD. Together with the known geometry of the Nordstream pipelines and the locations of the methane plumes on the sea surface, an identification of the explosions with the seismic events seems plausible.

On stations DK.BSD, which is the closest station to either event, and UP.DEL, we find sustained polarization after the first event: The P-wave polarization is present in the coda for several minutes. This is a clear indication that the signal duration is not caused primarily

by scattering but that seismic energy was radiated from the source over an extended period, at least 15 minutes. An explanation for this could be continued release of gas under high pressure. We can further investigate the peaks in the spectrogram (fig. 1) at about 3.5, 8, 15 and 24 Hz for event 1 and about 4, 15, 23 and 32 Hz for event 2. The two peaks at 3.5 and 15 Hz are confirmed to be consistently polarized for event 1, while the others are difficult to resolve. Assuming a speed of sound of 1470 m/s (typical for the Western Baltic Sea in September, see Grelowska, 2016), these two peaks would correspond to wave lengths of about 98 and 420 meter, respectively. The water depth at the source is 70 meter, so this suggests that the 15 Hz signal could be an actual reverberation within the water column, and the one at 23 and 32 Hz overtones. The 3.5 Hz signal (with the longer wavelength) is more likely an effect of the leak itself, potentially the Minnaert resonance of rising gas bubbles (Devaud et al., 2008).

Additional stations like GE.RGN on the Rügen island (Germany) or DK.COP near Kopenhagen were tried, but had poorer azimuth constraints than neighbouring stations. We thus did not include them in this analysis and figure. The SNSN operates several more stations in Southern Sweden that might give additional constraints and which were used for their location, but data from these was not publicly available at the time of writing.

Conclusion

The analysis of P-wave polarization on the signal of the Nordstream pipeline explosions shows the strong potential of the method for a model-agnostic location of seismic events. We clearly associate both leaks with the separate seismic events. Location uncertainties from 4 and 5 stations' polarization were larger than those based on travel time methods, but the latter used significantly more stations. As opposed to travel time methods, our approach does not need a velocity model, is robust against timing errors on stations and can easily be started from a single station, as soon as data is available there.

Both events show an absence of strong S-waves, consistent with a mostly isotropic source, such as an explosion. The closest station, DK.BSD on Bornholm, shows a clearly polarized coda, indicative of an ongoing source process over at least 10 minutes with several strong resonant peaks. This documents that polarization analysis of a small number of seismometer located onshore has the capability to locate and characterize seismic events in the water column.

Acknowledgements

We would like to thank editor Ryo Okuwaki and Kiran K. S. Thingbaijam for providing reviews that helped improve the manuscript. We would also like to thank Alice-Agnes Gabriel for helping improve the German abstract. The authors recognise support from the ETH+ funding scheme (ETH+02 19-1: "Planet Mars").

Data and code availability

The polarization code is available on github, the version used here on Zenodo (Zenhäusern et al., 2022b). Figure 1 was created with dailyspec (Stähler, 2022)

Seismic data were handled with ObsPy (Krischer et al., 2015). Calculations in Python were done with NumPy (Harris et al., 2020) and SciPy (Virtanen et al., 2020), and the results were visualized with Matplotlib (Hunter, 2007), seaborn (Waskom, 2021), and basemap. Seismic Data was collected using obspyDMT (Hosseini and Sigloch, 2017) from EIDA (<https://www.orfeus-eu.org/data/eida/>). We recognise the following networks for providing data: Network DK, GE (GEOFON Data Centre, 1993), PL, UP (Lund et al., 2021) and KQ (Christian Albrechts - Universität zu Kiel, 2017)

References

- Becker, J. J., Sandwell, D. T., Smith, W. H. F., et al. Global Bathymetry and Elevation Data at 30 Arc Seconds Resolution: SRTM30_PLUS. *Mar. Geod.*, 32(4):355–371, 2009. doi: 10.1080/01490410903297766.
- Böse, M., Clinton, J. F., Ceylan, S., et al. A Probabilistic Framework for Single-Station Location of Seismicity on Earth and Mars. *Phys. Earth Planet. Inter.*, 262:48–65, 2016. doi: 10.1016/j.pepi.2016.11.003.
- Ceylan, S., Clinton, J. F., Giardini, D., Stähler, S. C., et al. The marsquake catalogue from InSight, sols 0–1011. *Physics of the Earth and Planetary Interiors*, page 106943, Sept. 2022. doi: 10.1016/j.pepi.2022.106943.
- Christian Albrechts - Universität zu Kiel. Kiel University Earthquake Monitoring, 2017. doi: 10.7914/SN/KQ.
- Clinton, J. F., Ceylan, S., van Driel, M., et al. The Marsquake catalogue from InSight, sols 0–478. *Phys. Earth Planet. Inter.*, 310 (October 2020), 2021. doi: 10.1016/j.pepi.2020.106595.
- Devaud, M., Hocquet, T., Bacri, J.-C., and Leroy, V. The Minnaert bubble: An acoustic approach. *Eur. J. Phys.*, 29(6):1263–1285, Sept. 2008. doi: 10.1088/0143-0807/29/6/014.
- GEOFON Data Centre. GEOFON Seismic Network. 1993. doi: 10.14470/TR560404.
- Grelowska, G. Study of Seasonal Acoustic Properties of Sea Water in selected Waters of the Southern Baltic. *Pol. Marit. Res.*, 23 (1(89)):25–30, Apr. 2016. doi: 10.1515/pomr-2016-0004.
- Grünthal, G., Stromeier, D., Wylegalla, K., et al. The Mw 3.1–4.7 earthquakes in the southern Baltic Sea and adjacent areas in 2000, 2001 and 2004. *J Seismol*, 12(3):413–429, July 2008. doi: 10.1007/s10950-008-9096-0.
- Hall, A. and van Boeckel, M. Origin of the Baltic Sea basin by Pleistocene glacial erosion. *GFF*, 142(3):237–252, July 2020. doi: 10.1080/11035897.2020.1781246.
- Harris, C. R., Millman, K. J., van der Walt, S. J., et al. Array Programming with NumPy. *Nature*, 585(February):357–362, 2020. doi: 10.1038/s41586-020-2649-2.
- Hosseini, K. and Sigloch, K. ObspyDMT: A Python toolbox for retrieving and processing large seismological data sets. *Solid Earth*, 8(5):1047–1070, Oct. 2017. doi: 10.5194/se-8-1047-2017.
- Hunter, J. D. Matplotlib: A 2D graphics environment. *Comput. Sci. Eng.*, 9(3):90–95, 2007. doi: 10.1109/MCSE.2007.55.
- Krischer, L., Megies, T., Barsch, R., et al. ObsPy: A bridge for seismology into the scientific Python ecosystem.

- Comput. Sci. Discov.*, 8(1):014003–014003, 2015. doi: 10.1088/1749-4699/8/1/014003.
- Kristekova, M., Kristek, J., Moczo, P., and Day, S. M. Misfit Criteria for Quantitative Comparison of Seismograms. *Bull. Seismol. Soc. Am.*, 96(5):1836–1850, Oct. 2006. doi: 10.1785/0120060012.
- Lognonné, P., Banerdt, W. B., Giardini, D., Pike, W. T., et al. SEIS: Insight’s Seismic Experiment for Internal Structure of Mars. *Space Sci. Rev.*, 215(1):12–12, Jan. 2019. doi: 10.1007/s11214-018-0574-6.
- Lund, B., Schmidt, P., Hossein Shomali, Z., and Roth, M. The Modern Swedish National Seismic Network: Two Decades of Intraplate Microseismic Observation. *Seismological Research Letters*, 92(3):1747–1758, Mar. 2021. doi: 10.1785/0220200435.
- Ostrovsky, A. A., Flueh, E. R., and Luosto, U. Deep seismic structure of the Earth’s crust along the Baltic Sea profile. *Tectonophysics*, 233(3):279–292, May 1994. doi: 10.1016/0040-1951(94)90246-1.
- Peterson, J. Observations and Modeling of Seismic Background Noise. Technical report, Albuquerque, New Mexico, 1993.
- Samson, J. C. Pure states, polarized waves, and principal components in the spectra of multiple, geophysical time-series. *Geophysical Journal International*, 72(3):647–664, Mar. 1983. doi: 10.1111/j.1365-246X.1983.tb02825.x.
- Schimmel, M. and Gallart, J. The use of instantaneous polarization attributes for seismic signal detection and image enhancement. *Geophys. J. Int.*, 155(2):653–668, 2003. doi: 10.1046/j.1365-246X.2003.02077.x.
- Schweitzer, J., Köhler, A., and Christensen, J. M. Development of the NORSAR Network over the Last 50 Yr. *Seismological Research Letters*, 92(3):1501–1511, Jan. 2021. doi: 10.1785/0220200375.
- SNSN. Swedish National Seismic Network. Uppsala University, Uppsala, Sweden. Other/Seismic network, 1904. doi: 10.18159/SNSN.
- Stähler, S. C. *dailySpec: V0.2*. Zenodo, Oct. 2022. doi: 10.5281/zenodo.7220311
- Strollo, A., Cambaz, D., Clinton, J., et al. EIDA: The European Integrated Data Archive and Service Infrastructure within ORFEUS. *Seismological Research Letters*, 92(3):1788–1795, Mar. 2021. doi: 10.1785/0220200413.
- Vejbæk, O. V., Stouge, S., and Poulsen, K. D. Palaeozoic tectonic and sedimentary evolution and hydrocarbon prospectivity in the Bornholm area. *Dan. Geol. Unders. Ser. A*, 34:1–23, Sept. 1994. doi: 10.34194/seriea.v34.7054.
- Virtanen, P., Gommers, R., Oliphant, T. E., et al. SciPy 1.0: Fundamental algorithms for scientific computing in Python. *Nat. Methods*, 17(3):261–272, 2020. doi: 10.1038/s41592-019-0686-2.
- Waskom, M. L. Seaborn: Statistical data visualization. *J. Open Source Softw.*, 6(60):3021, 2021. doi: 10.21105/joss.03021.
- Zenhäusern, G., Stähler, S. C., et al. Low-Frequency Marsquakes and Where to Find Them: Back Azimuth Determination Using a Polarization Analysis Approach. *Bulletin of the Seismological Society of America*, May 2022a. doi: 10.1785/0120220019.
- Zenhäusern, G., Stähler, S. C., and van Driel, M. Polarisation analysis for seismic data. Zenodo, Oct. 2022b. doi: 10.5281/zenodo.7220543.

Source Model and Characteristics of the 27 July 2022 M_W 7.0 Northwestern Luzon Earthquake, Philippines

Jeremy M. Rimando ^{1,2}, Amy L. Williamson ³, Raul Benjamin C. Mendoza ^{1,4}, Tiegan E. Hobbs ^{* 1,4,5}

¹Geological Survey of Canada – Pacific, Natural Resources Canada, 605 Robson St Suite 1500, Vancouver, BC V6B 5J3, Canada, ²School of Earth, Environment & Society, McMaster University, 1280 Main Street West, Hamilton, ON, L8S 4K1, Canada, ³Berkeley Seismological Laboratory, University of California Berkeley, 307 McCone Hall #4760, Berkeley, CA 94720-4760, USA, ⁴Department of Earth, Ocean and Atmospheric Sciences, University of British Columbia, 2207 Main Mall #2020, Vancouver, BC, V6T 1Z4, Canada, ⁵School of Earth and Ocean Sciences, University of Victoria, Bob Wright Centre A405, University of Victoria, Victoria BC V8W 2Y2, Canada

Author contributions: *Conceptualization:* J.M. Rimando. *Software:* A.L. Williamson, R.B.C. Mendoza. *Formal Analysis:* J.M. Rimando, A.L. Williamson, R.B.C. Mendoza, T.E. Hobbs. *Writing - original draft:* J.M. Rimando, A.L. Williamson, R.B.C. Mendoza, T.E. Hobbs. *Writing - Review & Editing:* J.M. Rimando, A.L. Williamson, R.B.C. Mendoza, T.E. Hobbs.

Abstract The geometry and kinematics of the causative fault of the 27 July 2022 moment magnitude (M_W) 7.0 earthquake, which is one of the strongest to hit northern and central Luzon in the past 30 years, were estimated through inverse modeling of line-of-sight interferometric synthetic aperture radar deformation. We modeled rupture along multiple candidate faults based on fit with the pattern of line-of-sight deformation, consistency with focal mechanisms, and compatibility with the known kinematics of the mapped active faults in the region. Our preferred fault model, located west of and parallel to the Abra River Fault (ARF), exhibits localized reverse-slip (average 67° rake) at 15–35 km down-dip. Peak slip occurs at 13–16 km depth, with 95 cm of pure reverse-slip. The existence of a reverse-slip dominated ARF-parallel fault rupture is consistent with a complex shear partitioning model, wherein the NW-SE oblique plate convergence is accommodated not only by the sinistral strike-slip Philippine Fault Zone and the major subduction zones, but also by minor faults in intervening crustal blocks.

Non-technical summary A magnitude 7.0 earthquake occurred in the Philippines on 27 July 2022, on the northern island of Luzon. The earthquake does not seem to have occurred on a known fault plane, given what is known about its surface displacement and the seismic energy it radiated. In this paper, we use satellite remote sensing data to try to determine the fault plane on which the earthquake ruptured. Although these data can be fit, to varying degrees, by different faults, our preferred model is a northerly aligned fault plane, dipping to the east. The slip on the fault is more vertical than horizontal, which is different from the other nearby mapped faults, which are primarily horizontal. This earthquake may be helping to accommodate NW-SE compressional stress in the Northern Philippines, caused by the motion of nearby tectonic plates.

Introduction

On 27 July 2022 at 08:43 local time (UTC +8), the northwestern region of the island of Luzon, northern Philippines was hit by a moment magnitude (M_W) 7.0 earthquake (Fig. 1 A and B). The epicenter was located 10 km south of Tayum, Abra (17.5°N , 120.7°E), and had a focal depth of ~ 20 km (Fig. 1 B); (PHIVOLCS, 2022a,b). Focal mechanisms produced both by the Philippine Institute of Volcanology and Seismology (PHIVOLCS) and the United States Geological Survey (USGS), consistently suggest oblique-reverse faulting on either a N-striking, E-dipping or a SW-striking, NW-dipping fault (Fig. 1 B); (PHIVOLCS, 2022b; USGS, 2022). The PHIVOLCS focal mechanism has a strike of 8° , a dip of 28° , and rake of

49° . The USGS focal mechanism has a strike of 0° , a dip of 35° , and a rake of 40° . In map view, the two-week aftershock distribution forms a swath that is ~ 50 km-wide and ~ 80 km-long in the WNW-ESE and NNE-SSW directions, respectively (PHIVOLCS, 2022a). In cross-section, the aftershocks form an inverted triangle (Fig. 1 C) that is 40 km wide near the surface and ~ 20 km deep, a distribution which makes it difficult to ascertain the preferred fault plane from seismicity alone.

Geological impacts observed on the ground by the PHIVOLCS earthquake quick response team included landslides, liquefaction-induced lateral spreads, ground fissures, sand boils, and sea level disturbances (PHIVOLCS, 2022c,d). While PHIVOLCS suggests the Abra River Fault (ARF) as a candidate fault for the earthquake rupture (PHIVOLCS, 2022d), the surface rupture

Production Editor:
Gareth Funning
Handling Editor:
Mathilde Radiguet
Copy & Layout Editor:
Claudia Reis

Received:
August 27 2022
Accepted:
October 19 2022
Published:
November 8 2022

*Corresponding author: tiegan.hobbs@nrcan-rncan.gc.ca

for this event has yet to be located and properly mapped.

A total of 11 fatalities, 609 injuries, 49,803 displaced persons, and ~US\$45 million in damages to major public infrastructure and to the agricultural sector was reported (NDRRMC, 2022). The intensity values and distributions, though slightly different depending on the reporting agency, are in agreement with the highest felt intensity being centered in the province of Abra. A modified Mercalli intensity value of 7.5 was reported by the USGS, and a Philippine earthquake intensity scale (PEIS) value of 7 was reported by PHIVOLCS, which also included the western coastal towns in the province of Ilocos Sur (USGS, 2022; PHIVOLCS, 2022d).

In the past 50 years, 11 $M_W > 6.5$ earthquakes have occurred within 250 km of the 2022 Luzon epicenter in Tayum, Abra (USGS, 2022). The largest earthquake in history to occur in northern Luzon was the 1990 M_W 7.7 Luzon Earthquake, which was associated with a ~120 km-long surface rupture along the Digdig Segment of the Philippine Fault Zone (Punongbayan et al., 1991-07-16; Nakata et al., 1996).

This study presents the first interferometric synthetic-aperture radar (InSAR)-based fault source model for the 2022 M_W 7.0 northwestern Luzon earthquake, providing information such as the possible location, geometry, and slip distribution. Such data can contribute to a better understanding of this particular event, as well as generally the styles, mechanisms, and distribution of deformation in the Philippines— a tectonically complex, seismically active region which could benefit from a more comprehensive mapping and accurate kinematic analysis of active structures. This kind of effort would enhance the country's capability to assess seismic hazards and risks.

Tectonic Setting

The 8.0 cm/yr northwestward motion of the Philippine Sea Plate (PSP) towards the Sunda Plate (SP) (Seno et al., 1993) is accommodated throughout the Philippine archipelago by a system of crustal faults and subduction zones that exhibit complex shear partitioning (Fig. 1 A; e.g., Rimando et al. (2019, 2020)). To its west and east, the island arc is bound by the east-dipping Manila-Negros-Sulu-Cotabato Trench System and the west-dipping East Luzon Trough-Philippine Trench System, respectively. In between these trenches, is the 1400 km-long, sinistral Philippine Fault Zone (PFZ), which runs along the entire length of the archipelago, from the island of Luzon in the northwest to the island of Mindanao in the southeast (Allen, 1962; Hamilton, 1979; Acharya and Aggarwal, 1980; Bautista et al., 2001; Cardwell et al., 1980; Hamburger et al., 1983; Hayes and Lewis, 1985; Ozawa et al., 2004; Rimando and Knuepfer, 2006; Rimando and Rimando, 2020; Marfito et al., 2022) (Fig. 1 A). There is an estimated 80-100 km and 200 km of minimum displacement along the PFZ in northwest Luzon (Pinet and Stephan, 1990) and Mindanao (Mitchell et al., 1986), respectively, since the Miocene.

The boundary-perpendicular component of the overall oblique plate convergence is accommodated by

subduction zones, inferred thrust/reverse and oblique strike-slip faults in the crustal blocks bounded by major active faults, and by regional tectonic uplift, while the boundary-parallel component is accommodated mostly by the PFZ (Fig. 1 A; e.g., Rimando and Rimando (2020)). In northwestern Luzon, however, the Vigan-Aggao Fault (VAF), which forms the westernmost strand of the PFZ, also accommodates a significant portion of trench-perpendicular shortening through angled sinistral strike-slip faulting (e.g., Rimando and Rimando (2020) and Fig. 1 B). While other minor active faults likely exist within the crustal blocks, the exact traces and kinematics of these have yet to be comprehensively documented.

Methods and Data

InSAR processing

We used the descending track (20220721-20220802) Sentinel-1A synthetic-aperture radar (SAR) single-look complex images from the European Union's Copernicus Programme satellite constellation to create an interferogram and a line-of-sight (LOS) displacement map of the area between six days before and six days after the event. Unfortunately, there were no acquisitions for the ascending track, due to the end of Sentinel-1B's mission in late 2021 (ESA, 2022). Sentinel-1A uses the C-band, corresponding to a wavelength of 5.5 cm. The images were acquired in 'Terrain Observation with Progressive Scans' mode, which bundles three sub-swaths together to cover a greater area. However, given the limited size of the earthquake and distribution of deformation, only the westernmost sub-swath was processed and analyzed.

We used the Generic Mapping Tools Synthetic Aperture Radar (GMTSAR), an open source InSAR processing program (Sandwell et al., 2011), to carry out our analysis. The SAR images and their precise orbital information were obtained from the Copernicus Open Access Hub (Copernicus, 2022). A 30 m-resolution Shuttle Radar Topographic Mission Version 3 (SRTM1v3) digital elevation model (DEM) of the area was generated using the online GMTSAR DEM Generator (G.M.T.S.A.R., 2010), and was used to correct for topography. A Gaussian filter with a wavelength of 200 m was applied to the images, and the pixels were decimated by a factor of two along the azimuth and by a factor of eight along the range prior to creating the wrapped interferogram (Sandwell et al., 2011). A coherence mask with a threshold of 0.085 was applied to the data prior to unwrapping with the SNAPHU algorithm (Chen and Zebker, 2000, 2001; Chen, 2002). The unwrapped phase was corrected for tropospheric effects using data from the General Atmospheric Correction Online Service for InSAR (Yu et al., 2017, 2018a,b) before converting to LOS displacement (Fig. 2).

Earthquake Source Modeling

We solved for earthquake rupture using two simple planar fault geometries (Fig. 3 A and B), the selection of

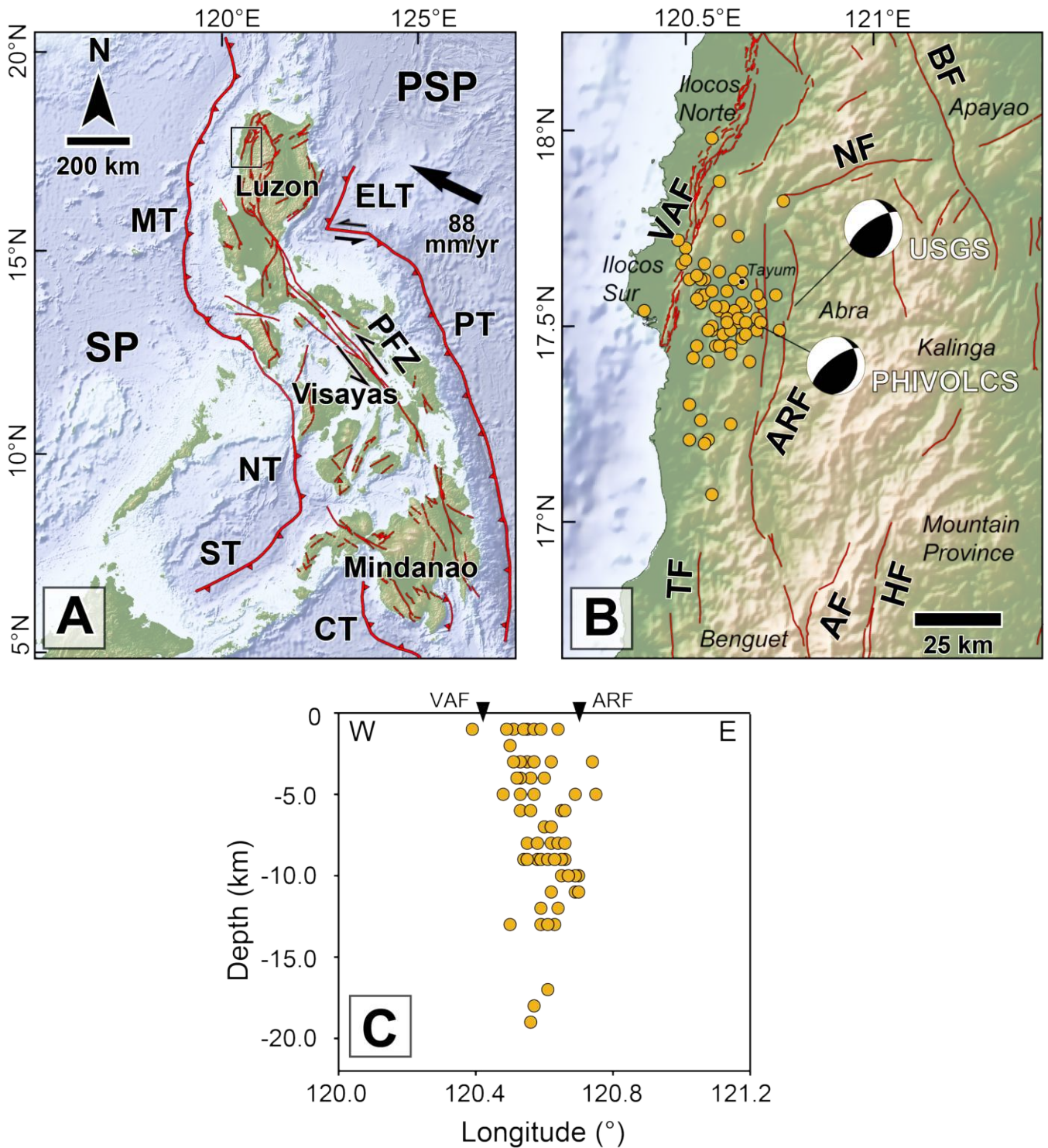


Figure 1 A) Active tectonic features of the Philippines (PHIVOLCS Faultfinder: <http://faultfinder.phivolcs.dost.gov.ph/>). SP: Sunda Plate, PSP: Philippine Sea Plate, MT: Manila Trench, NT: Negros Trench, ST: Sulu Trench, CT: Cotabato Trench, ELT: East Luzon Trough, PT: Philippine Trench, and PFZ: Philippine Fault Zone. Black arrow is the rate of convergence between the PT and SP (Seno et al., 1993). Black rectangle indicates the location of Figure 1 B. B) Map of study area with major faults (red lines), focal mechanism solutions from both the United States Geological Survey (USGS, 2022) and the Philippine Institute of Volcanology and Seismology (PHIVOLCS, 2022c) (white labels), and the 2-week $M_W > 3.5$ aftershocks (orange circles) from PHIVOLCS. VAF: Vigan-Aggao Fault, ARF: Abra River Fault, NF: Naglibacan Fault, BF: Bangui Fault, AF: Ambuklao Fault, HF: Hapap Fault, TF: Tubao Fault. C) All aftershocks shown in (B), plotted based on longitude to create a West-East cross section. The locations of the surface traces of the mapped active faults, VAF and ARF, are indicated by black inverse triangles.

which is guided by the PHIVOLCS and USGS focal mechanisms, the visible pattern of line-of-sight deformation from the unwrapped interferogram, and the mapped active faults in the region. Based on these considera-

tions, we explored the possibility of rupture along and parallel to two local faults: the Vigan-Aggao Fault (VAF) and the Abra River Fault (ARF), respectively. There are other faults that are local to the rupture, includ-

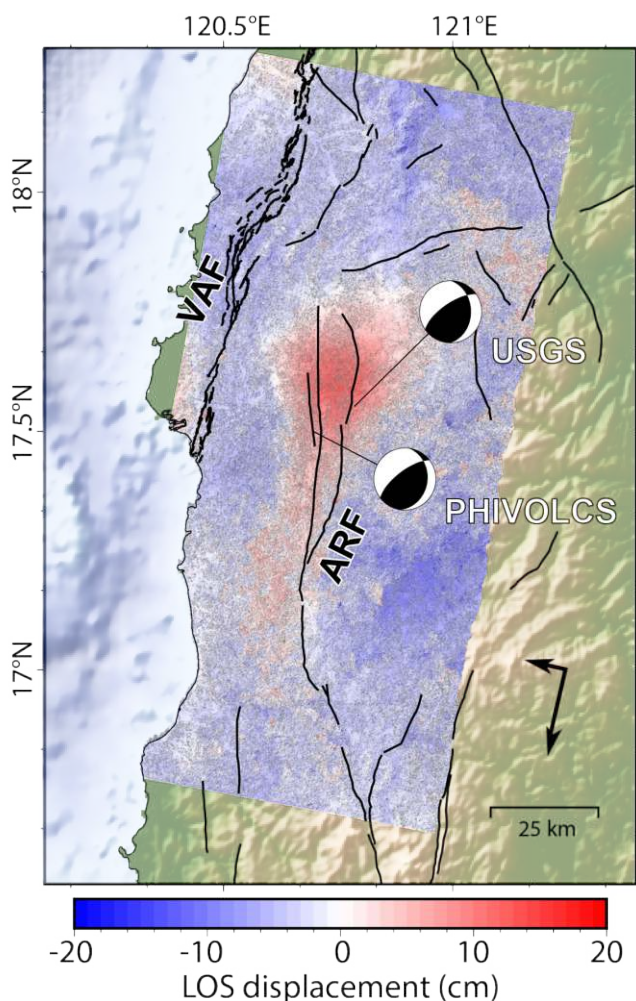


Figure 2 Line-of-sight displacement from Sentinel-1A descending track InSAR data. Red and blue correspond to positive and negative displacements, respectively. The USGS and PHIVOLCS moment tensors (USGS, 2022; PHIVOLCS, 2022b) are included for reference. The arrow in the bottom right shows the satellite heading (-167°) and look direction (right).

ing the Naglibacan Fault and Bangui Fault; however due to their sub-optimal orientations in relation to the PHIVOLCS focal mechanism, these were not considered to be ideal candidates for rupture and therefore were not tested. The well-documented NNE-SSW Vigan-Aggao Fault (VAF), is a range-bounding fault that is located close to the western coast of northern Luzon, and parallels both the trend of the hinge between the positive LOS and negative LOS deformation, and the trend of the aftershock distribution. This active fault is known to have primarily left-lateral displacement, and has been active since the Pliocene (Pinet and Stephan, 1990). Although the Luzon earthquake of 2022 was primarily a thrust mechanism, we allow for the possibility of rupture on the VAF due to its proximity. We also selected a more N-S fault plane to parallel the more proximal but less well studied Abra River Fault (ARF) (Pinet and Stephan, 1990). Since the ARF has been described as a dominantly strike-slip fault (Pinet and Stephan, 1990), rupture along the ARF itself, which has been suggested by PHIVOLCS to be the likely causative fault

(PHIVOLCS, 2022d), is unlikely. Therefore, we modeled a fault plane, which fits the LOS deformation, to the west of the ARF. While an investigation of the optimum fault plane was beyond the scope of this rapid study, future efforts may be able to better constrain the ideal fault plane for this event based on geodetic data and any additional information about surface rupture, if it is found. Both faults are modeled with 30°E dips, consistent with the USGS and PHIVOLCS focal mechanism solutions. For comparison, we also used the fault plane solution provided by the USGS (USGS (2022); Fig. 3 C), and modeled the expected LOS displacement at the same locations as used in our source inversion (Fig. 3 D, E and F). The USGS finite fault model uses teleseismic body and surface waves and follows the methods of Ji et al. (2002). The parameters of all three faults are presented in Table 1.

To invert for the slip, we used the MudPy modeling and source inversion toolkit (Melgar and Bock, 2015). Because InSAR data is insensitive to the earthquake rupture velocity, we solved for slip as a static rupture. Green's functions for the InSAR data are calculated using the frequency wavenumber methods from Zhu and Rivera (2002). We used a velocity model that is local to the epicenter through CRUST1 (Laske et al., 2013-04). Due to the tectonics of the region, left-lateral and thrust fault slip was enforced, limiting model slip to rakes in a window between 0° and 90° . The inversion results were constrained using a Tikhonov spatial regularization scheme (Mair, 1994; Tikhonov, 1963). This regularization scheme imposes equal amounts of smoothing across all subfaults in our model and is guided by a spatial regularization constant. As the constant approaches zero, the problem approaches a non-regularized least squares solution. We test our inversion results over a range of values, opting for the model that minimizes the data misfit without overfitting or allowing for too rough of a final solution (Fig. 3 A and B). The preferred solutions sit close to the bend in an L-curve test (Fig. S1).

Results

LOS Displacements

The LOS displacements, displayed in Fig. 2, are relative to a satellite heading of -167° looking right at an incidence angle of 44° . Results show a lobe of positive LOS deformation beneath the northern ARF, and a lobe of negative LOS deformation to the SSE. This satellite geometry is particularly well suited to image deformation in the dip-slip direction. Given focal mechanism results that suggest a N-striking fault plane, dipping to the E, the LOS displacements therefore suggest dominantly reverse motion, moving the eastern hanging wall vertically upwards.

Inversion Results

The inversion results for all three geometries tested are displayed in Table 1 and Fig. 3 and further details of each fault model are shown in Figs. S2-S8. Along with the amount of slip on the fault, we calculated the pre-

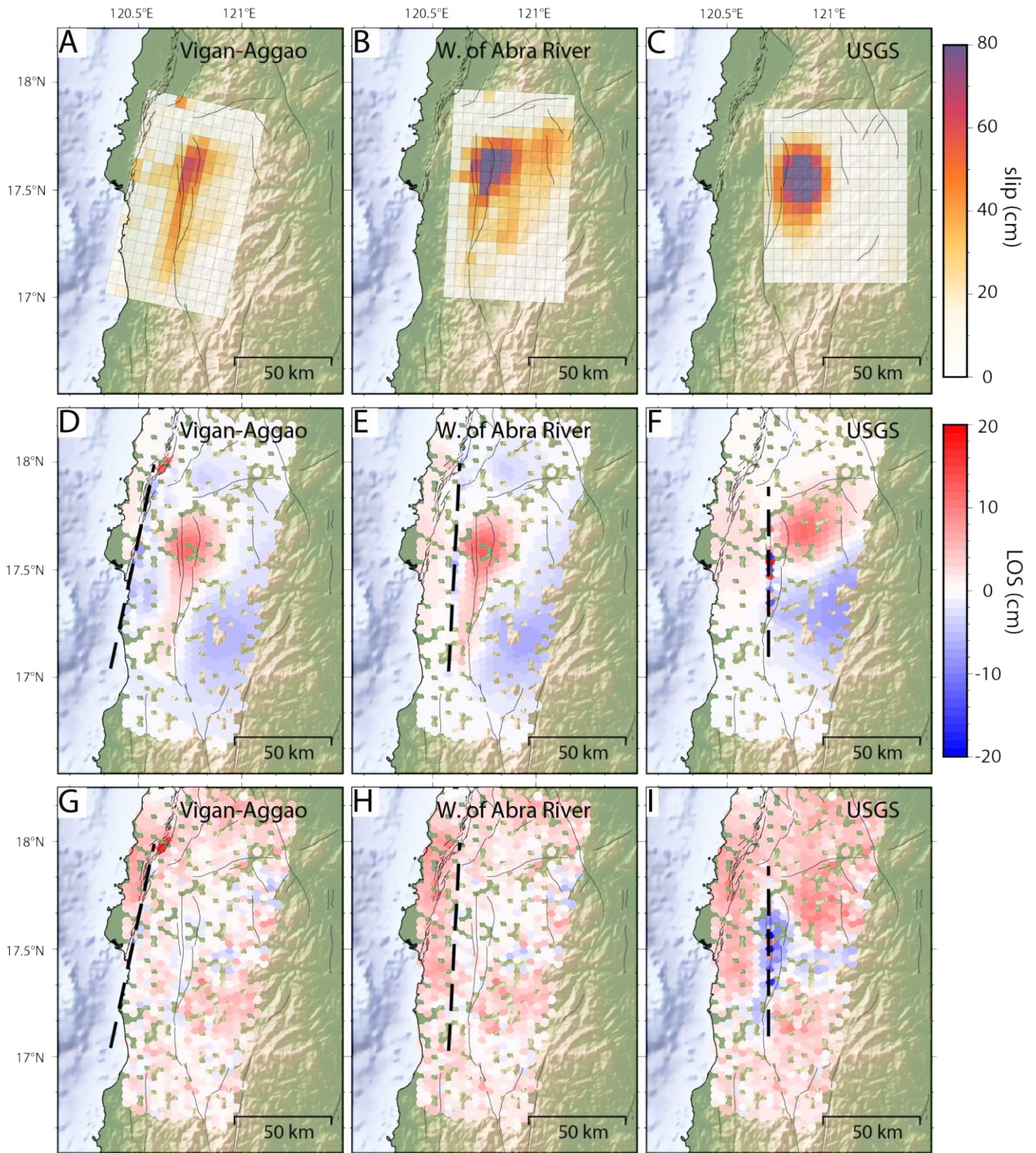


Figure 3 Results of InSAR inversion, for three rupture geometries discussed in text: the Vigan-Aggao Fault (A, D, G), a fault parallel to the Abra River Fault (B, E, H), and a forward model of the USGS finite fault inversion (C, F, I). Top row (A, B, C) shows the inversion results. The middle row (D, E, F) shows predicted LOS displacements from a forward model of the inversion results. The bottom row (G, H, I) shows the misfit between the observed LOS and the forward models for each rupture. The amount of LOS displacement, in cm, is shown in red-blue, as in Figure 2, and the amount of slip on the fault surface, in cm, is shown as white-purple. Dashed lines on the middle and bottom row panels are the surface traces of the modeled faults.

dicted LOS displacements at the surface from a forward model of the slip at depth (Fig. 3, D-F), and the misfit between that forward model and the observed LOS displacements (Fig. 3, G-I). Table 1 also includes the overall L2 norm misfit for each model. Here, a lower value rep-

resents a model that better fits the data. Full solution results for the ARF and VAF faults, including the partitioning of slip between dip-slip and strike-slip components, are shown in Figs. S2 and S3. Dashed lines show the surface projection of each fault plane, although none of

Fault model	M _w	Strike (°)	Dip (°)	Peak slip (cm)	Peak dip slip (cm)	Peak strike slip (cm)	Depth of peak slip (km)	Ave. Rake (°)	Misfit L2
VAF	7.02	12	30	64	64	30	16.5–20	63.6	0.79
W. of ARF	7.10	3	30	95	95	35	13–16	67.3	0.83
USGS	6.93	0	35	95	66	87	12.3	34	1.2

Table 1 Modeled source fault parameters and results of inversion. ‘Ave.’ refers to the average.

the results suggest significant slip near the surface.

VAF rupture model

This model exhibits a diffuse amount of primarily reverse slip (average 63.6° rake) over an along-strike band between 32–40 km down-dip (16–20 km depth) with peak slip of 64 cm (Figs. 3A, S2 A, and S2 B). Lesser amounts of left-lateral slip are mainly concentrated on a narrow band along the central segment of the fault plane, starting at 60 km down-dip (30 km depth) and shallowing to the north (Fig. S2 C).

Abra River Fault-parallel model

This model exhibits more localized reverse-slip (average 67° rake) at shallower depths and with a higher peak slip value (95 cm) (Figs. 3 B, S3 A, and S3 B) than the VAF rupture geometry. Left-lateral slip is mostly confined to the central segment of the plane, at 20–40 km down-dip distance (10–20 km depth).

USGS forward model

The USGS forward model, which is based on the finite fault model that was released shortly after the main event, exhibits a very focused region of slip beneath the lobe of positive LOS displacement, with a more dominant left-lateral slip (average rake 34°) and with peak slip of around 80 cm occurring near 12 km depth (Figs. 3 C, F and I).

Discussion and Conclusions

Although both the VAF and ARF-parallel fault planes produced similar L2 misfits (Table 1) and are therefore similarly good choices, the modeled rupture on the ARF-parallel fault plane is the preferred model for this study as it visually most closely reproduces the overall observed LOS displacements near the expected earthquake rupture (Fig. 3 H). While the surface projection of this model is currently not associated with any mapped active fault trace, it is expected that there must be significant margin-normal shortening across the northern Philippines given the opposing subduction zones to the east and west (e.g., [Bautista et al. \(2001\)](#)). In this sense, such a fault is kinematically congruent with the VAF and ARF, which are both accommodating the mostly sinistral strike-slip component of the oblique convergence in northern Luzon. If this is the causative fault of the 2022 Mw 7.0 Luzon earthquake, there may well be surface rupture to the west of Abra, near the most productive aftershock region (Fig.1 B). It may also be worth considering the possibility of stress transfer onto the Abra

River Fault, which would lie above the fault plane modeled herein.

On the other hand, rupture on the VAF, which is dominated by relatively deep reverse slip (peak slip between 30–40 km down-dip), is associated with the lowest misfit. It is worth noting, though, that there is a minimal difference in the misfit values of the VAF and ARF-parallel fault models. Additionally, while the surface projection of the VAF model coincides with the trace of a well-known fault, the dominantly reverse-slip kinematics that our model suggests is contradictory to the dominantly strike-slip displacement that has been documented through detailed mapping and a quantitative analysis of morphotectonic kinematic indicators along this fault zone ([Rimando and Rimando, 2020](#)). If this fault were the causative fault for this earthquake, there may not be any surface rupture due to the paucity of strong slip in the shallow 0–25 km depth range.

Among the earthquake source models, the USGS forward model is associated with the highest overall misfit and strongest residuals (Fig. 3 I). The high misfit is due to the incompatibility of the modeled slip distribution with the observed positive LOS deformation that is visible further to the south. We therefore consider this as an unlikely causative fault for this event.

The likely presence of a fault parallel to and west of the ARF that exhibits dominantly reverse-slip further supports a complex shear partitioning model for the Philippine archipelago, wherein the oblique plate convergence in Luzon is accommodated not only by the sinistral strike-slip PFZ and the major trenches, but is also taken up substantially by faults within crustal blocks (e.g., [Rimando et al. \(2020\)](#)).

Additionally, the fact that a previously unmapped ARF-parallel fault may exist underscores the importance of a comprehensive mapping of active tectonic structures even in areas where there is very subtle or poor topographic expression of faulting. This could be achieved through a combination of high-resolution DEM inspection, InSAR analysis and modeling, high-resolution subsurface imaging, high-resolution potential field surveys, seismotectonic analysis, measurement of geomorphic indices, and slip tendency analysis of geophysical or topographic lineaments.

In the absence of complete mapping of active seismotectonic structures, this earthquake serves as a reminder of the importance of comprehensive seismic hazard mapping that considers the effect of shallow crustal earthquakes on as-yet unknown faults. If this event were to have happened further to the south it may have caused much greater damages and losses, particularly if it were to have affected a major population center such as Baguio City.

Future studies may consider Bayesian inverse modeling that involves producing posterior probability distributions of source parameters of the fault rupture, for example through Markov-chain Monte Carlo- and Metropolis-Hastings-based algorithms of [Bagnardi and Hooper \(2018\)](#), to provide more constrained estimates of fault geometry and slip distributions. In the meantime, though, our models can serve as a guide for the ongoing search for surface rupture and/or nearby, pre-existing yet unmapped potentially active faults.

Acknowledgements

We would like to acknowledge the quick response of PHIVOLCS in obtaining and disseminating information about this event. This study was made possible using data from the European Union's Sentinel-1A satellite, and the following analysis codes: GMTSAR, SNAPHU, and MudPy. Some figures were constructed using PyGMT ([Wessel et al., 2019](#); [Uieda et al., 2021](#)) and Matplotlib ([Hunter, 2007](#)). We thank the editors, Dr. Mathilde Radiguet and Dr. Gareth Funning from Seismica Fast Reports, and the anonymous reviewers. This work is funded in part by NSERC DG RGPIN-2021-03031, and is NRCan ESS contribution number 20220267. We wish the people of Abra province a quick and complete recovery from this event.

Data and code availability

The data that support the findings of this study were derived from the following resources: European Union's Copernicus Copernicus Open Access Hub (<https://scihub.copernicus.eu/>) and PHIVOLCS (<https://www.phivolcs.dost.gov.ph/index.php/earthquake/earthquake-information3> and <https://www.phivolcs.dost.gov.ph/index.php/news>). The analysis codes for this study are freely available at the following: GMTSAR v6.2.2 (<https://github.com/gmtsar/gmtsar>), SNAPHU v2.0.4 (<https://web.stanford.edu/group/radar/softwareandlinks/sw/snaphu/>), and MudPy v1.0 (<https://github.com/dmelgarm/MudPy>). The interferogram data and slip model files are available in the open-access Zenodo repository: Source model inputs and results - The July 2022 Mw 7.0 Northwestern Luzon Earthquake, Philippines (<http://doi.org/10.5281/zenodo.7033117>).

Competing interests

The authors declare having no competing interests.

References

- Acharya, H. and Aggarwal, Y. Seismicity and tectonics of the Philippine Islands. *Journal of Geophysical Research: Solid Earth*, 85 (B6):3239–3250, 1980. doi: 10.1029/JB085iB06p03239.
- Allen, C. Circum-Pacific faulting in the Philippines-Taiwan region. *Journal of Geophysical Research*, 67(12):4795–4812, 1962. doi: 10.1029/JZ067i012p04795.
- Bagnardi, M. and Hooper, A. Inversion of surface deformation data for rapid estimates of source parameters and uncertainties: A Bayesian approach. *Geochemistry, Geophysics, Geosystems*, 19 (7):2194–2211, 2018. doi: 10.1029/2018GC007585.
- Bautista, B., Bautista, M., Oike, K., Wu, F., and Punongbayan, R. A new insight on the geometry of subducting slabs in northern Luzon, Philippines. *Tectonophysics*, 339(3-4):279–310, 2001. doi: 10.1016/S0040.
- Cardwell, R., Isaacks, B., and Karig, D. The spatial distribution of earthquakes, focal mechanism solutions, and subducted lithosphere in the Philippine and northeastern Indonesian islands. *Washington DC American Geophysical Union Geophysical Monograph Series*, 23:1–35, 1980. doi: 10.1029/GM023p0001.
- Chen, C. Phase unwrapping for large SAR interferograms: Statistical segmentation and Generalized Network Models. *IEEE Transactions on Geoscience and Remote Sensing*, 40(8):1709–1719, 2002. doi: 10.1109/tgrs.2002.802453.
- Chen, C. and Zebker, H. Network approaches to two-dimensional phase unwrapping: Intractability and two new algorithms. *Journal of the Optical Society of America A*, 17(3):401, 2000. doi: 10.1364/josaa.17.000401.
- Chen, C. and Zebker, H. Two-dimensional phase unwrapping with use of statistical models for cost functions in nonlinear optimization. *Journal of the Optical Society of America A*, 18(2):338, 2001. doi: 10.1364/josaa.18.000338.
- Copernicus. Copernicus Open Access Hub, 2022.
- ESA. Mission ends for Copernicus Sentinel-1B satellite, 2022. Accessed: 18 August 2022.
- G.M.T.S.A.R. Generate DEM files for use with GMTSAR, 2010.
- Hamburger, M., Cardwell, R., and Isaacks, B. Seismotectonics of the Luzon, Philippines, region. The tectonic and geologic evolution of southeast Asian seas and islands. *Am Geophys Union Geophys Monogr*, 27:1–22, 1983. doi: 10.1029/GM027p0001.
- Hamilton, W. *Tectonics of the Indonesian region*, volume 1078. US Government Printing Office, 1979.
- Hayes, D. and Lewis, S. Structure and tectonics of the Manila trench system, Western Luzon, Philippines. *Energy*, 10(3-4): 263–279, 1985. doi: 10.1016/0360.
- Hunter, J. Matplotlib: A 2D Graphics Environment. *Computing in Science & Engineering*, 9(3):90–95, 2007. doi: 10.1109/M-CSE.2007.55.
- Ji, C., Wald, D., and Helmberger, D. Source description of the 1999 Hector Mine, California, earthquake, part I: Wavelet domain inversion theory and resolution analysis. *Bulletin of the Seismological Society of America*, 92(4):1192–1207, 2002. doi: 10.1785/0120000916.
- Laske, G., Masters, G., Ma, Z., and Pasyanos, M. Update on CRUST1.0—A 1-degree global model of Earth's crust. In *Geophys. Res. Abstr*, volume 15, page 2658. EGU General Assembly, Vienna, Austria, 2013-04.
- Mair, B. Tikhonov regularization for finitely and infinitely smoothing operators. *SIAM Journal on Mathematical Analysis*, 25(1): 135–147, 1994. doi: 10.1137/S0036141092238060.
- Marfito, B., Llamas, D., and Aurelio, M. Geometry and Segmentation of the Philippine Fault in Surigao Strait. *Frontiers in Earth Science*, 76, 2022. doi: 10.3389/feart.2022.799803.
- Melgar, D. and Bock, Y. Kinematic earthquake source inversion and tsunami runup prediction with regional geophysical data. *Journal of Geophysical Research: Solid Earth*, 120(5):3324–3349, 2015. doi: 10.1002/2014JB011832.
- Mitchell, A., Hernandez, F., and Cruz, A. Cenozoic evolution of the Philippine archipelago. *Journal of Southeast Asian Earth Sci-*

- ences, 1(1):3–22, 1986. doi: 10.1016/0743-9547(86)90003-6.
- Nakata, T., Tsutsumi, H., Punongbayan, R., Rimando, R., Daligdig, J., Daag, A., and Besana, G. *Surface fault ruptures of the 1990 Luzon earthquake, Philippines, Special Publication 25*. Research Center for Regional Geography, Hiroshima University, Hiroshima, Japan, 1996.
- NDRRMC. Situational report for Magnitude 7.0 Earthquake in Tayum. *Abra - SitRep*, 1(19), 2022. Accessed: 18 August 2022.
- Ozawa, A., Tagami, T., Listanco, E., Arpa, C., and Sudo, M. Initiation and propagation of subduction along the Philippine Trench: evidence from the temporal and spatial distribution of volcanoes. *Journal of Asian Earth Sciences*, 23(1):105–111, 2004. doi: 10.1016/S1367.
- PHIVOLCS, 2022a. Latest earthquake information. Accessed: 05 August 2022.
- PHIVOLCS, 2022b. Source parameter determination based on Waveform Inversion of Fourier Transformed seismograms Centroid Moment Tensor (SWIFT CMT). Accessed: 05 August 2022.
- PHIVOLCS, 2022c. Primer on the 27 July 2022 magnitude (Mw) 7.0 northwestern Luzon earthquake. Accessed: 05 August 2022.
- PHIVOLCS, 2022d. Poster of the 27 July 2022 Magnitude 7.0 Northwestern Luzon Earthquake. Accessed: 18 August 2022.
- Pinet, N. and Stephan, J. The Philippine wrench fault system in the Ilocos Foothills, northwestern Luzon, Philippines. *Tectonophysics*, 183(1):207–224, 1990. doi: 10.1016/0040-1951(90)90417-7.
- Punongbayan, R., Rimando, R., Daligdig, J., Besana, G., Daag, A., Nakata, T., and Tsutsumi, H. Luzon earthquake ground rupture. *Department of Environment and Natural Resources*, Manila:1–32, 1991-07-16.
- Rimando, J., Aurelio, M., Dianala, J., Taguibao, K., Agustin, K., Beador, A., and Vasquez, A. Coseismic ground rupture of the 15 October 2013 magnitude (MW) 7.2 Bohol earthquake, Bohol Island, central Philippines. *Tectonics*, 38(8):2558–2580, 2019. doi: 10.1029/2019TC005503.
- Rimando, R. and Knuepfer, P. Neotectonics of the Marikina Valley fault system (MVFS) and tectonic framework of structures in northern and central Luzon, Philippines. *Tectonophysics*, 415(1-4):17–38, 2006. doi: 10.1016/j.tecto.2005.11.009.
- Rimando, R. and Rimando, J. Morphotectonic kinematic indicators along the Vigan-Aggao Fault: the western deformation front of the Philippine Fault Zone in Northern Luzon, the Philippines. *Geosciences*, 10(2):83, 2020. doi: 10.3390/geosciences10020083.
- Rimando, R., Rimando, J., and Lim, R. Complex Shear Partitioning Involving the 6 February 2012 MW 6.7 Negros Earthquake Ground Rupture in Central Philippines. *Geosciences*, 10(11):460, 2020. doi: 10.3390/geosciences10110460.
- Sandwell, D., Mellors, R., Tong, X., Wei, M., and Wessel, P. Open Radar Interferometry Software for Mapping Surface Deformation, *Eos Trans. AGU*, 92(28):234, 2011. doi: 10.1029/2011EO280002.
- Seno, T., Stein, S., and Gripp, A. A model for the motion of the Philippine Sea plate consistent with NUVEL-1 and geological data. *Journal of Geophysical Research: Solid Earth*, 98(B10): 17941–17948, 1993. doi: 10.1029/93JB00782.
- Tikhonov, A. Resolution of ill-posed problems and the regularization method. *Doklady Akademii Nauk SSSR*, 151:501–504, 1963.
- Uieda, L., Tian, D., Leong, W., Toney, L., Schlitzer, W., Grund, M., and Wessel, P. PyGMT: A Python interface for the generic mapping tools, 2021.
- USGS. M 7.0 - 13 km NNE of Bantay, Philippines, 2022. Accessed: 05 August 2022.
- Wessel, P., Luis, J., Uieda, L., Scharroo, R., Wobbe, F., Smith, W., and Tian, D. The generic mapping tools version 6. *Geochemistry, Geophysics, Geosystems*, 20(11):5556–5564, 2019. doi: 10.1029/2019GC008515.
- Yu, C., Penna, N., and Li, Z. Generation of real-time mode high-resolution water vapor fields from GPS observations. *Journal of Geophysical Research: Atmospheres*, 122(3):2008–2025, 2017. doi: 10.1002/2016jd025753.
- Yu, C., Li, Z., and Penna, N. Interferometric synthetic aperture radar atmospheric correction using a GPS-based iterative tropospheric decomposition model. *Remote Sensing of Environment*, 204:109–121, 2018a. doi: 10.1016/j.rse.2017.10.038.
- Yu, C., Li, Z., Penna, N., and Crippa, P. Generic atmospheric correction model for interferometric synthetic aperture radar observations. *Journal of Geophysical Research: Solid Earth*, 123(10): 9202–9222, 2018b. doi: 10.1029/2017jb015305.
- Zhu, L. and Rivera, L. A note on the dynamic and static displacements from a point source in multilayered media. *Geophysical Journal International*, 148(3):619–627, 2002. doi: 10.1046/j.1365-246X.2002.01610.x.

The launch of Seismica: a seismic shift in publishing

Christie D. Rowe ^{*1}, Matthew Agius ², Jaime Convers ³, Gareth Funning ⁴, Carmine Galasso ⁵, Stephen Hicks ⁶, Tran Huynh ⁷, Jessica Lange ⁸, Thomas Lecocq ⁹, Hannah Mark ¹⁰, Ryo Okuwaki ¹¹, Théa Ragon ¹², Catherine Rychert ¹⁰, Samantha Teplitzky ¹³, Martijn van den Ende ¹⁴

¹Department of Earth & Planetary Sciences, McGill University, Montréal, Canada, ²Dipartimento tal-Ġeoxjenza, L-Università ta' Malta, Msida, Malta, ³Instituto de Astronomia, Geofísica e Ciências Atmosféricas, Universidade de Sao Paulo, Brazil, ⁴Department of Earth & Planetary Sciences, University of California Riverside, Riverside, USA, ⁵Department of Civil, Environmental and Geomatic Engineering, University College London, London, United Kingdom, ⁶Department of Earth Science & Engineering, Imperial College London, UK, ⁷Southern California Earthquake Center, University of Southern California, Los Angeles, California, USA, ⁸McGill University Library, Montréal, Canada, ⁹Seismology and Gravimetry, Royal Observatory of Belgium, Brussels, Belgium, ¹⁰Department of Geology & Geophysics, Woods Hole Oceanographic Institution, Massachusetts, USA, ¹¹University of Tsukuba, Tsukuba, Japan, ¹²Division of Geological and Planetary Sciences, Caltech, Pasadena, USA, ¹³University of California Berkeley Library, Berkeley, USA, ¹⁴Université Côte d'Azur, IRD, CNRS, Observatoire de la Côte d'Azur, Géoazur, Valbonne, France

Author contributions: *Conceptualization:* All Seismica Board. *Writing - original draft:* Rowe, Teplitzky, Funning, Convers, Agius, Rychert, van den Ende, Hicks, Ragon, Mark, Lange, Huynh. *Writing - review & editing:* Rowe, Teplitzky, Funning, Hicks, Ragon, Mark, Galasso, Lecocq, Sumy. *Visualizations:* Rowe, Convers. *Translations:* Ragon, Lecocq, Galasso, Convers, Okuwaki. *Alphabetical ordering of the authors:* does not reflect their contributions to the manuscript.

Abstract Seismica, a community-run Diamond Open Access (OA) journal for seismology and earthquake science, opened for submissions in July 2022. We created Seismica to support a shift to OA publishing while pushing back against the extreme rise in the cost of OA author processing charges, and the inequities this is compounding. Seismica is run by an all-volunteer Board of 47 researchers who fulfil traditional editorial roles as well as forming functional teams to address the needs for technical design and support, copy editing, media and branding that would otherwise be covered by paid staff at a for-profit journal. We are supported by the McGill University Library (Québec, Canada), who host our website and provide several other services, so that Seismica does not have any income or financial expenditures. We report the process of developing the journal and explain how and why we made some of the major policy choices. We describe the organizational structure of the journal, and discuss future plans and challenges for the continued success and longevity of Seismica.

Résumé Seismica, une revue diamant en accès ouvert (OA) pour la sismologie, portée par la communauté scientifique, a été lancée en juillet 2022. Nous avons créé Seismica pour soutenir la publication en OA, tout en déjouant l'augmentation des frais de publication en OA à charge des auteurs, et les inégalités que cette augmentation aggrave. Seismica est dirigée par un comité composé de 47 chercheurs et chercheuses bénévoles qui remplissent des rôles éditoriaux traditionnels. Réparti en équipes fonctionnelles, le comité répond aussi aux besoins techniques ou d'accompagnement, par exemple en relecture, mise en forme, et stratégies de communication; des besoins qui seraient, dans un journal à but lucratif, couverts par du personnel rémunéré. Nous sommes soutenus financièrement par la Bibliothèque de l'Université McGill (Québec, Canada), qui héberge notre site Web et fournit plusieurs services de publication : Seismica n'a ni revenu, ni dépense financière. Ici, nous présentons l'élaboration de la revue et expliquons certains choix pratiques. Nous décrivons l'organisation de la revue et discutons des plans et des défis futurs pour le succès et la longévité de Seismica.

Resumen Seismica, una revista científica de sismología y ciencia de eventos sísmicos de acceso libre (OA) vía diamante y gestionada por la comunidad, abrió convocatoria de publicaciones en julio de 2022. Creamos Seismica para promover el cambio a publicaciones de acceso libre (OA) y a la vez resistir el pronunciado aumento en los costos editoriales y de publicación – conocidos como APC (Article Processing Charges) – de los artículos de acceso libre y las desigualdades a las que conllevan. Seismica es gestionada por un comité editorial de voluntarios, conformado por 47 investigadores, que desempeñan puestos editoriales tradicionales y que a la vez forman equipos funcionales que atienden las necesidades de diseño técnico y soporte, edición, medios de comunicación e imagen; que de otra manera serían cubiertas por personal pagado en una revista con fines de lucro. Contamos con el apoyo de la biblioteca de la universidad de McGill (Québec, Canadá), que auspicia nuestro sitio web y nos brinda otros servicios, permitiendo que Seismica no reciba ingresos o conlleve gastos de operación. Reportamos el proceso de desarrollo de la revista, y explicamos el cómo y el porqué de nuestras principales políticas editoriales. Describimos nuestra estructura organizacional y discutimos los planes de desarrollo y desafíos para asegurar el éxito continuo y la longevidad de Seismica.

Production Editor:
Gareth Funning
Handling Editor:
Danielle Sumy
Copy & Layout Editor:
Abhineet Gupta

Received:
October 18, 2022
Accepted:
October 25, 2022
Published:
November 16, 2022

Sommario Seismica, una rivista ad accesso libero (OA) di tipo 'diamante' sulla sismologia e la scienza dei terremoti, gestita direttamente dalla comunità scientifica, ha iniziato ad accettare contributi nel luglio 2022. Abbiamo creato Seismica per favorire il passaggio all'editoria OA e per contrastare l'estremo aumento dei costi editoriali e di pubblicazione - noti come APC (Article Processing Charge) - da parte degli autori e le disuguaglianze che ne derivano. Seismica è gestita da un comitato editoriale completamente volontario di 47 ricercatori che ricoprono ruoli editoriali tradizionali e fanno parte di team funzionali per soddisfare le esigenze di progettazione tecnica e di supporto alla rivista, copy editing, media e branding, che altrimenti sarebbero coperti, in una rivista tradizionale a scopo di lucro, da personale retribuito. Siamo supportati dalla McGill University Library (Quebec, Canada), che ospita il nostro sito Web e fornisce molti altri servizi, in modo che Seismica non debba considerare entrate o costi. In questo editoriale, riportiamo il processo di sviluppo del giornale e spieghiamo le motivazioni alla base di alcune scelte in termini di politiche editoriali. Descriviamo la struttura organizzativa della rivista e discutiamo i progetti futuri e le sfide per il continuo successo e la longevità di Seismica.

要旨 Seismica は、地震学に広く携わる研究者コミュニティ主導によって運営されるダイヤモンドオープンアクセス (OA) 学術雑誌として、2022 年 7 月に投稿受付を開始した。Seismica は、昨今、主要な営利目的の学術雑誌が著者負担の OA 費用を極端に引き上げたことを受け、公平性を担保する OA 学術雑誌の新たなトレンドを生み出し、またそれを支援するべく創刊された。Seismica は、47 名の研究者が理事メンバーとなり、すべて非営利のボランティアベースで運営されている。Seismica は、雑誌運営に不可欠な査読・編集作業に加え、組版作業をはじめとする各種デザイン、メディア・ブランディングなど、営利目的の学術雑誌であれば有給のスタッフがカバーするような幅広いプロセスに対応するため、役割分担された理事メンバーによって効率的な運営が行われている。Seismica は、McGill University Library (カナダ・ケベック州) の支援によりウェブサイトの運用等を行っているため、収入や財政支出の生じない非営利の学術雑誌である。本稿では、Seismica の誕生から現在に至る過程を報告し、Seismica の運営方針がどのように決定されたのかについて詳細に論じる。さらに、Seismica の組織体系および、Seismica の持続的な運営を実現するための今後の課題について議論する。

Non-technical summary Seismica is a new Diamond Open Access (OA) journal designed by and for the earthquake science and seismology communities. We explain our motivations and process in designing and establishing the journal. We outline our aspirations for building additional programs around the journal for supporting author, reviewer, and editor skills development, author resources for communication outside the research community, and increasing equity, diversity and inclusion in all aspects of the publication process.

1 Introducing Seismica

Seismica is a Diamond Open Access (OA) academic journal for the broad disciplines of seismology and earthquake science, and related education and outreach. Diamond OA means that it is free to read and free to publish. We launched Seismica because of the inequities in the current publishing landscape, and the increasing costs of access to research for both authors and potential readers of scientific papers. The shift to OA requirements in many countries has exacerbated biases in access to publishing, compounded the problems with merit assessment and academic competition, and highlighted the fact that the costs for Gold/Hybrid OA (author-pays for open access) models are far in excess of the costs of publishing (Khuo, 2019; Björk, 2021)¹. By returning control of the publishing process to the hands of the research community, we can address local and global inequities in access to research (Khanna et al., 2022). The opportunity to reimagine the publishing ecosystem for our community by developing a new

journal with not-for-profit motives, which is designed by and for researchers, has inspired us to volunteer our time for Seismica.

Here, we report the context and our motivation for creating Seismica, describe the journal as it exists at the launch in 2022, and outline our aspirations for building a new kind of scientific community that will support equitable and inclusive global collaboration across our disciplines into the future.

1.1 Our Diamond Open Access (OA) publishing model

Diamond OA Journals are distinct from other OA publishing models in that there are no subscription fees for institutions or individuals, nor do authors pay to publish. While Diamond OA journals have always existed, there is a greater interest than ever before in encouraging and developing this model further (Ancion et al., 2022). Lange and Severson (2021) identified 485 Diamond OA journals operating without the support of a commercial publisher in Canada alone. This mode of publishing is already very well established, although most of these journals are small-scale and 76% were in the fields of Social Sciences and Humanities. Khanna et al. (2022) found that Diamond OA journals published more scholarly works from the Global South, demon-

*Corresponding author: christie.rowe@mcgill.ca

¹Grossmann and Brembs (2021) estimated that the actual cost of publishing an academic article averages about US\$400; Siler and Frenken (2020) found that about a third of OA journals charge US\$200 or less, the median is US\$600, and that author charges increase with Journal Impact Factor. Journals publishing in seismology and earthquake science and related education and outreach typically charge ~ US\$1500 to >US\$11,000.

strating how Diamond OA expands the global reach and inclusivity of scientific research.

Traditionally, Science, Technology, Engineering and Mathematics (STEM) journals have been smaller players in the Diamond OA landscape (Lange and Severson, 2021; Bosman et al., 2021). STEM disciplines have taken different paths to OA publishing. Green OA involves posting preprint versions of articles (before submission or after acceptance) which is gaining popularity in the Earth Sciences (e.g., EarthArXiv, ESSOAr). However, the high value placed on peer review, fear of being ‘scooped’, and confusion surrounding preprint restrictions between different journals has prevented Green OA from fully serving the needs of the Earth Science community.

The field of Earth Science produces high-impact research that promises benefits to the public and society. Fulfilling this promise requires an open and inclusive publishing method to effectively communicate scientific results, such as new research on earthquake hazard and its implication for earthquake risk quantification and mitigation. Many professional organizations have produced longstanding publications prior to the consolidation of scholarly journals into a few large publishing companies, that were essentially Diamond OA before the classification existed in its own right (Shipp, 2000). This legacy of accessibility and knowledge sharing is continued by Seismica, joining a growing group of Diamond OA Journals in the Earth Sciences (e.g. Volcanica²; Tektonika³; The Sedimentary Record⁴; Palaeontologica Electronica⁵; and several others in planning stages⁶).

2 How Seismica began

In November 2020, Springer Nature journals announced a steep increase in article processing charges (APCs) for Gold OA of more than US\$10,000 (Else, 2020). This announcement generated reactions among Earth Scientists on social media on a spectrum from amazement to outrage. Many highlighted that such fees were way beyond the means of most researchers. Some seismologists and earthquake scientists on Twitter noted that the Diamond OA journal Volcanica was already in its third year and had been successful, so proposed that something similar should be developed for our field (Figure 1).

From this collective momentum came action. A self-appointed task force of early- and mid-career seismologists, earthquake geologists and geodesists coalesced within days, and began to put together a road map to founding a new journal. This initiative benefited from the desire for positive action and community building that arose during the months of pandemic-related isolation. We created a discussion space in Slack (a free messaging application), open to anyone who was interested,



Stephen Hicks
@seismo_steve

Plans are afoot to start up a new, free-to-publish and free-to-access journal for seismology, earthquake science, and related research fields. Want to show your interest, help out, or even join the team? DM myself or @martijnende. We're looking for a truly diverse group 🙌

Martijn van den Ende @martijnende · Nov 26, 2020
To everyone who missed the discussion on starting a seismology journal following the example of @WeAreVolcanica: we got the ball rolling and we just set-up a Slack workspace to do some brainstorming. Anyone who is interested in participating in the discussion can DM me twitter.com/seisatom/stat...
[Show this thread](#)

5:05 PM · Nov 30, 2020 · Twitter Web App

Figure 1 The beginning of Seismica’s recruitment of an initial task force to investigate the feasibility of a Diamond OA journal for Seismology and Earthquake Science, November 2020.

Légende. Les début de Seismica, avec la constitution d’un groupe de travail initial pour étudier la faisabilité d’un journal Diamond OA pour la sismologie, novembre 2020.

Leyenda. El inicio del proceso de reclutamiento por parte de Seismica, de un equipo para investigar la viabilidad de una revista de acceso libre (OA) Diamante en sismología y ciencia de eventos sísmicos, noviembre de 2020.

Nota. L’inizio del reclutamento da parte di Seismica di una task force iniziale per studiare la fattibilità di una rivista Diamond OA sulla sismologia e la scienza dei terremoti, Novembre 2020.

図 1 Seismica のタスクフォースは、地震学分野におけるダイヤモンド OA 学術雑誌の実現に向けて、志をともにする研究者のリクルートから始まった (2020 年 11 月)。

https://twitter.com/seismo_steve/status/1333532526179201027

where over 100 participants debated vigorously about journal scope, article types, open science, community-focused policies, improving representation, editorial structure, and journal branding (e.g., the journal name and logo). We invited Volcanica’s founders to speak with us and pass on their valuable insights. We explored possible institutional support and funding models to discover that several university libraries supported Diamond OA journals for free. We built a mailing list and surveyed our global community on who they were, what they wanted from a journal, and how they might help with it. We established an approach and philosophical basis for founding a new journal with a unique mission. The main findings of this initial task-force are reported by van den Ende et al. (2021).

With our road map in place, we formed an editorial selection committee, and openly invited applications for positions within Seismica. From the over 130 applications received by the September 2021 deadline, we appointed our Management Committee (comprising Executive Editors and Functional Team Chairs), Handling Editors and Functional Team Members. The organizational structure was designed with permeability between traditional editorial roles and the functional

²<https://jvolcanica.org>; Farquharson and Wadsworth (2018)

³<https://tektonika.online>

⁴<https://www.sepm.org/the-sedimentary-record>

⁵<https://palaeo-electronica.org/content/>

⁶E.g. Sedimentologica <https://twitter.com/sedimentologica>, Geomorphica <https://sites.google.com/view/geomorphica>

teams that run the day-to-day operations of the journal (Figure 2), with individuals opting in or out of finite or open-ended functional roles.

Five task forces (Appendix A), raised from the appointed Board, undertook a 10-month journal building process to prepare Seismica for launch. The task forces were in near constant communication through the Management Committee to integrate our work as a coherent organization. We adapted our initial vision for the editorial structure as we realized the scope of some tasks, like Media & Branding, was larger than anticipated, and added members to certain task forces where required.

A major step toward ensuring Seismica's future was signing a Memorandum of Agreement with the McGill University Library. Like many university libraries in Canada, McGill Library is equipped to support OA journals through the installation and maintenance of the open-source Open Journal Systems (OJS)⁷ platform from the Public Knowledge Project (PKP), as well as to train journal editors and guide new journals through customization of the OJS interface. McGill Library acquired an International Standard Serial Number (ISSN) for Seismica, assigns Digital Object Identifiers (DOIs) for all published content through CrossRef, and will also help Seismica to apply for inclusion in indices like Scopus and Web of Science. Critically, McGill Library takes on the cost of these services, through purchasing the services from relevant vendors and through in-kind contribution of the Library and IT staff time. If Seismica separates from McGill Library for any reason, both parties commit to give a six months notice, and Seismica would retain any archives previously hosted on the McGill Library servers. This agreement gives Seismica the stability to ensure that our articles will remain open and available for perpetuity. McGill University Library covers all of the necessary functions for publishing a peer-reviewed journal that would require funding to acquire; remaining functions are supported by the time and expertise of our volunteers.

3 Journal Design

3.1 Seismica's Key Values

Through months of discussion, the character of our community became more distinct and we distilled some common values. These key values (Table 1) form the basis of Seismica's policies, which are implemented as guidelines for authors, reviewers, and editors⁸. This section describes how some of the policies in place at the time of launch implement these values; these values will be cyclically reviewed through new policies described in Section 5.

To create an **Accessible** publishing venue, we designed a suite of peer-reviewed article types, including traditional research papers, but uniquely, we also offer a *Report* format designed for: fast publication (e.g., in the aftermath of a significant earthquake); instrument/field deployments; software; null results. We also encourage

submission of reviews and opinion papers after consultation with the Editorial Board. Seismica recommends that our authors publish their articles under a Creative Commons CC-BY license⁹, and we provide support for authors to help them make an informed choice of CC license if CC-BY is not appropriate for their contribution. We encourage authors to post preprints under the same license at any time from pre-submission up until acceptance (after which it would be redundant). We require authors to make data and code publicly downloadable (not "by request"). We also support the inclusion of multiple languages to encourage global readership within and beyond the research community.

To promote a **Transparent** scientific process, upon manuscript acceptance and publication, peer review reports and author replies are published alongside articles. Our manuscript template includes the Contributor Roles Taxonomy (CRediT)¹⁰ to promote recognition and acknowledgement of everyone who contributed to the work, and assist authors in making decisions about authorship.

Our **Respectful** journal design means that the promotion of equity, diversity and inclusion (EDI) must form a basis for policy decisions (described further in Section 3.2) and that the community must have a direct and decisive input on Seismica's future development. For example, we discussed peer-review modes at length, with some Seismica Board members advocating for double-anonymous review due to its potential to reduce reviewer bias (e.g. Parks, 2020). Due to concerns about the capacity of authors and of OJS to truly anonymize manuscripts, and wanting not to create deterrents for potential submitting authors unaccustomed to double-anonymized reviews, we implemented a policy of publishing reviews. This and other policy choices will be re-examined in subsequent policy review cycles.

Seismica's **Credibility** derives from informed and thorough editorial handling by knowledgeable researchers, and through trust in one another and in the organization. Our editorial board is designed to grow along with demand and rate of paper submission, to keep individual editors' workloads lower, and ensure that each manuscript within Seismica's broad scope is handled by someone with meaningful expertise. When Seismica receives a manuscript focused on a specific geographical area, editors will prioritize recruiting at least one reviewer from that area, with the help of author suggestions. This ensures a wider diversity of reviewers and increases the impact of the scientific work. All members of the Seismica community are bound by our Code of Conduct¹¹ and competing interest policies¹² which are updated regularly to reflect evolving understanding of best practices.

Progressive policies require reaching outside the research community to potential readers who may have an interest in participating or may benefit from publications in Seismica. Seismica publishes multiple language abstracts and are developing author support pro-

⁷<https://pkp.sfu.ca/ojs/>

⁸<https://seismica.org/policies>

⁹<https://creativecommons.org/licenses/by/2.0/>

¹⁰<https://credit.niso.org/>

¹¹<https://seismica.org/code-of-conduct>

¹²<https://seismica.library.mcgill.ca/policies>



Figure 2 Seismica Organization Chart at launch, July 2022. See [Appendix A](#) for individual contributor credits and [Appendix B](#) for description of roles and responsibilities.

Légende. Organigramme de Seismica au lancement, juillet 2022. Voir l'Annexe A pour la description des rôles et responsabilités, et l'Annexe B pour les contributions individuelles.

Leyenda. Organigrama en el lanzamiento de Seismica, Julio de 2022. Ver el Apéndice A para la descripción de roles y responsabilidades, y el Apéndice B para el reconocimiento de aportes individuales.

Nota. Organigramma di Seismica al lancio, Luglio 2022. Vedere [Appendice A](#) per la descrizione di ruoli e responsabilità, e [Appendice B](#) per i vari contributi individuali.

図 2 2022 年 7 月現在における Seismica の組織チャート。担当者のクレジットは [Appendix A](#) を、各役割の詳細については [Appendix B](#) を参照されたい。

grams to facilitate outreach. This also means promoting literacy in Open Science principals within the Seismica community as well as the broader circles of authors and consumers of research. Our biennial review cycle is designed to promote flexibility and adaptability as the publishing climate rapidly changes.

3.2 An equitable, diverse, and inclusive journal

Equity, diversity, and inclusion (EDI) are intrinsic to our motivations in founding Seismica and the desire

to address inequities in the scientific community is at the center of Seismica’s mission. Inequities are structurally engrained into the culture and practice of scientific research, but the last few years have seen a surge in its recognition and acknowledgement, along with some proposed solutions (e.g. [Dutt, 2020](#); [Ali et al., 2021](#); [Li-boiron, 2021](#); [Pico et al., 2020](#)). Seismica has ensured its key values align with many of these expert recommendations for institutional change in the academy.

A necessary step to understanding how Seismica can play a role in strengthening EDI, is to identify who Seis-

Key values	Seismica's new approach to publishing: how and why?
Accessible	Seismica believes that science should be accessible to everyone, and has created an open platform for sharing peer-reviewed research in seismology and earthquake science. By removing all fees, we encourage participation on many levels to share knowledge and data with the global community.
Transparent	Seismica publicly recognizes the volunteer labor of reviewers, editors, typesetters and contributors, along with the wide breadth of teamwork needed in research. We have a transparent review process by publishing reviews alongside research articles, as well as a list of authorship contributions. To address challenges with reproducibility in science, Seismica also promotes best practices in open data and software, helping research to achieve its full potential.
Respectful	The scientific publishing ecosystem can sometimes produce discouraging language for researchers so Seismica will take a mindful approach. All parties must agree to our Code of Conduct, and do not tolerate disrespectful language. Seismica aims to combat reviewer fatigue by only sending papers out for review that meet our guidelines, which are made available to authors before submission. We will mentor reviewers, editors, and authors to achieve an inclusive, responsive, and productive publishing process.
Credible	Readers, authors, reviewers, and members of the Seismica Board can depend on Seismica and one another to uphold these values. Seismica's editors contribute their expertise and reputation in their respective fields so that Seismica can emerge as a scientifically trustworthy journal. Our distributed leadership and adaptability of our organization serve to keep us aligned with the community values.
Progressive	Seismica aims to promote innovation and creativity in academic publishing. We aim to capture more scientific contributions through less-traditional formats such as field campaign reports, null results, and software articles, which may not be accepted at other journals. We will continue to innovate with organizational structure and roles, and share the outcomes of our experiments to accelerate the pace of change.

Table 1 Seismica's Key Values, Editorial Policies 2022.

Légende. Valeurs clés de Seismica, politiques éditoriales 2022.

Leyenda. Valores claves de Seismica, Políticas Editoriales 2022.

Nota. Valori chiave di Seismica, Politiche editoriali 2022.

表 1 Seismica の編集方針一覧 (2022).

mica represents and who we can serve. Our communities include: members of the Seismica Board (Editors and Functional Team Members, [Appendix A](#)); our community of authors and reviewers; and the wider global audience who read either our articles or our public-facing materials. Ideally, our Board should be a reflection of our community. The variety of essential roles within Seismica and our distributed decision-making by consensus and discussion means that policy decisions reflect the input of senior and junior researchers from across our disciplinary and global spectrum. To know how well the Board reflects the community, we need to understand who we are. Self-surveys during initial development stages provided a baseline for describing the Seismica community ([van den Ende et al., 2021](#)). Longitudinal voluntary surveys tracking the composition of the Board and of the reviewer/author community will provide a basis for ensuring that new rounds of recruitment keep the Board aligned with the broader community.

A long-term goal is to create opportunities for participation in publishing for members of the third community – interested readers, professionals in geophysics or earthquake hazard/risk whose employment does not include a publishing mandate but who produce new knowledge and insights, and researchers with relevant expertise who face financial barriers to publishing. Community-run journals using the free OJS platform are overwhelmingly concentrated in the Global South,

but the chemical and physical sciences combined make up ~1% of these journals by discipline ([Khanna et al., 2022](#)). Our suite of report types was designed to facilitate participation by recognizing a more inclusive range of contributions. We support multi-language abstracts and encourage authors to provide one or more translations to support local interest in regions covered by their studies.

Seismica's Equity, Diversity, and Inclusion (EDI) team has the mandate to be everywhere at once - members are distributed on key task forces. Although these individuals have EDI as their formal mandate at Seismica, everyone in the organization shares responsibility for pursuing these ideals and learning from the experiences of others. The dialog between members of different backgrounds and perspectives is ongoing and will continue to drive the evolution of the journal as we mature and grow.

3.3 Brand and communications

The success of a journal depends on its ability to attract authors to submit high-quality manuscripts that will build reader confidence in the journal. Authors look for an editorial board which inspires respect and authority, as well as convincing evidence of professionalism in the operation of the journal ([Feldman, 2008](#); [Shapiro and Bartunek, 2008](#)). If a journal does not inspire confidence, through demonstration of integrity, authority,

and broad-based support, then submissions would not come in, and the journal would fail (Hodgkinson, 2008). Journal *branding* inspires confidence. Therefore, early in the planning process, we developed a strong vision for Seismica's profile in the research community and for stakeholders outside of academia.

A brand is more than just a name, a logo design, or a clever tagline for our scientific journal. It is everything that encompasses Seismica, how we came to be, who we are, and what separates us from other scientific publications. We take inspiration from our vision, our mission, and the power of our collaboration. We believe that if we can communicate our vision clearly to the public and broader community, people will join us. We want people producing research from all over the world to know and feel that Seismica guarantees an equitable opportunity to publish their research, assuring a fair and open review process regardless of where they come from or who they are. We want to foster a sense of community ownership and loyalty, enough to build a group of ambassadors of Seismica who communicate our values around Diamond OA publishing. Because these values come from our community, they reflect its needs and guide our brand positioning to help attract like-minded researchers and foster their motivation and passion for the type of journal that Seismica aspires to be.

3.3.1 Visual Identity

Practically, the first branding task was to design a logo for the journal. In the Seismica spirit, an open logo design competition led to the submission of 18 logo designs, and the final one, designed by Adam Pascale¹³, was chosen by popular vote. Geophysicist and illustrator Lucía Pérez Díaz¹⁴ volunteered to polish the logo for a variety of uses (Figure 3). The logo represents seismic wiggles with an offset, but it can also represent Earth's topography. The color and design variants of the logo were selected to inspire confidence, invoke both trustworthiness and ambition, and be used across different spaces and themes, such as the various journal branches, websites, and social media pages (Twitter¹⁵, Facebook¹⁶, Instagram¹⁷, YouTube¹⁸). Close coordination between the Media & Branding Team and the Standards & Copy Editing Team for the Seismica manuscript formatting, and the Tech Team for the website appearance and functions, have given Seismica a distinctive and recognizable look.

3.3.2 Growing Our Community

It is essential to build recognition and familiarity with Seismica's aims and mission to recruit Seismica Board volunteers, and to inspire authors to contribute their work and reviewers to volunteer their time. Alongside the building of our mailing list, social media ac-



Figure 3 Seismica logos, designed by Adam Pascale and developed into a logo pack by Lucía Pérez Díaz. Color pack developed by Media & Branding team with input from the Seismica Board.

Légende. Logos Seismica, conçus par Adam Pascale et développés par Lucía Pérez Díaz. Gamme de couleurs développée par l'équipe Media & Branding avec la contribution du comité Seismica.

Leyenda. Logos de Seismica, diseñados por Adam Pascale y desarrollados en un paquete de logos por Lucía Pérez Díaz. Paleta de colores desarrollada por el equipo de Medios y Marca, con el aporte del comité de Seismica.

Nota. Loghi Seismica, progettati da Adam Pascale e sviluppati in un pacchetto di loghi da Lucía Pérez Díaz. Sviluppo pacchetto colori gestito dal team Media & Branding con il contributo del comitato editoriale.

図 3 Seismica の公式ロゴマーク。Adam Pascale 氏により考案され、Lucía Pérez Díaz 氏によって最終的なデザインがつけられた。ロゴマークのカラーセットは、Seismica 理事メンバーのアイデアを取り込んだ Media & Branding チームによるもの。

counts were opened in the early days of planning for launch. A dedicated team was formed to maintain online communication, entrusted with news, announcements, press releases, promoting the brand, and explaining what Seismica is all about. Our posts take different formats: text, images, and video interviews with Seismica Board members. Videos show the human side of the volunteering team behind Seismica. To date, in total, Seismica has over 4000 followers across our active social media platforms.

To connect directly to the research community, and to potential authors and reviewers, Seismica Board members are continuing to present at conferences (e.g. [Funning et al., 2021](#); [Gabriel et al., 2022](#)). These multi-format presentations have allowed members of the Seismica team to talk and answer questions from fellow scientists. Support from the Media & Branding team enables presenters to stay on-message with Seismica's brand and maintain the professional appearance with logos and slide templates.

Currently, our message to the community goes beyond promoting a new journal and guides our path forward. Seismica is the first Diamond OA journal built

¹³<https://twitter.com/seislogist>

¹⁴[luciaperezdiaz.com](https://twitter.com/luciaperezdiaz)

¹⁵<https://twitter.com/WeAreSeismica>

¹⁶<https://www.facebook.com/WeAreSeismica/>

¹⁷<https://www.instagram.com/weareseismica/>

¹⁸<https://www.youtube.com/c/WeAreSeismica>

for and by seismologists and earthquake scientists. Our tagline, *Our Seismic Moment*, showcases Seismica as an avenue for people who want to drive change and advance research and scientific discovery with genuine openness.

3.4 Journal Operations

Seismica uses a suite of technical tools to manage communications, the journal website, editorial workflow, and a reviewer database. We use tools that are free or low-cost, usually open source; and are confident that these tools will remain supported for the foreseeable future.

Our website and paper handling are managed through OJS. Seismica's visual brand identity is built into the public-facing website using a custom Cascading Style Sheet (CSS). While OJS limits customization of the editorial workflow, we have adjusted the settings to suit Seismica's purposes, for example, by updating the list of article components that authors are able to upload to match our needs, and editing the templates for emails used at different stages of paper handling. This simplifies the workflows for authors, editors, and reviewers, creating a smooth experience for everyone who needs to interact with the editorial process.

Where current out-of-the-box OJS functions did not fulfil our needs, our Tech team created purpose-built tools. For example, OJS cannot assign expertise tags to registered users. To help Handling Editors find reviewers, we built an independent reviewer database that allows individuals to register using their Open Researcher and Contributor Identifier (ORCID)¹⁹ and tag their expertise within Seismica's scope²⁰. These pre-defined tags were derived from the keywords mentioned in the journal scope. Our database enables Handling Editors to find qualified reviewers more easily, and contact them based on their ORCID or email address. To ensure privacy protection and GDPR²¹ compliance, we do not currently collect personal and/or demographic data that is not already publicly displayed on a user's ORCID profile, except for an email address that a user can optionally provide. By the time we launched, over 200 reviewers had self-registered, providing a large pool of potential reviewers to evaluate the submitted manuscripts.

Although article templates are not required for initial submission, this can speed up the final typesetting process, so we provide templates in L^AT_EX, odt, and docx formats²². We use L^AT_EX (Lamport, 1985) and Journal Article Tag Suite (JATS) eXtensible Markup Language (XML) (Needleman, 2012) to format articles for publication. Seismica L^AT_EX templates use a custom class, based on the article document class, with simple commands for entering article metadata and incorporating multiple language abstracts and/or a non-technical summary. The submission template includes an *anonymous* option, which generates a pdf without author names, author contributions, and acknowledgements, even if that

information is included in the input T_EX file, making it easier for authors to submit their work for double-anonymous peer review if they choose. The publication template, which differs from the submission template, also incorporates the Seismica logo and colors to tie into the overall visual branding scheme²³. Author contributions are printed below the list of authors for improved transparency, and volunteer editors' and typesetters' names appear on the first page. The Standards and Copy Editing team has developed tools to automate the conversion from odt or docx files to T_EX and JATS XML, using Pandoc²⁴ and various Python packages. In particular, we try to automate the parsing of in-text citations, as reformatting these from plain text to T_EX by hand is very time-consuming. The L^AT_EX template for article submission can be used for preprints, and is available on Overleaf²⁵.

Slack continues to be the primary communication medium for internal discussions amongst the Seismica Board and ongoing Task Forces. General announcements can be broadcast to the whole workspace, while editorial and technical discussions happen in private Slack channels. Seismica also has a mailing list²⁶ where larger journal announcements (e.g., journal launch) are broadcast to more than 500 subscribers (as of October 2022).

Other tools used by the Tech team include Google Docs and GitHub. Seismica's core constitutional documents, including Editorial Policies and Guidelines, are currently maintained in Google Docs, which enable collaboration and edit tracking. Scripts, template, and website files are hosted on GitHub, and the Tech team uses GitHub to track and discuss tech support issues.

4 Post-launch insights

Seismica has only just launched. To date, we have been open for submissions for about 120 days. We have received on average 2-3 submissions per week. Seismica has been well received in the community, following our high levels of community engagement with our social media and conference presentations. Given these factors, together with a strong uptake with both our mailing list and reviewer database, we consider the launch of Seismica to have been highly successful. There are several early and important insights we have gained from this experience.

Our research community values community-led scholarly publishing. The opportunity to influence the journal incentivizes volunteering efforts. Seismica responds to community needs in all aspects of our design. Our organization is growing according to our mission and philosophy of non-profit motive. We hope our novel peer-reviewed *Reports* format²⁷ will gather

²³For both templates, we use the Source-Sans OpenType fonts suite, Latin Modern font for equations, and a 2-column text format for ease of reading (Dumont, 2009)

²⁴<https://pandoc.org>

²⁵<https://www.overleaf.com/latex/templates/seismica/bvnbjbykcydjb>

²⁶<https://seismica.us1.list-manage.com/subscribe/post?u=6b3197489014e98f2b3014398&id=b3a5fc0e04>

²⁷<https://seismica.org/policies#publication-types>

¹⁹<https://orcid.org>

²⁰<http://reviewer-database.seismica.org>

²¹<https://gdpr-info.eu/>

²²<https://seismica.org/templates/>

more data and insights which might otherwise end up uncredited and in *gray literature* or unreleased. Our inaugural Board represents a diverse international group of researchers, which connects us to a diverse and international community of authors and readers.

Pre-launch community-building made a big difference in soliciting submissions. We extensively used our outward-facing communications channels during the run-up to opening for submissions to improve name recognition and awareness of our values in the research community. Several authors who submitted papers in the first weeks of Seismica, and reviewers who accepted our requests, announced their participation on Twitter. This early community building is unusual among community-run journals (Lange, 2022).

Researchers can provide the functions a traditional publisher provides. With modern tools and software, along with institutional support, key journal functions, including work that has been traditionally charged for, can be accomplished by the scientific community:

- Initial editorial assessment and final decision-making
- Reviewing manuscripts and coordinating reviewer reports
- Transforming research into shareable outputs, for example, through social media
- Customising and maintaining a website-hosted publication workflow system
- Copy editing, typesetting, and persistent archiving for longevity and stability

With the increasing stress on library budgets, supporting community-run OA journals offers an institutional mechanism for addressing the cost crisis in academic publishing (Benz et al., 2022).

Collaborative design of journal policies identifies common values and motivates volunteers. Seismica Board members shared their own anecdotes and experiences during discussions that helped refine our policies, and doing so created optimism that smart policy choices could ameliorate some of the known general issues with traditional publishing systems, such as the peer review process. Just like every other journal, we are operating in a climate of reviewer burnout, but with shared not-for-profit motives, together with workload tracking and a dynamic organizational structure, we believe that these issues can be alleviated by cultivating a sense of community and a shared mission. This shared design has yielded clear communications and expectations from Seismica.

5 Future growth opportunities

Seismica's initial few months post-launch have proven successful. Nevertheless, we are acutely aware that as we move past the launch phase, several immediate challenges surrounding the reputation, growth, and sustainability of Seismica lie ahead. Such challenges are common for other Diamond OA journals (Becerril et al., 2021; Bosman et al., 2021; Björk et al., 2016).

First, Seismica must build an international reputation for quality and rigor that meets the expectations of the research community. Our pre-launch information campaigns have been very effective at growing name recognition within the research communities of our Board members. Continued support and article submissions, as well as reviewer engagement, depend on the journal establishing itself as a serious venue for academic research. The success of our launch was supported by the professional reputations of our volunteers (Appendix A), and we have relied on their name recognition to build our own. Seismica will establish itself as a brand that researchers are eager to affiliate with using these approaches: a rigorous and supportive review process led by disciplinary experts will ensure that our published papers are of high quality; the *Seismica Ambassador program* will inform the broader community of our mission and the issues in the scholarly publishing industry that we can address through community-led publishing; we will continue to visibly evolve our policies to stay on top of best practices in Open Science, EDI, and community needs.

Second, we must be prepared to grow and sustain our community. The excitement of journal-building has motivated generous contributions of time and labor from a large number of people. We need to keep our original community members engaged while also expanding to take up extra workload as submissions increase. We must develop a culture that maintains our mission amidst a growing Seismica Board. Seismica's broad scope with a diverse set of Handling Editors that cover these different disciplines in seismology and earthquake science is more scalable than other structures. Early career researchers (ECRs) make up a disproportionate share of our volunteers; they bring an exceptional energy, responsiveness, and highly relevant skills to Seismica. We recognize and must respond to the need for ECRs to document their professional contributions in a way that supports their career advancement to mitigate the time away from research (Lange and Severson, 2022). We are building collaborations with researchers and experts in scholarly publishing, to inform the documentation of every role at Seismica as an academic and scholarly service to publishing. Many upcoming initiatives will support skills development for scholars across our community, hopefully creating ripples that extend beyond Seismica. These include editorial mentoring (underway), and reviewer and author workshops (in development). Our organizational structure is designed to best utilize the skills and available time from a variety of volunteers with different experiences and at different career levels. By tracking roles, responsibilities and workload, we can take care to avoid overloading individual volunteers, and respond quickly to changing demands. We are exploring ways to appropriately document and express gratitude for service to Seismica, beginning with prominent recognition on the published articles themselves.

Third, we must apply for, and anticipate the potential effects of, listing in scholarly journal indices. The Journal Impact Factor is used in many funding systems as a proxy for quality or value of scientific output, which in-

tensifies a number of negative impacts related to competition and assessment of researchers (Casadevall and Fang, 2014; Lariviere and Sugimoto, 2019). Recognizing that potential Seismica contributors are dissuaded from submitting their work to Seismica because the journal is not currently indexed by Clarivate/Web of Science, we will apply for an Impact Factor when Seismica becomes eligible after two years of publishing. We recognize that this may open the gates to new segments of the international research community accessing Seismica as a publishing venue, so we must be ready with a global and knowledgeable Board in place to support these changing needs. We recognize the implications of the misuse of Impact Factor and related citation-counting metrics for scientific assessment (e.g. Aksnes et al., 2019); we prioritize accessibility to a broader author pool in seeking listing, and will not compromise our core values in pursuit of rankings.

Finally, we are aware of our positioning in the landscape of seismology and earthquake science research. As we brainstormed ways to better serve our communities with author, reviewer, and editor support, we recognized how many traditional publishers profit from our voluntary labor and research funds, and that the cost structure has become increasingly inequitable. We also recognize that journals published by professional societies are operating within this cost structure and are passing benefits back to the academic community from their publishing profits. For researchers who can afford it, choosing to publish with professional societies continues to be a positive and ethical use of public research funds. We also want to demonstrate to our scientific community that there is another option which has helped other disciplines – Diamond OA publishing. Changes to funding agency policies increasing the requirements for OA publishing (e.g. cOAlition S; Office of Science and Technology Policy, 2022) can either drive even greater cost increases through Gold/Hybrid OA, or can represent a turning point toward the restoration of community-controlled journals.

We plan to develop specific initiatives for the first 12-24 months of Seismica's operation:

- *Better promotion of published research:* Traditional journals do very little to help authors promote their work after the acceptance notice. Seismica will support authors beyond the date of acceptance, by providing support and tools for outreach, social media and raising the profile of published research. We will also support authors in disseminating their work toward the public and policy makers.
- *Spreading the word about Diamond OA publishing:* The Seismica Ambassador program, due to launch in early 2023, will empower members of the broader research community to understand the publishing landscape and community-based solutions to address it – including researcher-led journals like Seismica.
- *Advancing open outputs beyond research articles:* Seismica will continue to publish research articles while also piloting non-traditional publication types and open options for data, software and code.

- *Formalization and documentation of Seismica workflows:* We aim to create resilience and consistency in our volunteer-run organization through careful standardization and documentation of workflows, from selecting handling editors, to copy editing, to social media strategies, to recruitment of new Board members. This could be a resource for other startup Diamond OA journals, particularly in STEM where there are fewer community-run examples.
- *Soliciting helpful and useful reviews:* Review quality and tone will be addressed through workshops and explicit messaging, modeling reviewing as a respectful and supportive service rather than a gate-keeping exercise. Reviewer appreciation strategies will support positive experiences for reviewers and maintain our current benefit of reviewer preference over for-profit journals.
- *Editorial wisdom:* Effective and efficient editorial handling can reduce workload throughout the manuscript handling process and result in higher satisfaction for all parties. Our editorial mentoring program, currently launching, aims to support editors with expert advice, opportunity for confidential discussion of decisions, and resources on best practices.
- *Collecting vital EDI data:* In conjunction with our EDI goals, we are considering mechanisms for collecting such data in the future in ways that comply with privacy regulations.
- *Improving our global social media reach:* Seismica is currently active on platforms such as Twitter and Facebook, that are most popular in the western world. However, other platforms are equally as popular across the globe in Asia and Africa, such as Sina, Weibo or VKontakte. Seismica plans to set up accounts on these platforms to reach a global audience.

Acknowledgements

The volunteer Board of Seismica (listed in Appendix A) is grateful for the support we have received from the research community, McGill University Libraries, and one another during the ongoing adventure and challenge of building a community-led journal. We recognize there are significant challenges ahead, challenges that face the global research community on a much broader scale, but to whose resolution we can make a small contribution. We are enthusiastic about the work ahead and invite you to join us!

We thank the members of the original Seismica Task Force who initiated this effort (van den Ende et al., 2021), and the leadership of Volcanica and Tektonika for inspiration, sharing knowledge, and support. We thank PKP and McGill Library. We thank the broader Seismica community, including participants in our Slack group, researchers who engage with us at conferences and on social media, those who have added themselves to our reviewer database, and members of our mailing list.

We are also indebted to Fabian Wadsworth and Jamie Farquharson of Volcanica for taking the time to brief the

original Seismica Task Force on their experience setting up Volcanica and inspiring us to initiate the Seismica project.

References

- Aksnes, D. W., Langfeldt, L., and Wouters, P. Citations, citation indicators, and research quality: An overview of basic concepts and theories. *Sage Open*, 9(1):2158244019829575, 2019.
- Ali, H. N., Sheffield, S. L., Bauer, J. E., Caballero-Gill, R. P., Gasparini, N. M., Libarkin, J., Gonzales, K. K., Willenbring, J., Amir-Lin, E., Cisneros, J., et al. An actionable anti-racism plan for geoscience organizations. *Nature Communications*, 12(1):1–6, 2021. doi: 10.1038/s41467-021-23936-w.
- Ancion, Z., Borrell-Damián, L., Mounier, P., Rooryck, J., and Saenen, B. Action Plan for Diamond Open Access. Mar. 2022. doi: 10.5281/zenodo.6282403.
- Becerril, A., Bosman, J., Bjørnshauge, L., Frantsvåg, J. E., Kramer, B., Langlais, P.-C., Mounier, P., Proudman, V., Redhead, C., and Torny, D. OA Diamond Journals Study. Part 2: Recommendations. 2021. doi: 10.5281/zenodo.4562790.
- Benz, M., van Edig, X., Schulz, K., Finger, J., and Verbeke, D. Supporting Diamond Open Access: Research libraries as funders, intermediaries and publishers. *Libraries in the Research and Innovation Landscape (LIBER 2022)*, 2022. doi: 10.5281/zenodo.6818082.
- Björk, B.-C. Why is access to the scholarly journal literature so expensive? *Portal: Libraries and the academy*, 21(2):177–192, 2021. doi: 10.1353/pla.2021.0010.
- Björk, B.-C., Shen, C., and Laakso, M. A longitudinal study of independent scholar-published open access journals. *PeerJ*, 4: e1990, 2016. doi: 10.7717/peerj.1990.
- Bosman, J., Frantsvåg, J. E., Kramer, B., Langlais, P.-C., and Proudman, V. OA Diamond Journals Study. Part 1: Findings. Mar. 2021. doi: 10.5281/zenodo.4558704.
- Casadevall, A. and Fang, F. C. Causes for the persistence of impact factor mania. *MBio*, 5(2):e00064–14, 2014. doi: 10.1128/mBio.00064-14.
- coalition S. Plan S: Making full and immediate Open Access a reality. Memorandum for the Heads of Executive Departments and Agencies. <https://www.coalition-s.org/>, accessed October 16, 2022.
- Doumont, J.-L. *Trees, Maps, and Theorems: Effective communication for rational minds.*, volume 17/2. Principia, Belgium, 2009.
- Dutt, K. Race and racism in the geosciences. *Nature Geoscience*, 13(1):2–3, 2020. doi: 10.1038/s41561-019-0519-z.
- Else, H. Nature journals reveal terms of landmark open-access option. *Nature*, 588(7836):19–20, 2020. doi: 10.1038/d41586-020-03324-y.
- Farquharson, J. I. and Wadsworth, F. B. Introducing Volcanica: The first diamond open-access journal for volcanology. *Volcanica*, 1(1):i–ix, 2018. doi: 10.30909/vol.01.01.i-ix.
- Feldman, D. C. Building and maintaining a strong editorial board and cadre of ad hoc reviewers. In Baruch, Y., Konrad, A., Aguinis, H., and Starbuck, W., editors, *Opening the Black Box of Editorship*, pages 68–74. Springer, 2008. doi: 10.1057/9780230582590_7.
- Funning, G., Bruhat, L., van den Ende, M., Gabriel, A.-A., Hicks, S., Jolivet, R., Lecocq, T., and Rowe, C. Seismica: a community-led Diamond Open-Access journal for seismology and earthquake science. 2021, 2021. AGU Fall Meeting Abstracts.
- Gabriel, A.-A., Bruhat, L., van den Ende, M., Funning, G., Hicks, S. P., Jolivet, R., Lecocq, T., and Rowe, C. Seismica: a community-led Diamond Open-Access journal for seismology and earthquake science. 2022. doi: 10.5194/egusphere-egu22-11264. EGU General Assembly Conference Abstracts.
- Grossmann, A. and Brembs, B. Current market rates for scholarly publishing services. *F1000Research*, 10(20), 2021. doi: 10.12688/f1000research.27468.2.
- Hodgkinson, G. P. Moving a Journal up the Rankings. In Baruch, Y., Konrad, A. M., Aguinis, H., and Starbuck, W. H., editors, *Opening the Black Box of Editorship*, pages 104–113. Palgrave Macmillan UK, London, 2008. doi: 10.1057/9780230582590_11.
- Khanna, S., Ball, J., Alperin, J. P., and Willinsky, J. Recalibrating the Scope of Scholarly Publishing: A Modest Step in a Vast Decolonization Process. *SciELO Preprints*, 2022. doi: 10.1590/SciELO-Preprints.4729.
- Khoo, S. Y.-S. Article Processing Charge Hyperinflation and Price Insensitivity: An Open Access Sequel to the Serials Crisis. *LIBER Quarterly: The Journal of the Association of European Research Libraries*, 29(1):1 – 18, May 2019. doi: 10.18352/lq.10280.
- Lamport, L. *LATEX: a document preparation system*. Addison-Wesley, Reading, 1985. OCLC: 1131315554.
- Lange, J. Removing author fees can help open access journals make research available to everyone. The Conversation, September 2022. <https://theconversation.com/removing-author-fees-can-help-open-access-journals-make-research-available-to-everyone-189675>, accessed September 25, 2022.
- Lange, J. and Severson, S. What Are the Characteristics of Canadian Independent, Scholarly Journals? Results from a Website Analysis. *The Journal of Electronic Publishing*, 24(1), 2021. doi: 10.3998/jep.153.
- Lange, J. and Severson, S. Work It: Looking at Labour and Compensation in Canadian Non-Commercial Scholarly Journals. *KULA: Knowledge Creation, Dissemination, and Preservation Studies*, 6(2):1–21, 2022. doi: 10.18357/kula.151.
- Lariviere, V. and Sugimoto, C. R. The journal impact factor: A brief history, critique, and discussion of adverse effects. In *Springer handbook of science and technology indicators*, pages 3–24. Springer, 2019.
- Liboiron, M. Decolonizing geoscience requires more than equity and inclusion. *Nature Geoscience*, 14(12):876–877, 2021. doi: 10.1038/s41561-021-00861-7.
- Needleman, M. H. NISO Z39.96-201x, JATS: Journal Article Tag Suite. *Serials Review*, 38(3):213–214, 2012. doi: 10.1080/00987913.2012.10765464.
- Office of Science and Technology Policy. Ensuring Free, Immediate, and equitable access to federally funded research. Memorandum for the Heads of Executive Departments and Agencies, August 2022. <https://www.whitehouse.gov/wp-content/uploads/2022/08/08-2022-OSTP-Public-Access-Memo.pdf>, accessed October 16, 2022.
- Parks, B. AJP adopts double-anonymous reviewing. *American Journal of Physics*, 88(12):1035–1035, 2020. doi: 10.1119/10.0002460.
- Pico, T., Bierman, P., Doyle, K., and Richardson, S. First authorship gender gap in the geosciences. *Earth and Space Science*, 7(8), 2020. doi: e2020EA001203.
- Shapiro, D. L. and Bartunek, J. Being an Ethical Editorial Board Member and Editor: The Integral Role of Earned Trust. In Baruch, Y., Konrad, A. M., Aguinis, H., and Starbuck, W. H., editors, *Opening the Black Box of Editorship*, pages 88–96. Palgrave Macmillan UK, London, 2008. doi: 10.1057/9780230582590_9.
- Shipp, J. Commercial scholarly publishing: the devil incarnate or divine saviour? *History of Economics Review*, 32(1):37–45, 2000.

doi: 10.1080/10370196.2000.11733339.

Siler, K. and Frenken, K. The pricing of open access journals: Diverse niches and sources of value in academic publishing. *Quantitative Science Studies*, 1(1):28–59, 02 2020. doi: 10.1162/qss_a_00016.

van den Ende, M., Bruhat, L., Funning, G., Gabriel, A.-A., Hicks, S. P., Jolivet, R., Lecocq, T., and Rowe, C. Creating a Diamond Open Access community journal for Seismology and Earthquake Science. 2021. doi: 10.31223/X5304V. <https://eartharxiv.org/repository/view/2557/>.

A Appendix : Contributors to Seismica

Management Committee, 2022

The Management Committee consists of the five Executive Editors and the Chairs of the Functional Teams. Decisions at Seismica are undertaken by appropriate members of the Management Committee, who also ensure coordination between all parts of the organization:

- *Executive Editor for Community*: Christie Rowe
- *Executive Editor for Production*: Gareth Funning
- *Executive Editor for Open Science*: Samantha Teplitzky
- *Executive Editor for Operations*: Carmine Galasso
- *Executive Editor for Equity, Diversity and Inclusion*: Catherine Rychert
- *Chair, Fast Reports*: Kiran Kumar Thingbaijam
- *Co-chair, Tech Team*: Martijn van den Ende
- *Co-chair, Tech Team*: Thomas Lecocq
- *Chair, Media & Branding*: Tran Huynh
- *Co-chair, Standards & Copy Editing*: Théa Ragon
- *Co-chair, Standards & Copy Editing*: Hannah Mark

2021-2022 Journal-Building Task Forces

After recruitment of the Seismica Board in late 2021-early 2022, Task Forces were struck to accelerate the journal-building process. Some of the task forces evolved into permanent functional teams within Seismica's organizational structure and others were retired or replaced.

Policy Development - retired 2022

This task force led decisions on journal policies, including designing article types, drafting the scope, addressing ethics and competing interests.

- Carmine Galasso (Chair)
- Martijn van den Ende
- Åke Fagerang
- Gareth Funning
- Stephen Hicks
- Kiran Kumar Thingbaijam
- Nicola Piana Agostinetti
- Théa Ragon
- Randy Williams

Guidelines Development - retired 2021

This task force drafted guidance for editors, reviewers, and authors, delineated the peer review process and paper handling workflows.

- Stephen Hicks (Chair)
- Théa Ragon
- Hannah Mark
- Martijn van den Ende
- Kiran Kumar Thingbaijam
- Thomas Lecocq
- Samantha Teplitzky
- Carmine Galasso
- Tran Huynh
- Andrea Llenos

Tech Team

This task force built the journal website using OJS, coordinated with McGill University Library and IT staff, and developed article templates, and collaborated on data/code availability policies.

- Samantha Teplitzky
- Thomas Lecocq (co-Chair)
- Martijn van den Ende (co-Chair)
- Théa Ragon
- Hannah Mark
- Dragos Toma-Danila
- Jesper Sören Dramsch

Equity, Diversity & Inclusion Team

This team is responsible for EDI policies and oversight at Seismica, through independent initiatives and embedding in all other processes at the journal.

- Catherine Rychert (Chair)
- Kasey Aderhold
- Danielle Sumy
- Lauren Waszek
- Marino Protti

Organizational Structure Team

This team is responsible for completing and maintaining the organizational structure of Seismica through policy development and review.

- Christie Rowe (Chair)
- Samantha Teplitzky
- Åke Fagerang
- Nicola Piana Agostinetti
- Greg Beroza
- Kasey Aderhold
- Daniellle Sumy
- Gareth Funning
- Martijn van den Ende
- Carmine Galasso
- Catherine Rychert

Media & Branding Team

This task force developed a brand identity for Seismica and develops polished, coherent, professional messaging across all platforms to promote Seismica and grow our international community.

- Tran Huynh (Chair)
- Jaime Convers
- Matthew Agius
- Ezgi Karasozen
- Quentin Brissaud
- Shiba Subedi
- Abhineet Gupta

Standards & Copy Editing Team

This team creates and maintains the manuscript submission and publication templates, copy edits manuscripts, interfaces with authors to quality check figures and data/code availability.

- Hannah Mark (Chair)
- Théa Ragon (Chair)
- Karen M. Pearson
- Keyla Carlina Ramirez Loaiza
- Cláudia Reis
- Kirsty Bayliss
- Abhineet Gupta

Fast Reports

This task force drafted the Fast Reports guidelines and continues to serve as Handling Editors managing Fast Reports submissions.

- Kiran Kumar Thingbaijam (Chair)
- Tiegan Hobbs
- Ryo Okuwaki

Handling Editors

These Seismica Board Members manage the review process, interact with authors, and are led by the Editorial Mentoring group. The Editorial Mentoring team joins with senior editors from Tektonika to develop Mentoring Resources to serve both journal communities.

- Greg Beroza (Chair: Editorial Mentoring)
- Åke Fagereng (Editorial Mentoring)
- Suzan van der Lee (Editorial Mentoring)
- Yen Joe Tan (Editorial Mentoring)
- Vitor Silva
- Pathikrit Bhattacharya
- Andrea Llenos
- Atalay Ayele
- Mathilde Radiguet
- Alice-Agnes Gabriel
- Randy Williams
- Lise Retailleau
- Pablo Heresi
- Paula Koelemeijer
- Wenbin Xu

Logo Design

- Adam Pascale
- Lucía Pérez-Díaz

B Appendix : Seismica Board Role Descriptions

These roles descriptions include tasks related to startup/journal building as well as long-term management and operations of Seismica as we are at the time of this writing in the early months of operation. The Management Board is comprised of the Executive Editors and the Team Chairs (Figure 2).

Executive Editors

Production: Check over incoming submissions for compliance with Seismica policy, communicate with authors over needed changes, assign handling editors, monitor progress of articles through the workflow, identify gaps in policy or board member thematic coverage, attend Executive Editors and Board meetings, monitor and occasionally raise issues in Slack, possibly more things that will arise once articles go into production.

Operations: Coordinate development of editorial policies, including guidelines for authors and reviewers. Collect feedback on editorial policies and support their periodic review based on identified gaps. Attend Executive Editors and Board meetings. Support Executive Editor for production, assigning handling editor and monitoring progress of articles through the workflow.

Community: Manage communications within Seismica, plan meetings including Executive, Management Committee and Board, represent Seismica to other organizations (including sister journals and scientific societies), coordinate activities of Teams and Task Forces.

Equity Diversity Inclusion: Plan, organize, run meetings; solicit input on journal policies, procedures, philosophies, mission statement; run brain storming sessions on wish list/ways to enhance EDI; recruiting handling editors from a diverse background; drafting/editing code of conduct; developing and revising plan for demographic data collection; communicating with Seismica.

Open Science: work with Tech team to incorporate open science practices, look for opportunities to extend the usefulness of OJS and connect with other products to expand Seismica's *openness* beyond articles, generally critique workflows.

Teams

Media & Branding Chair: Create and maintain an online brand identity across all media platforms used for the journal and its community. Ensure the key messages about Seismica are consistent, engage the broader

community promoting the journal and the opportunities for contributing to the Seismica initiative. Coordinate the different activities pertaining to the Media and Branding of Seismica across different social media and communication platforms.

Media & Branding Team Member: Carry out the work ensuring the success of Seismica's branding strategy, led by the Team Chair in discussion with Team Members. Members are organized in task forces focusing on: Meetings & Conferences, Seismica Ambassadors Program, Social Media Communications, Upcoming Publications and News, and Creative Content & Messaging. Task forces consist of a lead and a support member. Weekly meetings of the entire Team and coordination with the Management Committee ensure continuity.

Tech Team Chair: Handle incoming requests for additions/changes on the Seismica website, the editorial system, and the reviewer database. Assign plannable tasks to Tech team members, handle urgent tasks yourself. Monitor the tech@seismica.org mailbox. Answer technical queries in Board meetings and on Slack. Maintain the test editorial system sandbox and interact with the copy editing/production team to produce the pdf/html articles.

Tech Team Member: Work on assigned tasks (listed on GitHub or assigned directly on Slack), participate in technical discussions/queries on Slack.

Standards & Copy Editing Team Chair: Develop and maintain templates for article submission and publication; develop and maintain tools for converting submissions into $\text{T}_\text{E}\text{X}$ and JATS formats (with help from the Tech team as needed). Work with team members to set standards and expectations for copy editing accepted articles. When articles are accepted, assign them to team members (team chairs included) for copy editing and typesetting, ensuring workload is evenly distributed. Help team members with any issues related to typesetting, copy editing, or communication with authors/editors. Answer questions in Board meetings and on Slack.

Standards & Copy Editing Team Member: Set standards and expectations for style guides and copy editing accepted articles. When handling a manuscript, correct typos and grammatical errors that were not caught during review, and provide suggestions for style-related edits. Convert submission template to proofs and engage with the authors to check proofs before publication. Convert proofs to PDF and XML galleys, including article metadata.

Fast Reports Chair: Facilitate effective team collaborations through active communications with team members, organizing team meetings and developing work plans. Coordinating with Media & Branding for promotion of Fast Reports. Establishing and communicating criteria for publishability, providing rapid reviews and seeking external reviewers, author commu-

nications, maintaining fast workflows.

Fast Reports Team Member: Handle submissions, provide rapid review of the submissions, assess state of revised manuscripts and make decisions, communicate with authors regarding process and decisions, contribute to the Fast Reports activities. Attend team meetings.

Editorial Mentoring: Provide ad hoc advising on editorial decisions to support Handling Editors, participate in the Organizational Structure design process, develop editor and reviewer best-practices and trainings, coordinating Mentoring Committee meetings and reporting back to the Seismica Board.

Handling Editors: Quality control of manuscripts, establish and maintain contact with reviewers, communicate with authors regarding process and decisions, handle conflicts in reviewers' opinions, assess state of revised manuscripts and make decisions, upload reviews report to website, attend Board meetings. Volunteer for Seismica Board task forces as able.